MODELING OF METAL CUTTING AS PURPOSEFUL FRACTURE OF WORK MATERIAL

By

Yalla Mussa Abushawashi

A DISSERTATION

Submitted to
Michigan State University
in partial fulfillment of the requirements
for the degree of

Mechanical Engineering – Doctor of Philosophy

2013

ABSTRACT

MODELING METAL CUTTING AS PURPOSEFUL FRACTURE OF WORK MATERIAL

By

Yalla Mussa Abushawashi

Metal cutting, or simply machining, is one of the oldest processes for shaping components in the manufacturing industry. It is widely quoted that 15% of the value of all mechanical components manufactured worldwide is derived from machining operations. The most influential model for metal cutting is the single–shear plane model (SSPM) of chip formation. The common notion is that new surfaces are formed simply by ‘plastic flow around the tool tip’ so that metal cutting is one of the deforming processes. A number of cutting theories and the finite element method (FEM) models have been developed based on this concept. Metal cutting simulation models are available in commercial FEM packages. However, these model predictions and numerical simulations do not agree with the trends and phenomena observed in metal cutting experiments. Therefore, it is of the utmost importance to have a physically sound model of metal cutting.

This thesis is based on the concept that metal cutting is the purposeful fracture of the work material. To reduce the energy required for fracture, one should minimize the energy of plastic deformation of the work material in its transformation into the chip because this energy constitutes up to 80% of the total energy required by the cutting system. Increased tool life and machining efficiency are the outcomes of such an optimization. To investigate this concept requires a work material model which considers the entire process from plastic deformation, damage initiation to final fracture.

In this thesis, a work material model was developed based on the recent advancement in ductile fracture of metals. The model parameters must be determined under conditions that are pertinent to metal cutting. In machining, the work material experiences a complex, evolving multi–axial stress history. The existing testing specimens such as the notched bars and flat grooved specimens do not cover the stress triaxiality range found in machining. To generate material parameters needed in the model, a novel double–notched specimen is developed. This new specimen can cover a wide range of stress triaxiality from -0.25 to 0.6. For steel AISI1045, the plastic strain at damage initiation decreased from 0.81 to 0.17 in this range.

The developed model was implemented in the FEM package ABAQUS as a user material model and used in the investigation of orthogonal metal cutting. A number of practical machining cases were investigated, including the effect of the cutting tool rake angle, cutting feed, tool–chip interface friction, and chip breaking tool features. The model predictions for these cases agreed with the trends known in metal cutting. This is a significant improvement from the published works where the model predictions often yielded different trends from the experimental results.

Different from the common practice to report the stress, strain and temperature plots, this work examined the stress triaxiality state in the primary deformation zone. It shows that the influence of the above machining parameters on the stress triaxiality correlated to the cutting force. A parameter change that resulted in an increase in the stress triaxiality reduced the cutting force, i.e. reducing the strain energy to fracture, and vice versa. This work demonstrates that metal cutting should be considered as the purposefully fracture of work material. A machining process can be optimized by minimizing the energy of plastic deformation of the work material in its transformation into the chip.

Dedicated to the memory of my beloved brother Tarek

ACKNOWLEDGEMENTS

My deepest gratitude is to my adviser Dr. Xinran Xiao. I have been amazingly fortunate to have an advisor who gave me the freedom to explore on my own and at the same time the guidance to recover when my steps faltered. Xinran taught me how to question thoughts, express ideas, and become an independent researcher. Her words always inspire me and bring me to a higher level of thinking.

My profoundest appreciation is to my co–adviser Professor Viktor Astakhov for his unreserved help, advice and guidance. His unsurpassed knowledge and experience have played a crucial role in the development of the ideas and approaches presented in this research. His insightful comments and constructive criticisms helped me consistently improve my work. I am grateful to him for holding me to a high research standard.

Special thanks to my committee members, Professors Martin Crimp, Patrick Kwon, and Thomas Pence for their direction, guidance and helpful suggestions. Their remarks have served me well and I owe them my heartfelt appreciation.

I am thankful to my colleagues and best friends, Chris Cater, Danghe Shi, Fang Hou, Husam Abdulrahman, Malek Alaweni, Marie Wang, Shutian Yan, Vahid Khademi, Wei Zhang, and Dr. Wei Wu for their interest in my work and for all the great memories. I also would like to extend my appreciation to the University of Tripoli in Libya for the scholarship award.

Finally, and most importantly, I would like to thank my family for their truthful care and support. My warmest thanks to my parents for their patience and everything they have done for me to become what I am today.

TABLE OF CONTENTS

LIST OF TABLES ix

LIST OF FIGURES x

KEY TO SYMBOLS AND ABBREVIATIONS xviii

Chapter 1: Introduction 1
1.1 Justification to the Prerequisite Criteria 1
1.1.1 Practical Need 1
1.1.2 Technological Development and Timing of Scientific Research 2
1.1.2.1 Machine Tools 4
1.1.2.2 Tool Holders and Tool Pre–setting Practice 4
1.1.2.3 Advanced Cutting Process Monitoring 5
1.1.2.4 Advances in Cutting Tool Materials and Tool Manufacturing 6
1.1.3 Inadequacy of Current Body of Knowledge to Solve Emerging Issues 8
1.1.3.1 The Prevailing Physical Model 9
1.1.3.2 FEM Developments 12
1.1.3.3 Commercial FEM Metal Cutting Modeling Packages 13
1.1.3.4 Specialists Qualification 14
1.2 Limitation of the Current Physical Model 15
1.3 Stages in Developing a Realistic Model of Metal Cutting 20
1.3.1 Work Material Flow Behavior 20
1.3.2 Fracture in Metal Cutting 21
1.3.2.1 Historic Debate on the Presence of Crack in Metal Cutting 22
1.3.2.2 Common Perception of Crack Absence 25
1.3.2.3 Ductile vs. Brittle Work Materials 30
1.3.2.4 Crack Notion by Recent Studies 31
1.4 Underlying Principles of the Thesis 36
1.4.1 System Definition of Metal Cutting 36
1.4.2 Deformation Law 40
1.5 Objective/Sub–Objectives and Scope of Research 40
1.6 Overview of Dissertation 42

Chapter 2: Material Modeling 44
2.1 Multi–Axial State of Stress in Metal Cutting 44
2.2 Considerations for Constitutive Models 49
2.2.1 Fracture Criteria in Ductile Metals 49
2.2.2 Stress State Parameterization 52

2.2.3 Fracture Locus under Special Loading Conditions 53
2.3 Metal Cutting Specific Loading Condition....53
2.3.1 Stress State....54
2.3.2 Strain Rate 56
2.3.3 Thermal Softening 57
2.4 Material Constitutive Equations 58
2.4.1 Plasticity Model 58
2.4.2 Damage Model....59
2.4.2.1 Damage Initiation Model 60
2.4.2.2 Post Damage Contribution 62
2.4.2.3 Strain Rate Sensitivity....65
2.5 Conclusions....68

Chapter 3: Material Characterization Experiment....70
3.1 Ductile Fracture Experiments 70
3.1.1 The Classical Flat Grooved Specimen....72
3.1.2 The Proposed Plane Strain Specimen 81
3.1.3 Experimental Setup....84
3.2 Model Calibration Approach 86
3.3 Results and Discussions....88
3.3.1 Material Young's Modulus Parameter Identification 90
3.3.2 Plasticity Parameters Identification 93
3.3.3 Material Damage Initiation....99
3.3.3.1 Fracture Locus....99
3.3.3.2 Crack Propagation....103
3.3.4 Material Model Validation 104
3.3.4.1 Material Flow and Damage Initiation 104
3.3.4.2 Material Damage Evolution 110
3.4 Conclusions....112

Chapter 4: FE Simulations and Validation of the Developed Model....115
4.1 Metal Cutting Validation Experiment....115
4.2 Computational Considerations for Metal Cutting Simulations....120
4.2.1 Chip Separation Mechanism....122
4.2.2 Tool–Chip Interface Friction Model....123
4.3 Model Validation 124
4.3.1 Geometrical and Chip Structure Similarities....125
4.3.2 Deformation Similarity....126
4.4 Results and Discussions....127
4.4.1 Chip Morphology 128
4.4.2 Cutting Forces....130
4.5 Conclusions....132

Chapter 5: Practical Applications of the “Energy–Triaxiality” State Relationship in Metal Cutting 135
5.1 Rake Angle 135
5.1.1 Known Facts and Unexplained Phenomena 135
5.1.2 Physics of Material Causing the Influence of the Rake Angle 137
5.1.3 Practical Considerations 144
5.1.3.1 Strength of the Cutting Tool Wedge 144
5.1.3.2 Chip Breakability 147
5.2 Uncut Chip Thickness (UCT) 147
5.3 Chip Tool Interface 151
5.4 Rake Face Shape 154
5.5 Conclusions 165

Chapter 6: Conclusions, Contributions, and Future Work 167
6.1 Concluding Remarks 167
6.2 Contributions to Science and Technology of Metal Cutting 170
6.2.1 Damage and Fracture in Metal Cutting 170
6.2.2 Deformation Law of Metal Cutting 173
6.2.3 Testing Methodology for Metal Cutting Model Validation 174
6.3 Recommendations and Future Work 176

APPENDICES 180
Appendix A: Analysis of the Prevailing Model of the Materials Behavior in Metal Cutting 181
Appendix B: Energy Measures in Orthogonal Metal Cutting 204
Appendix C: Material User Subroutine 222

BIBLIOGRAPHY 231

LIST OF TABLES

Table 3.1: The initial, final, and average stress triaxiality calculated using numerical simulation results for steel AISI 1045 78

Table 3.2: Specimen geometrical configurations used in the experiment 88

Table 3.3: JC material model parameters for steel AISI 1045 obtained from the double–notched testpiece and compared with other references 97

Table 3.4: Experimental equivalent plastic strains matched with the numerical stress triaxiality state at damage initiation for steel AISI 1045... 101

Table 4.1: Cutting condition used in the FE validation model 121

Table 4.2: Characteristics of chip morphology and cutting forces (F_c) 129

Table 5.1: Test matrix and the cutting conditions used to investigate triaxiality state effect on the cutting process energy.. 136

Table A.1: Energy balance in machining (steel 1045).. 186

Table B.1: Values for n and K for metals at room temperature [147]....................................... 212

Table B.2: Work materials and flow curve constants used in the tests [76]............................... 214

Table B.3: *Po–criterion* and contact length obtained from FE and Equation (B.23)................. 217

LIST OF FIGURES

Figure 1.1: Components of the successful modeling. For interpretation of the references to color in this and all other figures, the reader is referred to the electronic version of this dissertation. 8

Figure 1.2: Single–shear plane model 10

Figure 1.3: Original (a) and modified (b) force diagrams 11

Figure 1.4: Typical results of FEM simulation: (a) temperatures, (b) plastic strains [18] 13

Figure 1.5: Result of FEM modeling of turning using Third wave AdvantEdge commercial package [19] 14

Figure 1.6: Relation between φ and (μ - γ) for lead: (1) Ernst and Merchant solution, (2) Lee and Shafer solution, (3) experimental results [26] 17

Figure 1.7: Comparison between calculated and experimental results for tin, aluminum, mild steel, lead and copper [26] 17

Figure 1.8: Relation between φ and (μ - γ) for steel SAE 1113 [27] 18

Figure 1.9: Comparison between the estimated and experimentally obtained relationship "shear stress–normal stress" for copper (a) and steel (b) [24] 18

Figure 1.10: Comparison of the cutting force components in longitudinal turning [2] 21

Figure 1.11: Mechanisms of chip formation at low (left) and high (right) cutting speed by Nicolson [41] (the texts in this figure are the dimensions of the cutting system and the interpretation of the chip formation by Nicolson. Left: grid scale is 9x40, size 0.016 in, rake angle is 60º, and shear plane angle is 109º. Right: 6 in rad) 23

Figure 1.12: Models of the cutting process: (a) preset–day model, (b) earlier misconception [8] 25

Figure 1.13: Crater wear on turning tools according to ANSI/ASME tool life testing with single–point turning tools (B94.55M–1985) 27

Figure 1.14: Tool–chip interface (a) and distribution of the normal and shear stress over this interface (b) [28] 27

Figure 1.15: Regions of tool wear in metal cutting [8] 28

Figure 1.16: Card model to represent chip formation 29

Figure 1.17: Typical structure of medium–carbon steel chip 30

Figure 1.18: Photomicrograph of partially formed discontinuous chip. Material: β brass; rake angle: 15º; depth of cut: 0.008 in; cutting speed: 0.5 in/min; no cutting fluid [47] ... 32

Figure 1.19: Formation of a typical discontinuous chip. Work material: high lead bronze; depth of cut: 2.7 mm; rake angle: 10º; cutting speed: 25.4 mm/min; no coolant [62] 32

Figure 1.20: Cracks observed ahead of the cutting tool (a) and between different phases of the work material (b) [49] 34

Figure 1.21: SEM images of chip–workpiece interface showing ductile tearing by void growth (OFHC Copper, t_1 = 0.050 mm, rake angle = 30º, cutting speed 1.2 m/min, edge radius = 0.007 mm) [67] 35

Figure 1.22: System consideration of the metal cutting model [73] 39

Figure 2.1: Formation of the neck and fracture in tensile testing [77] 45

Figure 2.2. Deformation pattern in compression: (a) specimen with the scribed grid, (b) distortion of the initial grid due to frictionless contact (c) distortion of the initial grid due to interface friction 47

Figure 2.3. Deformation pattern in cutting: (a) distortion of the initial grid, (b) the interaction between the tool rake face and the partially formed chip 48

Figure 2.4: Typical fracture locus for a number of special loading conditions in strain–triaxiality space 54

Figure 2.5: Representations of orthogonal (a) and oblique (b) cutting 55

Figure 2.6: Experimental vs. JC stress–strain curve for steel AISI 1045 59

Figure 2.7: Typical metal true stress–strain response in a uniaxial test 63

Figure 2.8: Scalar damage variable at different values of the exponent parameter β 64

Figure 2.9: The strain rate impact on the equivalent fracture strain at different stress states for steel AISI 1045 68

Figure 3.1: General fracture locus surface for ductile metals as postulated by Bai et al. [87] (reproduced) 71

Figure 3.2: Steel AISI 1045 plane strain flat specimens with different groove radius [87] 72

Figure 3.3: Symmetric FE simulation with the stress triaxiality contours at fracture for three selected flat–grooved specimens made of steel AISI 1045. Specimen (a) groove radius R=12.7 mm, ligament thickness t_o=1.62 mm, specimen (b) R=3.97 mm, t_o=1.55 mm, and specimen (c) R=1.59 mm, t_o=1.60 mm.. 74

Figure 3.4: Stress triaxiality evolution diagram of steel AISI 1045 obtained from FE simulation for three selected flat–grooved specimens 75

Figure 3.5: Steel AISI 1045 fracture locus in plane strain condition fitted to Rice and Tracey [78] model based on initial stress triaxiality, average using displacement limit simulation model, average using strain limit model, and the fracture locus based on strain at fracture. Stress triaxiality evolution curves are also shown. 77

Figure 3.6: Fracture locus visibility for steel AISI 1045 using flat–grooved and tubular specimen [87] 80

Figure 3.7: The double–notched specimen (a) design drawing and (b) prototype 81

Figure 3.8: FEA stress triaxiality evolution for the developed specimen made of steel AISI 1045 82

Figure 3.9: FEA stress triaxiality state contours of the proposed specimen made of steel AISI 1045 for pressure angle equal to 60º 83

Figure 3.10: DIC and INSTRON testing equipment setup 85

Figure 3.11: Flowchart for the material model calibration using the plane strain specimen and DIC/LE measurement 87

Figure 3.12: Load–displacement material response for steel AISI 1045 obtained using the developed specimens. 89

Figure 3.13: C90 double–notched specimen drawing shows the parameters for Equation (3.5). 90

Figure 3.14: Modulus of elasticity of steel AISI 1045 calculated from DIC measurements. 91

Figure 3.15: Secant modulus of elasticity of steel AISI 1045 optimized based on LE measurements using LS–Opt™ 93

Figure 3.16: Material plasticity identification program flowchart 94

Figure 3.17: Piecewise plasticity results for steel AISI 1045 using the proposed optimization reverse strategy 96

Figure 3.18: Steel AISI 1045 material plasticity modeled using JC law and obtained by a number of researchers 98

Figure 3.19: Piecewise material plasticity flow for steel AISI 1045 obtained by the double–notched testpiece and compared with the results from Bai et al. [87] using standard torsional testpiece 99

Figure 3.20: Typical contour of the shear strain field of C90 DIC experiment 100

Figure 3.21: Shear strain progression along the spacemen gauge line AB (Figure 3.20) using DIC 101

Figure 3.22: Fracture locus obtained from DIC experiment in plane strain condition for steel AISI 1045 102

Figure 3.23: FE simulations of the damage initiation site and crack propagation in the double–notched specimen. High triaxiality or tensile (C110). Law triaxiality or compressive (C60) 104

Figure 3.24: FE simulation of the double notched specimen made of steel AISI 1045 compared with the DIC experiments. (a) Plane–symmetry plane strain FE mesh. (b) FE shear strain contours. (c) DIC shear strain contours 105

Figure 3.25: FE load–displacement response compared with the experiments of C60 specimen 106

Figure 3.26: FE load–displacement response compared with the experiments of C80 specimen 107

Figure 3.27: FE load–displacement response compared with the experiments of C90 specimen 107

Figure 3.28: FE load–displacement response compared with the experiments of C100 specimen 108

Figure 3.29: FE load–displacement response compared with the experiments of C110 specimen 108

Figure 3.30: Double–notched specimens after fracture experiment 109

Figure 3.31: FE load–displacement response for steel AISI 1045 compared with the experiments – without damage evolution model 111

Figure 3.32: FE load–displacement response for steel AISI 1045 compared with the experiments–with damage evolution model 111

Figure 3.33: Fracture locus of steel AISI 1045 obtained from experiments using double–notched and flat–grooved specimens and fitted to Rice and Tracey (RT) model 113

Figure 3.34: Fracture locus of steel AISI 1045 obtained from experiments using double–notched and flat–grooved specimens and fitted to Johnson and Cook (JC) model 113

Figure 4.1: Design and prototype of the tool holder fixture developed for metal cutting model validation 116

Figure 4.2: Setup of metal cutting validation experiment 117

Figure 4.3: Optical microscope images of experimentally–obtained chips with different uncut chip thicknesses (t_1) at various magnifications 119

Figure 4.4: FE model: the undeformed mesh and the prescribed boundary conditions 121

Figure 4.5: Comparison of the basic parameters of the modeled and experimentally–obtained chips 125

Figure 4.6: Chip–A FE prediction vs. experiment – chip morphology 128

Figure 4.7: Chip–B FE prediction vs. experiment – chip morphology...................................... 129

Figure 4.8: Chip–A FE prediction vs. experiment – cutting forces 131

Figure 4.9: Chip–B FE prediction vs. experiment – cutting forces 131

Figure 4.10: Chip–A triaxiality state parameter contours obtained from FEA.......................... 132

Figure 4.11: The SEM microstructure of chip formation at cutting speed of: (a) 30.8 m/s, (b) 38.6 m/s, (c) 67.3 m/s obtained by Ye et al. [110].. 133

Figure 5.1: Sense of the positive (a), neutral (b), and negative (c) rake angles in turning 136

Figure 5.2: FE simulations of chip formation showing triaxiality state contours obtained from cutting tools with different rake angles.. 139

Figure 5.3: FE simulations of chip formation showing chip structure obtained from cutting tools with different rake angles.. 140

Figure 5.4: FE predictions of the cutting force for the cutting tools having different rake angles 141

Figure 5.5: Simplified force model for machining with a tool having a high rake angle 142

Figure 5.6: Chatter marks on the machined surface 143

Figure 5.7: FE predictions of radial forces obtained from cutting tools with different rake angles 144

Figure 5.8: Shear Geometry® cutting tool, formed chip and high–rake insert (Robertson Precision, Inc (Redwood City, CA))... 146

Figure 5.9: Typical high rakes CCGT insert.. 147

Figure 5.10: FE simulations of chip formation showing chip structure and stress triaxiality state contours obtained for various uncut chip thicknesses.. 148

Figure 5.11: FE predictions of cutting forces obtained for various uncut chip thicknesses 149

Figure 5.12: Energy required per unit volume of removed material for various uncut chip thicknesses 150

Figure 5.13: FE predictions of radial forces obtained for various uncut chip thicknesses 150

Figure 5.14: FE simulations of chip formation showing chip structure and stress triaxiality state contours obtained for different friction values of the tool–chip interface 152

Figure 5.15: FE predictions of the cutting forces obtained for different friction values of the tool–chip interface 153

Figure 5.16: FE predictions of radial forces obtained for different friction values of the tool–chip interface 154

Figure 5.17: Chipbreaking steps on the tool rake face 155

Figure 5.18: Conventional chip groove 155

Figure 5.19: Some designs of the rake face of modern cutting inserts 156

Figure 5.20: Basic rake face shapes used by Seco Tools Co. 157

Figure 5.21: Chip shape and morphology in OMC of steel 1045 with zero rake angle 159

Figure 5.22: Chip shape and morphology in OMC of steel 1045 with zero rake angle when a chipbreaking step is applied on the tool rake face 160

Figure 5.23: Chip shape and morphology in OMC of steel 1045 with zero rake angle when a standard chipbreaking groove is applied on the tool rake face 160

Figure 5.24: Chip breaking mechanism (a) by chip/work surface contact, (b) by chip/tool flank surface contact (three–dimensional chip breaking) [126] 161

Figure 5.25: Chip shape and morphology in OMC of steel 1045 with zero rake angle and a bulge or ‘bump’ on the tool rake face 164

Figure 6.1: FE model of chip formation showing equivalent plastic strain fringes (MC–RA20–UCT150, MAT STEEL AISI1045) (a) deformation only material model (b) material modeled with active damage and fracture 172

Figure 6.2: The double–notched testpiece (a) testpiece installation image (b) testpiece after fracture 173

Figure 6.3: Metal cutting model validation experiment (a) experiment setup (b) tool holder fixture (c) tool holder fixture installation 175

Figure 6.4: Optical microscope images of experimentally–obtained chips from steel AISI 1045. (a) t_1=*0.048 mm*, v_1=*0.001 m/min*, obtained by current experiment at low cutting

speed. (b) t_1=0.1 mm, v_1=120 m/min, obtained by Jaspers and Dautzenberg using quick–stop device [92] ... 178

Figure A.1: Typical distribution of heat in the workpiece, the tool, and the chips with cutting speed; after Schmidt and Roubik [133] ... 184

Figure A.2: Heat distribution between the chip, workpiece and tool [135] ... 184

Figure A.3: Areas of heat generation on the tool, workpiece and chip [138] ... 186

Figure A.4: Energies spent in the cutting system. Work material: AISI steel E52100, cutting speed v = 1 m/s, depth of cut d_w = 3 mm, cutting feed f = 0.4 mm/rev; Tool – standard inserts SNMG 432–MF2 TP2500 Materials Group 4 (SECO) installed into a tool holder 453–120141 R1–1 (Sandvik) [31] ... 188

Figure A.5: Typical temperature field in metal cutting: Isotherms for dry orthogonal cutting of free machined steel with a carbide tool at cutting speed of 155 m/min and cutting feed of 0.274 mm/rev [69] ... 189

Figure A.6: Typical temperature field in metal cutting: (a) Isotherms for dry orthogonal cutting of ANSI 1045 steel with a carbide (P10) tool (rake angle 12º) at cutting speed of 60 m/min and uncut chip thickness 2 mm, (b) Temperature distributions over the tool rake and flank faces. Turning, a carbide cutting tool carbide M20 (92% WC, 8% Co), depth of cut a_p = 1.5 mm cutting speeds in machining of steel 1045 – 240 m/min, titanium alloy (Ti6Al4V) – 160 m/min, cutting feed – 0.25 mm/rev [2] ... 190

Figure A.7: Machine used in the tests ... 192

Figure A.8: Power reading on the controller's monitor ... 192

Figure A.9: Cutting tool used in the test ... 193

Figure A.10: Relative impact of the heat generating sources in the heat balance Equation (A.2) ... 194

Figure A.11: Heat partition in the machining system in three cutting speed ranges ... 195

Figure A.12: Simplified model of chip formation in metal cutting ... 199

Figure A.13: Example of use of the Péclet number ... 200

Figure B.1: Simple model of chip plastic deformation in orthogonal cutting ... 205

Figure B.2: Log–log plot of true stress–true strain curve to determine strain–hardening exponent n and the strength coefficient K ... 211

Figure B.3: Various forms of power curve $\sigma = \varepsilon n$ ... 211

Figure B.4: Influence of the cutting speed on CCR and the work done in plastic deformation: (1) AISI steel E52100, (2) Copper, (3) Aluminum 1050 [145] 214

Figure B.5: *Po–criterion* obtained by FE for various cutting conditions and CCR 218

KEY TO SYMBOLS AND ABBREVIATIONS

A	initial yield strength parameter for Johnson–Cook material model
A_u	volume of the work material
B	hardening modulus parameter for Johnson–Cook material model
C	strain rate sensitivity parameter for Johnson–Cook material model
C_i	material fracture constants for Rice model
CZM	cohesive zone model
D	scalar damage parameter
d	specimen thickness
dA	elementary work
d_w	depth of cut
D_i	material damage constants for Johnson–Cook damage model
DIC	digital image correlation
e_x, e_y, e_z	direct strain components
E	Young's modulus
E_s	secant modulus of elasticity
f	cutting feed
F	axial reaction force
Fc	cutting forces
Fd	feed force
FE	finite element
FEA	finite element analysis

FEM	finite elements method
G_f	material fracture energy density
G_s	secant shear modulus
J_3	third invariant of the deviatoric tensor
JC	Johnson–Cook
K	strength coefficient
l_c	tool–chip contact length
L_1	length of the cut
L_2	length of the chip
LE	laser extensometer
m	thermal softening coefficients for Johnson–Cook material model
MSE	mean square error
n	hardening coefficients
OMC	orthogonal metal cutting
Pe	Péclet number
P_{pd}	power spent on the plastic deformation of the layer being removed
r	radius of the groove
SRSM	sequential response surface method
SSPM	single shear plane model
t	ligament or specimen gauge thickness
t_1, *UCT*	uncut chip thickness
t_2	chip thickness

t_f	specimen thickness at fracture
t_o	original specimen thickness
T	temperature
T_m	material melting temperature
T_o	reference or ambient temperature
u_x, u_y, u_z	projections of the displacement components
v	cutting speed
v_2	chip velocity
w	chip width
w_1	function of the hydrostatic pressure
w_2	function of deviatoric stress tensor
XFEM	extended finite element method
α	clearance angle
β	angle of chip maximum deformation
θ	Lode angle
$\bar{\theta}$	normalized Lode angle
ζ, *CCR*	chip compression ratio
$\Delta\bar{\varepsilon}^p$	equivalent plastic strain increase during the loading increment
$\bar{\varepsilon}$	equivalent plastic strain
$\bar{\varepsilon}_f$	equivalent strain at damage initiation
$\bar{\varepsilon}_{fd}$, $\bar{\varepsilon}_{fs}$	ductile and a shear equivalent plastic strains
$\bar{\varepsilon}_c^p$	plastic strain at damage initiation

$\bar{\varepsilon}_f^p$	plastic strain at the point where material has lost all its stiffness
$\dot{\bar{\varepsilon}}$	equivalent strain rate
$\dot{\bar{\varepsilon}}_o$	reference strain rate
η	stress triaxiality state parameter
η_f	stress triaxiality state parameter at fracture
η_{av}	average stress triaxiality state parameter
φ	shear plane (pressure) angle
γ	rack angle
γ_{xy}, γ_{yz},γ_{zx}	engineering shear strain components
λ	exponent parameter for damage evolution model
μ	Tool–chip friction
υ	Poisson's ratio
ω	damage indicator
ψ	material energy density
$\bar{\sigma}$	effective stress
σ_m	hydrostatic or mean stress
$\bar{\sigma}_h$	hypothetic undamaged stress
τ	shear stress
τ_{ct}	time of cutting
ξ	deviatoric stress state parameter

Chapter 1: Introduction

1.1 Justification to the Prerequisite Criteria

1.1.1 Practical Need

Many of today's metal cutting operations are conducted under less than optimal conditions. A recent survey indicates that in the automotive and mold–making industries [1]:

1. The correct cutting tool geometry is selected less than 30% of the time.
2. The tool is used at the rated cutting regime only 48% of the time.
3. Only 57% of the tools are used up to their full tool–life capability.
4. The correct tool material is selected less than 30% of the time.
5. The correct cutting fluid (coolant) parameters are used 42% of the time.

These subpar results affect the economy of manufacturing as follows:

1. *National level*. Because the USA spends approximately 160 billion dollars annually to perform its conventional metal cutting operation, the cost of subpar metal cutting performance results in overwhelming losses [2].
2. *Industry level*. Low reliability of cutting tools and random tool failures in advanced manufacturing facilities (i.e., in the automotive industry) are the major obstacles in the way of wide use of efficient unattended machining production lines and manufacturing cells to decrease the direct labor costs and improve efficiency of machining operations.

3. *Machine shop level*. In all industries, on average, perishable cutting tools seldom represent more than 8% of the total direct/indirect product manufacturing costs. For CNC machining centers and manufacturing cells where $1.00 as the benchmark; for 2,200 operating hours per year, $1.00 minute means an operating cost of $132,000 per year for just one machine (cell). Even factoring in 75% efficiency for loading/unloading, changing tools, and setup, an increase in the cutting tool penetration rate by 50% amounts to a potential yearly savings of $24,750 per CNC machining center per year. The average automotive powertrain plan has hundreds of such machine (cells). Often, doubling drilling machining can be accomplished with a simple optimization of the machining operation through proper modeling. Doubling tool life and increase its reliability up to 95% often result in savings of additional $25,000 per CNC per year due to direct labor cost, downtime and scrap reduction.

1.1.2 Technological Development and Timing of Scientific Research

Even in the recent past, the modeling of the cutting process using FEA based simulations was an expensive game, as its result could not be implemented in order to increase the efficiency of machining systems. The real cause for that is that neither the machining system as a whole nor its components was ready for the implementation of the advancements. However, the industrial technology advancements nowadays dramatically improved many of these components which become ready to fully utilize the results of such modeling.

In the not too distant past, the components of the machining system were far from perfect in terms of assuring normal tool performance, and thus gaining any application advantage of process modeling (optimization) was not possible. Tool specialists (design, manufacturing, and application) were frustrated with old machine tools having spindles that could be rocked by hands; part fixtures that clamped parts differently every time; part materials with inclusions and great scatter in the essential properties; tool holders that could not hold tools without excessive runouts assuring their proper position; low–concentration often contaminated metal working fluids (commonly referred to as coolants) which brought more damage than benefits to the cutting tool; manual sharpening and pre–setting of cutting tools; limited ranges of cutting speeds and feeds as well as insufficient power available on machines; low dynamic rigidity of machines; etc. As such, the best optimized cutting operation was performed practically the same (or even worse) as a usual set based upon machine operator's experience. As a result, any further development in the modeling of metal cutting was discouraged as leading tool manufacturers did not see any return on the investments in such a modeling.

For many years, a stable though fragile balance between low–quality (and thus relatively inexpensive) drilling tools and poor machining system characteristics was maintained. Metal cutting research was attributed mainly to university labs and their results were mostly of academic interest rather than of practical significance. It is clear that the metal cutting theory and the cutting tool designs based on this theory were not requested by the practice, as many practical specialists have not observed any application benefits of such tools.

This has been rapidly changing since the beginning of the 21st century as global competition forced many manufacturing companies, firstly the automotive manufacturers, to increase efficiency and quality of machining operations. To address these issues, leading tool and machine manufacturers have developed a number of new products – new powerful precision machines having a wide range of speeds and feeds, tool materials and coatings, new tool holders, automated part fixtures, advanced machine controllers, etc. Unfortunately, these dramatic changes were not noticed by many tool manufacturers and even researchers. Therefore, it is instructive to briefly list the major significant changes.

1.1.2.1 Machine Tools

Dramatic changes in the machine tools can be summarized as follows:

1. *Machines with powerful digitally–controlled truly–high–speed motor–spindles*. For example, machines with working rotational speed of 25,000 rpm and 35 kW motor–spindles are used in the advanced manufacturing powertrain facilities in the automotive industry. New multi–axis CNC machines with excess of power and spindles capable of 35,000 rpm rotational speed are rapidly being introduced in the mold–making industry.
2. *New spindles that assure tool runout less than 0.5 micrometers* were implemented on many machines. High static and dynamic rigidity of such spindles and machines made with granite beds result in chatter (vibration)–free performance even for the heaviest cuts at truly high–speed machining conditions.
3. *High–pressure through–tool metal working fluid (MWF) supply*. New machines are equipped with high–pressure (70 bars and more if needed) MWF (coolant) supply through the cutting tools to provide the cooling and lubrication needed for high–speed operations. MWFs cleaned up to 5 micrometers are delivered at constant controlled temperatures suitable for a given machining operation.

1.1.2.2 Tool Holders and Tool Pre–setting Practice

Old fashioned tool holders have a 7/24 taper developed over half a century ago, and are sold today as CAT, BT and ISO which are rapidly replaced with high–precision HSK holders developed according to DIN (German Institute for Standards). Balanced hydraulic, shrink fit, and steerable tool holders have been developed and widely implemented for high–speed machining to minimize tool runout and to maximize tool holding rigidity. With shrink fit the tool holder's vibration is reduced and cutting is noticeably faster and smoother, due in part to the lack of set screws and component tolerance variances.

For years, tool pre–setting was one of the weakest links in assuring tool proper position and performance. Nowadays, advanced CNC driven tool pre–setting machines (Zollar and Kelch, for example) are widely used in high–speed machining applications. Each tool assembly includes an electronically written ID number to enable users to retrieve and use this data later on. Such pre–setting machine can provide accuracy to within 3 microns on each tool, which in turn results in improved machining quality.

1.1.2.3 Advanced Cutting Process Monitoring

Many recent technologies offer tool and machine monitoring, from detecting whether an intact tool is present to measuring a tool's profile. Some can even measure the power consumed by the spindle motor and use that information to control the feed rate and minimize machining time. The most common feature of modern machine tool controllers developed for high–speed unattended manufacturing are:

- Detecting broken or absent tools.
- Power monitoring which provides performance feedback and detects broken or worn tools.
- Adaptive control option that uses power monitoring systems to optimize cutting process conditions.

1.1.2.4 Advances in Cutting Tool Materials and Tool Manufacturing

Improved quality of the machining systems allowed a wide use of modern grades of polycrystalline diamond (PCD) tool material capable of milling, drilling, and reaming of high–silicon aluminum alloys at speeds of 1,000–11,000 m/min. Modern grades of carbide tools combined with advanced coatings which allow the machining of alloyed steels at speeds of 300–600 m/min. Modern grades of PCBN *(*polycrystalline cubic boron nitride) allowed to introduce hard machining operation which substituted grinding operations. Such new tool materials and advanced grades of existing tool materials, including nanocoatings, expanded the range of machining regimes and operational limits.

There are a number of significant advances in the cutting tool manufacturing taking place rapidly. Among many, the introduction of CNC tool grinders/sharpeners and tool geometry measuring machines are probably the most significant.

For decades, manual tool grinding/sharpening machines were used in the cutting tool industry. It was not possible to maintain the geometry of ground/sharpened tool with reasonable accuracy which, moreover, varied significantly from one re–sharpening to the next. An exact tool geometry simulated by any advanced tool design program could not be reproduced by such machines. It was also not possible to grind any complicated profile of the tool, as it might be necessary in order to optimize tool performance. Naturally, any advanced tool geometry suitable for optimal performance of a machining operation was simply rejected by the machining practice as being "impractical" for a real world application. Such a situation with tool grinding has been changing rapidly since the beginning of 21st century. Today's tool grinder is typically a CNC machine tool having usually 4, 5, or 6 axes with high levels of automation, as well as automatic in–machine tool measurement and compensation which allows extended periods of unmanned production.

No matter how good is the fully optimized cutting tool geometry (using, for example, FEM simulation software) and how well it is depicted in multiple section planes on the tool drawing made using a 3D CAD program, it is practically useless if such an optimized geometry cannot be reproduced and then inspected with high accuracy. Until very recently, the most common practice of measuring tool geometry was manual inspection with not very accurate, subjective results that depend on the inspector experience, tool complexity and many other factors. Naturally, the accuracy of such inspection was not nearly sufficient for the assurance of effective performance of the cutting tool.

To address this important issue, advanced CNC tool inspection machines have been developed. For example, ZOLLER–Genius 3 measuring and inspection machine is equipped with 5 CNC–controlled axes for measurement and fully automatic inspection of virtually any tool parameter. Equipped with a 500–fold magnification incident light camera, Genius 3 can automatically inspect micro tools down to 0.1 microns. The machine includes measuring programs for practically every parameter (effective cutting angle, clearance angle, helical pitch and angle, groove depth, tumble and concentricity compensation, step measurement, etc.) of cutting tools.

All the listed and other developments were summarized as the 4th Industrial revolution in the 2013 HANNOVER MESSE trade fair – the world's biggest industrial fair held on the Hanover fairground in Hanover, Germany.

The foregoing consideration suggests that many components of modern machining systems are ready to fully implement the most efficient machining operations, and while the equipment available for tool manufacturing is fully supporting the high–efficiency production with practically no restrictions. For the first time in the manufacturing history, the capability of the machining system has becoming greater than that of the machining itself. In other words, any metal cutting process optimization effort which would result in improved machining regime efficiency can and will be fully utilized in the real word applications.

1.1.3 Inadequacy of Current Body of Knowledge to Solve Emerging Issues

The foregoing analysis suggests that the weakest link in the design of high–efficiency machining operations is the ability of its efficient modeling. Such a modeling is not an efficient tool for metal cutting specialists, namely process designers/planers, cutting tool and machine tool designs, manufacturing engineers, etc., to use it in their daily activities for the development, improvement and optimization of practical machining operations. The logical chain shown in Figure 1.1 shows the four necessary components for successful metal cutting modeling. In order to explain the cause of such deficiency, the role of each of these components will be addressed separately in the following sections.

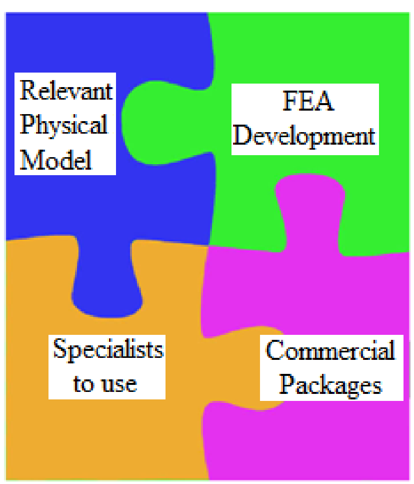

Figure 1.1: Components of the successful modeling. For interpretation of the references to color in this and all other figures, the reader is referred to the electronic version of this dissertation.

1.1.3.1 The Prevailing Physical Model

Historically, the complicated model of metal cutting is reduced to a model of chip formation that constitutes the very core of the theory and practice [3, 4]. Although a number of various models of chip formation are known to specialists in this field (e.g. those developed by Briks, Lee and Shafer, Zorev, Oxley, Jawahir, etc.), the single–shear plane model (hereafter SSPM) is still the only option for studies on metal cutting [5], computer simulations programs including the most advanced FEA packages (e.g. [6]), and student textbooks (e.g. [4, 7]).

SSPM shown in Figure 1.2 was developed using simple observations of the simplest case of machining, otherwise known as orthogonal cutting [5]. Figure 1.2 indicates that the tool is actually a cutting wedge having the rake and the flank faces that meet to form the cutting edge. The cutting force is applied to the tool so that it removes the stock of thickness t_1 (known as the uncut chip thickness) by shearing (as assumed and widely accepted in the literature on metal cutting [5, 8]) it ahead of the tool in a zone that is quite thin compared to its length, and thus can be well represented by the shear plane AB. The position of the shear plane is customarily defined by the so–called shear angle φ, as shown in Figure 1.2.

After being sheared, the layer being cut becomes the chip, which slides first along the tool rake face, following its shape (the straight portion of the chip in Figure 1.2), and then, beyond a particular point O on the tool face, it curls away from that tool face.

Merchant [9] added a force diagram to the model shown in Figure 1.2, considering forces acting in metal cutting, arrived to the force system shown in Figure 1.3 (a) (Fig. 7 in [9]). In this figure, the total force is represented by two equal, opposite forces (action and reaction) R and R', which hold the chip in equilibrium. The force R' in which the tool exerts on the chip and is resolved into the tool face–chip friction force F and normal force N. The angle μ between R and

N is thus the friction angle. The force R where the workpiece exerts on the chip is resolved along the shear plane into the shearing force, F_s which, in Merchant's opinion, is responsible for the work expended in shearing the metal, and into normal force F_n, which exerts a compressive stress on the shear plane. Force R is also resolved along the direction of tool motion into F_c, termed by Merchant as the cutting force, and into F_T , the thrust force.

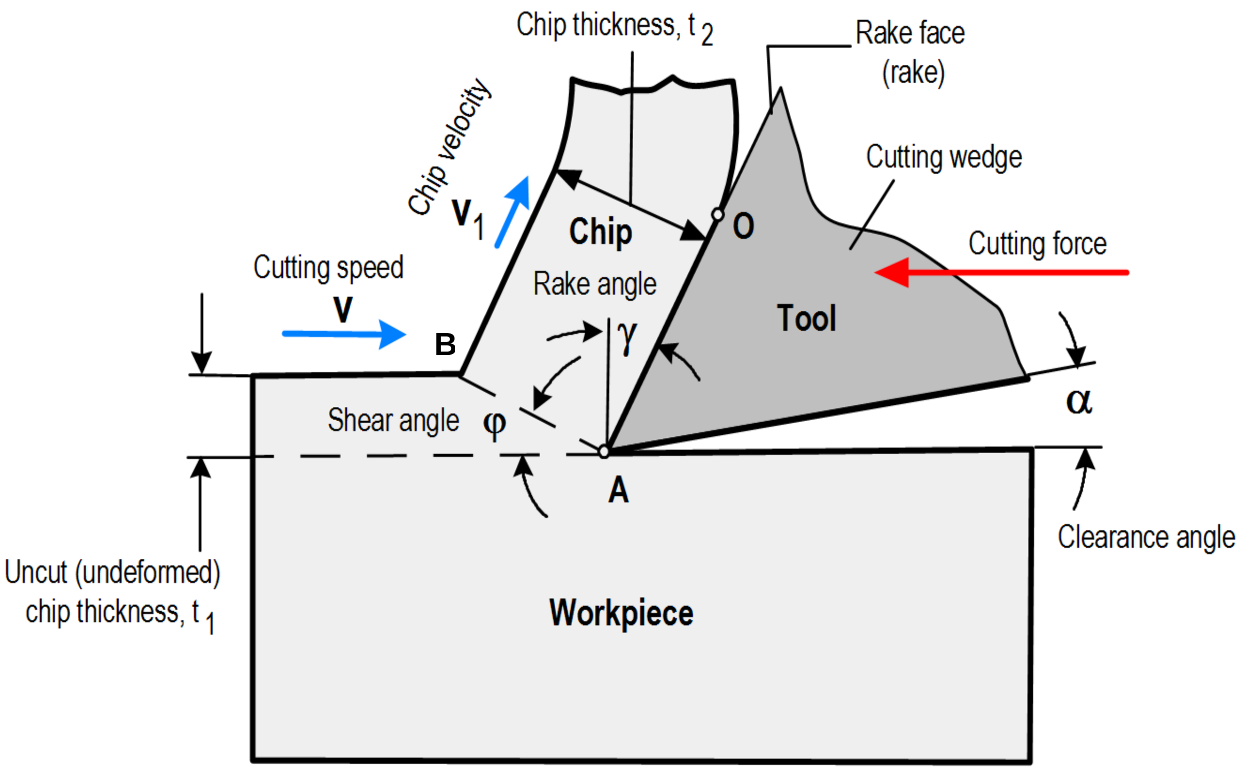

Figure 1.2: Single–shear plane model

The force and energy calculations in metal cutting are based upon determination of the shearing force, F_s using the equation proposed by Ernst and Merchant in 1941 [10]

$$F_s = s_s A_c = s_s \frac{t_1 d_w}{\sin \varphi} \tag{1.1}$$

where s_s is the shear strength of the work material, A_c is the shearing area, t_1 is the uncut chip thickness, and d_w is the width of cut in orthogonal cutting.

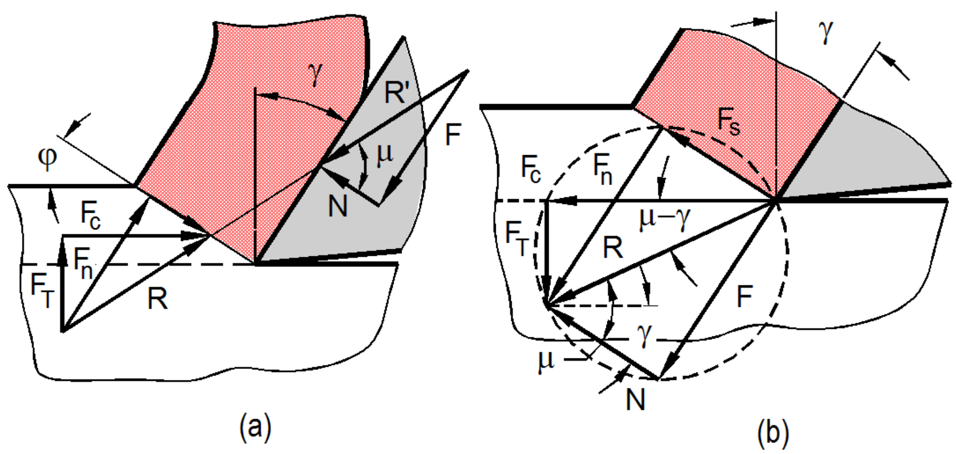

Figure 1.3: Original (a) and modified (b) force diagrams

According to Ernst and Merchant, the work material deforms when the stress on the shear plane reaches the ultimate shear strength of the work material. Later researchers published a great number of papers showing that s_s should be thought of as the shear flow stress, which is somehow higher than the shear strength of the work material depending on particular cutting conditions [11]. Still, this stress remains today the only relevant characteristic of the work material characterizing its resistance to cutting [12].

It follows from Figure 1.3 (b) that

$$F_c = \frac{F_s \cos(\mu - \gamma)}{\cos(\varphi + \mu - \gamma)} \tag{1.2}$$

Combining Equations (1.1) and (1.2), one can obtain

$$F_c = \frac{s_s A_c \cos(\mu - \gamma)}{\sin\varphi \cos(\varphi + \mu - \gamma)} \tag{1.3}$$

The cutting power P_c then is calculated as

$$P_c = F_c v \tag{1.4}$$

This power defines the energy required for cutting, cutting temperatures, plastic deformation of the work material, machining residual stress and other parameters.

The foregoing considerations show that the shear strength or, in its modern interpretation known as the shear flow, stress is the only relevant characteristic of the work material that defines its resistance to cutting and thus the power used in this process.

1.1.3.2 FEM Developments

Several numerical methods have been used in metal cutting studies, for instance, Finite Difference Method, Finite Elements Method (FEM), Boundary Element Method etc. Amongst the numerical methods, FEM is the most frequently used over the last 40 years in metal cutting simulations. Starting with two–dimensional simulations of the orthogonal cutting more than two decades ago, research progressed to the three–dimensional FEM models of the oblique cutting, capable to simulate the metal cutting operations like turning and milling [13, 14, 15, 16, 17]. Increased computation power and developed robust calculation algorithms (thus widely availability of FEM programs) are two major contributors to this progress. More than 8,000 papers have been published on the subject of finite element (FE) simulation of metal cutting, which apparently should cover all aspects of such a simulation. Figure 1.4 shows typical results of FEM used in metal cutting. The temperature and equivalent plastic strain distributions were modeled in the deformation zone, chip and the cutting tool.

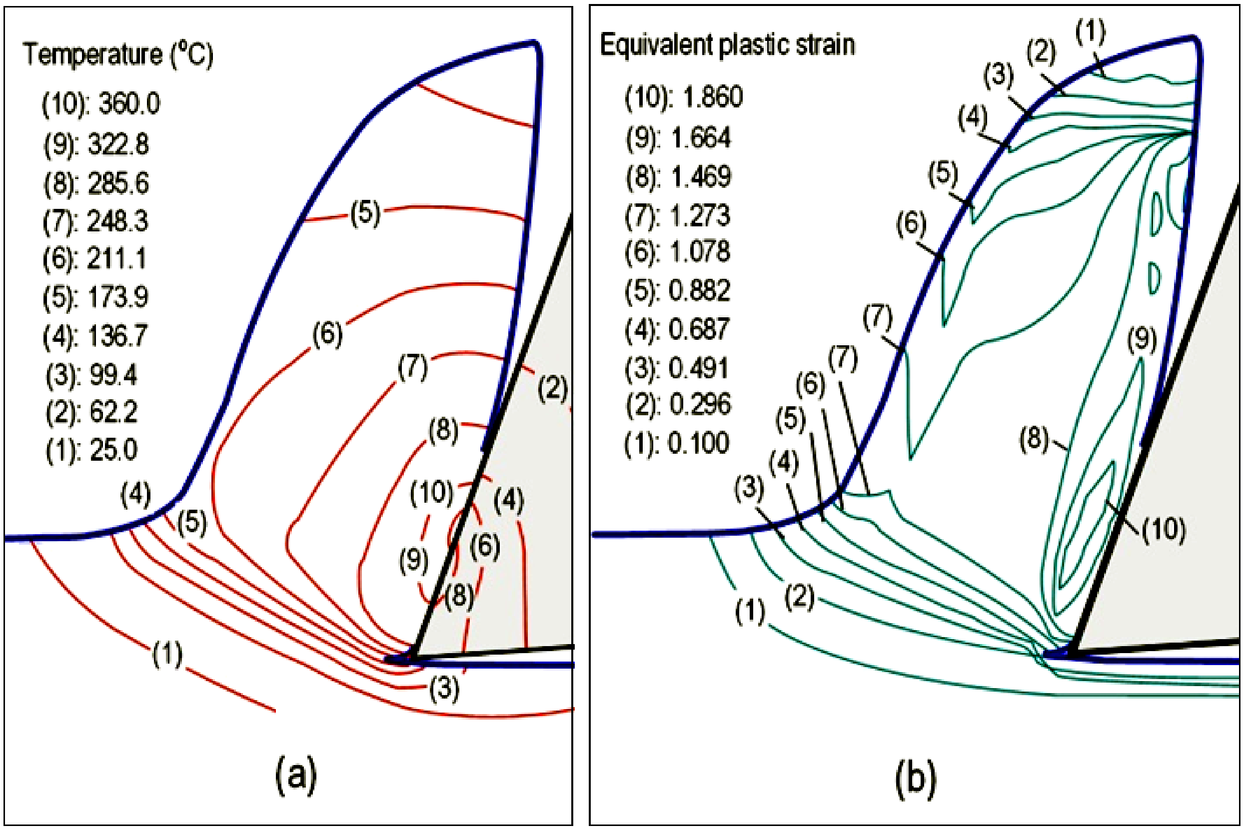

Figure 1.4: Typical results of FEM simulation: (a) temperatures, (b) plastic strains [18]

1.1.3.3 Commercial FEM Metal Cutting Modeling Packages

The commercial codes ***MSC.Marc©***, ***Deform2D©***, and ***Thirdwave AdvantEdge©*** are available to carry out 2D and 3D metal cutting simulations. Figure 1.5 shows an example of the results of FEM modeling of turning using the Thirdwave AdvantEdge commercial package. AdvantEdge 6.0 provides detailed information about chip formation, temperatures, stresses, forces, and other material behavior not accessible during trial and error tests. As claimed by the developer, the technology has become an invaluable tool for analyzing cutting tool design and performance.

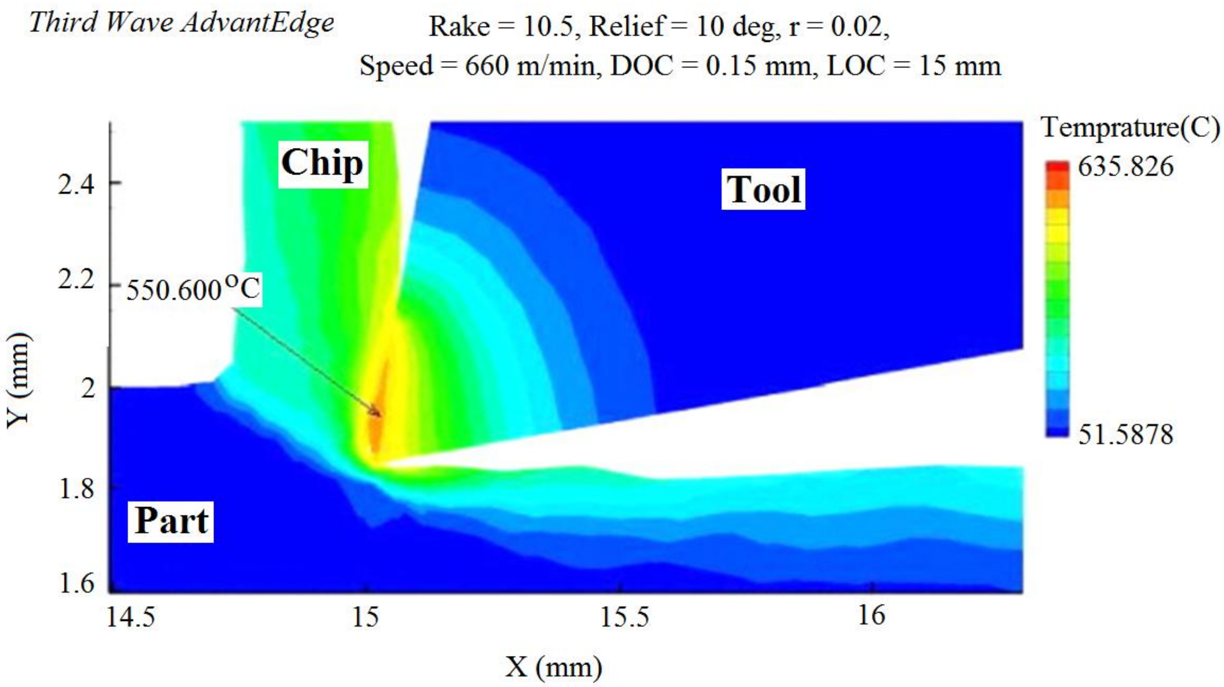

Figure 1.5: Result of FEM modeling of turning using Third wave AdvantEdge commercial package [19]

1.1.3.4 Specialists Qualification

Limited personal experience with FEM in general, and metal cutting commercial FEM packages in particular, may prevent metal cutting systems and tool developers from such technological benefits. However, today computer aided engineering (CAE) including FEM are the irreplaceable tool to almost any industry. FEM is being used worldwide to conduct research and development of new products by highly qualified engineers. As pointed out by Astakhov [20], this is not the case as many of these companies have engineers well–trained in FEM. For example in the automotive industry, FEM is used in crash safety, durability analysis, NVH (noise, vibration, and harshness), etc. In the assessment of crashworthiness of cars, engineers model hundreds of components with millions of elements that requires high performance computing (HPC), advanced FEM programs, and highly–trained specialists. As a result, only few real crash tests are performed mainly for post correlations and verifications purposes. Today's industries increasingly rely on this technology and its qualified engineers to improve quality and efficiency. To meet the economical demand, companies and educational institutions have offered their employees and students trainings and classes on FEM and its commercial packages. As a result more qualified engineers are capable to perform analyses using FEM. However unlike most other industries, the experienced specialists in metal cutting with FEM qualification in a company are less likely to use FEM for their metal cutting analysis.

The above discussion of the four components of successful metal cutting modeling reveals that FEM and its commercial package availability, and its lack of trained specialists is not breaking the chain of modeling technology in metal cutting industry. Therefore the prevailing physical model and the adequacy of the SSPM theory should be farther investigated.

1.2 Limitation of the Current Physical Model

Although SSPM is still exclusively used in metal cutting modeling (except for few exceptions), its validity was questioned even shortly after it was completed with force and energy consideration (see Equations (1.1)–(1.4)) by Merchant [9, 21]. As this model assumes simple shearing as the prime deformation mode so that metal cutting was classified as one of deforming processes, it was logical to apply engineering plasticity principles. The best known attempt was by Hill, one of the founders of engineering plasticity [22]. Trying to apply these principles, Hill noticed [23] that "it is notorious that the extent theories of mechanics of machining do not agree well with experiment."

During the period of 1950–1960, when decent dynamometers and metallographic equipment became widely available, a number of fundamental works were carried out. The results of this extensive research are well summarized by Pugh [24] and Chisholm [25]. The results obtained by Pugh were discussed by Bailey and Boothroyd ten years later [26]. In this study, it was concluded that the experimental setups used were adequate and its results were compared to the Ernest and Merchant, Merchant, and Lee and Shafer theories [12, 2]. It was shown that for every work material tested, there was a significant disagreement in the 'φ *vs.* (μ - γ)' relation between experiment and the prediction. The examples of the obtained experimental results are shown in Figure 1.6 through Figure 1.9.

Figure 1.6 shows experimental results for lead as the work material. Lead was chose as the work material because lead is chemically passive, so it forms neither solid state solutions nor chemical compositions with common cutting tool materials. Therefore, the use of lead as the work material allows for much more "pure" cutting tests. In Figure 1.6, line (1) graphically represents the Ernst and Merchant solution, (2) Lee and Shafer solution and (3) approximates the experimental results. Figure 1.7 shows the results for the various tested work materials. As seen, the experimental results are not even close to those predicted theoretically. Similar results were presented by Creveling et al. [27], and by Chisholm [25]. An example is shown in Figure 1.8 for steel 1113 where various cutting fluids were used [27].

According to Merchant, τo and k1 are work material constants and have also been examined for a wide variety of work materials. Equation (1.5) is shown plotted in Figure 1.9 (a) and (b) for copper and mild steel, respectively, together with the experimentally obtained values [24]. As can be seen, the shear stress does not increase with the normal stress at the rate required by the modified Merchant solution, i.e. to fit experimental results. In fact, it would appear that the shear stress is almost independent of the normal stress on the single shear plane.

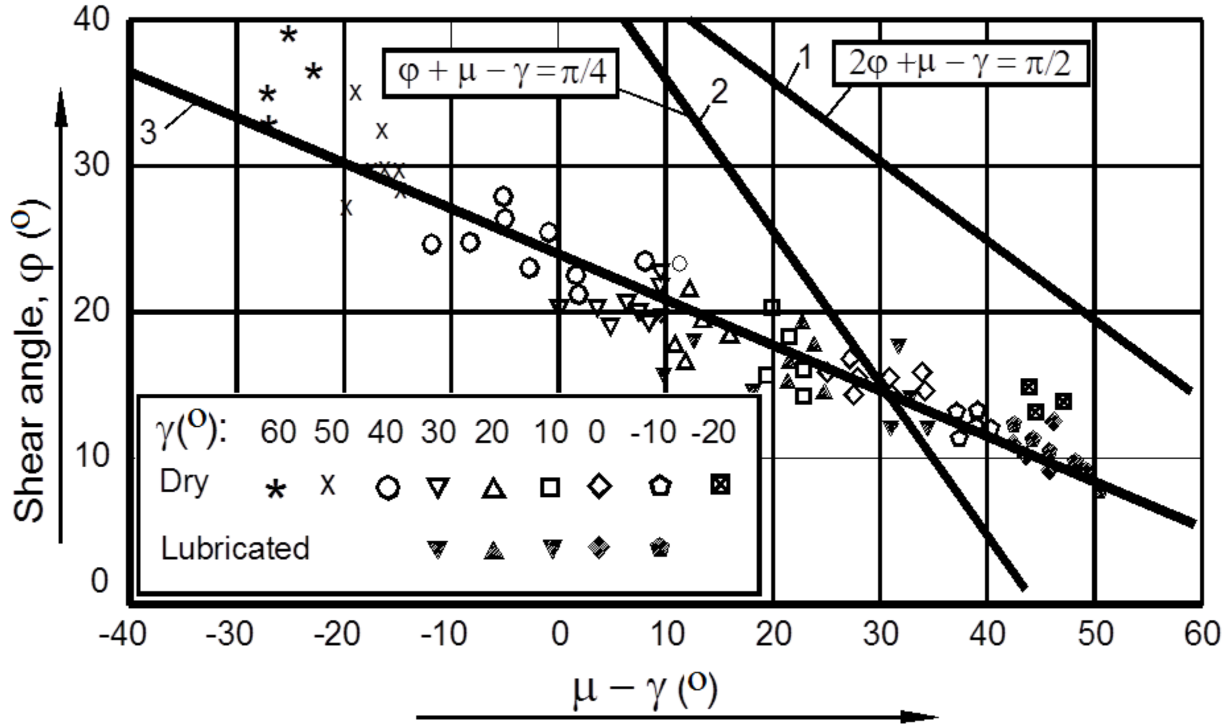

Figure 1.6: Relation between φ and (μ - γ) for lead: (1) Ernst and Merchant solution, (2) Lee and Shafer solution, (3) experimental results [26]

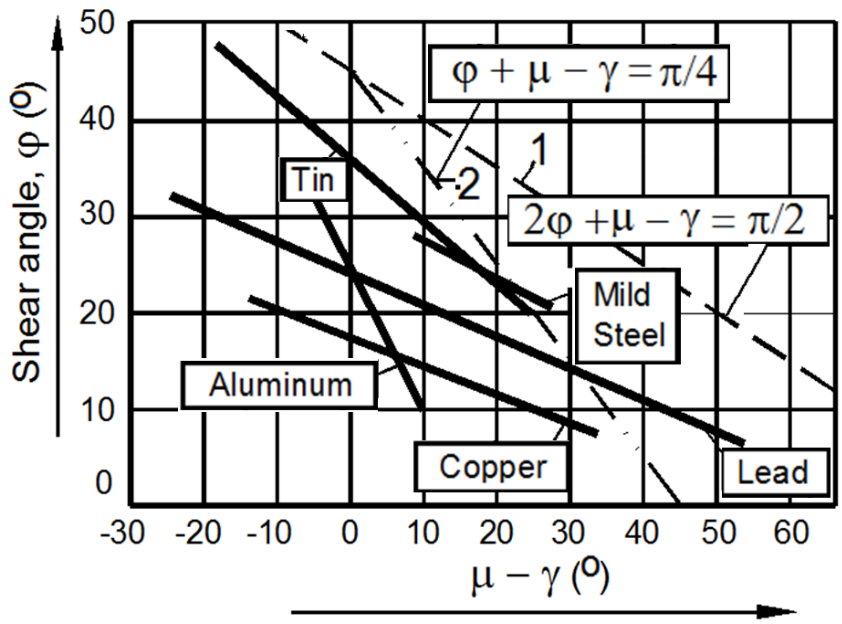

Figure 1.7: Comparison between calculated and experimental results for tin, aluminum, mild steel, lead and copper [26]

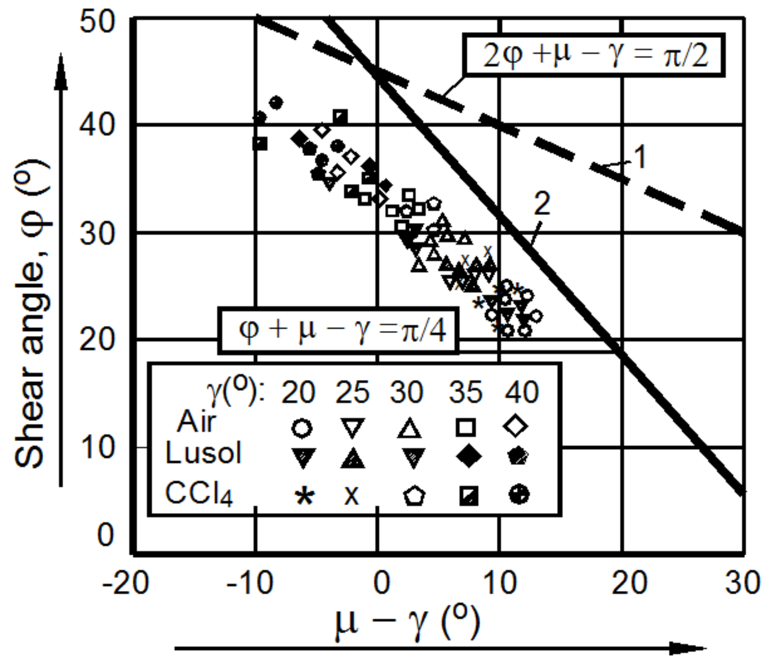

Figure 1.8: Relation between φ and (μ - γ) for steel SAE 1113 [27]

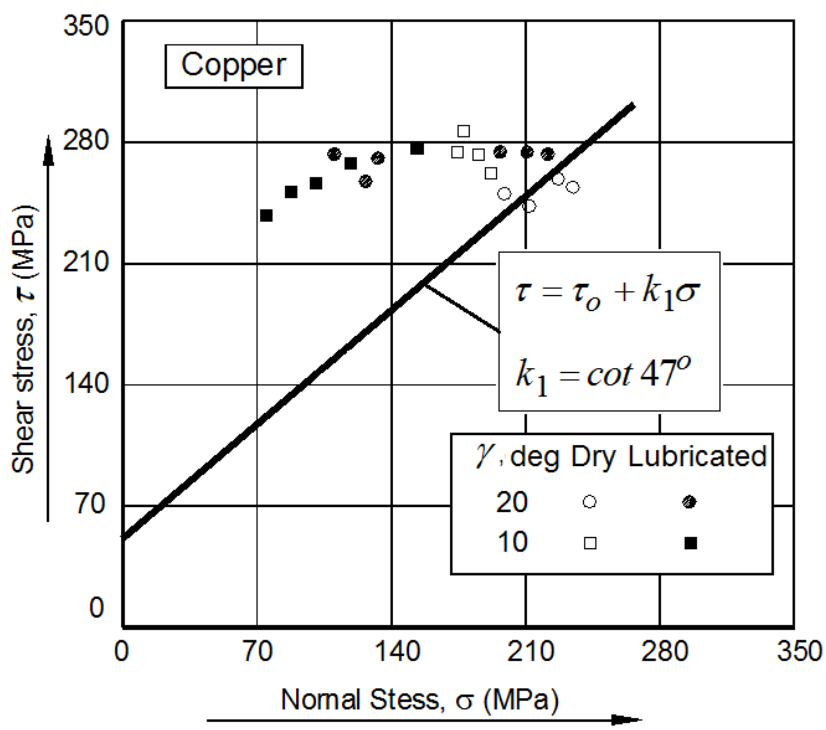

Figure 1.9: Comparison between the estimated and experimentally obtained relationship "shear stress–normal stress" for copper (a) and steel (b) [24]

The modified Merchant solution in which the shear stress is assumed to be linearly dependent on the normal stress through a factor $k_1\left(c=\cot^{-1}k_1\right)$ as

$$\tau=\tau_o+k_1\sigma \tag{1.5}$$

The above conclusions were confirmed by Bisacre [24] who conducted very similar cutting experiments. The results of these experiments enabled Bisacre to conclude that if the Merchant solution was correct, there would be a marked effect of the normal stress on the shear stress acting along the shear plane. To support his point, Bisacre noted that the results of tests carried out, in which the same material was subjected simultaneously to torsion and axial compression, showed that the shear strength of the material was almost independent of normal stress. As a result, the difference of the theoretical and experimental results cannot be attributed to the effect of the normal stress on the shear strength of the work material as suggested by Merchant.

Zorev published a book [28] which offers the results of many reliably conducted experiments using a number of different work materials, tools, and cutting conditions. He also presented clear experimental evidences that the discussed solutions are inadequate [29]. Other prominent researchers in the field conclusively proved that the experimental results are not even close to those predicted theoretically [24, 25, 27, 29]. Recent research further clarified this issue by presenting more theoretical and experimental evidence [30, 31, 2]. One of the pioneers of metal cutting research, Milton Shaw, in his book [5, p. 200] summarizing his lifetime of experience in the field, came to the discouraging conclusion that it “is next to impossible to predict metal cutting performance.”

As one might expect, knowing these results, SSPM would be just a part of history. In reality, however, this is not the case and the SSPM is still the first choice for practically all the textbooks on metal cutting used today [3, 7, 32, 33], regardless of the numerous evidences of its lack of predictability of the real word applications.

Therefore it can be concluded that the problem with the modeling of metal cutting cannot be solved using the current physical model where SSPM is the basis of all modeling efforts, including FEM.

1.3 Stages in Developing a Realistic Model of Metal Cutting

1.3.1 Work Material Flow Behavior

As pointed out by Astakhov [34], SSPM suffers severe drawbacks so it cannot be used even as a principle in modeling of metal cutting. Among many problems, the work material behavior is of prime concern. As mentioned before, Ernst and Merchant assume the work material is deforming when the stress on the shear plane reaches the shear strength of the work material as it follows from Equation (1.1). Having noticed great discrepancy of such an approach and experimental results, many researchers believed that τ_y should be thought of as the shear flow stress. Nevertheless, this material characteristic is still the only physical parameter that characterizes material behavior of the workpiece and thus the only material property which controls the chip formation.

Everyday practice of machining shows that these considerations do not match reality. For example, machining of medium carbon steel AISI 1045 (tensile strength, ultimate $\sigma_R = 655 MPa$, yield $\sigma_{y\,0.2} = 375 MPa$) results in much lower total cutting force (see Figure 1.10), greater tool life, lower required energy, cutting temperature, and machining residual stresses than those obtained in the machining of stainless steel AISI 316L ($\sigma_R = 517 MPa$;

$\sigma_{y\,0.2} = 218\,MPa$) [35]. The prime reason is that any kind of strength of the work material in terms of its characteristic stresses cannot be considered alone without corresponding strains, and most importantly a material strain limit which controls material fracture behavior and the overall required energy for a particular cutting regime.

1.3.2 Fracture in Metal Cutting

Analysing the differences between metal cutting and deforming process, Astakhov showed that fracturing in metal cutting must occur to match experimental results [1]. However, this is in direct contradiction with the prevailing notion of metal cutting as a process accomplished by plastic deformation of the work material. The idea of fracture was and is still the most criticized notion in the history of metal cutting.

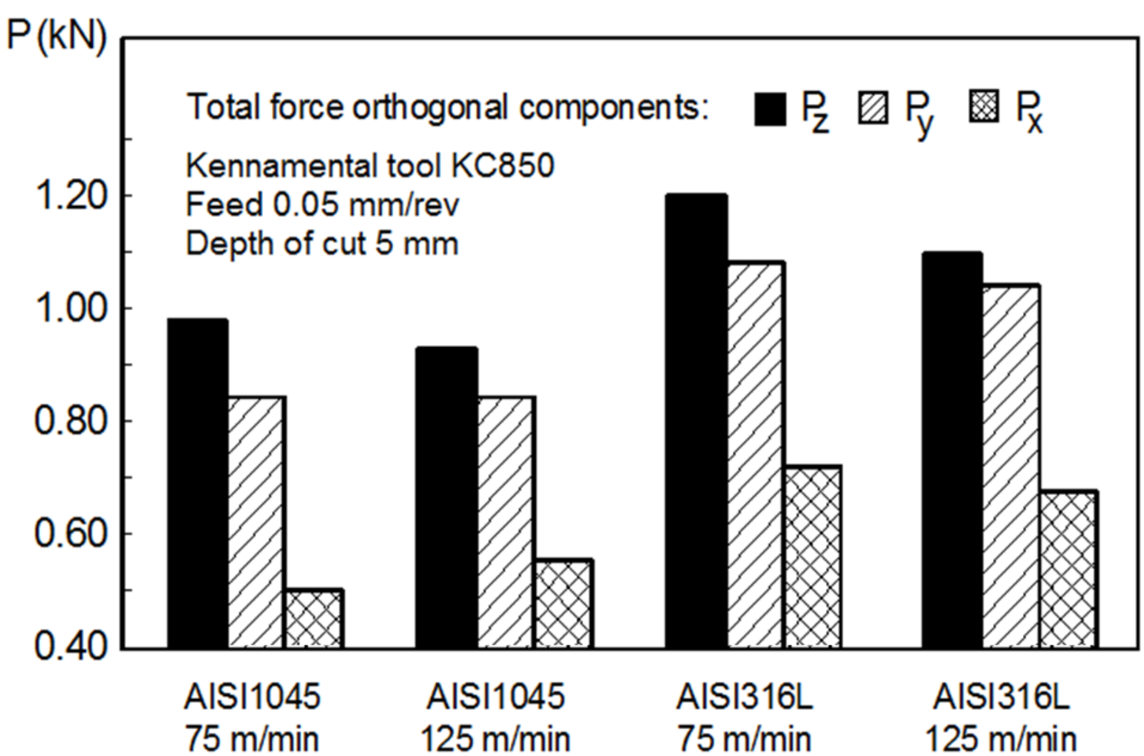

Figure 1.10: Comparison of the cutting force components in longitudinal turning [2]

1.3.2.1 Historic Debate on the Presence of Crack in Metal Cutting

The debate about the existence of crack in metal cutting goes for over a century. Franz Reuleaux of the Berlin Royal Technical Academy suggested in 1890 that fracture occurs in metal cutting, and thus cracks forms ahead of the tool [36]. This was confirmed by observations made by Kingsbury [37], who claimed that a crack ran ahead of the tool. The metal cutting fluid (coolant) was apparently reaching the point of the tool, and it was felt that this would be impossible without a crack. Reuleaux's idea was entirely rejected by the scientific and engineering community in the beginning of the 20th century. The science of metal cutting was entirely based on the ideas of Mallock [38] whose notion was a common belief that simple shearing is the prime deformation mode in metal cutting. This idea has been carried out since 1901 [39] till today [8, 40].

Probably the most convincing early results on fracture in metal cutting were presented by Frederic Taylor in his famous address to ASME in 1906 that summarized a 26–year research on metal cutting [41]. Taylor described the cutting mechanism as chip formed by tearing. His model showed that a crack forms ahead of the cutting edge along the separation line between the workpiece and the chip.

In the same volume, supplementing Taylor's published his findings in the ASME transactions (pp. 325 – in [41]), Nicolson, the chairmen Of Manchester Metal Cutting Committee (U.K.), and the inventor of the first metal cutting practical hydraulic dynamometer used in Taylor's research, presented mechanism of chip formation at low and high cutting speed shown in Figure 1.11. In his detailed explanation of the process mechanism, Nicolson showed that the tool crashes up the material, causing it to flow outwards and in cyclical nature when material slip occurs. He wrote "each slip is accomplished by a small tear or crack running in front of the cutting edge."

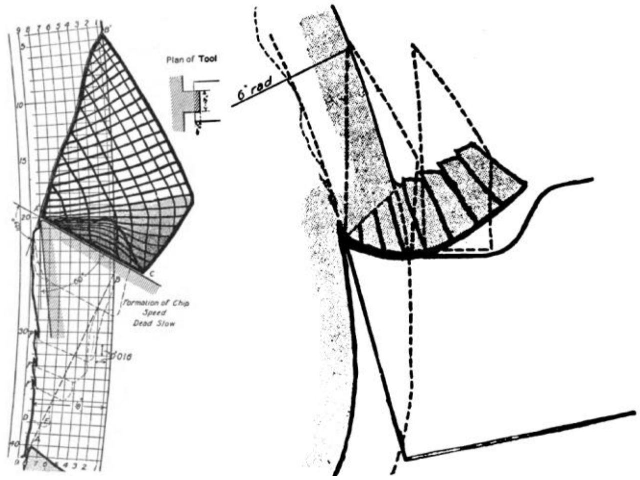

Figure 1.11: Mechanisms of chip formation at low (left) and high (right) cutting speed by Nicolson [41] (the texts in this figure are the dimensions of the cutting system and the interpretation of the chip formation by Nicolson. Left: grid scale is 9x40, size 0.016 in, rake angle is 60º, and shear plane angle is 109º. Right: 6 in rad)

After these important findings, the books (including textbooks) and papers on metal cutting described the cutting process based on the above–discovered mechanism of chip formation with crack formation ahead of the tool and healing the cracks in ductile work materials while chip moves over the rake face [42, 43, 44]. The chip formation was considered a cyclical process. Such a representation, however, ended after World War II as the works by Merchant [9, 21] and the emerging theory of plasticity by Hill [22] was attempted in metal cutting studies [23]. Since then all new models of chip formation (e.g. by Lee and Shafer [45], Oxley [46]) were developed with the assumption that metal cutting is a continuous process belonging to the group of deforming processes.

Finnie in his review paper [47] devoted a section "*A Misconception*" to criticize the "crack" idea of Reuleaux. He stated that "crack" idea was immediately refuted by Kick [39] in a paper he wrote a year after Reuleaux's. Kick pointed out that what Reuleaux had seen was probably an optical illusion. Experiments were made by Kick, who showed that there was no crack ahead of the tool. Because Kick did not find a crack ahead of the tool, it was proclaimed that there is no crack. Finnie's paper [47] does not point out under which cutting conditions Reuleaux and Kingsbury observed cracks, as well as the cutting conditions and experimental apparatus used in the Kick's experimentation where no cracks were found. It has to be pointed out, however that the time Finnie's paper was written was very special in the history of metal cutting: It was when the theory of engineering plasticity rapidly developed by Hill [22, 23] so that the general impression was that the metal cutting problem would be solved soon by using this theory. Because "the crack" was a disturbing factor that makes it impossible to apply the theory of engineering plasticity in metal cutting, the researchers of this time overlooked the facts that can be observed experimentally and the fundamental findings by Taylor and Nicolson were not mentioned.

Since then, practically all books on metal cutting (monographs and texts) repeat the statement about misconception of Reuleaux by referring Finnie's paper. For example, a textbook on metal cutting by Boothroyd and Knight [8] in the Introduction to Chapter 2, Mechanics of Metal Cutting, states: "Finnie [47] reports that a step backward in the understanding of the metal cutting process was taken in 1900 when Reuleaux [36] suggested that a crack occurred ahead of the tool and that the process could be linked to splitting of wood. This theory suggests a model of cutting similar to Figure 1.12 and a misconception that found popular support for many years."

To show that the crack idea is not realistic, Boothroyd and Knight [8] presented a graphical comparison of two models shown in Figure 1.12. As seen, the "earlier misconception" because the tool does not touch the machined surface the crack runs ahead of the tool, which has never been observed in the machining of metals. However microcracks that can only be observed with the aid of a scanning electron microscope [12, 30, 48, 49] were not available in those days, which led to such conclusions.

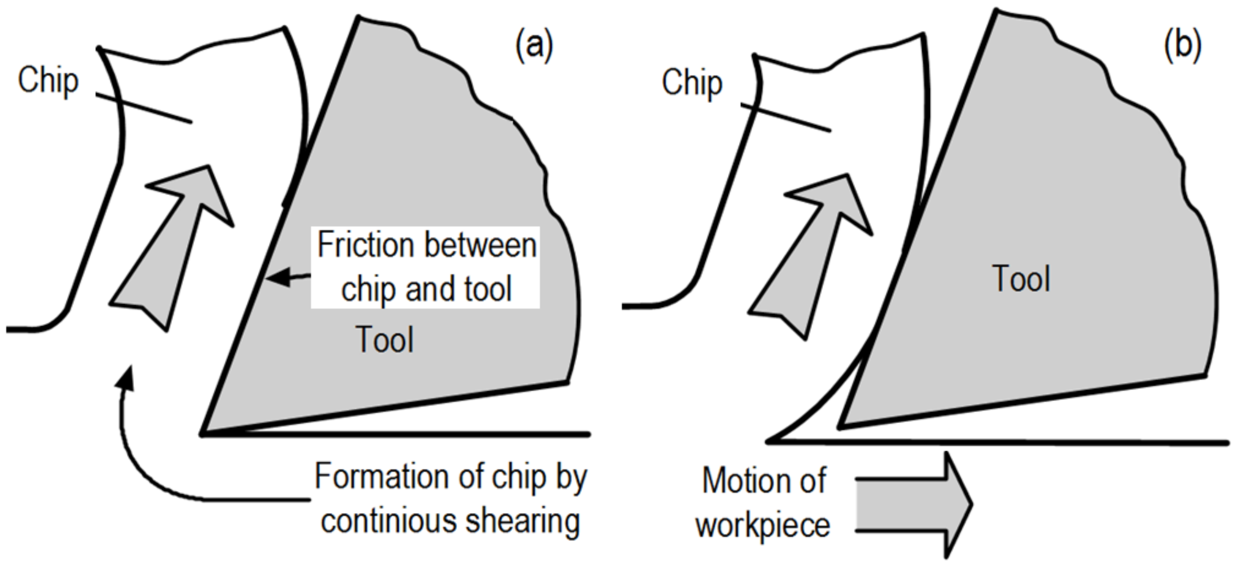

Figure 1.12: Models of the cutting process: (a) preset–day model, (b) earlier misconception [8]

1.3.2.2 Common Perception of Crack Absence

Although there are a number of physical contradictions with the “no crack” notion [12, 34], three of them are outstanding. They are:

1. *Unrealistically high shear strain:*

Merchant [50, 9, 9] derived the following equation for the final shear strain in metal cutting

$$\varepsilon = \frac{\cos\gamma}{\cos(\varphi-\gamma)\sin\varphi} = \frac{\zeta^2 - 2\zeta\sin\gamma + 1}{\zeta\cos\gamma} \tag{1.6}$$

where ζ is the chip compression ratio defined and used later in this work (Equation (4.2) in Chapter 4). For the present consideration ζ is the ratio of the chip thickness t_2 and the uncut chip thickness, t_1 i.e. $\zeta = t_2/t_1$ (see Figure 1.2).

Equation (1.6) is a form of the continuity conditions for a single–shear plane model [12]. In other words, Equation (1.6) is valid if metal cutting involves pure plastic deformation without cracking. Although Equation (1.6) appears in almost any book in metal cutting, there is a problem with the strain obtained using this equation. The calculated shear strain in metal cutting is a way greater than the strain at fracture achieved in the mechanical testing of materials under various conditions including increment compression and pure torsion. Moreover, when the chip compression ratio, $\zeta = 1$ i.e. the uncut chip thickness is equal to the chip thickness, no plastic deformation occurs in metal cutting [2]. The shear strain, calculated by the model is still significant.

2. Wear pattern:

As classified in the national and international standards [51, 52], one of the two prime wear regions of cutting tool is the so–called crater wear that occurs on the tool's rake face as shown in Figure 1.13. As seen, the maximum crater wear occurs at certain distance KM from the cutting edge. However, this wear pattern does not follow from the single–shear plane model shown in Figure 1.2 and idealized by Boothroyd and Knight as shown in Figure 1.12 (a) as there is no apparent reason for a crater to occur in the middle of the tool–chip interface. This is because if no crack occurs in front of the cutting edge, the distributions of the normal and shear contact stresses along the tool–chip interface of length l_c (Figure 1.14 (a)) are as shown in Figure 1.14 (b)[28]. It directly follows from Figure 1.14 (b) that the maximum combined stress (normal plus shear) occurs at the cutting edge, hence there is no apparent reason for crater wear to occur at the middle of the tool chip interface. Moreover, Zorev had pointed out [28] that a singularity of the normal contact stress exist at the cutting edge. i.e. this stress tends to infinity at the cutting edge.

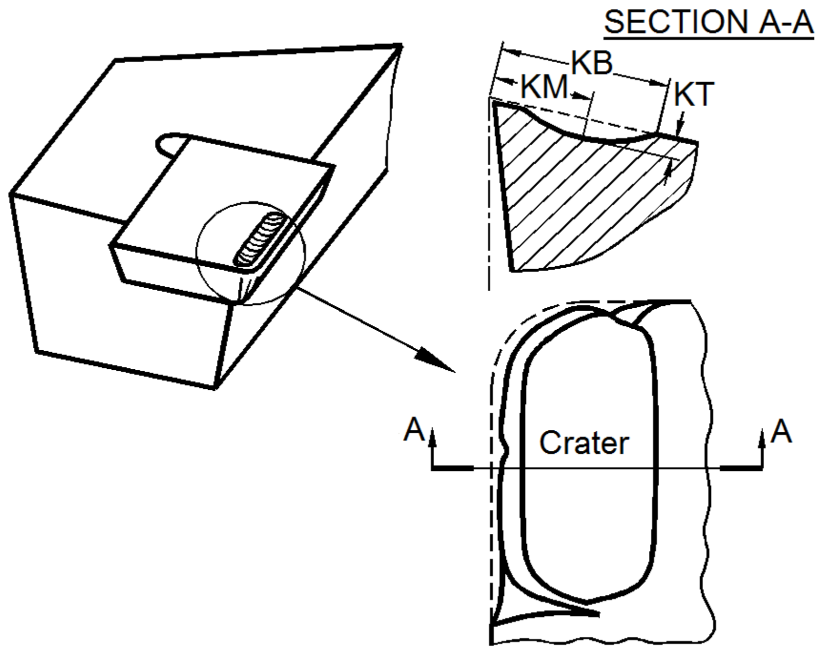

Figure 1.13: Crater wear on turning tools according to ANSI/ASME tool life testing with single–point turning tools (B94.55M–1985)

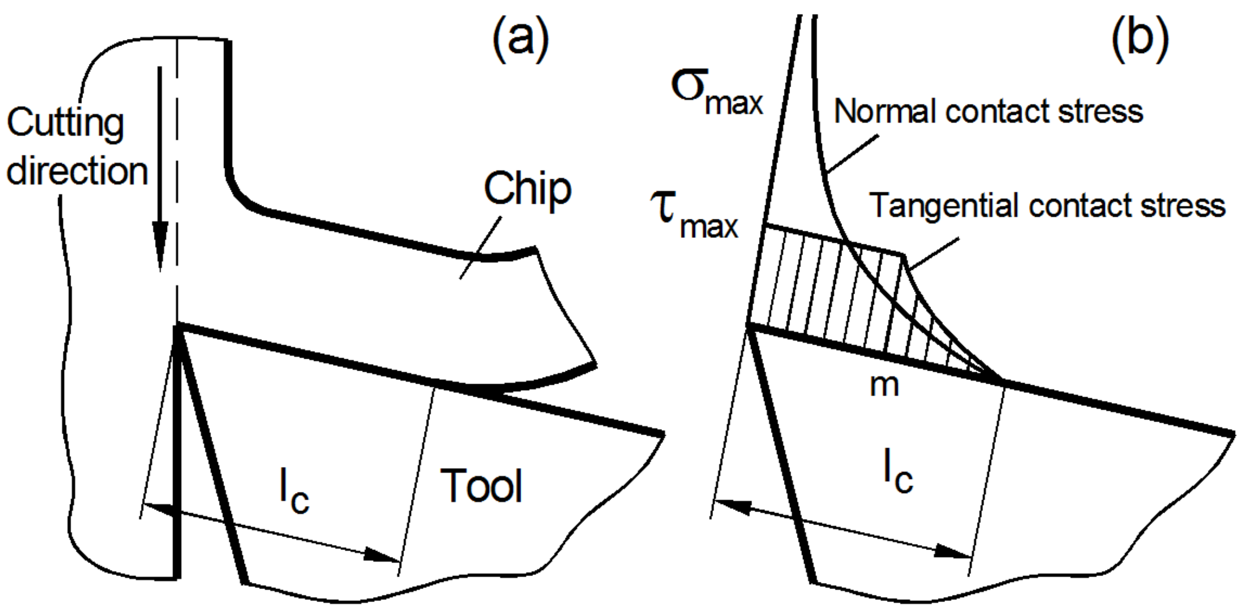

Figure 1.14: Tool–chip interface (a) and distribution of the normal and shear stress over this interface (b) [28]

It is interesting to mention that Boothroyd and Knight discussing the regions of tool wear in metal cutting, presented a figure of crater wear [8] shown in Figure 1.15 that rather resembles the "misconception" picture (Figure 1.12 (b)) than the "correct" model (Figure 1.12 (a)). Therefore, the two discussed issues are namely the crater wear pattern and the singularity of the normal contact stress, neither of which have been resolved.

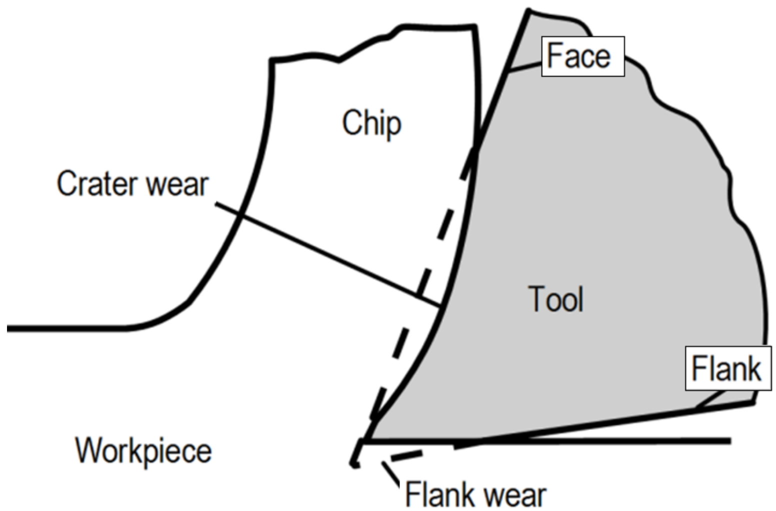

Figure 1.15: Regions of tool wear in metal cutting [8]

3. Chip Structure:

According to Merchant, the so–called card model of the cutting process proposed by Piispanen [53] is very useful to illustrate the physical significance of shear strain and to develop the velocity diagram of the cutting process. This model is shown in Figure 1.16. The card–like elements displaced by the cutting tool were assumed to have a finite thickness Δx. Then each element of thickness Δx is displaced through a distance Δs with respect to its neighbour during the formation of the chip.

Although the card model is widely used and referred by researchers, two obvious problems have never been pointed out. First is that the separation of each chip fragment should conveniently take place along line ab which then become a'b', ergo a chip fragment should be fractured from the rest of the workpiece in the direction of the feed motion, which is physically impossible under the force model shown in Figure 1.3 and conceptually, as the idea of the model does not include fracture. Second, it is unclear how to deal with empty spaces (triangle aa'b' in Figure 1.16), as they have never been observed in practice. To solve these issues, Merchant [9] assumed thickness as $\Delta x \rightarrow 0$ in the real cutting process so that there would be no fracture and no empty spaces. As such, the chip structure should be uniform. However, this assumption not only failed to solve the problems (as the fracture would take place even for infinitesimal thickness of a chip fragment), but also created two more severe problems.

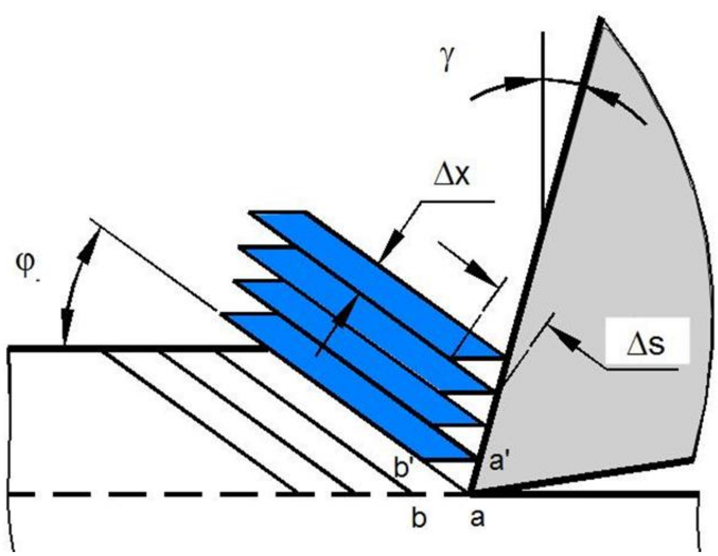

Figure 1.16: Card model to represent chip formation

The first problem is that the real chip structure does include the chip fragments and separators as shown in Figure 1.17. Moreover, the distribution of plastic deformation is not uniform even within a fragment as established by microhardness tests [12]. These two facts disagree with the idea of continuous chip formation and support the idea of cyclical chip formation pointed out by Time [54, 55], Taylor, Nicolson [41] and many others.

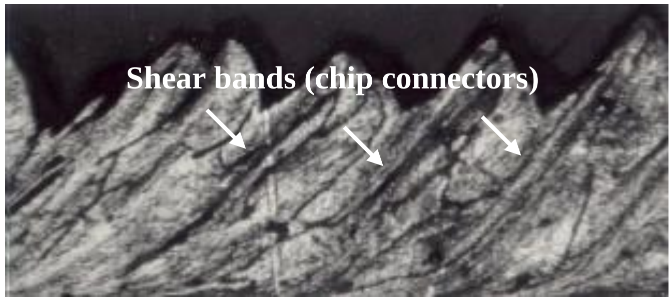

Figure 1.17: Typical structure of medium–carbon steel chip

As soon as decent FEM programs became available to specialists in metal cutting modeling, the second problem of chip separation came into existence. The researches were forced to induce a crack between the chip and the workpiece to make models work, i.e. to allow the physical advance of the cutting tool into the workpiece. A great number of numerical techniques to model chip separation and a number of separation criteria grouped as *geometrical* and *physical* were developed [14, 56, 57, 58, 59, 60, 61].

1.3.2.3 Ductile vs. Brittle Work Materials

It is widely accepted by the specialists in the field, including most supporters of the "no–crack" idea, that unlike ductile materials, cracks may form in machining of brittle materials. For example, Finnie presented a micrograph of a partially formed chip where a crack can be clearly observed in what was considered as a brittle work material (Figure 1.18)[47]. Such evidences were reported by earlier researchers, such as Ernst observations in 1938 (Figure 1.19)[62]. However, the question of how brittle the material needs to be for the crack to form in metal cutting was never clarified.

The convention measures of ductility that are obtained from the tension test are the engineering strain at fracture e_f (usually called elongation) and the reduction of area at fracture q

$$e_f = \frac{L_f - L_0}{L_0} \tag{1.7}$$

$$q = \frac{A_0 - A_f}{A_0} \tag{1.8}$$

where L is the original gage length of the specimen, L_f is the gage length at fracture, A_0 is the original area of the cross section of the specimen, and A_f is this area at fracture.

Both the elongation and reduction of the area are expressed as a percentage [63]. A ductile material is usually classified as a material that has yield strength and that exhibits more than 5% elongation in the standard tension test [64, 65].

According to this standard classification, the work materials used in the cutting test in Figure 1.18 and Figure 1.19 are ductile materials, having more than 12% of elongation and very distinctive yield strengths. As clearly seen in these figures, a great deal of plastic deformation of the layer which is being removed is achieved before a crack appears. The slip line on Figure 1.18 and grid distortion due to plastic deformation on Figure 1.19 are direct indications that the work materials used are ductile. Note that ANSI 1045 as rolled steel has elongation 12% and it is always considered as to be a ductile material. Moreover, many cast irons, usually considered as brittle materials in the literature on metal cutting, have an elongation of more than 10% and the ductility of ductile cast irons reaches 25%. Therefore, formation of a visible crack and the so–called discontinuous chip should not only be attributed to brittle work materials.

1.3.2.4 Crack Notion by Recent Studies

In 1983, Sampath and Shaw [48], in a study of an elastic–plastic finite element stress field based on an assumed a continuum and experimentally observed chip geometry and cutting forces, found that to be consistent with physical conditions fracturing must pertain along the shear plane. It was concluded that the material does not behave as a continuum, and that microcracks along the shear plane play a significant role just as they do on the tool face. Although this very important finding explains many known contradictive results, it has not been observed further by researchers.

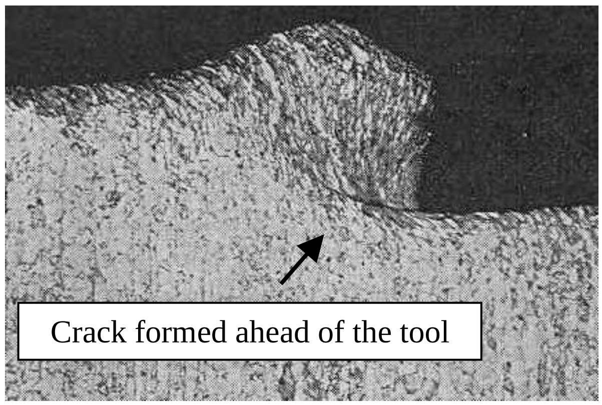

Figure 1.18: Photomicrograph of partially formed discontinuous chip. Material: β brass; rake angle: 15º; depth of cut: 0.008 in; cutting speed: 0.5 in/min; no cutting fluid [47]

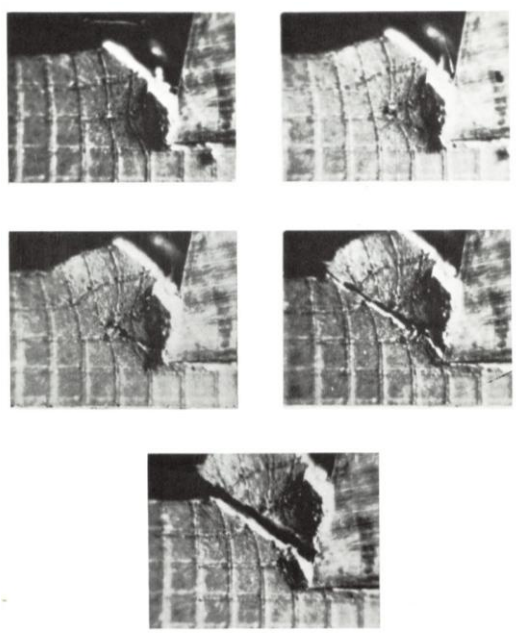

Figure 1.19: Formation of a typical discontinuous chip. Work material: high lead bronze; depth of cut: 2.7 mm; rake angle: 10º; cutting speed: 25.4 mm/min; no coolant [62]

When more sophisticated techniques emerged, the presence of cracks in chip formation was conclusively proven in the machining of a wide variety of work material on macro and micro levels [66, 49]. Conducting a very detailed study of chip formation, Itawa and Ueda proved that the continuous chip forms only under relatively specific (or exotic) cutting conditions, such as when pure single crystal aluminum is machined [66]. Under common cutting conditions, cracking is the real phenomenon in chip formation which is classified to be:

- Quasi–continuous chip formation that takes place in machining ductile materials (such as steels) under favourable cutting conditions; a crack occurs along the shear direction.
- Discontinuous chip formation that occurs typically when machining brittle materials; as such, the crack nucleated below the flank face and propagated ahead of the cutting tool due to void coalescence.
- Chip formation with a built–up edge that takes place in machining for "materials which can adhere to the tool face." Cracks initially form below the flank face and then ahead of the tool.

Similar phenomena were observed by Didjanin and Kovac [49]. Their basic result is shown in Figure 1.20 (a). Besides, since most of the work materials are alloys and thus have different phases and inclusions, cracking in metal cutting occur between different phases and voids as shown in Figure 1.20 (b).

Atkins, a world–known specialist on fracture who supported the "crack" (fracture) notion for years [30], pointed out in his very extensive analysis of the problem [31] that fracturing must occur along the surface, separating the layer being removed and the rest of the workpiece, i.e. exactly [41] in the place pointed out by Taylor and Nicolson. Atkins stated that ductile fracture mechanics can be used to explain chip formation in ductile metals by incorporating material fracture toughness in addition to energy spent in shear and friction.

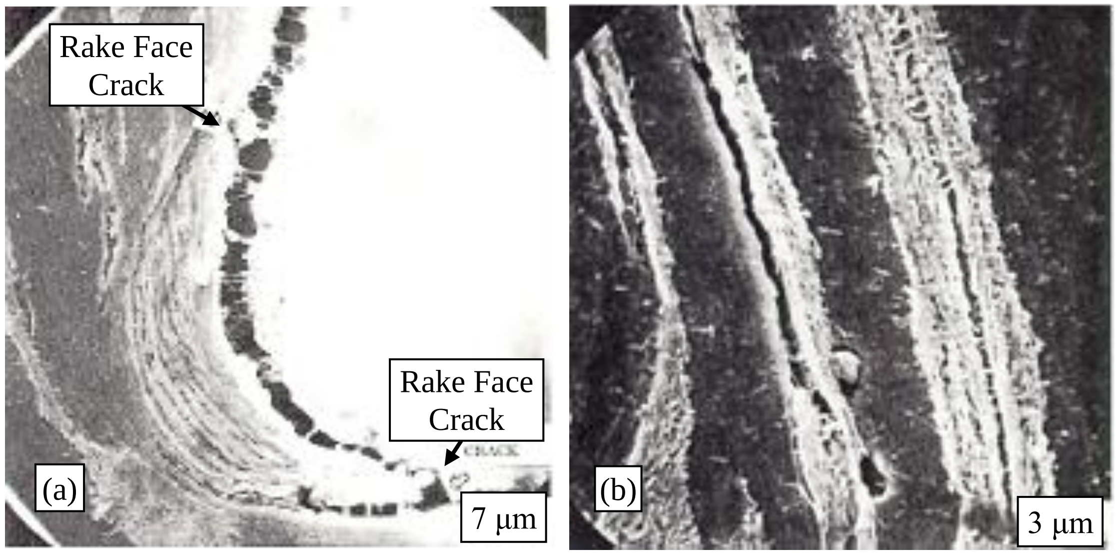

Figure 1.20: Cracks observed ahead of the cutting tool (a) and between different phases of the work material (b) [49]

Following Atkins third energy sink approach, recently Subbiah and Melkote [67] provided an experimental evidence of ductile tearing, which causes material separation using scanning electron micrographs of the chip–workpiece interface. In their testing, a small uncut chip thickness was removed at low cutting speed to increase what was considered as the size–effect of the tool tip radius. Figure 1.21 shows images of the void creation, which leads to ductile fracture due to the formation, enlargement, and coalescence of the microscopic voids.

In addition to the recent studies above, those of which directly support the occurrence of fracture in metal cutting, other indirect evidence may still be found by a comparison between state of the art of metal cutting and a closely–related deforming process of metal forming. Until about a decade ago, the mold design for metal forming was mostly based on knowledge gained through experience and often required a protracted and expensive trial–and–error testing. Today, it is based entirely on FE simulations. Starting from the design model and through practically all process steps as far as the actual design of the press tool, the production of a component can be fully simulated before the first prototype is built [68]. As a result, great savings have been achieved. In recent years, tool development and production time has been reduced by about *50%* and a further 30% reduction over the next few years appears to be realistic. These savings originate from more rapid development of tools and from dramatic shortening of trial–and–error testing [12].

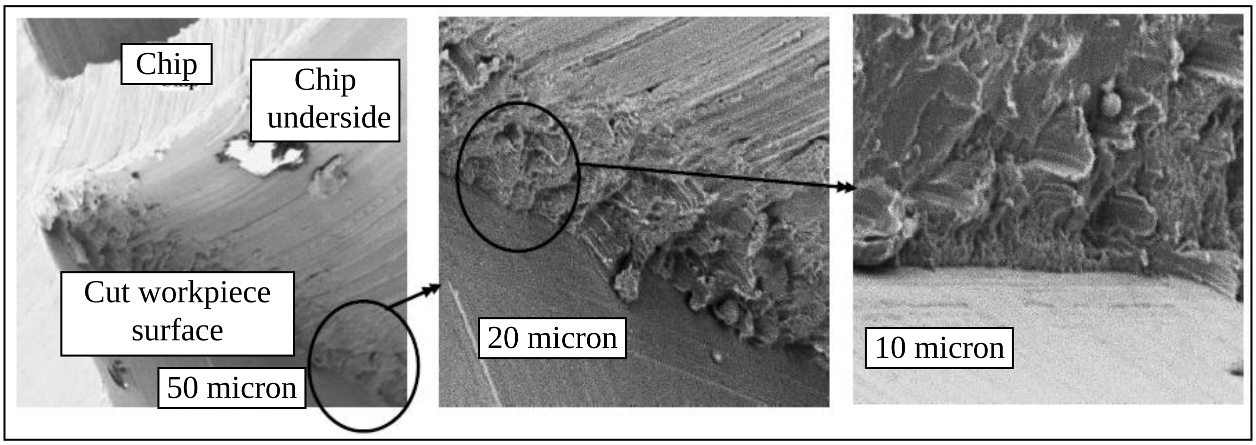

Figure 1.21: SEM images of chip–workpiece interface showing ductile tearing by void growth (OFHC Copper, t_1 = 0.050 mm, rake angle = 30º, cutting speed 1.2 m/min, edge radius = 0.007 mm) [67]

It is clear that FE simulation in metal cutting is not utilized nearly as much in metal forming, although according to the prevailed notion that new surfaces in metal cutting are formed simply by ‘plastic flow around the tool tip [69]. In other words, the metal cutting process is one of the deforming processes where a single–shear plane constitutes the very core of metal cutting theory, and thus this process is thought of primarily as a cutting tool *deforming* a particular part of the workpiece by means of shearing. A number of cutting theories and FE models have been developed based on this concept [70]. If it was correct, the common finite element analysis

(FEA) package developed for the design of the deforming operation should be easily implemented in metal cutting. Therefore they can be as useful in the process and tool design in metal cutting as they are in metal forming. Obviously, this is not the case in spite of enormous resources and tremendous efforts spent on the matter.

Although this discussion does not explicitly prove fracture in metal cutting, it indicates that the material behavior in metal cutting must be different from metal forming, and a phenomenon other than deformation was not captured in the metal cutting. Considering the similar nature of the two processes where large deformation and contact exist in both processes, it may be concluded that cracking, which was never observed in a successful forming operation, is the key difference which justifies such discrepancy.

1.4 Underlying Principles of the Thesis

There are two basic underlying principles in the current thesis: (1) the system definition of metal cutting, and (2) the deformation law.

1.4.1 System Definition of Metal Cutting

Based upon the observations, findings, and lessons learned from the history of metal cutting research (such as the conclusions from Time and Tresca [54, 55, 71, 72], Reuleaux [36] Taylor and Nicolson [41] and other pioneer engineers) Astakhov and Shvets [73] formulated the system concept in metal cutting. According to this concept, the process of metal cutting is defined as a forming process, which takes place in the components of the cutting system that are so arranged that the external energy applied to the cutting system causes the *purposeful fracture* of the layer being removed. This fracture occurs due to the combined stress, including the continuously changing bending stress causing a cyclical nature of this process. The most important property in metal cutting studies is the system time. The system time was introduced as a new variable in the analysis of the metal cutting system, and it was conclusively proven that the relevant properties of the cutting system's components are time dependent [73].

It follows from this definition that, considered together (the system approach), the following features distinguish metal cutting among other closely related manufacturing processes and operations:

1. *Bending moment*. The bending moment forms the combined stress in the deformation zone which significantly reduces the resistance of the work material being cut. As a result, metal cutting is the most energy efficient material removal process (that is, energy per removed volume accounting for the achieved accuracy) compared to other closely related operations.
2. *Purposeful (micro) fracture* of the layer being removed under combined stress. The fracture occurs in each successive cycle of chip formation.
3. *Stress singularity at the cutting edge*. The maximum combined stress does not act at the cutting edge compared to other closely related forming operations; rather, a (micro) crack forms in front of the cutting edge. As a result, when the cutting system is rigid and the cutting tool is made and run properly, the wear occurs at a certain distance from the cutting edge that allows it to maintain the accuracy of machining over the entire time of tool life.
4. *Cyclical nature*. Metal cutting is inherently a cyclical process. As such, a single chip fragment forms in each chip formation cycle. As a result, considered at the appropriate magnification, the chip structure is not uniform. Rather, it consists of chip fragments and connectors. The frequency of the chip formation process, known also as the chip

segmentation frequency, primarily depends on the cutting speed and the work material. The cutting feed and the depth of cut (>1 mm) have a very small influence on this frequency.

It follows from the above consideration that the load (the cutting force), temperature field and other output parameters of the process should have cyclical variation. The shape of the chip and its structure should also reflect the cyclical nature of the metal cutting.

Figure 1.22 shows the system consideration of the metal cutting model [2]. Phase 1 shows the initial stage. When the tool is in contact with the workpiece, the application of the cutting force F_c leads to the formation of a deformation zone ahead of the cutting edge. The tool moves forward with the cutting speed v. The workpiece first deforms elastically and then plastically. As a result, a certain elastic–plastic zone forms ahead of the tool that allows the tool to advance farther into the workpiece so that a part of the layer being removed comes into close contact with the tool rake face (Phase 2). When the full contact is achieved, the state of stress ahead of the tool becomes complex including a combination of the bending and compressive stresses.

As the tool penetrates farther, the dimensions of the deformation zone and the maximum stress increase due to the cutting force F_c. When the combined stress in this zone reaches the limit for a given work material, a sliding surface forms in the direction of the maximum combined stress (Phase 3). The partially formed chip starts to slide with velocity v_{ch1} relative to the tool rake face. This instant may be considered as the very beginning of the chip formation. As soon as the sliding surface forms, all of the chip–cantilever material starts to slide along this surface with velocity v_{ch2} while the whole chip slides with velocity v_{ch1} along the rake face (Phase 4). Upon sliding, the resistance to the tool penetration decreases, leading to a decrease in the dimensions of the plastic part of the deformation zone. However, the structure of the work material, which has been deformed plastically and now returns to the elastic state, is different from that of the original material. Its appearance corresponds to the structure of the cold–worked material. Experimental studies [12, 28, 11, 74, 75] showed that the hardness of this material is much higher than that of the original material. The results of the experimental study using a computer–triggered, quick–stop device proved that this material spread over the tool–chip interface by the moving chip constitutes the well–known chip contact layer (Phase 5), which is now believed to be formed due to severe friction conditions in the so–called secondary deformation zone [28]. The sliding of the chip fragment continues until the force acting on this fragment from the tool reduces because a new portion of the work material is entering into contact with the tool rake face. This new portion attracts a part of the cutting force F_c. As a result, the stress along the sliding surface diminishes, becoming less than the limiting stress that ceases the sliding. A new fragment of the chip starts to form (Phase 6).

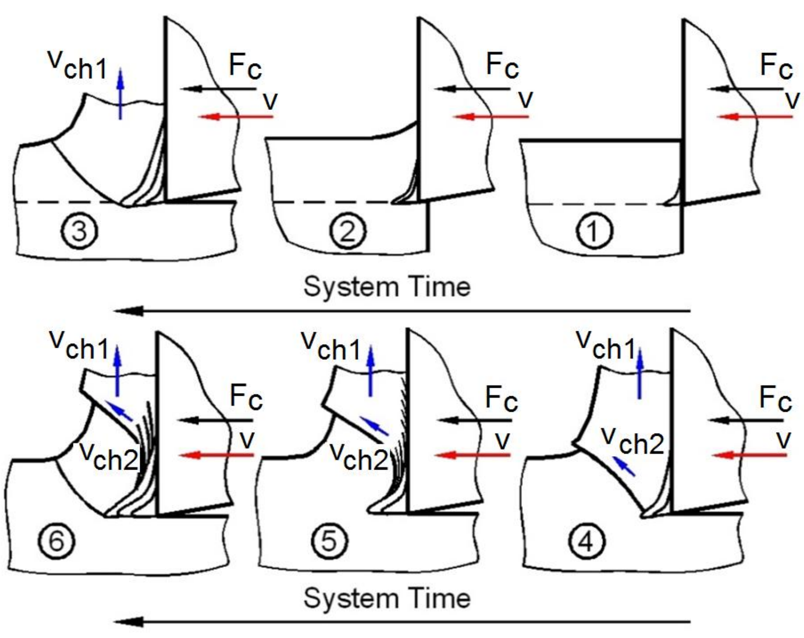

Figure 1.22: System consideration of the metal cutting model [73]

The chip formed in this way is referred to as *the continuous fragmentary chip* [75]. Its shape resembles that obtained experimentally (Figure 1.17).

1.4.2 Deformation Law

The deformation law in metal cutting was formulated by Astakhov [1] as:

Plastic deformation of the layer being removed in its transformation into the chip is the greatest nuisance in metal cutting, i.e., while it is needed to accomplish the process, it does not add any value to the finished part. Therefore, being by far the greatest part of the total energy required by the cutting system, the energy spent on this deformation must be considered as a waste which should be minimized to achieve higher process efficiency.

It has been revealed that the energy of plastic deformation of the layer being removed in its transformation into the chip is the greatest in machining of ductile materials, e.g. steels [76]. The greater the energy of plastic deformation, the lower the tool life, the quality of the machined surface, and the process efficiency. Therefore, the prime objective of the cutting process design is to reduce this energy to its possible minimum by the proper selection of the tool geometry, tool material, machining regime, MWF and other design and process parameters.

1.5 Objective/Sub–Objectives and Scope of Research

The prime objective of this thesis is ‘to convert’ the general definitions set by the system concept of metal cutting and the deformation law into a physics–sound model to be used in the modeling of the metal cutting and its optimization. This prime objective includes sub–objectives.

Following the suggestions by Astakhov [1], as the material behavior being the weakest link in metal cutting modeling, a proper material modeling approach will be investigated. The response of the material, particularly material fracture response, greatly depends on the conditions under which the deformation takes place. The ***first sub–objective*** is to understand the uniqueness of the loading condition in the conventional orthogonal metal cutting (OMC) and provide/develop a mathematical description of such conditions and the material response based on the latest advancements in the field of damage and fracture mechanics of ductile metals. Chapter 2 is devoted to address this objective.

The ***second sub–objective*** is to develop a suitable experimental methodology for the evaluation of the influence of the different loading conditions on the material constitutive law. This includes the evaluation of the existing methods and their applicability and limitations. The proposed approach includes a methodology for the determination of the elastic modulus, yield surface and fracture locus in characterization of ductile metals. Chapter 3 introduces both the conventional approach and its limitations, and a new specimen design and the experimental setup. The overall effectiveness of the current approach in the OMC modeling will be demonstrated in Chapter 3.

The ***third sub–objective*** is to construct a 2D FE model for OMC based on the proposed system definition and the developed physical model. An experimental setup for model validation will be developed and proposed in Chapter 4. The validation will include the cutting force analysis, the similarity rules, and the microstructure examination.

Upon completion of the above sub–objectives, the ***final sub–objective*** is to introduce an optimization approach for minimizing the energy of plastic deformation by manipulating the process stress triaxiality state through the cutting tool and process configurations. According to the above–described deformation law, the primary goal of all machining investigations should focus on increasing the process' technical efficiency, i.e. minimizing the energy spent on the plastic deformation of the layer being removed in its transformation into the chip, as the unavoidable plastic energy is a waste and does not benefit process outcomes. Although this waste of energy cannot be totally avoided, there are a number of parameters that may alter this energy and improve the overall system performance. For example, loading conditions may be adjusted according to the process and/or operational parameters; this in turn would change the material response, and consequently altering the total amount of required energy.

1.6 Overview of Dissertation

The dissertation begins with an overall research background justifying the prerequisite criteria. The introduction chapter provides an overview of the technological development of machining systems throughout history which justifies the research timing. It also provides a literary overview of mechanics and physics of metal cutting which defines the thesis principles. Research objectives are also stated in this chapter.

Chapter 2 is devoted to develop a material model suitable for applications where the loading conditions are similar to metal cutting. The development is based on the recent advancements in fracture mechanics of ductile metals. It illustrates the material strain limit sensitivity to a fracture based on the strain energy density and stress triaxiality. In addition, this chapter provides a mathematical model of the material degradation beyond damage initiation.

Chapter 3 provides an overview of the available experimental approaches for material fracture parameters, calibration, and their limitations. It also presents a novel approach to determine the material model parameters which utilize a new adjustable stress state specimen, digital image correlation (DIC) measurements, and an inverse method for parameter identification.

Chapter 4 presents elements and issues related to FE simulation and validation experiment of OMC. It emphasizes the major computational restrictions such as the chip–tool interface friction model and chip separation mechanism. A metal cutting validation experiment is developed to examine the validity of the FE model by evaluating the predicted cutting forces and chip morphology.

Chapter 5 presents the role of the stress triaxiality state on the energy spent on the machining process. The study uses the material model developed in this research to investigate the cutting configuration effect on the process efficiency. The significance of the developed approaches and results and its contributions to the science and technology of metal cutting are also introduced in this chapter. Final conclusions, contributions and suggested future work are stated in Chapter 6.

Chapter 2: Material Modeling

As discussed in Chapter 1, metal cutting is defined as the purposeful fracture of the work material. For many real–world work materials used in industry, such fracture is preceded by significant plastic deformation of the work material until strain at fracture under a given state of stress is achieved. Therefore, a material model to be used in metal cutting simulations should include plastic deformation and fracture of the work material. This chapter discusses the theoretical background and uses recent advances and understanding of ductile damage and fracture in order to formulate a constitutive model suitable for loading conditions exists in OMC.

2.1 Multi–Axial State of Stress in Metal Cutting

The first step is to realize that fracture requires a certain multi–axial state of stress in the deformation zone as the major condition for fracture. One may argue, however, that fracture occurs in the tensile test, although the specimen is subjected to uniaxial loading in this test. To understand how fracture occurs in a uniaxial–axial load case, let's consider Figure 2.1 [77] which shows the schematic of the deformed and then later fractured tensile specimen at different stage of loading. As seen, the specimen first undergoes elastic deformation. As the force is increased further, the material reaches its elastic limit. If strained beyond this point, permanent plastic strains will be developed. If the stress is increased even further, a neck forms on the specimen, i.e. a small section will be stretched and narrowed instead of the entire gage length (Figure 2.1). Inside the neck, small voids start to form which then coalescence into a crack and finally rupture.

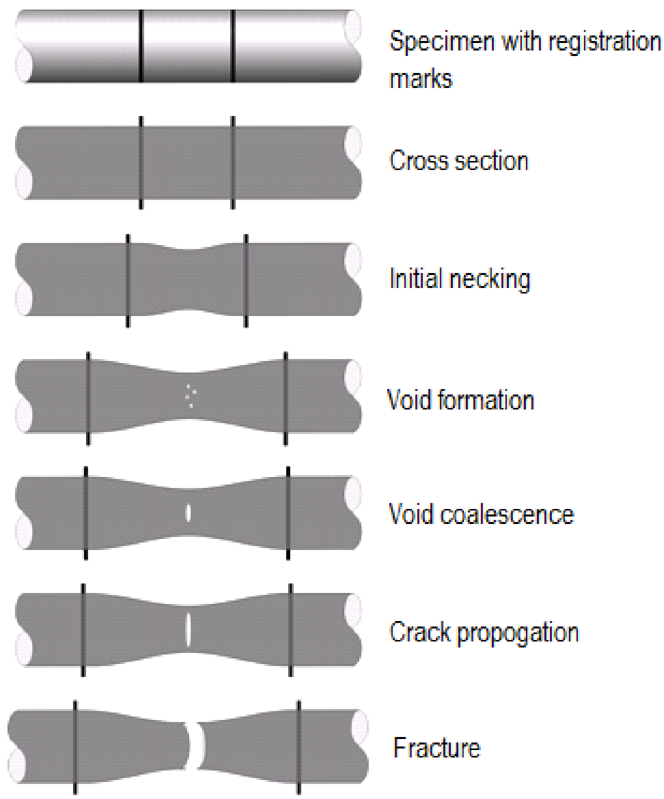

Figure 2.1: Formation of the neck and fracture in tensile testing [77]

The deformation under a multi–axial stress state is described through the use of stress tensor. The stress tensor σ_{ij} can be decomposed into two components

$$\sigma_{ij} = S_{ij} + \sigma_m \delta_{ij} \tag{2.1}$$

where S_{ij} is the deviatoric component called the stress deviator tensor, which tends to distort the material, and $\sigma_m \delta_{ij}$ as the volumetric stress tensor component which tends to change the material volume. The material flow is usually characterized by the first component of the stress tensor whereas the volumetric stress component $(\sigma_m \delta_{ij})$ (also known as the mean hydrostatic stress) generally has no effect on the effective stress–strain behavior of the material. In this component $\sigma_m = \sigma_{kk} / 3$ is the mean stress and δ_{ij} is the Kronecker Delta tensor.

Unless a body is under a pure hydrostatic stress, S_{ij} tensor would always exist, including the case of uniaxial loading. In other words, the multi axial state of stress required for material deformation and fracture can be achieved by any arbitrary stress tensor other than volumetric. Furthermore, the principle orientation of the stress tensor is also irrelevant as far as the isotropic material flow and fracture occurrence are concerned. However, the volumetric stress tensor plays a significant role in controlling material fracture. A material deforming under high hydrostatic pressure would resist fracture more as compared with under low hydrostatic pressure (high σ_m) [78]. A very low σ_m may result in a very high material strain limit where excessive deformation does not cause material fracture. Therefore, for a uniaxial load case the volumetric component, as well as S_{ij} , are condescend to the fracture condition.

One may argue, however, that the cutting tool compresses the layer being removed by its rake face, as a result a high hydrostatic pressure state occurs, which prevents fracture so that the plastic deformation by simple shearing occurs in a manner accepted by the traditional theories of metal cutting [9, 23, 5]. It is true that a pure compressive instead of tensile stress will develop a very large negative σ_m . According to the above discussion, fracture may never take place. However such a condition does not exist in the actual uniaxial compressive test and certainly does not represent metal cutting. Figure 2.2 (a) shows a specimen made of a ductile material with a grid scribed on its cylindrical surface. Figure 2.2 (b) shows that when a hypothetically perfect frictionless punch is used, a uniaxial homogeneous deformation takes place. In comparison, when on actual interface with friction as seen in the testing environment, a barrel–like shape of the specimen (Figure 2.2 (c)) develops and simple shearing may cause fracture even under relatively low σ_m . Such a phenomenon is known as barreling in compression and it is the full equivalent to necking in tension. Once barreling occurs, the state of stress in the specimen becomes inhomogeneous, which eventually leads to fracture as the load *P* increases. As early as in 1906, F. Taylor attributed such barreling to the friction at die–specimen interfaces, demonstrating that side spread of the chip (the chip width is equal to the width of cut) is not occurring in metal cutting [41].

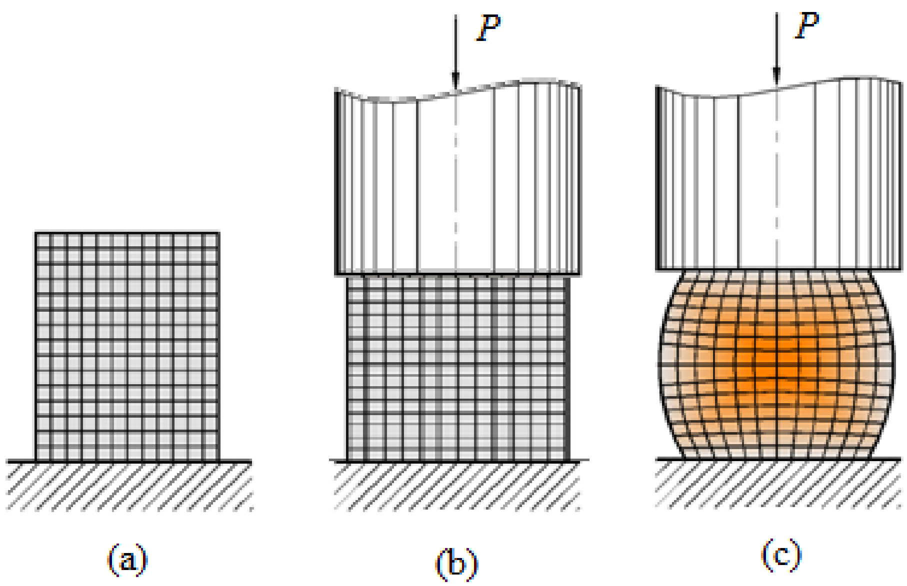

Figure 2.2. Deformation pattern in compression: (a) specimen with the scribed grid, (b) distortion of the initial grid due to frictionless contact (c) distortion of the initial grid due to interface friction

However, the deformation in metal cutting is way more complex than that of uniaxial compression. A more realistic analogy is shown in Figure 2.3, where the punch in a compression test is shifted from the axis of the specimen to a position similar to that found in cutting. If one compares deformation patterns due to compression and cutting, one observes significant difference. At the initial stage of punch penetration, a deformation zone forms in front of the punch face due to mostly compression of the affected layer (analog of the layer to be removed in machining). As a result, the plastic deformation of this layer takes place by shearing during this stage. As the punch advances further, the plastically deformed part gradually comes into close contact with the punch face, so a bump is formed in front of this face. As soon as the bump begins to form, the distortion of the initial grid does not resemble that found in pure (simple) shearing. This explains that simple shearing, as suggested by the single–shear plane and otherwise known models of chip formation [69], is not the prime deformation mode in metal cutting.

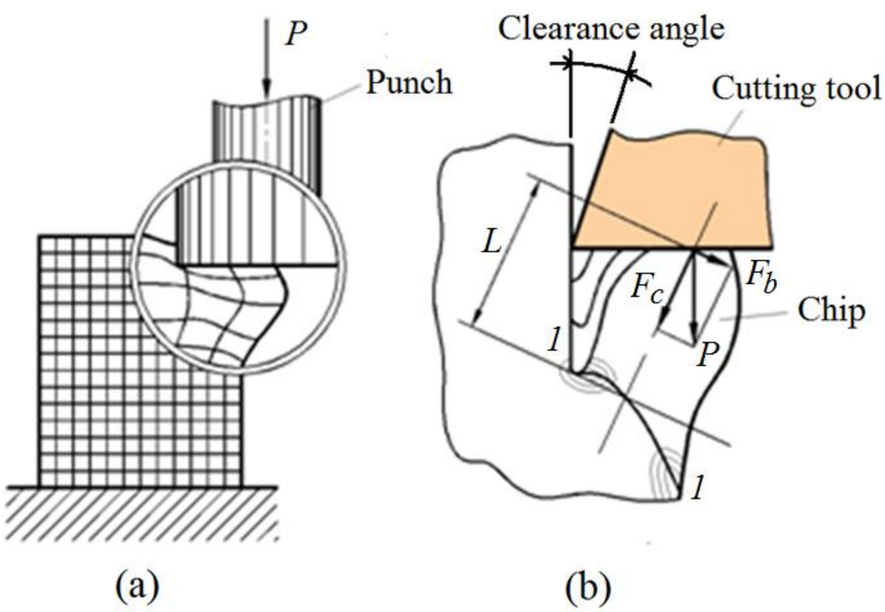

Figure 2.3. Deformation pattern in cutting: (a) distortion of the initial grid, (b) the interaction between the tool rake face and the partially formed chip

As explained by Astakhov [1], any significant penetration of the punch shown in Figure 2.3 (a) is impossible as the punch does not have the clearance angle (see Figure 2.3 (b)). Once the clearance angle is applied to the deforming tool, it becomes a cutting tool. Figure 2.3 (b) shows a simple model of the cutting tool (a punch with a clearance angle) penetration into the specimen considered as the workpiece. As shown, a partially formed chip forms in front of the tool that starts to slide over the tool rake face. This penetration force applied to the partially formed chip through the rake face of the tool can be resolved into two components, namely a compressive force F_c, acting along the direction of the conditional axis of the partially formed chip, and a bending force F_b, acting along the transverse direction, as shown in Figure 2.3 (b). Therefore, the partially formed chip is subjected to a mutual action of compression and bending (the bending moment $M = F_b L$). This is in line with the observation made by F. Taylor (page 75 in [41]) who explained that the portion of the chip that is still pressing upon the lip of the tool is acting as a lever, causing the chip to turn away from the workpiece. As a result, the state of stress in the chip root (where the chip connects to the rest of the workpiece through the plastic–plastic joint) becomes complex, including a combination of tensile and compressive stresses. Because of this complex triaxiality state of stress, the purposeful fracture of the layer being removed can take place.

2.2 Considerations for Constitutive Models

2.2.1 Fracture Criteria in Ductile Metals

Material separation into two or more pieces, known as fracture, is the result of a complex physical process occurring first at the atomic scale. At the macro scale, the only variables that control fracture are the current values of stress and strain components and their histories [79]. Fracture criteria are formulated based on the stress, strain, and their combinations. Among the known criteria, the constant equivalent strain criterion is often used. According to this criterion, material fracture occurs when the equivalent plastic strain $\bar{\varepsilon}$ reaches a certain predefined value $\bar{\varepsilon}_f$. Throughout the history of fracture studies, it was observed that fracture could also occur due to material strength limitations on certain stress components [79]. For example, the maximum shear stress criterion predicts fracture on a plane where its shear stress component τ exceeds the critical value $\tau_{\max}$. Nevertheless, the suitability of such criteria is limited to particular engineering problems, and thus for many applications, a more general approach is needed.

The mechanism of ductile fracture of metals is identified as the formation, growth, and coalescence of microscopic voids. The growth rate of microvoids under a combined state of stress that includes the normal and shear stresses has been investigated by a number of authors. McClintock [80] studied the growth of voids of a cylindrical shape and concluded that the ratio of the hydrostatic stress (σ_m) to the equivalent stress $(\bar{\sigma})$, also known as the stress triaxiality state parameter (η), is a predominant parameter in damage formulation. A similar work was conducted by Rice and Tracey [78], who investigated stress triaxiality effects on the microvoids growth of a spherical shape and observed that the growth rate is significantly affected by the superposition of hydrostatic tension on a remotely uniform plastic deformation field. For both the cylindrical and spherical void shapes, Rice and Tracey indicated that moderate and high stress triaxiality leads to amplification of the relative void growth rates over imposed strain rates by a factor depending exponentially on the mean normal stress.

Atkins [81] studied fracture in bulk and shear forming processes and stated that the hydrostatic stress state is an important parameter that seems to have a predominant effect on the volume change of the voids. Although such growth theories consider only a volume change of a particular void shape, the volume changing contribution to the void growth is found to overwhelm the shape changing part when the mean remote normal stress is large [78, 81]. Such justification is necessary to assume a symmetrical growth throughout the deformation process.

It was pointed out that material ductile fracture may be affected not only by the state of hydrostatic stress, but also by the path under which this deformation was developed [81, 82]. The process of fracture is strictly path–dependent and the fracture strain in one process may differ from that found in another. For this reason, the damage function defined by Equation (2.2) is always represented in an integral form of the equivalent strain $(\bar{\varepsilon})$ path and weighted by an "arbitrary function f ". The damage is assumed to initiate when a damage indicator ω reaches a certain predefined critical value i.e.

$$\omega = \int_0^{\bar{\varepsilon}_f} f\ (state\ \text{of}\ stress)\, d\,\bar{\varepsilon} \tag{2.2}$$

Studies have shown that the state of stress in Equation (2.2) is limited not only to the state of the hydrostatic stress (or equivalently, stress triaxiality state), ductile and brittle metals may also rupture due to shear stresses. For example, Leppin et al. [83] have combined the ductile and shear fracture mechanisms and postulated that fracture occurs when the maximum value of the two components (ductile and shear scalar damage indicators) reaches unity. In addition to the triaxiality state parameter, the authors included the ratio of the maximum shear stress and equivalent stress in crashworthiness simulations.

Wilkins et al. [84] proposed a cumulative fracture criterion in which a weighting function f is defined as $f = w_1 w_2$. The first term w_1 is a function of the hydrostatic pressure whereas w_2 represents the effect of the deviatoric stress tensor. The effect of deviatoric stress tensor was introduced in many recent studies as the second fracture dependent state parameter [85, 86].

The deviatoric state parameter (ξ) has been formulated as a function of the third deviatoric invariant and equivalent stress ratio. Wierzbicki and Xue [86] suggested a new fracture criterion and assumed an accumulated equivalent plastic strain model similar to Equation (2.2). The model damage function involves two stress state dependent parameters: the stress triaxiality and the deviatoric state parameter. It accurately explains most, if not all, experimental observations. Another significant advantage is the relative simplicity of its calibration [79].

2.2.2 Stress State Parameterization

Bai and Wierzbicki [85] showed that two parameters may be used to describe the material state of stress, the stress triaxiality state parameter (η) and the deviatoric state parameter (ξ).

The stress triaxiality state reflects the effect of the mean stress (σ_m) which is equivalent to the spherical part of the stress tensor. The stress triaxiality state is defined by a non–dimensional parameter

$$\eta = \frac{\sigma_m}{\bar{\sigma}} \tag{2.3}$$

and is considered in the literature [87, 83, 86, 88, 79] as an important factor in formulating ductile fracture models.

Another parameter of the stress state, known as the normalized third deviatoric invariant, affects a material’s ductility, and thus affects its fracture strain [88, 79, 89]. This parameter considers the influence of some combination of the deviatoric part of the stress tensor, which relates to the so–called Lode angle (θ). The deviatoric state parameter and the Lode angle are defined as follows:

$$\xi = \frac{27}{2}\frac{J_3}{\bar{\sigma}^3} = \cos(3\theta) \tag{2.4}$$

$$\bar{\theta} = 1 - \frac{6\theta}{\pi} \tag{2.5}$$

where J_3 is the third invariant of the deviatoric tensor and $\bar{\theta}$ is the normalized Lode angle. The deviatoric state parameter (ξ) and $\bar{\theta}$ both have a valid range of [-1, 1].

2.2.3 Fracture Locus under Special Loading Conditions

Bai and Wierzbicki [85] introduced an asymmetric fracture locus in the space of equivalent fracture strain, stress triaxiality state parameter, and the Lode angle parameter. The authors proposed a fracture model based on the experimental observations of the material fracture dependency on the stress state parameters.

Figure 2.4 shows a number of important spatial loading cases which have significant practical meaning. This diagram can be viewed as a 2D projection of the 3D fracture surface. For example, it is possible to relate ξ and η by Equation (2.6) in the case of plane stress state [86].

$$\xi = -\frac{27}{2}\eta\left(\eta^2 - \frac{1}{3}\right) \tag{2.6}$$

The tensile and compression axial symmetry loading states $\xi = 1$ and $\xi = -1$ can be achieved experimentally by using the classical notched or smooth round bar specimen. Also, a similar state of stress is achieved in equibiaxial tension and compression experiments [85].

The plane strain state is another special loading condition, which is represented by the gray line in Figure 2.4 where $\xi = 0$. This particular loading condition is the interest of the current study. The orthogonal metal cutting (OMC) investigated here is in the plane strain condition.

2.3 Metal Cutting Specific Loading Condition

Complete understanding of the work material behavior under the loading conditions similar to that which occur in the cutting process is critical in the development of FE–based models. For example, the material behavior may change significantly depending on the loading state. Particularly, the material ductility and damage evolution behavior may change according to its state of stress. Moreover, the deformation rate and temperature state may also alter the overall material strength and its fracture properties [90, 91, 92].

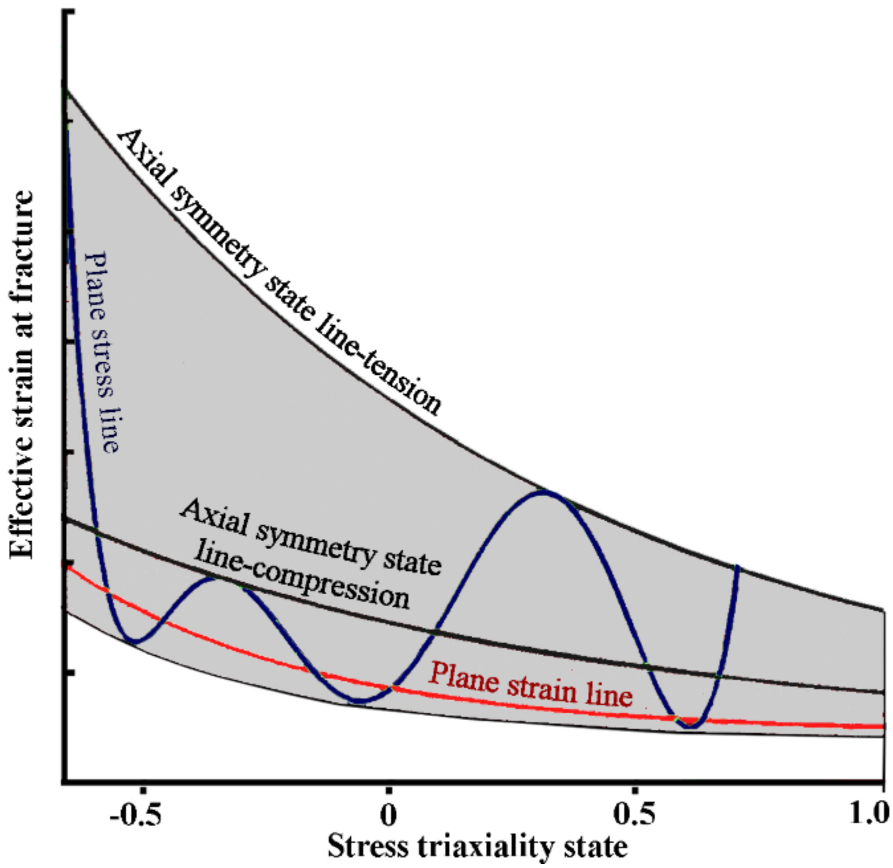

Figure 2.4: Typical fracture locus for a number of special loading conditions in strain–triaxiality space

2.3.1 Stress State

OMC where the cutting edge is perpendicular to the direction of the cutting velocity (see Figure 2.5) is generally taking place as a plane strain condition. This notion is widely accepted and used extensively in FE modeling of metal cutting. For example, Zhang et al. [93]

implemented the two–dimensional plane–strain elements to investigate the chip–tool interface in machining of a Titanium alloy workpiece. The same approach was adopted by Duan et al. [94] who focused on modeling the serrated chip morphology when cutting steel AISI 1045 under a high speed condition.

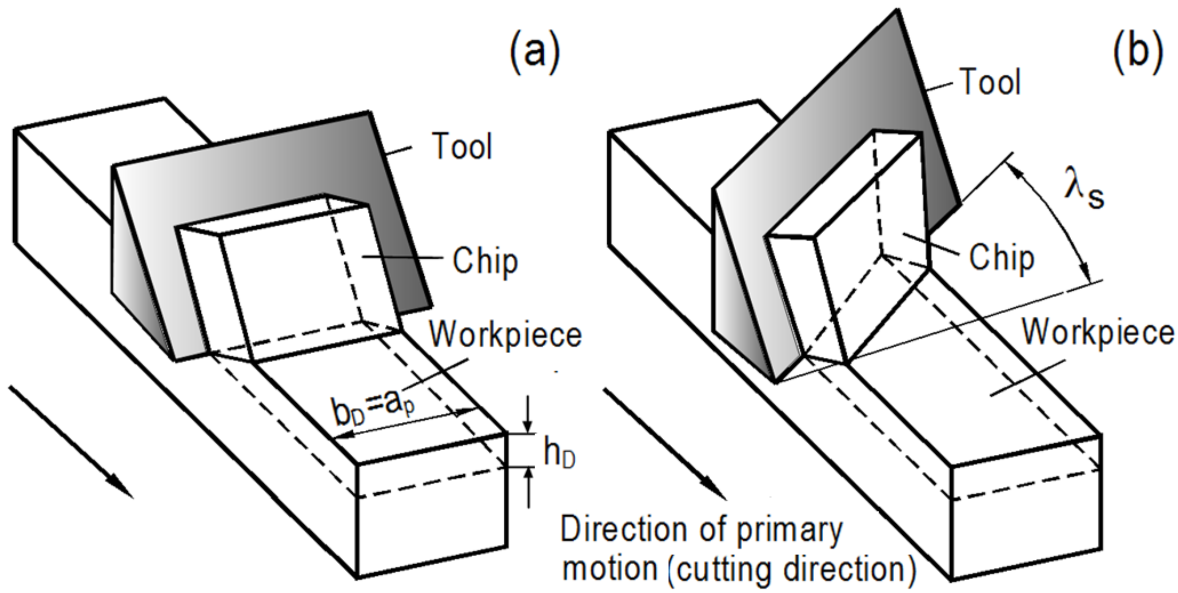

Figure 2.5: Representations of orthogonal (a) and oblique (b) cutting

Although most of the previous works have considered the above portion of the stress state (the plane strain condition) in their material deformation formulations, few have included the influence of the state of stress in material plasticity limit and fracture models. Furthermore, material fracture parameters in metal cutting conditions were never investigated. On the other hand, researchers made significant progress in fracture mechanics based models and methodologies for stress state parameterization and material characterization, but this knowledge has not been linked to metal cutting conditions.

The large and heterogeneous deformation occurring in the cutting process causes the dilatational stress component to vary inconsistently, depending on the specific cutting condition.

For example, in addition to the zero deviatoric effect on the chip separation zone near tool tip due to plane strain condition, this zone is also under a positive stress triaxiality because of the hydrostatic tensile stress originated before separation. A negative triaxiality, on the other hand, can be the case in the zone of plastic deformation ahead of the tool.

As described by Astakhov [2], the greatest amount of energy spent in the machining operations is due to plastic deformation of the layer being removed in its transformation into the chip. As shown by Astakhov and Xiao [76], this portion of energy is in the range of 65–80% of the total energy required by the cutting system. Therefore, reduction of this plastic deformation is needed to improve the cutting process in terms of reducing the cutting forces and cutting tool wear, i.e. improving the overall process efficiency. The total plastic deformation depends on the ductility of the work material and the state of stress in the deformation zone. Specific cutting arrangements may lead to different state of stresses and therefore affects work material ductility. For example, altering the tool geometry and/or process parameters in the OMC may change the stress triaxiality state map of the workpiece. As a result, the amount of plastic deformation (strain) required to achieve the fracture of the work material also varies. Therefore, a set of criteria for the selection of cutting tool parameters, together with setting the optimal machining regime, may be developed based on this hypothesis.

2.3.2 Strain Rate

High Speed Machining (HSM) as an idea and now an industrial technology was developed to improve the machining efficiency [95]. HSM has many advantages over conventional machining, such as improving the quality of the machined surface and reducing manufacturing costs. In addition to the high material removal rate, it is also observed that the cutting speed often reduces the cutting force and increases tool life [96]. Due to these economical and technical advantages, HSM technology has becoming very popular in many industries. HSM, however, also introduces new challenges. Unlike the conventional machining, HSM develops elevated strain rates ranging from 10^3 to 10^6 s^{-1} [92]. Generally, the strain rates can be classified into three regions that range from low $(\dot{\bar{\varepsilon}} < 1\, s^{-1})$, medium $(1\, s^{-1} < \dot{\bar{\varepsilon}} < 10^3\, s)$, to high $(\dot{\bar{\varepsilon}} > 10^3\ s^{-1})$. According to Davim and Maranhao (2009), HSM strain rates are considered to be high and the influence of the equivalent strain rate $(\dot{\bar{\varepsilon}})$ can be substantial [90].

2.3.3 Thermal Softening

Nearly all investigations on metal cutting have considered, or at least mentioned, the importance of the heat generation in the machining process. The heat generated in the deformation zone gives rise to a high temperature of the work material, which in turn affects its ductility. Naturally, all modern material models used in metal cutting simulation, including those used in the commercial FEM packages for metal cutting simulations, include the influence of temperature on the mechanical properties of the work material.

Detailed analysis of the heat partition and temperatures in the deformation zone in metal cutting is presented in Appendix B. It is shown that the metal cutting process is a cold–working process where temperatures due to the work material deformation and chip friction on the tool–chip interface cannot affect the properties of the work material at the primary deformation zone to any noticeable level. Although the temperature effect on the work material exists, its effect on the work material is negligible.

2.4 Material Constitutive Equations

2.4.1 Plasticity Model

Generally, the plastic flow of a material depends on its equivalent strain $(\bar{\varepsilon})$, equivalent strain rate $(\dot{\bar{\varepsilon}})$, and its temperature (T). The material plastic flow is often described as the product of these three functions as:

$$\bar{\sigma} = f\left(\bar{\varepsilon}\right) g\left(\dot{\bar{\varepsilon}}\right) h\left(T\right) \tag{2.7}$$

where $\bar{\sigma}$ is the equivalent stress.

The Johnson–Cook (JC) model, developed in 1983 [97], is a material constitutive equation widely used in FEA of metal cutting, which describes the material constitutive behavior in terms of the above three functions as:

$$\bar{\sigma} = \left[A + B\bar{\varepsilon}^{n}\right]\left[1 + C\ln\left(\frac{\dot{\bar{\varepsilon}}}{\dot{\bar{\varepsilon}}_{o}}\right)\right]\left[1 - \left(\frac{T - T_{o}}{T_{m} - T_{o}}\right)^{m}\right] \tag{2.8}$$

where A is the initial yield strength, B is the hardening modulus, and C is the strain rate sensitivity. These parameters, as well as the hardening (n) and thermal softening (m) coefficients, can be obtained by conducting material tests at low strain rates, various temperature levels by conventional tests, and at high strain rates using the Split Hopkinson Pressure Bar (SHPB) tests [97]. Parameters $\dot{\bar{\varepsilon}}_{o}$, T_{o}, and T_{m} in the JC model are the reference strain rate, the reference or ambient temperature, and the material melting temperature, respectively.

As discussed in Section 2.3.3, the temperature effect is neglected so the model can be reduced to

$$\bar{\sigma} = \left[A + B\,\bar{\varepsilon}^{n}\right]\left[1 + C\ln\left(\frac{\dot{\varepsilon}}{\dot{\varepsilon}_{o}}\right)\right] \tag{2.9}$$

Figure 2.6 shows experimental data of the material plasticity for steel AISI 1045 and the least square fitting of the JC plasticity model. Only the static loading condition is presented in this figure. The dynamic effects due to elevated strain rate will be considered using the JC strain rate sensitivity function in Equation (2.9).

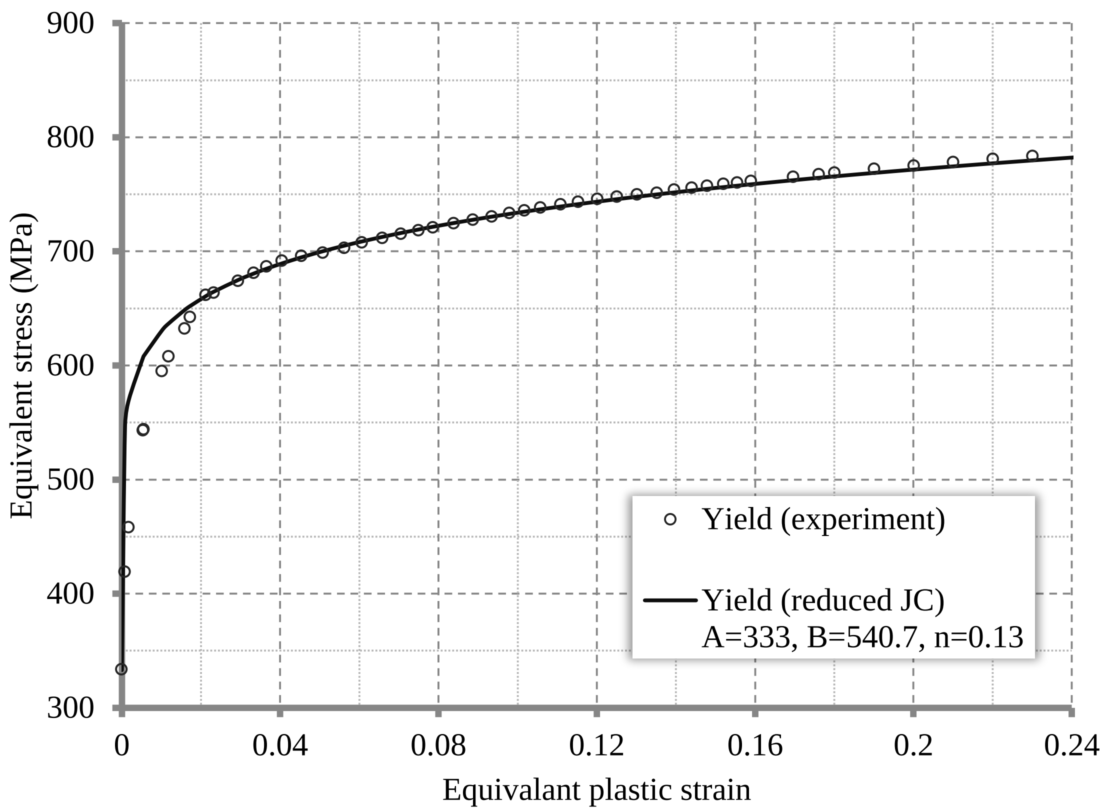

Figure 2.6: Experimental vs. JC stress–strain curve for steel AISI 1045

2.4.2 Damage Model

Most engineering design and applications are concentrated on the material elastic range with less interest on the plastic limit. On the contrary, a fracture model in metal cutting operations is of extreme importance in obtaining a realistic chip microstructure modality and its physical characteristics.

In ductile metals, such as steel AISI 1045, the term ‘fracture’ must be clearly defined. In such materials, the propagation of cracks is the last stage of progressive damage evolution, after the nucleation, growth, and coalescence of microscopic voids. In the literature, the fracture locus in ductile metals is often referred to as the final fracture stage, where the material has lost all of its load carrying capacity. However, because the damage process starts with the creation of microscopic voids in a considerably earlier stage in ductile metals, the fracture locus by itself may not precisely describe the material fracture behavior in local sense. Instead, damage initiation, i.e. “the nucleation of microscopic voids”, may be referred to as the local fracture locus. In addition, the state of loading conditions under which the damage is initiated is considered as a dependent parameter of the fracture locus. By our opinion, neither the initial nor the path of the state of stress would play a role in governing the fracture process. However, other parameters such as the deformation rate may have a significant impact on the damage onset. Therefore, the current approach considers the fracture locus as the damage initiation at a reference static state. The dynamic loading effect is accounted for through the material toughness which is assumed to vary depending on the state of stress.

2.4.2.1 Damage Initiation Model

Generally, metallic materials rupture either through ductile fracture (based on initiation, growth and coalescence of voids) or shear fracture (based on shear band localization) [83]. Depending upon the stress state, rupture could also occur through a process involving both mechanisms. Furthermore, fracture properties and damage behavior may change significantly within a single or across the two different mechanisms.

The equivalent plastic strain limit is usually used to characterize the rupture of ductile materials. As discussed before, the strain at which damage is initiated typically depends on the loading condition.

As mentioned above, McClintock [80] and Rice and Tracey [78] studied the ductile growth and coalescence of microscopic voids under the superposition of hydrostatic stresses. Their analytical study used idealized cylindrical and spherical cavities to investigate the effect of the hydrostatic stress on growth rate. It was found that for any remote strain rate field, the void enlargement rate is amplified over the remote strain rate by a factor rising exponentially with the stress triaxiality parameter (η), according to the following function:

$$\bar{\varepsilon} = C_1 \mathrm{e}^{C_2 \eta} \tag{2.10}$$

where C_1 and C_2 are material fracture constants to be determined experimentally and $\bar{\varepsilon}$ is the corresponding equivalent fracture strain. Other researchers have developed similar relations. For instance, Johnson and Cook [98] introduced a fracture model that integrates the effect of stress triaxiality, strain rate, and temperature in a separable function with five independent material fracture constants. Equation (2.11) shows the reduced form of the JC damage model with three material damage constants (D_1, D_2, D_3).

$$\bar{\varepsilon} = D_1 + D_2 \mathrm{e}^{D_3 \eta} \tag{2.11}$$

The calibration of the above two models will be conducted using a double–notched plane–strain specimen which permits triaxiality adjustments. This experiment approach will be discussed in Chapter 3.

2.4.2.2 Post Damage Contribution

In ductile metals, final fracture is preceded by extreme plastic deformation and damage evolution. As discussed above, specimens in a uniaxial tensile stress test at some point start to develop microscopic voids in a process called void formation and coalescence. Those growing voids initiate microcracks in a progressive way, which eventually leads to fracture. The damage initiation site may be different from the observed fracture site. Figure 2.7 shows a hypothetic undamaged stress–strain curve shown by the dashed line. Such a curve is used in the existing FEM model of materials behavior. In the same figure, the real curve is the one obtained from a conventional uniaxial stress test, and is shown by the solid line. The elastic–plastic undamaged path ***abc*** is followed by the departure of the experimental yield surface from the virtual undamaged yield surface at point ***c***. Point ***c*** can be considered as the hypothetic damage initiation site where the material hardening modulus becomes progressively sensitive to the amount of damage leading to the declination of the material loading capacity. The hypothetic damage initiation site ***c*** also marks the start of elasticity modulus degradation. Due to increased damage, the material reaches its ultimate stress capacity at *d* where the hardening modulus becomes zero. This usually occurs in ductile metals when the material loading capacity decreases by 30% to 70% of its full capacity due to the accumulated damage [93]. The observed fracture initiation site is denoted by point ***e*** and finally the theoretical failure is indicated by point ***f***.

To estimate the material stiffness degradation after damage initiation at point ***c***, the material fracture energy concept introduced by Hillerborg et al. [99] was considered. Hillerborg postulated that the energy dissipated during the material degradation process is characterized by the amount of energy required to open a unit area of crack based on linear elastic fracture mechanics (LEFM). The LEFM has been successfully implemented in estimating the fracture energy in brittle materials. For ductile materials, however, the energy absorption (toughness) can be significantly higher because it resists crack propagation and creates a stability condition. To account for the plasticity effect on the fracture of ductile metals properly, the fracture energy density portion of the material toughness was used.

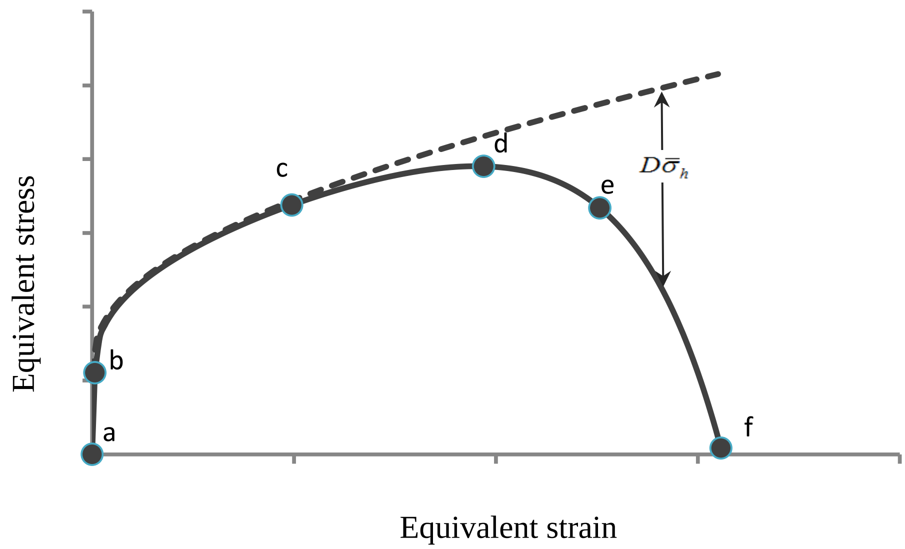

Figure 2.7: Typical metal true stress–strain response in a uniaxial test

Material strength degradation behavior beyond damage initiation is controlled by a scalar damage parameter D, which is assumed to grow exponentially according to the following equation:

$$D = \frac{1-\exp\left(\lambda\varepsilon^{*}\right)}{1-\exp\left(\lambda\right)}, \ \varepsilon^{*} = \frac{\bar{\varepsilon}^{p} - \bar{\varepsilon}_{c}^{p}}{\bar{\varepsilon}_{f}^{p} - \bar{\varepsilon}_{c}^{p}} \tag{2.12}$$

where λ is the exponent parameter that controls the material degradation rate, $\bar{\varepsilon}_{c}^{p}$ *and* $\bar{\varepsilon}_{f}^{p}$ are the equivalent plastic strains at points ***c*** and ***f*** in Figure 2.7. The degradation rate may vary depending on λ, which can be considered as a material fracture parameter. In other words, the rate under which the fracture energy is dissipated is controlled by λ (Figure 2.8).

In Equation (2.12), $\bar{\varepsilon}_c^p$ is the plastic strain at damage initiation, which can be calculated by Equation (2.11), $\bar{\varepsilon}_f^p$ is the plastic strain at the point where material has lost all its stiffness and dissipated all the fracture energy. Therefore $\bar{\varepsilon}_f^p$ can be calculated using the following equation

$$G_f = \int_{\bar{\varepsilon}_c^p}^{\bar{\varepsilon}_f^p} \bar{\sigma} d\bar{\varepsilon}^p \tag{2.13}$$

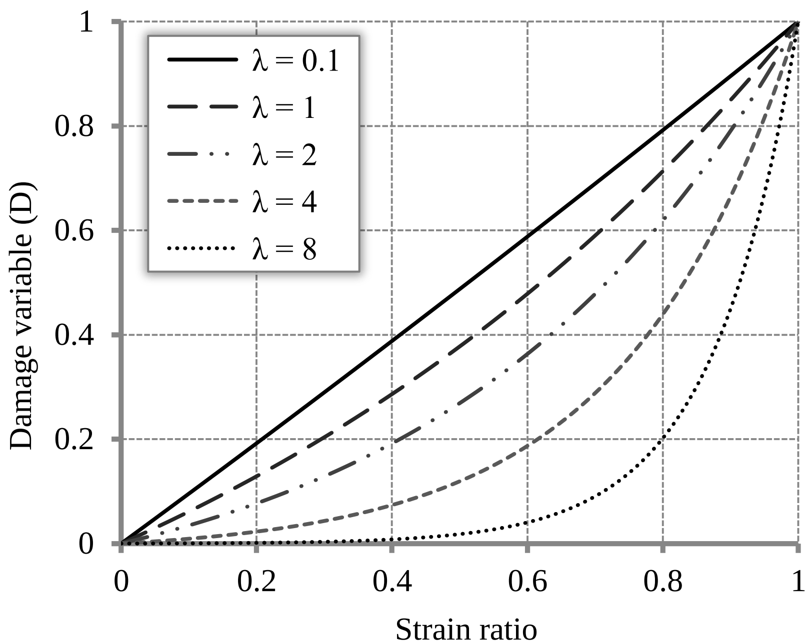

Figure 2.8: Scalar damage variable at different values of the exponent parameter β

The material is assumed to start the strain softening and degradation when the damage indicator (ω)

$$\omega = \sum_{j=1}^{m} \frac{\Delta\bar{\varepsilon}^p}{\bar{\varepsilon}_c^p} \tag{2.14}$$

reaches unity. In this equation, m is the total number of loading increments and $\Delta\bar{\varepsilon}^{p}$ is the equivalent plastic strain increase during the loading increment j.

The scalar damage parameter (D) is used to describe the material flow past damage initiation by the following relationship

$$\bar{\sigma} = (1 - D)\bar{\sigma}_h \tag{2.15}$$

where $\bar{\sigma}_h$ is the hypothetic undamaged stress estimated by Equation (2.9).

2.4.2.3 Strain Rate Sensitivity

Most of the fracture models including the JC model developed by Johnson and Cook in 1985 [98], include a strain rate influence factor. However, the JC damage model does not include all stress state parameters. Even with the separable nature of this model and its availability in most commercial FE packages such as ***ABAQUS*™** and ***LS–DYNA*™**, it remains unclear how the five material fracture constants are calibrated. Recently, Leppin et al. [83] successfully predicted the results of dynamic axial crash test using numerical simulation. The fracture model treats the ductile and shear fracture modes separately through the introduction of ductile and shear equivalent plastic strains $(\bar{\varepsilon}_{fd}, \bar{\varepsilon}_{fs})$, both of which are functions of the strain rate. It was assumed that fracture occurs when one of these equivalent plastic strain accumulations reaches a critical value.

In the context of the current development, the generalized equivalent plastic strain fracture model introduced by Clift et al. [100] was considered. In this model it is postulated that fracture occurs when the integration of the equivalent plastic strain weighted by the equivalent stress $(\bar{\sigma})$ achieves a predefined critical value ψ.

$$\psi = \int_0^{\bar{\varepsilon}_f} \bar{\sigma} d\bar{\varepsilon} \tag{2.16}$$

Note that dimension of ψ in Equation (2.16) is the energy density.

This model suggests that the material toughness is a constant value because the area underneath the stress–strain curve is an invariable. However, since the equivalent strain at fracture $(\bar{\varepsilon}_f)$ in general is a function of the stress state, it is reasonable to assume that the critical value of ψ is dependent of the stress state. In other words, a given state of stress at fracture (η_f, ξ_f) results in a particular ψ that is different from that obtained at other states of stress. Therefore, ψ in Equation (2.16) should not be a constant but rather a function of a given state of stress, i.e.

$$\psi(stress\ state\ at\ fracture) = \int_0^{\bar{\varepsilon}_f} \bar{\sigma} d\bar{\varepsilon} \tag{2.17}$$

Although Equation (2.17) contains the equivalent stress which depends upon the strain rate according to Equation (2.9), the total amount of specific energy to fracture E is independent of the strain rate. Nevertheless, the equivalent strain at fracture $(\bar{\varepsilon}_f)$ is dependent of the strain rate because of the material strain rate hardening. This parameter was calibrated for the JC plasticity model by a number of researchers (see Table 3.3). For example, Jaspers and Dautzenberg (2002) concluded that the strain rate hardening for steel AISI 1045 is 0.0134 [91].

To investigate the effect of the strain rate on the material ductility, consider an adiabatic loading condition where no heat flows from the surrounding to the system, the substitution of Equation (2.7) into Equation (2.17) gives:

$$\psi(\xi_f, \eta_f) = \int_0^{\bar{\varepsilon}_f} f(\bar{\varepsilon}) g(\dot{\bar{\varepsilon}}) d\bar{\varepsilon} \tag{2.18}$$

For a separable strain fracture model that depends on both stress state at fracture and strain rate, we may introduce the general equivalent strain at fracture in the following form.

$$\bar{\varepsilon}_f(\xi_f, \eta_f, \dot{\bar{\varepsilon}}) = S(\xi_f, \eta_f) R(\dot{\bar{\varepsilon}}) \tag{2.19}$$

where S is the fracture locus at the reference equivalent strain rate $\dot{\bar{\varepsilon}}_o$ and R is the fracture strain rate sensitivity function. Considering the special case where $\dot{\bar{\varepsilon}}$ is constant during plastic deformation and all the way to the fracture, the integration and separation of Equations (2.18) and (2.19) provide the following result

$$R(\dot{\bar{\varepsilon}}) = \left[g(\dot{\bar{\varepsilon}}) \right]^{-2/(n+2)} \tag{2.20}$$

Note that for the case of plane strain loading the reference fracture locus S depends only on the stress triaxiality at fracture as described by Equation (2.10) and (2.11). The overall equivalent plastic strain at fracture can be obtained by combining Equations (2.19) and (2.20)

$$\bar{\varepsilon}_f(\xi_f, \eta_f, \dot{\bar{\varepsilon}}) = S(\xi_f, \eta_f) \left[g(\dot{\bar{\varepsilon}}) \right]^{-2/(n+2)} \tag{2.21}$$

Using the JC strain rate sensitivity function term $g(\dot{\bar{\varepsilon}})$ from Equation (2.8) and the reference fracture locus $(S = \bar{\varepsilon}_f^{(0)})$ from Equation (2.10), the following plane strain fracture model can be obtained.

$$\bar{\varepsilon}_f^{(0)}(\eta_f, \dot{\bar{\varepsilon}}) = C_1 e^{C_2 \eta_f} \left[1 + C \ln\left(\frac{\dot{\bar{\varepsilon}}}{\dot{\bar{\varepsilon}}_o} \right) \right]^{-2/(n+2)} \tag{2.22}$$

This result governs the material ductile fracture which obeys the JC constitutive law and uses material flow sensitivity to the strain rate to account for the fracture strain rate sensitivity. Equation (2.22) represents a special case where the loading process maintains a constant $\dot{\bar{\varepsilon}}$. To account for the case where the strain rate path is not constant and/or using a different constitutive model, Equation (2.17) should be used. Figure 2.9 shows the stress triaxiality contours in the $\bar{\varepsilon}_f^{(0)}$ and $\dot{\bar{\varepsilon}}$ space for steel AISI 1045. The curves indicate material ductility declination with increase of strain rate. Another observation is that for the conditions at low and negative stress triaxiality similar to the conventional metal cutting, it is expected that $\bar{\varepsilon}_f^{(0)}$ will drop significantly with increasing the rate when compared to higher values of stress triaxiality.

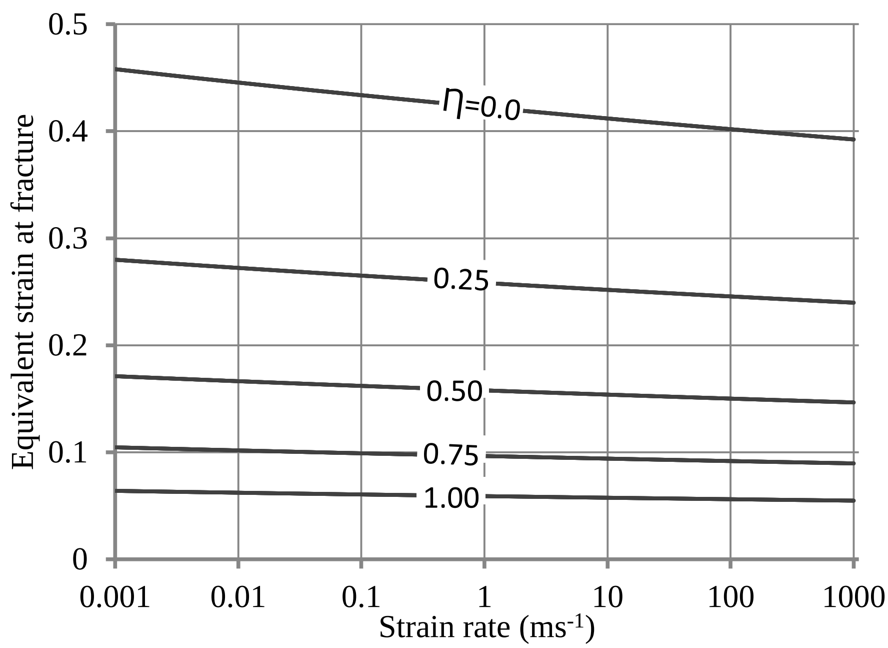

Figure 2.9: The strain rate impact on the equivalent fracture strain at different stress states for steel AISI 1045

2.5 Conclusions

In metal cutting, including its simplest case OMC, the deformation of the layer being removed during its transformation into the chip takes place under a complex multi axial stress state. The effect of stress state is characterized by the stress triaxiality.

The real damage curve that describes the realistic behavior of the work material was introduced in the analysis of plastic deformation and fracture conditions of the work material instead of the hypothetical flow curve having no deformation limit used in current FEM of metal cutting.

The constitutive model of the work material behavior in the cutting process was developed by accounting for the stress triaxiality and the strain rate. It is postulated that the area under the damage curve, which represents the energy needed for the plastic deformation of the work material before it fractures, varies with the state of stress. The proposed model accounts for the material strength degradation phase by a scalar damage parameter prior final fracture. The flow, damage, and fracture parameters introduced in this model will be determined experimentally in the next chapter.

It was hypothesized that the total strain energy to fracture can be minimized by adjusting the degree of triaxiality and the strain rate. Because the energy of plastic deformation constituted 65–80% of the total energy required for cutting, such a reduction can be a powerful mean to improve the cutting process in terms of a significant reduction of the total energy spent in cutting that, in turn, can result in significant reduction of the cutting force, improvement of the quality of the machined surface, and increased tool life.

Chapter 3: Material Characterization Experiment

This chapter presents a new experimental approach to obtaining material constitutive parameters for orthogonal cutting, i.e. under plane strain condition. The approach utilizes a new, adjustable stress state specimen, Digital Image Correlation (DIC) measurements, and an inverse method for parameter identification. The developed double–notched specimen is purposely designed to allow the identification of damage and fracture parameters for the plane strain condition. The corresponding equivalent plastic strains at different stages of deformation and damage were calculated using DIC measurements. The elastic modulus and yield surface were obtained using a numerical optimization based inverse method. Ultimately, the fracture locus was obtained and the parameters of the Rice and the reduced form of the Johnson Cook (JC) damage models were identified. The model validation is also provided.

3.1 Ductile Fracture Experiments

Although conventional material characterization methodologies can find the material flow parameters, a non–conventional approach is often required to obtain material fracture parameters. The experimental setup for material fracture characterization should be designed focusing on the examination of fracture under loading conditions similar to those found in the intended application. In order to characterize the material damage behavior, damage initiation, and post damage evolution in conventional orthogonal cutting (OMC), the specimen must ensure the plane strain condition and allow stress triaxiality adjustments.

It was discussed in the previews chapter that the OMC generally maintains the deviatoric state parameter $\xi = 0$. This reveals that as long as plane strain condition is fixed, the ductility of the work material is affected only by the stress triaxiality state parameter (η). In order to construct a fracture model for such a process, the experimental setup should be designed to allow the examination of fracture at conditions where η varies while $\xi = 0$ (or equivalently normalized Lode angle $\bar{\theta} = 0$). Figure 3.1 shows a typical fracture surface of ductile metals in η and $\bar{\theta}$ [87].

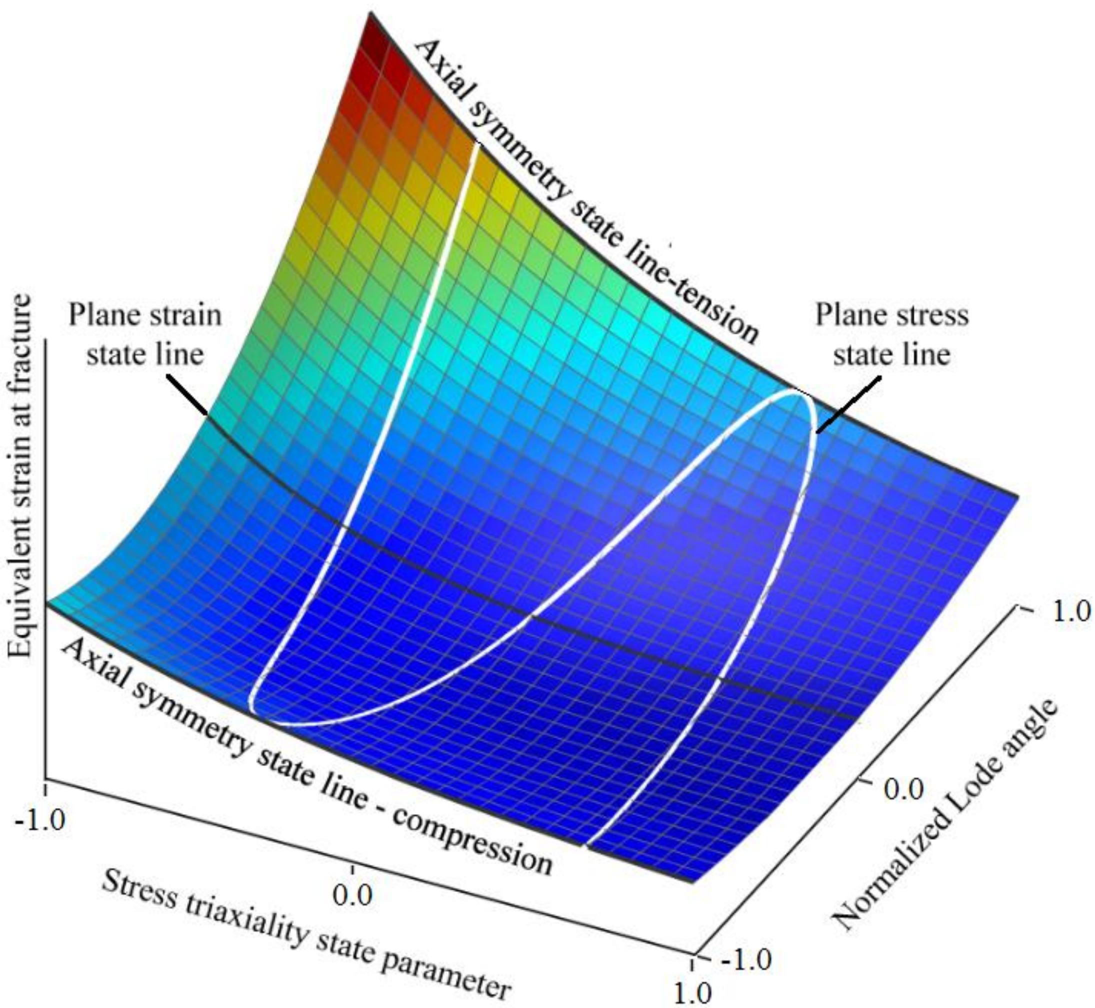

Figure 3.1: General fracture locus surface for ductile metals as postulated by Bai et al. [87] (reproduced)

3.1.1 The Classical Flat Grooved Specimen

Several specimens have been developed to generate data under triaxial stress conditions. Testing of a flat–grooved specimen can provide experimental data on material fracture mechanics at regions of stress state where $\xi = 0$ that is different from those obtained with round–notched bars. Specimens of a circular bar shape provide information at the axial symmetry lines $\xi = \pm 1$, which is far away from the plane strain state. The plane strain fracture model may be calibrated using grooved plane strain specimen [87]. For calibration purposes, the pure shear torsion test may also be combined with other plane strain experiments superimposed with the hydrostatic pressure to account for various stress triaxiality state parameter (η). The stress triaxiality variation can be accomplished by changing geometrical configuration of the flat–grooved test specimen as shown in Figure 3.2.

Figure 3.2: Steel AISI 1045 plane strain flat specimens with different groove radius [87]

Bai et al. [87] developed a stress triaxiality expression, Equation (3.1), for flat–grooved plate specimens. The formulation is similar to that of round notched bars developed by Bridgman in 1952 [101]. The developed relationship relates the triaxiality parameter to the ratio of the ligament thickness (t) and the radius of the groove (r). It is assumed that the material flow obeys a rigid–perfect–plastic law, where the strain hardening of the material was assumed to have a minor effect on the stress triaxiality parameter because the mean stress is normalized by the equivalent stress.

$$\eta = \frac{\sqrt{3}}{3}\left[1 + 2\ln\left(1 + \frac{t}{4r}\right)\right] \tag{3.1}$$

The equivalent fracture strain $(\bar{\varepsilon}_f)$ is determined using the following equation [87]:

$$\bar{\varepsilon}_f = \frac{2}{\sqrt{3}}\ln\left(\frac{t_o}{t_f}\right) \tag{3.2}$$

Equation (3.2) requires the original specimen thickness (t_o) and the specimen thickness at fracture (t_f) to be known, which may be measured directly from the specimen before and after experiment respectivily. However, unless the material has a brittle like rupture behavior, the necking may introduce practical difficulties in finding the exact onset of the fracture strain. As a result, the calculated $\bar{\varepsilon}_f$ may be overestimated and reflect the material strain beyond its damage initiation (onset site) where the material may have lost all its stiffness.

Numerical analyses were carried out to investigate the effect of the specimen's groove radius on the triaxiality state of stress. Figure 3.3 shows the triaxiality state contours obtained from symmetric FEM simulations of a tensile test for a number of flat grooved specimens with different groove radius (r) and initial gauge thickness (t_o). Considering the symmetry of the specimen, only half–plane of the specimens are modeled. The specimens dimensions are chosen to simulate the actual experiment conducted by Wierzbicki's group [87]. The analysis shows that the intensity of η increases by reducing the grove radius r. The maximum value of η is found in the gauge zone at the center plane of the specimen.

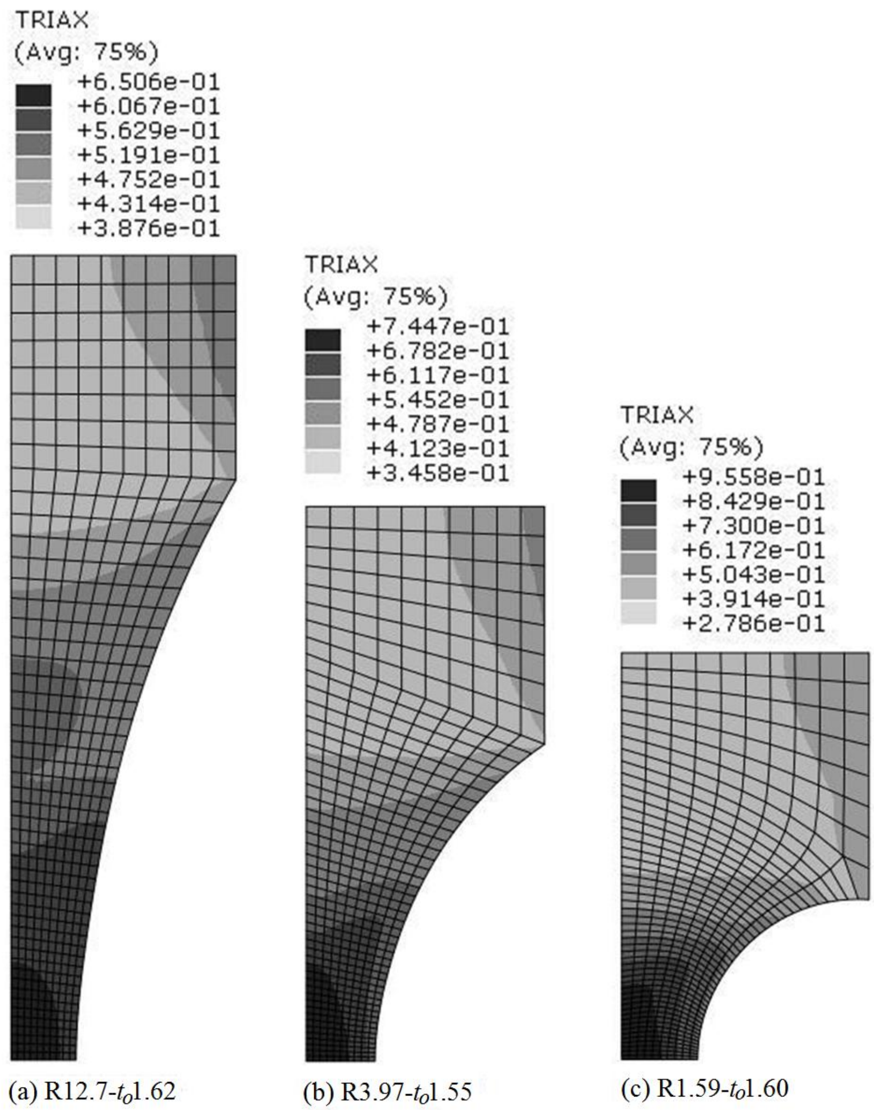

Figure 3.3: Symmetric FE simulation with the stress triaxiality contours at fracture for three selected flat–grooved specimens made of steel AISI 1045. Specimen (a) groove radius R=12.7 mm, ligament thickness t_o=1.62 mm, specimen (b) R=3.97 mm, t_o=1.55 mm, and specimen (c) R=1.59 mm, t_o=1.60 mm

The initial η calculated directly using Equation (3.1) may differ from the final value at fracture. The triaxiality stress state development during plastic loading is restrained by the material constitutive equation and the amount of plastic deformation gained by the specimen during loading progression (Figure 3.4). Therefore, it is expected to end up with a larger stress triaxiality value at fracture compared to the initial value, calculated by Equation (3.1), which estimates triaxiality based on perfect plasticity flow assumption – rigid–perfectly plastic work material behavior.

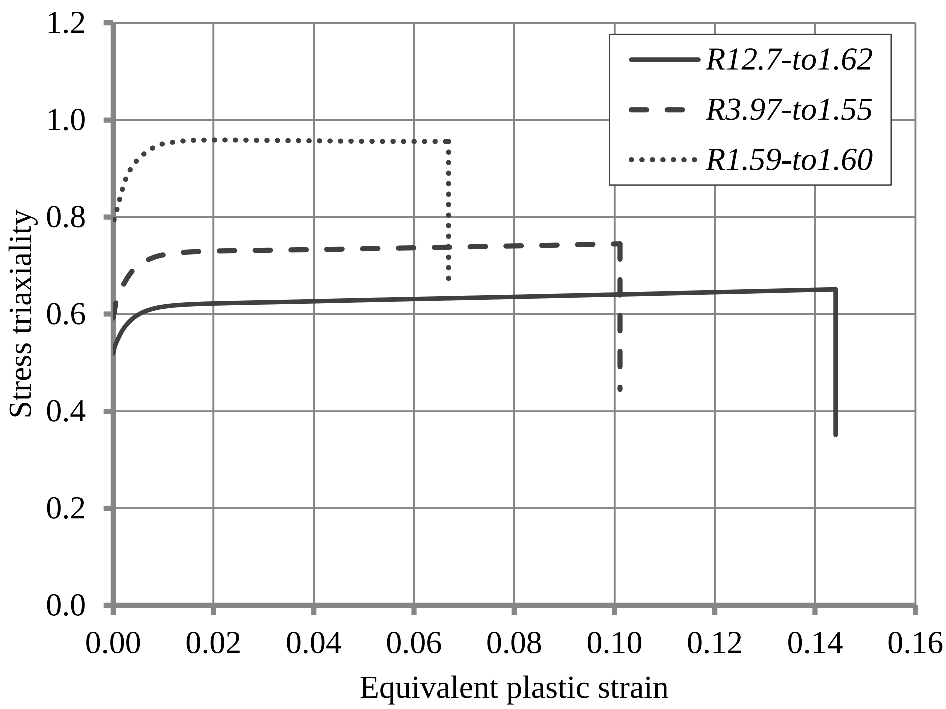

Figure 3.4: Stress triaxiality evolution diagram of steel AISI 1045 obtained from FE simulation for three selected flat–grooved specimens

To account for the variation of stress triaxiality during loading, the average stress triaxiality value (η_{av}) may be used instead of the initial value. Knowing the required stress triaxiality history data, one can calculate η_{av} using the following equation:

$$\eta_{av} = \frac{1}{\bar{\varepsilon}_f} \int_0^{\bar{\varepsilon}_f} \eta(\bar{\varepsilon}) d\bar{\varepsilon} \tag{3.3}$$

Wierzbicki et al. [87, 102] performed parallel numerical simulations and used the triaxiality history output field with Equation (3.3) to construct the fracture locus. The authors used the experimentally measured displacement to indicate fracture in their FE model. This approach can be used with a flat–grooved plate (or round–notched bar) specimen, where η is expected to vary during experiments. For example, the experimental results obtained using the results of the pure shear test with a tubular specimen require no averaging because no axial loading is imposed $(\eta = \eta_{av} = 0)$.

Although the use of Equation (3.3) indicates a complex contribution of the stress state path, it is still not clear whether this stress state path $\left(\eta(\bar{\varepsilon}) \, and \, \xi(\bar{\varepsilon})\right)$ has an effect on the fracture locus and the nature of its role. However, the motivation for using Equation (3.3) could be a consequence of the uncertainty on the definition of the onset material fracture. Due to the evolution nature of fracture mechanics, the material loading capacity gradually degrades beyond the fracture initiation point, but does not drop suddenly. Therefore, depending on the method of measurement, the measured displacement to fracture may not precisely indicate the fracture initiation. Furthermore, the prominent decrease in the specimen local cross–sectional area during necking results in localized large strains which severely affect the state of stress. These dramatic changes occurring during damage evolution may mislead the identification of the state of stress at fracture initiation.

Figure 3.5 shows a comparison of the different approaches, along with the numerical analysis, based on the fracture strain limit calculated directly by Equation (3.2). The fracture locus calculated by this method indicates much lower $\bar{\varepsilon}_f$ compared to the displacement limit model. However, the fracture locus suggested by Bai et al. [87], which uses values of η_{av} obtained from simulation based on the displacement limit, did not include the tubular specimen results. Unlike flat–grooved specimen, a pure shear experiment does not have the complications of a changing triaxiality, and therefore should not be excluded from the analysis.

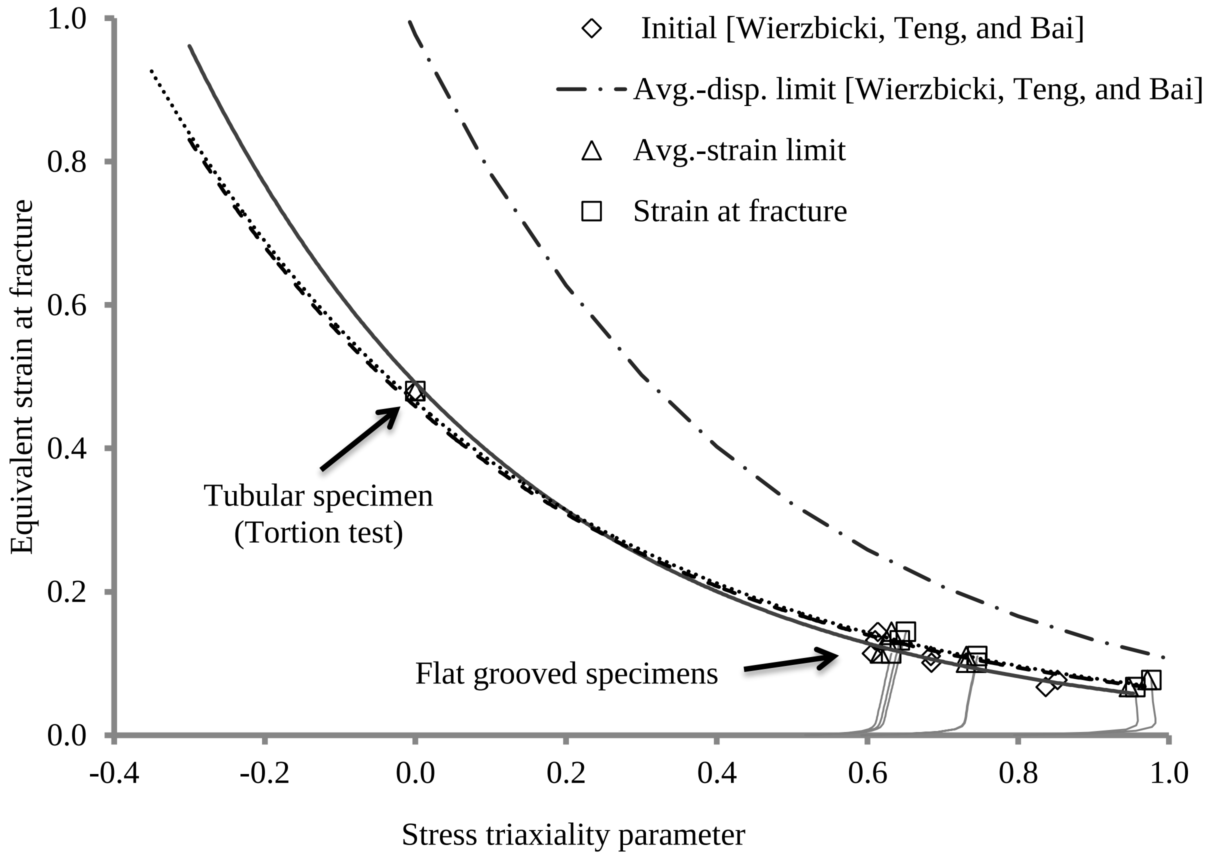

Figure 3.5: Steel AISI 1045 fracture locus in plane strain condition fitted to Rice and Tracey [78] model based on initial stress triaxiality, average using displacement limit simulation model, average using strain limit model, and the fracture locus based on strain at fracture. Stress triaxiality evolution curves are also shown.

Table 3.1 shows the results of the stress triaxiality calculations using the different approaches shown in Figure 3.5.

Table 3.1: The initial, final, and average stress triaxiality calculated using numerical simulation results for steel AISI 1045

Experiment [a]	Stress triaxiality			Fracture strain [c]
	Initial [b]	At fracture	Average	
R12.7–t_o1.62	0.6136	0.6511	0.6319	0.1441
R12.7–t_o1.48	0.6105	0.6430	0.6256	0.1321
R12.7–t_o1.28	0.6061	0.6316	0.6166	0.1137
R3.97–t_o1.55	0.6849	0.7449	0.7310	0.1011
R3.97–t_o1.54	0.6842	0.7459	0.7312	0.1101
R1.59–t_o1.60	0.8365	0.9557	0.9471	0.0669
R1.59–t_o1.71	0.8523	0.9767	0.9717	0.0768
Tubular–torsion	0.0000	0.0000	0.0000	0.4787

[a] For detailed experimental data refer to [87].

[b] Calculated directly from Equation (3.1).

[c] Calculated directly from Equation (3.2). For tubular specimen refer to [87].

The above analysis of the different approaches results in various approximations of the material fracture locus. However, except for the displacement–limit approach, the other approximations are quite similar. This is because the stress state variation during the loading course is not significant in this type of specimen with this particular material. It is expected that these results vary more significantly if the triaxiality state evolution, similar to that shown in Figure 3.4, is changing more radically. However, as discussed above, the role of the stress state evolution is still unclear due to lack of relevant experimental studies and the uncertainty around the damage initiation site and damage evolution phase. It is in the author's opinion that under the current context the following are valid assumptions:

- The term fracture strain $\bar{\varepsilon}_f$ is defined as the equivalent strain at damage initiation site where the damage evolution phase starts.
- Only the stress state at the fracture onset may affect the stain limit under static loading condition. The stress state path has no influence on $\bar{\varepsilon}_f$.
- The damage evolution beyond the onset of fracture is characterized independently as a function of the material fracture energy density G_f.

Based on these assumptions and the above experimental/numerical analysis of the flat–grooved specimen, one may obtain the fracture parameters in Rice and Tracey [78] model (Equation (2.10)) by fitting the corresponding data in Table 3.1 as shown in Figure 3.5.

$$\bar{\varepsilon}_f = 0.465\mathrm{e}^{-1.96\eta} \tag{3.4}$$

Equation (3.4) represents the material strain limit formulated based on the stress state at fracture in static loading.

The use of flat grooved specimens in a uniaxial tensile test provides important data on the fracture onset under positive η. However, flat grooved specimens may not be suitable for predicting fracture at low and negative η, such as that found in OMC. For example, the work material in the chip separation zone near the tool tip is under $+\eta$ because of the hydrostatic tensile stress originated before chip separation. On the other hand, in the deformation zone where shear bands may be formed, the work material is mostly under $-\eta$ due to compressive stress (negative mean stress value). According to Bai et al. [87], the classical flat, smooth, and grooved specimens provide information on the material fracture behavior under stress triaxiality levels similar to the round bar specimen, but under plane strain conditions. It follows from Equation

(3.1) that for any arbitrary specimen geometry, the only attainable stress triaxiality range is $\eta \geq 1/\sqrt{3}$.

The experimental of Bai et al. [87] (Figure 3.6) shows the attainable range of stress triaxiality state using the flat–grooved specimens. The results are consistant with the above limitation. The triaxiality state parameter shown in Figure 3.6 are calculated based on Equation (3.1) (the initial values of η) and Equation (3.3) (the average values (η_{av})) to account for the fracture strain limit with and without the effect of triaxiality evolution path. Moreover, the compressive uniaxial test results in impractical negative values of η, where the pressure may exceed the cutoff pressure value. Under compressive loading, the cutoff pressure is defined as the maximum pressure under which fracture can occur whereas beyond this limit separation would never take place. Therefore, there is a need for a new plane strain specimen to uncover the exact material fracture response under a wide range of stress triaxiality.

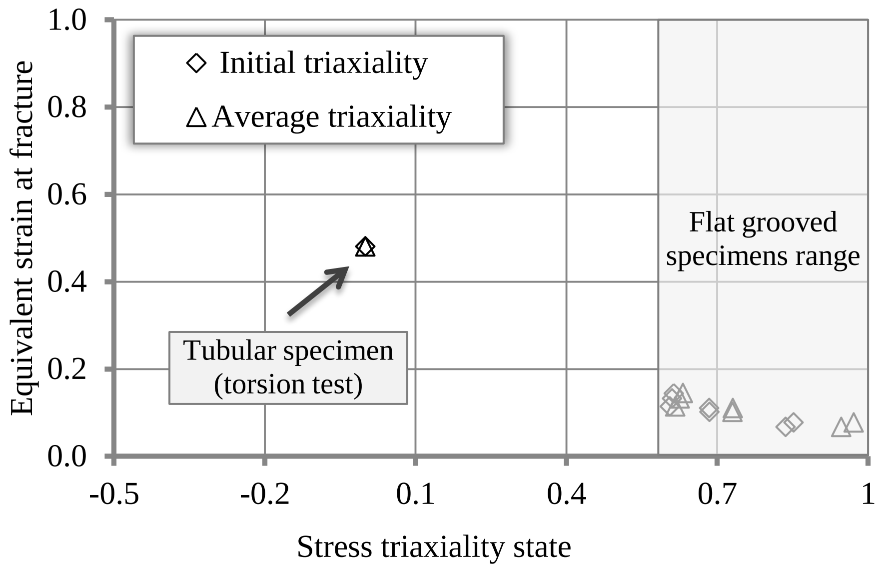

Figure 3.6: Fracture locus visibility for steel AISI 1045 using flat–grooved and tubular specimen [87]

3.1.2 The Proposed Plane Strain Specimen

In this work, a new plane strain specimen with a double–notched configuration is developed. The specimen was designed to investigate the fracture behavior of the material at levels of triaxiality not covered by the classical grooved specimens. The proposed specimen configuration shown in Figure 3.7 is a plane strain specimen with a thickness of 25 mm. The symmetrical design of the specimen provides symmetrical stress and strain distributions, and therefore the test can be performed under conventional uniaxial tensile or compressive loadings. The nominal gauge thickness is 2 mm but this value may be varied depending on the pressure angle defined as the angle between the centers of the two holes as shown in Figure 3.7. By varying the pressure angle, one can achieve the desired variation in the stress triaxiality state due to the specimen compliance to the lateral displacement. A change in the pressure angle changes the lateral displacement and therefore the induced lateral force and the gauge mean stress.

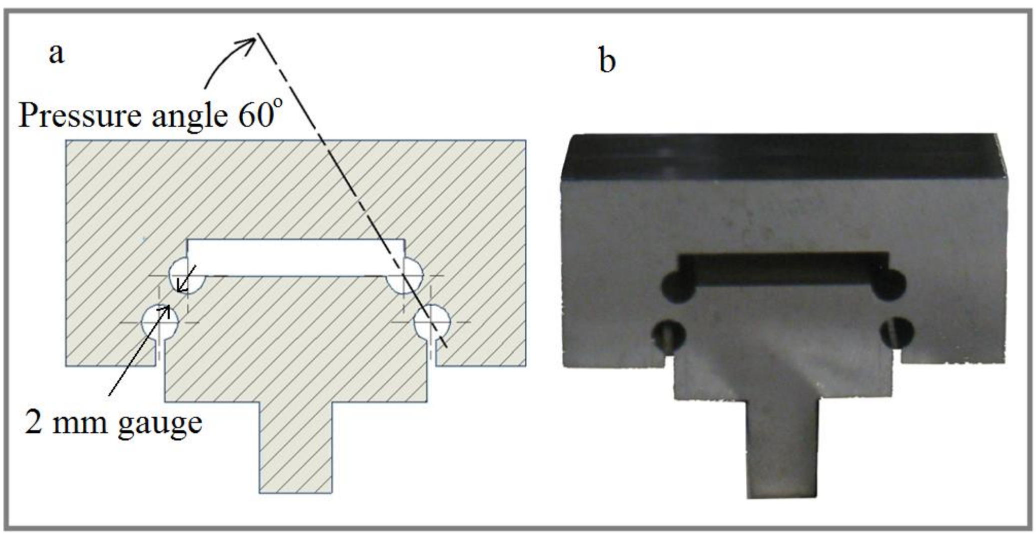

Figure 3.7: The double–notched specimen (a) design drawing and (b) prototype

When the pressure angle is at 90^{o}, the stress transmitted develops a stress state with nearly zero lateral stress. As a result, the stress triaxiality effect is minimized. Depending on the loading condition – compressive or tensile – the pressure angle will either rise or lower the local stress triaxiality. Figure 3.8 shows the stress triaxiality evolution obtained from a set of simulations using test specimens made of steel AISI 1045 with pressure angles ranging from 60º to 110º. Due to the symmetry, only a half section was discretized using the 2D plane strain elements. The simulation was conducted under conditions similar to the actual practical experiment, including the symmetric condition, the appropriate fixtures, and the upsetting speed of 0.1 mm/sec. The numerical analysis confirms the stress triaxiality sensitivity to the pressure plane angle and implies that the relationship between the pressure angle and the stress triaxiality state (η) is proportional. While in the specimens made with a pressure angle less than 90º lead to a positive stress triaxiality state (η), a negative η can be obtained from the specimens with pressure angles greater than 90º.

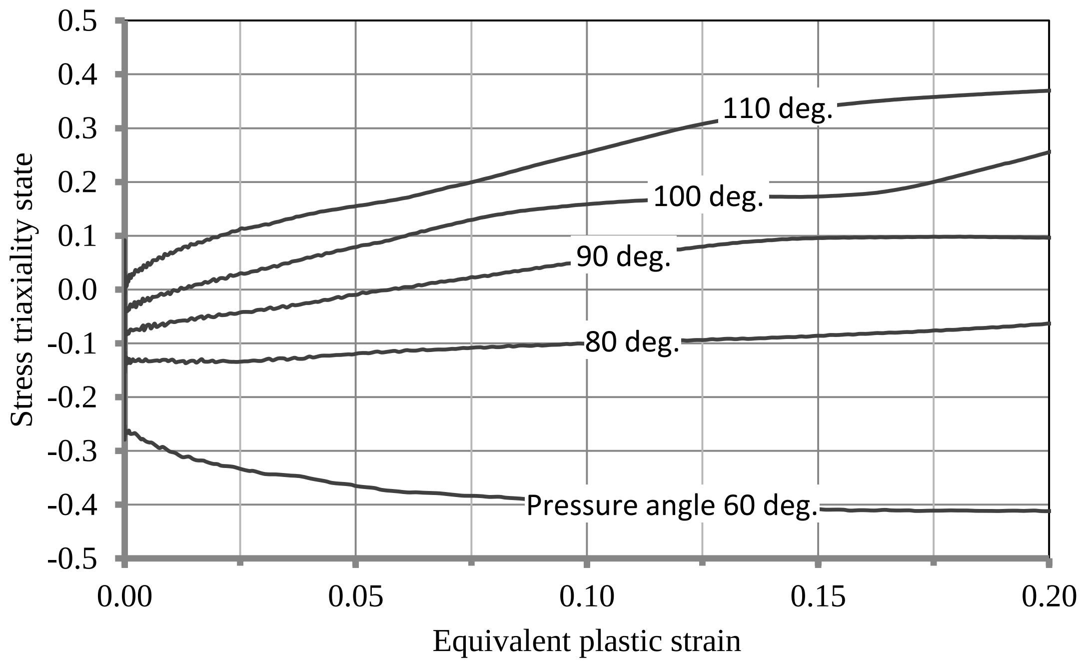

Figure 3.8: FEA stress triaxiality evolution for the developed specimen made of steel AISI 1045

The stress triaxiality state contours obtained by the FEA are shown in Figure 3.9 for a specific case where the pressure angle is 60º.

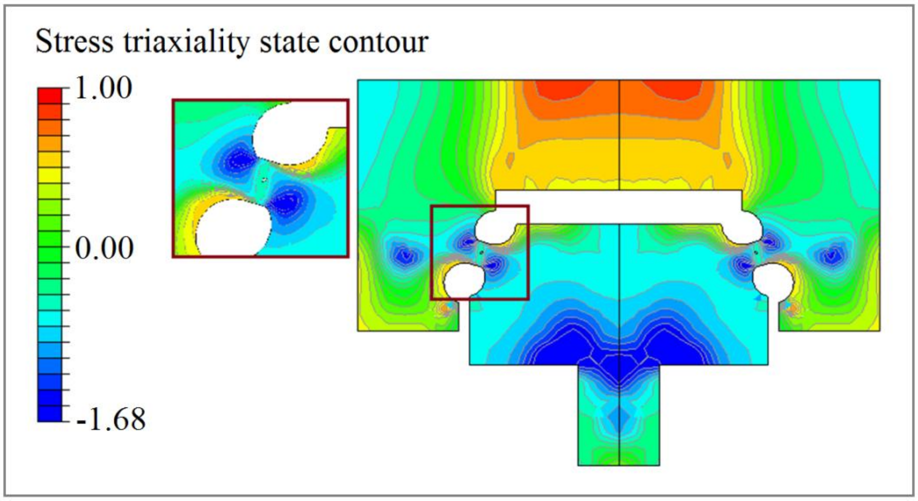

Figure 3.9: FEA stress triaxiality state contours of the proposed specimen made of steel AISI 1045 for pressure angle equal to 60º

It is important to locate the exact damage initiation site in order to estimate the corresponding strain and triaxiality fields. The analysis conducted for all five specimen configurations confirms the obvious site of the maximum equivalent stress/strain at the region of interest. An almost vertical fracture plane, even for specimens with a pressure angle different from 90º, was observed in numerical simulations as well as in the conducted experiments. On the other hand, the stress triaxiality state intensity angle, shown on Figure 3.9, tends to vary depending upon the pressure angle. Because the damage initiation changes according to the triaxiality state, the initiation site may vary. For example, in the upsetting test when the pressure angle is 60º, one may expect the crack to initiate at the center of the gauges (the middle distance between the each pair of holes) where the stress triaxiality state parameter along the shear plane is maximum, and to propagate toward the surface. However, this may not be true if the material sensitivity to stress triaxiality is high. Therefore, the actual crack propagation path obtained from experiment is important to locate the exact crack initiation site to be used for triaxiality state calculations.

3.1.3 Experimental Setup

The Digital Image Correlation (DIC) is an optical technique that effectively measures the displacement field by tracking the surface pattern evolution. The use of digital images as a strain measurement technique was first introduced by Peters et al. [103] and since then it has been widely used in experimental strain analysis [104]. DIC has been demonstrated great suitability in the material characterization studies.

The ability of DIC to measure the entire displacement field provides detailed information on the material flow and damage behavior. It is a valuable tool particularly in the analysis of material damage and crack propagation. Using this technique, an accurate description of the strain distribution in large and heterogeneous deformation can be revealed. For example, the formation and evolution of local shear bands, as well as their physical characteristics, can be attained. Furthermore, DIC measurement is not affected by necking phenomena, which often cause problems in finding the exact onset fracture strain.

Figure 3.10 shows the system setup used for material characterization experiment.

The major system components, equipment, and setup parameters are as follows:

Optical system components (DIC)

- ALLIED™ FireWire 1394b, ideal OEM camera, IEEE 1394b (800 Mb/s)
- Edmund™ Optics, In–Line Illumination Telecentric Lens (0.75X, 120 mm WD)
- Edmund™ Optics, Flexible Fiber Optic Light Guide
- Edmund™ Optics, Dolan–Jenner DC–950H DC–Regulated Fiber Optic Illuminators

- DANTEC DYNAMICS™ Calibration target (9x9 Glass, 5 mm)
- DANTEC DYNAMICS™ Istra4D software version 4.2.0

Optical system components (none DIC)

- Laser Extensometer – LE (Electronic Instrument Research, EIR, Irwin, PA)

INSTRON™ biaxial testing equipment

- Biaxial testing machine (load frame model 1321)
- 8800 Series system controller
- INSTRON™ Console V8.1 and Wavematrix V1.4 application software

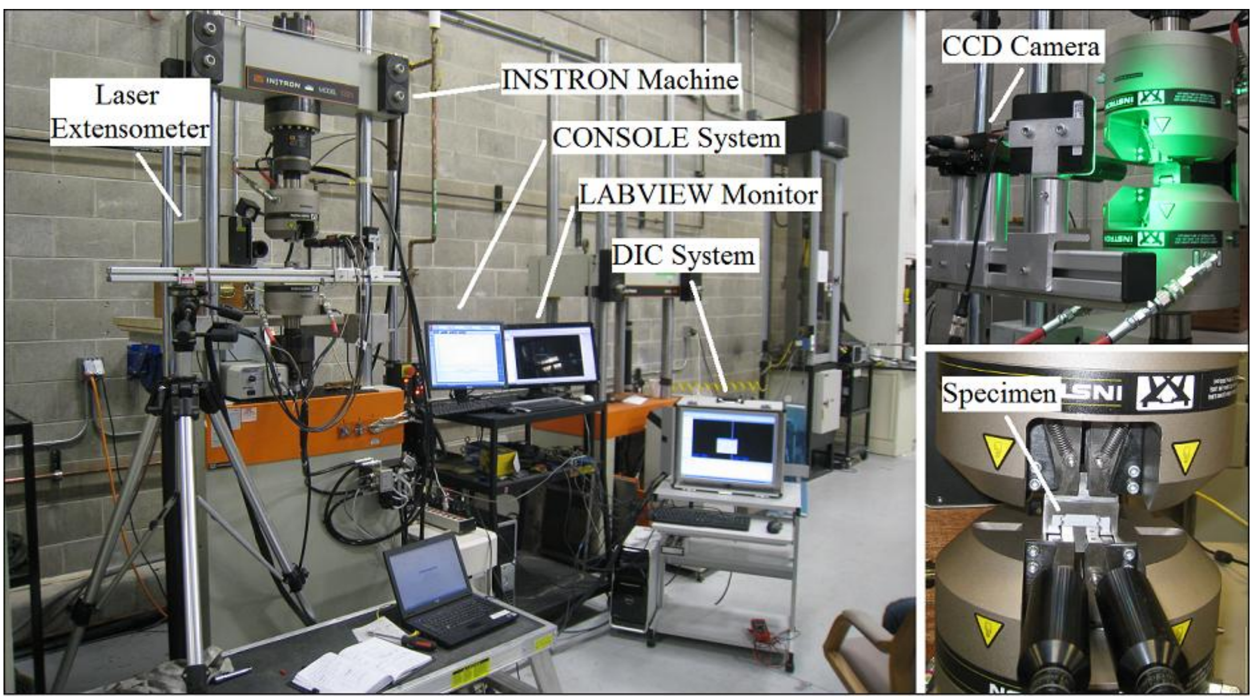

Figure 3.10: DIC and INSTRON testing equipment setup

Setup Parameters

- Deformation speed (1 mm/min)
- Sampling rate:

- Console (100 Hz)
- Istra4D (5 Hz)

- Total recording time (4 min)
- Total number of steps (1200 step)
- Field of view size:
  - (6x6 mm)
  - (600x600 pixels)
- Maximum load limit (70 kN compressive)

3.2 Model Calibration Approach

Figure 3.11 presents the flowchart for calibration using the developed specimens. The recorded loading history and the resultant displacement field measured using DIC in the time domain can be 'translated' into the corresponding equivalent strain and stress for all specimens. In particular, the test results of the specimen with a 90º pressure angle may be used to obtain the material elastic/plastic parameters, which provide all necessary material data for FEA simulations to compute deformations without fracture. The deformation only FE analysis, which does not include fracture, is capable of predicting the required stress triaxiality state parameter before and at damage initiation for all possible scenarios. On the other hand, the determination of the damage initiation site $(\bar{\varepsilon}_f)$ should be determined by recognizing the departure of the actual stress–strain curve from the obtained undamaged plasticity model. Furthermore, material fracture energy (G_f) can also be estimated for each case by numerical integration of the area below the stress–strain curve and beyond damage initiation.

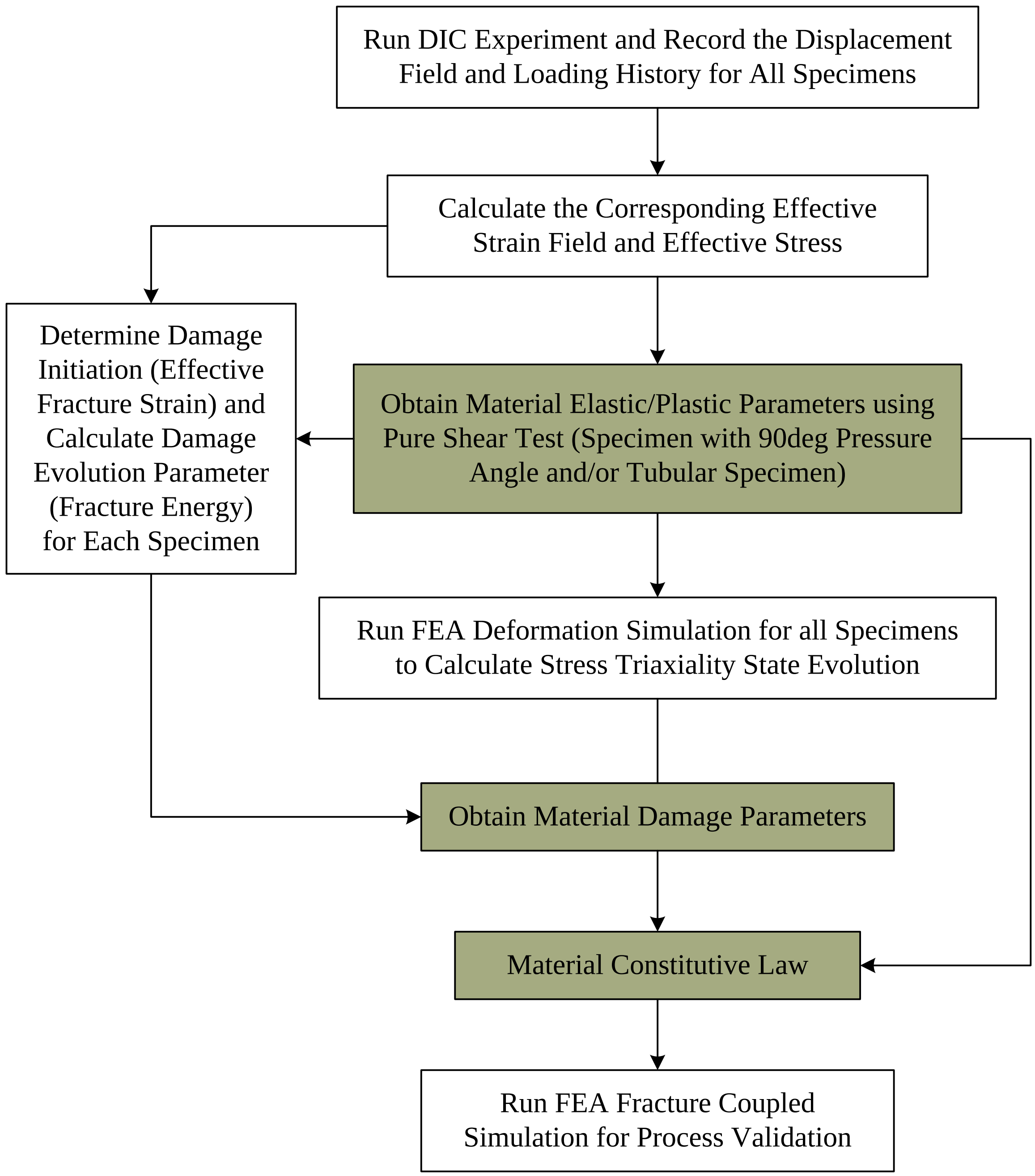

Figure 3.11: Flowchart for the material model calibration using the plane strain specimen and DIC/LE measurement

Upon calculating the three elements of the material damage model ($\bar{\varepsilon}_f$ η_f , and G_f), the complete assembly of the material constitutive law parameters can be obtained. As a verification step for the obtained material parameters, the obtained constitutive law may be used to perform, one more time, a complete version of the FEA, including fracture, and for comparison of the obtained results with the original displacement/loading experimental data. This step ensures the validity of the approach and the experimental procedure used. It also allows one to assess the uncertainty in locating the damage initiation site.

3.3 Results and Discussions

A total of five specimens (Table 3.2) were tested under similar loading conditions using the above described experimental setup and methodology. Figure 3.12 shows the load vs. displacement curves. The load axis represents the upsetting force recorded using the INSTRON load cell, while the displacement was measured by INSTRON transducer measurements. The displacement was also measured using the laser extensometer, which was used in the calibration procedure.

Table 3.2: Specimen geometrical configurations used in the experiment

Exp. #	*Pressure angle*	*Gauge (mm)*
C60	60º	2.00
C80	80º	2.09
C90	90º	2.03
C100	100º	2.40
C110	110º	2.27

As discussed above, the developed plane strain specimen can be used to find the material flow parameters. In theory, any of the above–tested specimen configurations can be used to find the material elastic–plastic parameters. However, for simplicity it may be a natural choice to use the 90º configuration, which is expected to provide vertical shear bands with minimal stress triaxiality effects. Because of the geometrical complexity of the double-notched specimen, a direct identification of the material parameters may result in unreliable conclusions. Particularly, when a large heterogeneous deformation pattern is present, the stress–strain formulation, based on the pure shear component and the initial gauge thickness, becomes oversimplified. Alternatively, the combined reverse numerical–experimental approach is used to identify the optimum material's elastic, plastic and damage parameters.

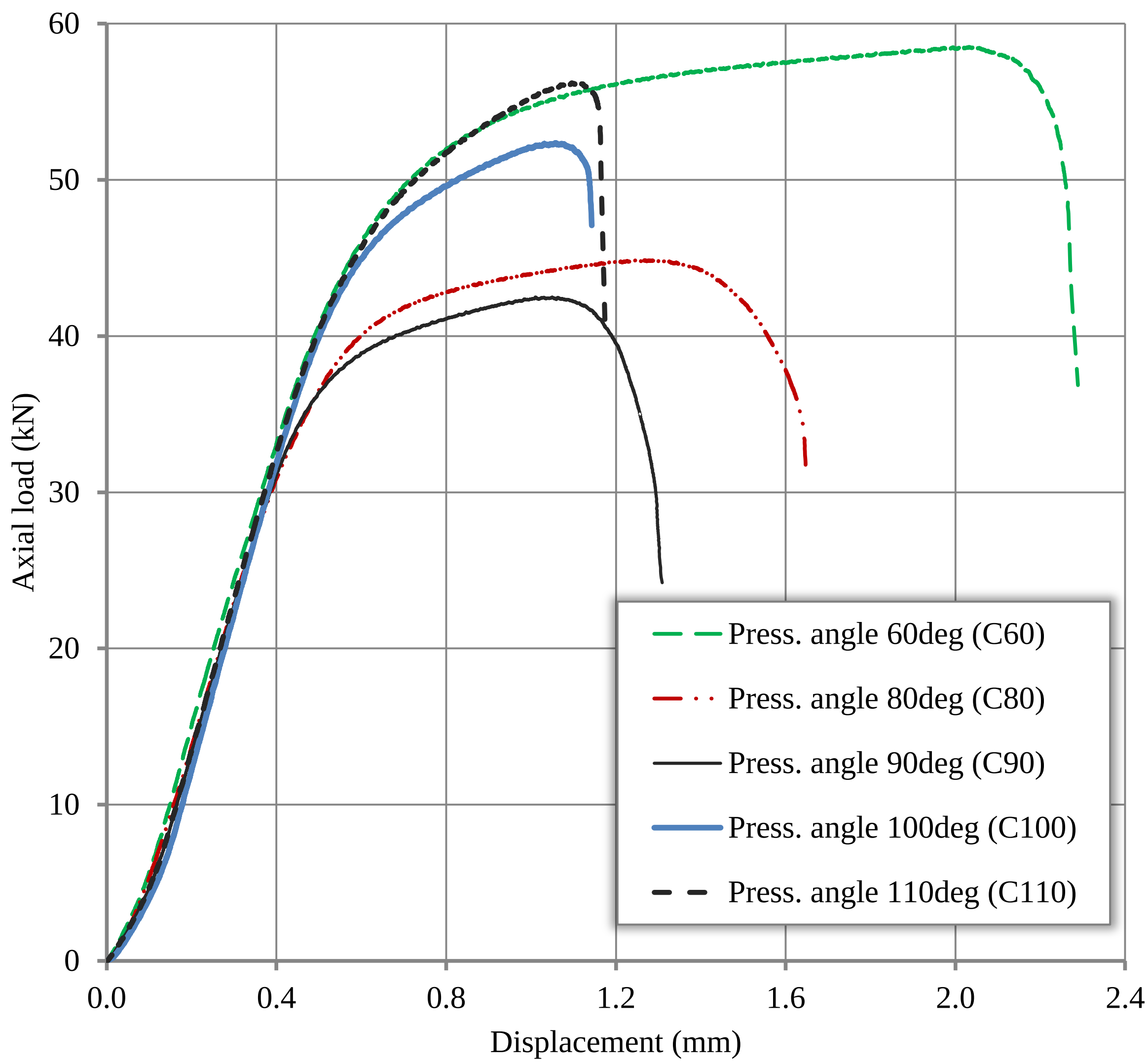

Figure 3.12: Load–displacement material response for steel AISI 1045 obtained using the developed specimens.

3.3.1 Material Young's Modulus Parameter Identification

To determine the material Young's modulus (E) using the proposed specimen, two approaches can be used; (1) the direct approach, (2) the indirect (reverse) numerical optimization approach.

The maximum representative shear strains (γ) at the gauge can be obtained directly from the DIC measurement. In addition, the corresponding maximum shear stress (τ) can also be calculated within acceptable tolerance in the small deformation range of the elastic limit. This is calculated based on the axial reaction force (F) and the gauge section dimensions as

$$\tau = \frac{F}{2 \cdot t \cdot d} \tag{3.5}$$

where t is the specimen gauge thickness and d is the specimen thickness (see Figure 3.13).

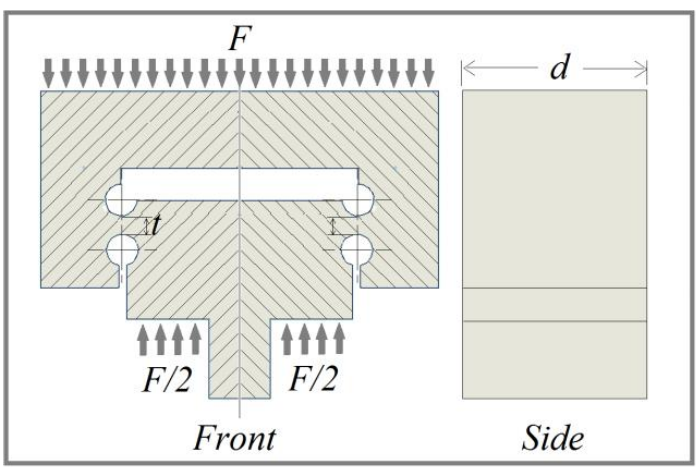

Figure 3.13: C90 double–notched specimen drawing shows the parameters for Equation (3.5).

Applying Equation (3.5) for the loading history of the C90 specimen along with the use of the DIC strain measurements, one can obtain the shear stress vs. strain curve as shown in Figure 3.14. In order to best represent the elastic–plastic transition, the modulus of elasticity is calculated at various strains to include some non–linearity effects. The slope of the line connecting an arbitrary point on the shear stress–strain curve to the origin in the elastic range is the estimated material's secant shear modulus (G_S). Figure 3.14 shows the curves of the secant shear modulus (G_S) and the secant modulus of elasticity $(E_S = 2G_S(1+\upsilon))$, where υ is the Poisson's ratio $(\upsilon = 0.3)$.

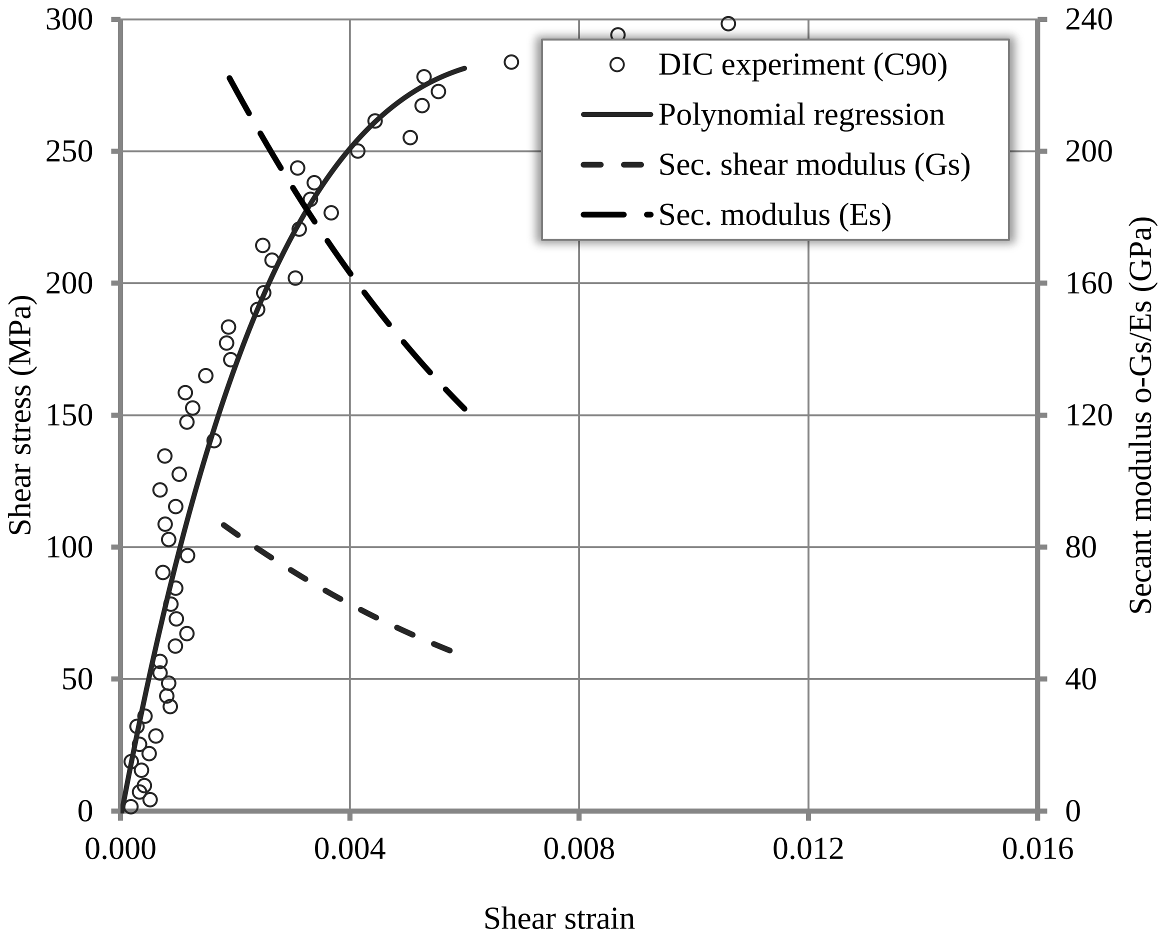

Figure 3.14: Modulus of elasticity of steel AISI 1045 calculated from DIC measurements.

The typical Young's modulus (E) value for steels is 200 GPa. This value is determined from the initial slop of the stress–strain curve. On the other hand, the yield strength is often determined at a small offset plastic strain such as 0.2%. The stress–strain curve constructed using the Young's modulus and the obtained yield strength does not represent the non–linear stress–strain behavior in a small strain region. Furthermore, the use of the Young's modulus estimated by the offset methodology causes discontinuity in computation. To avoid this problem, a linear elasticity FE model was prepared to simulate the C90 specimen under similar experimental boundary and loading conditions to be used to find E_S in a reverse manner. LS–Opt ™ is then used to find the optimized value of E_S with a predefined Poisson's ratio $(\upsilon = 0.3)$. The secant modulus of elasticity $\left(E_S\right)$ was defined as the design variable to minimize the residual reaction forces by the means of mean square error (MSE). The history force–displacement curves obtained from linear elastic simulations of the C90 experiment at a number of sampling points are to be correlated with the experiments. A laser extensometer was used to measure the global displacement of the specimen. The displacements of the corresponding FE nodes located at the laser targeted points on the specimen are compared with the experimental data.

The optimization analysis was carried out using the sequential response surface method (SRSM), which ensured the convergence of the solution to a prescribed tolerance of either the MSE objective and/or design variables. The SRSM uses the domain reduction strategy by adaptively moving and reducing the predefined region of interest [105]. The final calculated force–displacement curve was matched with the experiment as the target curve within the elastic range as shown in Figure 3.15.

The elasticity model limit was estimated using the obtained elastic parameters to ensure a smooth elastic–plastic phase transition. The value of the equivalent stress proportionality limit is found to be about 333 MPa.

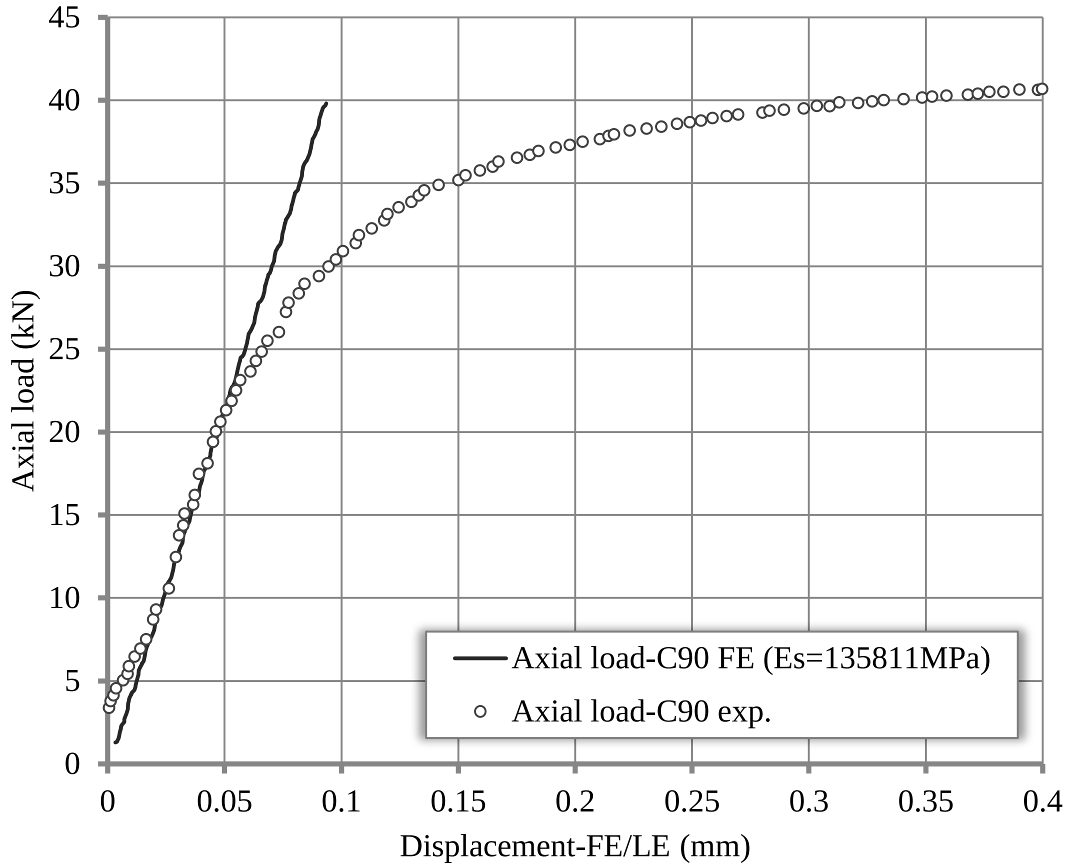

Figure 3.15: Secant modulus of elasticity of steel AISI 1045 optimized based on LE measurements using LS–Opt™

3.3.2 Plasticity Parameters Identification

Figure 3.16 presents a flowchart for the system identification algorithm used for the determination of material plasticity parameters. The proposed procedure was developed to accommodate the complexity of the developed specimen and the difficulties of estimating the equivalent stresses in such large heterogeneous deformations. The algorithm script is written in Python™ language and integrated with Abaqus™. The proposed methodology assumes no pre–defined constitutive equation; instead, the optimized piecewise yield surface is to be generated in a sequential manner.

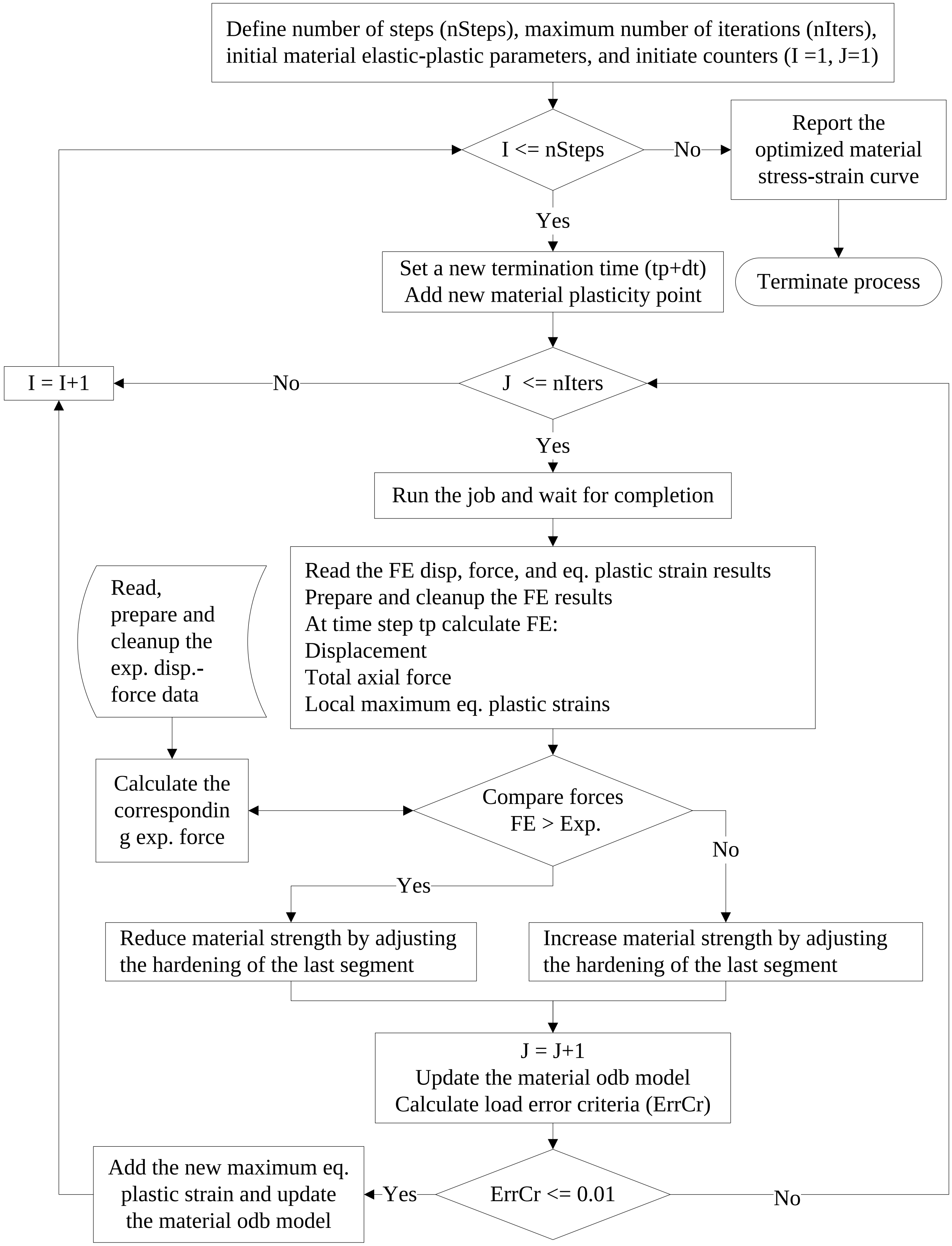

Figure 3.16: Material plasticity identification program flowchart

The use of the proposed strategy minimizes the uncertainty by focusing only on the last segment that causes the load change rather than including a complete target curve. For example, if the analysis underestimated the material strength at a particular time step “termination time increment” which did not happen in the previous step, then only the part of the stress–strain curve that causes it becomes the most recent segment. The focus, therefore, is on adjusting the hardening parameter of the last segment – in this case, increasing the hardening value by a suitable amount to minimize the difference.

As an example, C90 specimen is considered. The FE model for the C90 experiment is evaluated in multiple steps and at each step the analysis termination time is slightly increased. The maximum axial force is compared with the corresponding axial force obtained from the experiment at specific LE displacement to match the analysis. Depending on the results of this comparison, the material strength is then adjusted proportionally, either being increased or decreased. This adjustment is to be made only to the most recent created segment. Iteratively, a new FE analysis is then resubmitted using the updated material state curve. The procedure continues until the predefined loading tolerance (chosen to be *0.02 kN*) is satisfied for each step. Once the solution is converged, a new termination time is set for the next step to determine the material state at the new point. At each step, a new maximum equivalent stress is calculated and assigned to the global maximum equivalent plastic strain which always occurs at the specimen gauge.

Initially, all yield sampling points are extrapolated based on the previous estimations of the material hardening segment except for the first increment where the extrapolation was calculated using the Young’s modulus. Eventually, the procedure produced a total number of material state points equal to the selected number of steps. Figure 3.17 shows the piecewise material plasticity obtained using the described approach.

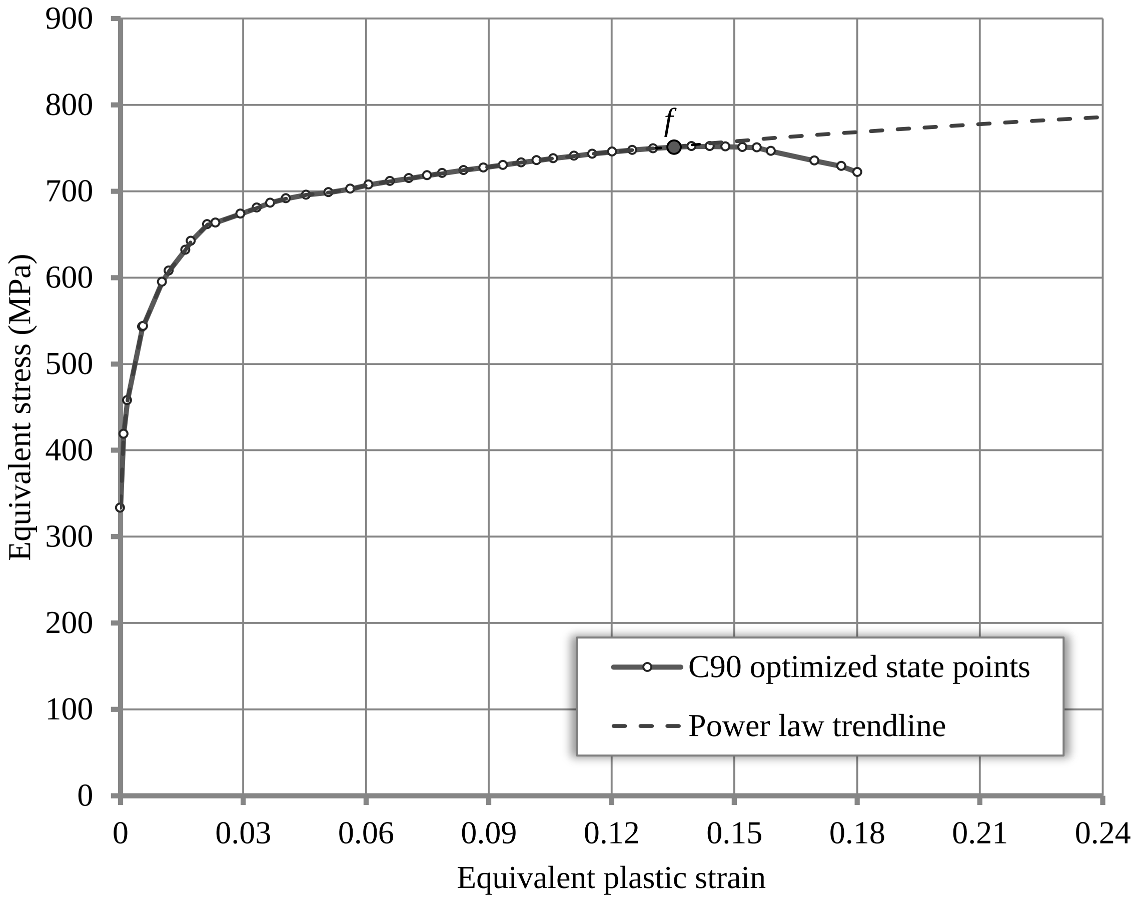

Figure 3.17: Piecewise plasticity results for steel AISI 1045 using the proposed optimization reverse strategy

As mentioned above, the material flow surface obtained using this approach does not require a pre–defined plasticity law, instead it creates the surface through a series of discreet points based on the load response. In addition to the applicability of such approach to a non–traditional testpiece such as that used in the tests, the approach provides an opportunity to choose the form of the material flow law independently based on the obtained results. In order to obtain a mathematical description of the stress–strain curve shown in Figure 3.17, the JC plasticity model parameters (Equation (2.8)) were optimized using least square regression analysis. In addition, these parameters were compared with a number of references and shown in Table 3.3.

Table 3.3: JC material model parameters for steel AISI 1045 obtained from the double–notched testpiece and compared with other references

Author/experiment	*Initial yield A (Mpa)*	*Hardening modulus B (Mpa)*	*Strain hardening n*	*Strain rate sensitivity C*	*Thermal softening m*
Borkovec	375.0	552.0	0.4570	0.020	1.400
Forejt	375.0	580.0	0.5000	0.020	1.040
Jaspers	553.1	600.8	0.2340	0.0134	1.000
Ozel	451.6	819.5	0.1730	9.00E-07	1.095
Based on Bai's exp.	553.1	309.9	0.1952	0.0134[a]	1.000 [a]
Double–notched testpiece	333.0	538.9	0.1299	0.0134 [a]	1.000 [a]

[a] Based on Jaspers's results [91]

Although Table 3.3 shows the JC parameters from different sources, they all represent the material flow properties for steel AISI 1045. However, it's clear that these parameters do not represent the same metallurgical state of this steel. The results found in the literature indicate different material initial yield, strength, and strain hardening due to a number of possible reasons. Such variation could be the result of the different material treatment, manufacturing process, pre–existing residual stresses, material calibration methodology, etc. Figure 3.18 shows a comparison of the JC models from all different sources including the optimized JC model obtained from the current experiment. In addition, Figure 3.19 shows a comparison of the current experiment outcomes with Bai's raw data. The most noticeable difference is in the prediction of the initial yield and the elastic–plastic transition zone. Even though the overall material flows are similar in the two experiments, the transition zone is critically important in many applications spatially in metal cutting modeling. Therefore special attention was paid to this zone which led to the above elasticity modeling approach.

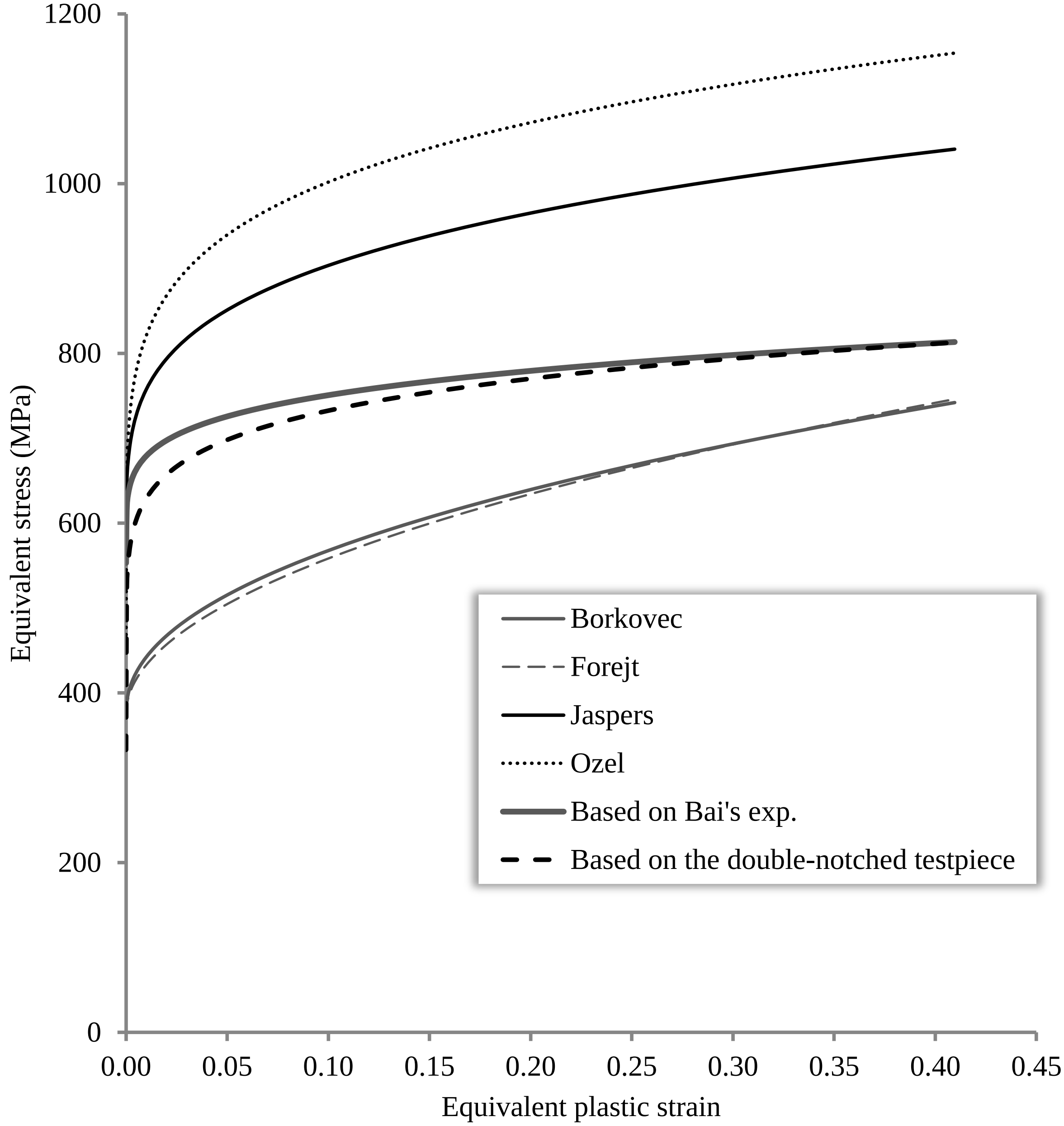

Figure 3.18: Steel AISI 1045 material plasticity modeled using JC law and obtained by a number of researchers

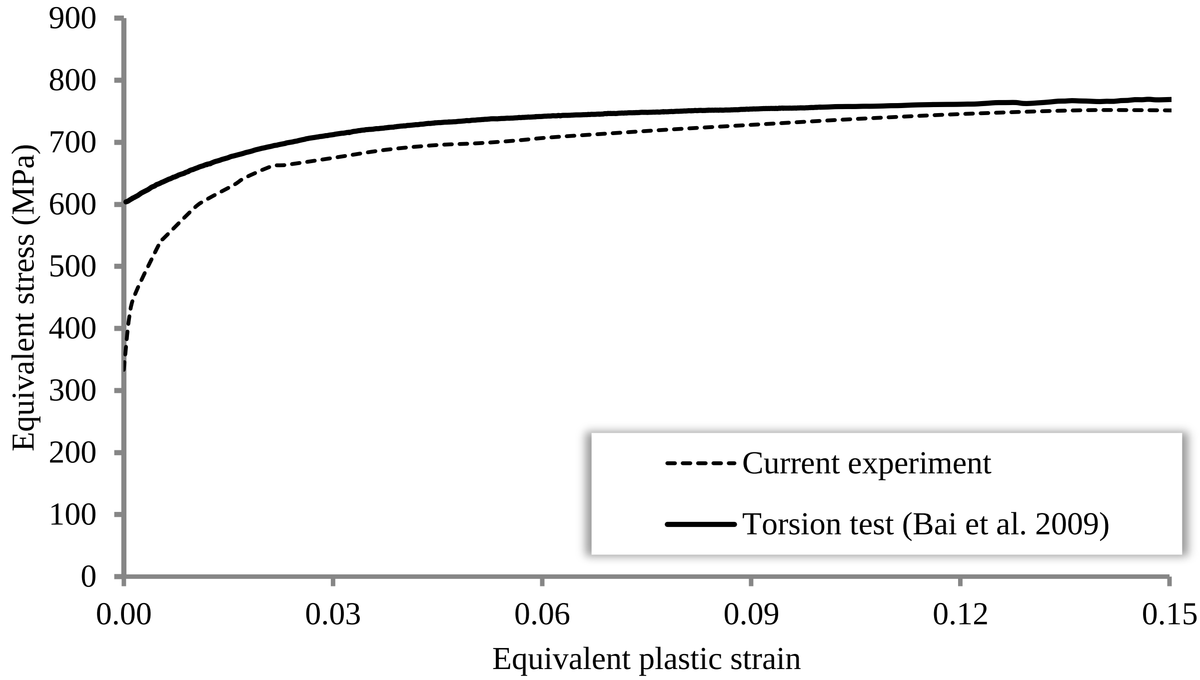

Figure 3.19: Piecewise material plasticity flow for steel AISI 1045 obtained by the double–notched testpiece and compared with the results from Bai et al. [87] using standard torsional testpiece

3.3.3 Material Damage Initiation

3.3.3.1 Fracture Locus

The DIC measurement is used to determine the equivalent plastic strain at damage initiation $\bar{\varepsilon}_f$. The $\bar{\varepsilon}_f$ was calculated from the DIC results along the centerline (AB) of the specimen gauge (Figure 3.20) where strains are maximum. The amplitude of the shear strain along the line AB (Figure 3.21) is progressively increasing during the loading. Ultimately the material reaches its maximum strain limit causing fracture. The step/frame at which the material strength starts to degrade due to damage initiation is used to calculate the equivalent plastic strain $\bar{\varepsilon}_f$.

Referring to Figure 3.17 which shows a hypothetic undamaged stress–strain curve along with the stress–strain curve obtained from the C90 experiment, one can see that the elastic–plastic undamaged path is followed by the departure of the experimental yield surface from the virtual undamaged yield surface at point ***f***. Point ***f*** can be considered as the hypothetic damage initiation site where the material elastic and hardening modulus becomes progressively sensitive to the amount of damage leading to declination of the material loading capacity.

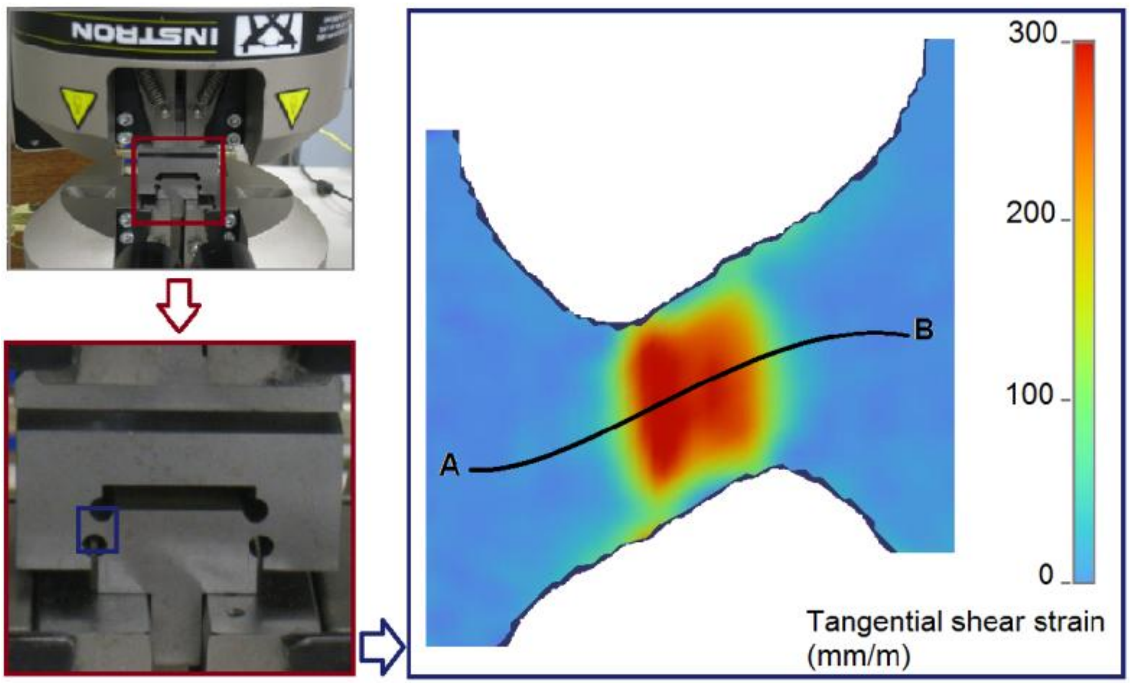

Figure 3.20: Typical contour of the shear strain field of C90 DIC experiment

The fracture strain $\bar{\varepsilon}_f$ scalar values calculated from the DIC measurements for all specimens with the pressure angle ranging from 60º to 110º are given in Table 3.4. As expected, the overall trend is observed, i.e. the amount of the material plasticity is proportional to the pressure angle. In order to represent the material fracture locus in the strain–triaxiality space, a FEA with no fracture was carried out for all the specimens using the elastic–plastic constitutive parameters obtained above. Despite the fact that the stress triaxiality state parameter changes during the loading course, this parameter is numerically evaluated for each case at the corresponding value of $\bar{\varepsilon}_f$.

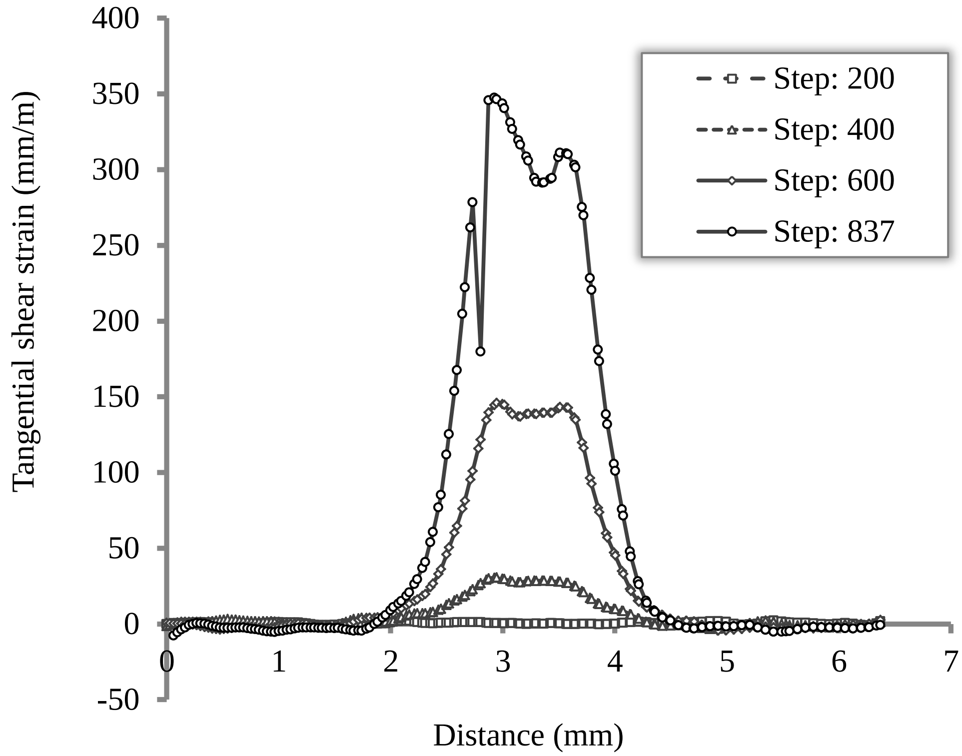

Figure 3.21: Shear strain progression along the spacemen gauge line AB (Figure 3.20) using DIC

Table 3.4: Experimental equivalent plastic strains matched with the numerical stress triaxiality state at damage initiation for steel AISI 1045

Exp. #	*LE Disp.(mm)*	*Force (kN)*	$\bar{\varepsilon}_f$ *(DIC)*	η_f *(FE)*
C60	1.1151	57.638	0.8295	-0.2418
C80	0.7495	44.631	0.3019	0.0614
C90	0.5853	41.980	0.2128	0.3345
C100	0.5920	52.148	0.1730	0.4614
C110	0.5859	55.486	0.1548	0.6041

Figure 3.22 presents the material fracture locus obtained from the double–notched specimen experiment and the fitted curves using the Rice (Equation (2.10)) and the reduced JC damage models (Equation (2.11)). The Rice the material fracture constants C_1 and C_2, and the JC material damage constants D_1, D_2 and D_3 are being found to be

$$\bar{\varepsilon}_f = 0.446\mathrm{e}^{-2.455\eta} \quad (3.6)$$

$$\bar{\varepsilon}_f = 0.154 + D_2\mathrm{e}^{-4.862\eta} \quad (3.7)$$

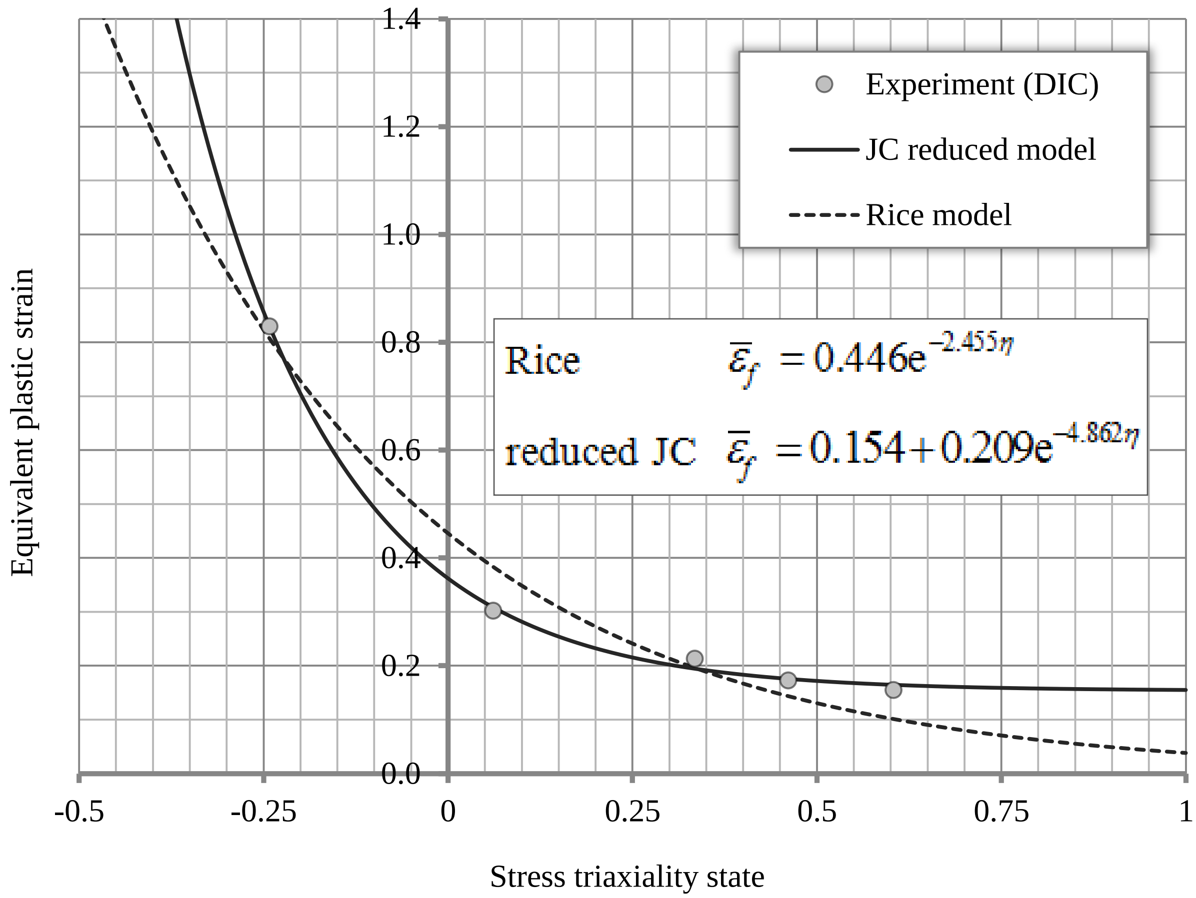

Figure 3.22: Fracture locus obtained from DIC experiment in plane strain condition for steel AISI 1045

Although the Rice model is often preferred by many researchers to represent the material fracture locus [87, 85] (perhaps because of its adequate fracture mechanics fundamental rationale), the reduced JC damage model is found to be a better fit in the plane strain condition investigated in the current work. Figure 3.22 shows that under the considered plains strain conditions, the Rice model tends to underestimate the ductility of the material at high/low pressure regions. The plasticity sensitivity to pressure in ductile metals becomes less significant at low pressure state. This phenomenon is naturally recovered by the reduced JC damage model with the three damage parameters being free for calibration. The JC additional parameter D_1 can be recognized as the initial/minimum equivalent plastic strain of a material under plane strain condition.

3.3.3.2 Crack Propagation

The state of stress "triaxiality" changes from high pressure (60º) to low pressure (110º) (as shown in Figure 3.8) when the pressure angle is varied in the specimen. In doing so, the crack mode would change accordingly but never become a pure tensile or pure shear one. The fracture in the 90º case is mostly due to shear while the 110º case will introduce the tensile cracking mode. Crack mode could be a reason behind a change in the direction of the crack propagation path. However this may not be easy to confirm because of the strain variation (see Figure 3.20) and the difficulties in quantifying the crack mode state. Furthermore, from the stress state stand point, the crack path direction strongly depends on the strain field and material sensitivity to the triaxiality state. The crack may start where the combination of the strain/triaxiality reaches its limit according to Figure 3.22.

The results of FE simulations shown in Figure 3.23 demonstrate two different crack propagation modes. When the pressure angle is small (law triaxiality or compressive), the crack propagates from the center of the specimen gauge toward the surface. In contrast, when the pressure angle is high (high triaxiality or tensile), the crack propagation shows surface to center path.

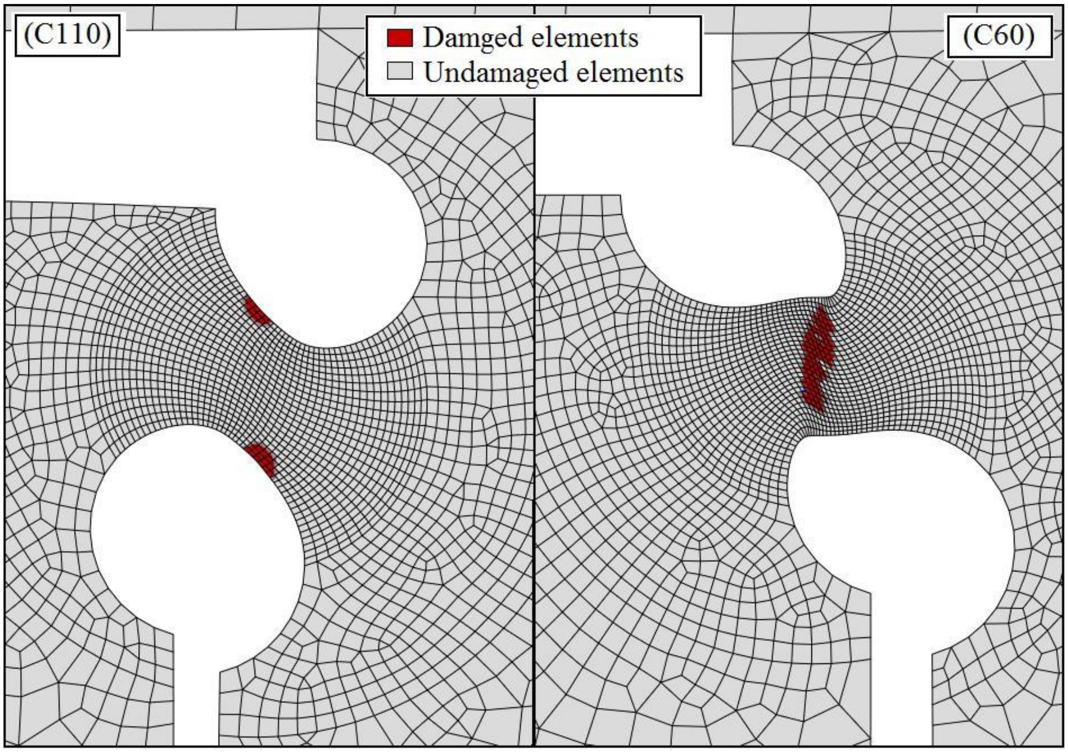

Figure 3.23: FE simulations of the damage initiation site and crack propagation in the double–notched specimen. High triaxiality or tensile (C110). Law triaxiality or compressive (C60)

3.3.4 Material Model Validation

3.3.4.1 Material Flow and Damage Initiation

To investigate the validity of the material model presented in Chapter 2, the proposed experimental approach and its capability of reproducing experimental load/displacement responses, simulations of the plane strain double–notched specimen were conducted. Figure 3.24 shows the FE simulation results for the double–notched 90^{o} pressure angle specimen (C90) made of steel AISI 1045 in comparison with DIC measurement. Figure 3.24 (b) and (c) show the shear strain contours obtained by FE and DIC, respectively. Both were taken at the same point of time just before fracture.

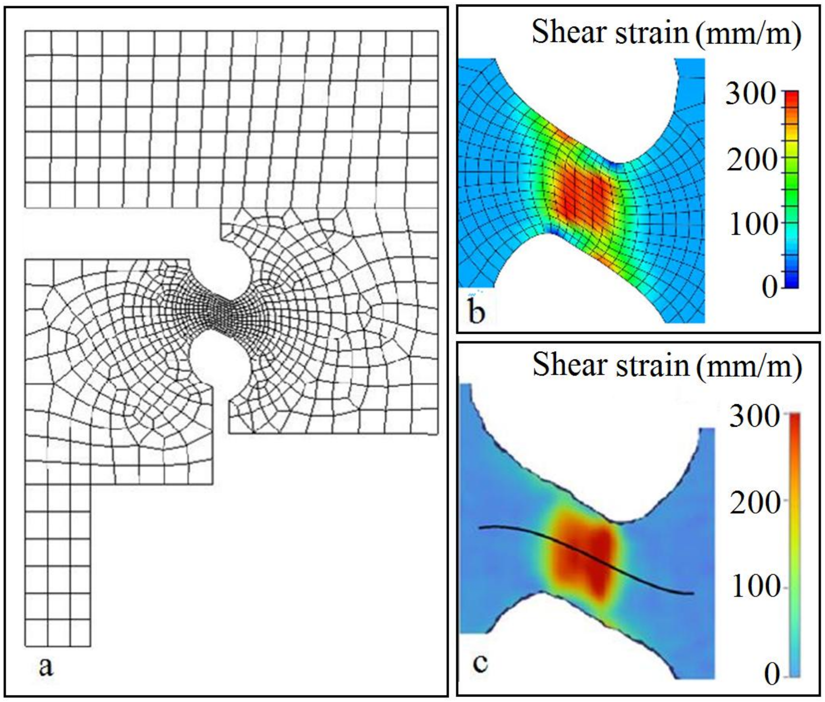

Figure 3.24: FE simulation of the double notched specimen made of steel AISI 1045 compared with the DIC experiments. (a) Plane–symmetry plane strain FE mesh. (b) FE shear strain contours. (c) DIC shear strain contours

The strain fringes obtained using FEA shows a similar pattern as those in the DIC measurements. A close inspection of the strain field reveals that the generations of the shear bands in the experiment were actually reproduced successfully by FEA. This is critically important in OMC because shear bands create the chip connectors during chip formation. In addition, to reproduce the correct chip morphology, in OMC in particular and machining in general, the model must be capable of reproducing the shear bands with the right intensity and frequency.

The experimental displacement–loading curves were compared with corresponding data obtained by FEA for all load cases. As the first step, only the material elastic–plastic and damage initiation models are included in the analysis. Material damage evolution will be added in the final model.

The load–displacement curves shown in Figure 3.25 through Figure 3.29 demonstrate the results of the developed material model for steel AISI 1045 in comparison with the experimental data for each specimen. With all the significant variation in load levels, the predicted axial reaction forces are reasonably in good agreement with the experimental results. The elastic response and the plastic flow and hardening were captured by FE analysis. Particularly, the obtained material yield surface was found to be able to trace all the variations of the axial reaction forces caused by the unique loading conditions of each case.

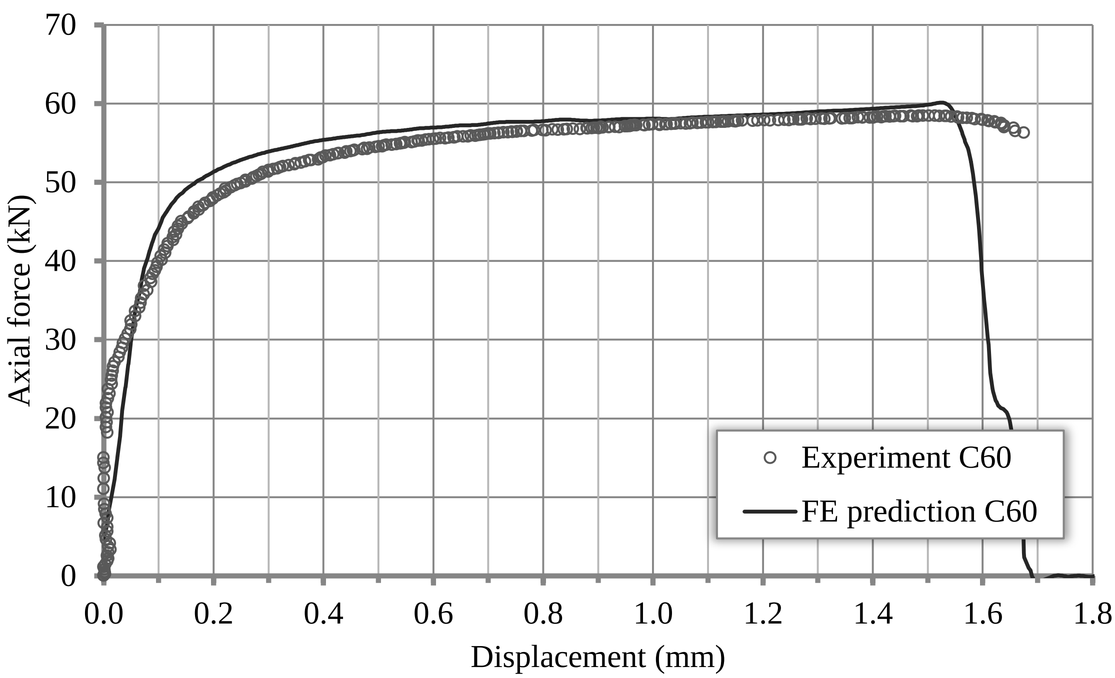

Figure 3.25: FE load–displacement response compared with the experiments of C60 specimen

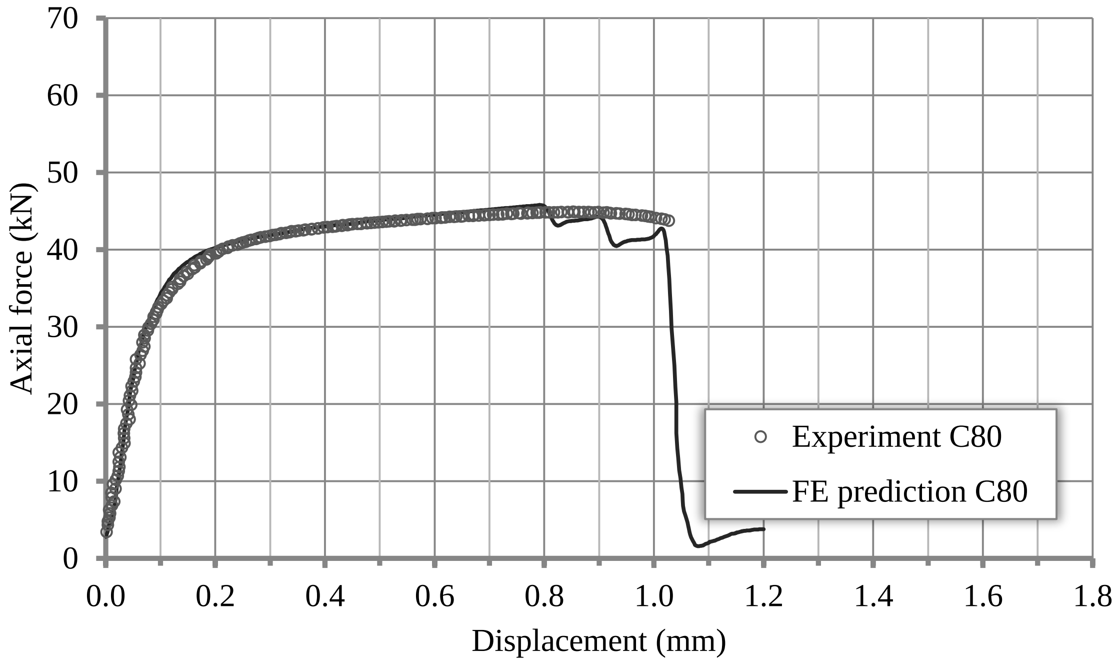

Figure 3.26: FE load–displacement response compared with the experiments of C80 specimen

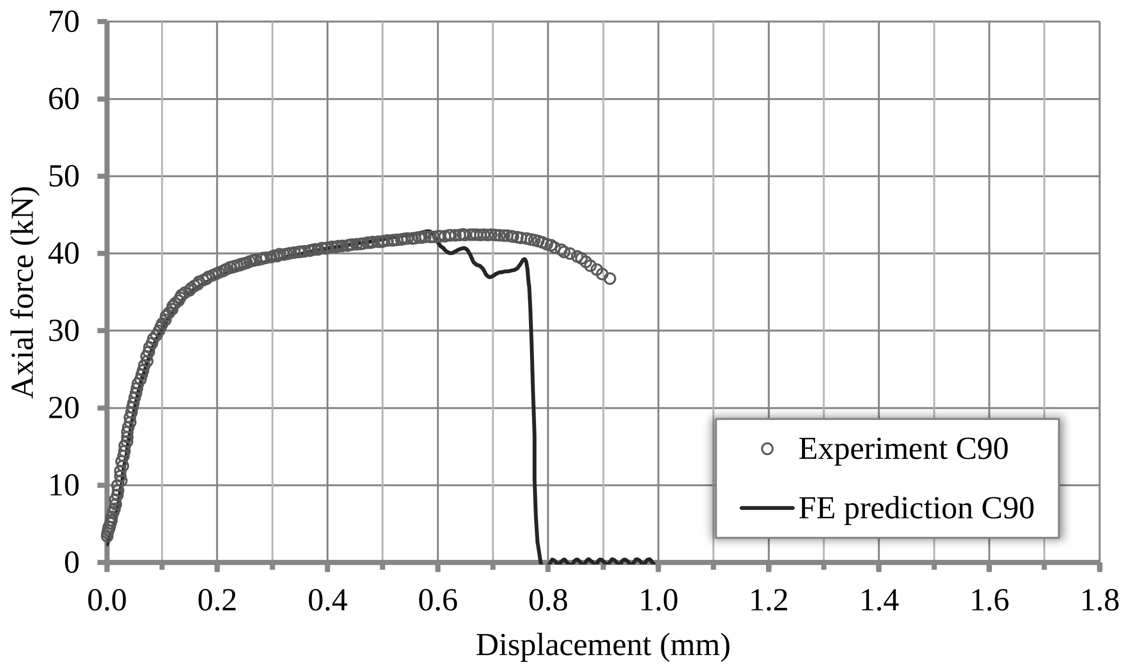

Figure 3.27: FE load–displacement response compared with the experiments of C90 specimen

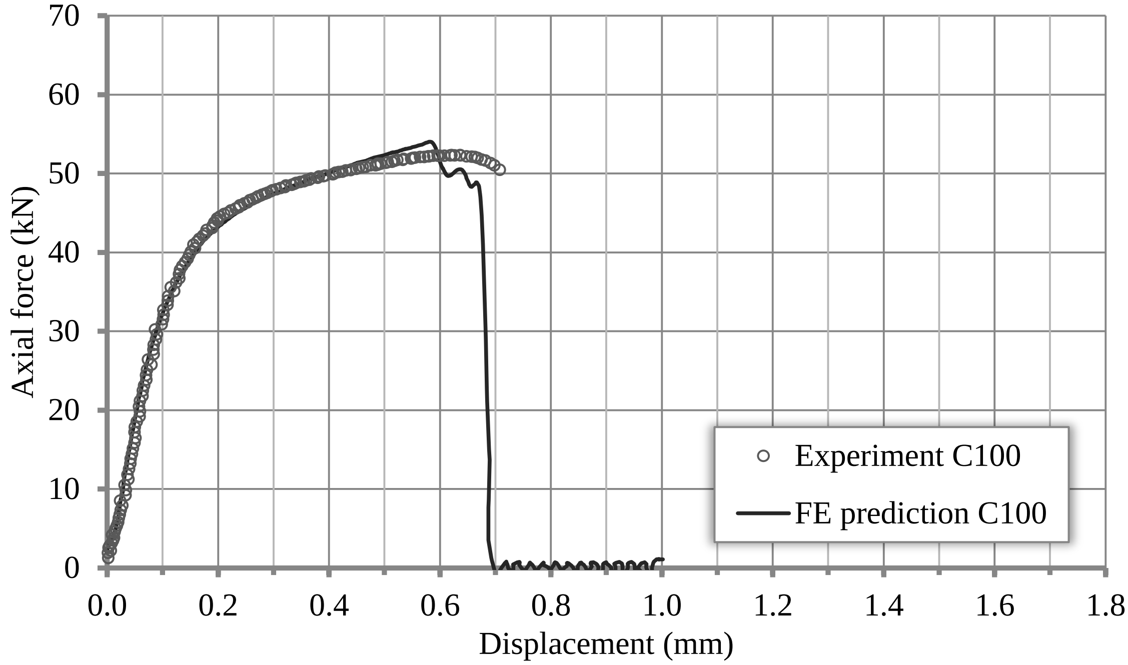

Figure 3.28: FE load–displacement response compared with the experiments of C100 specimen

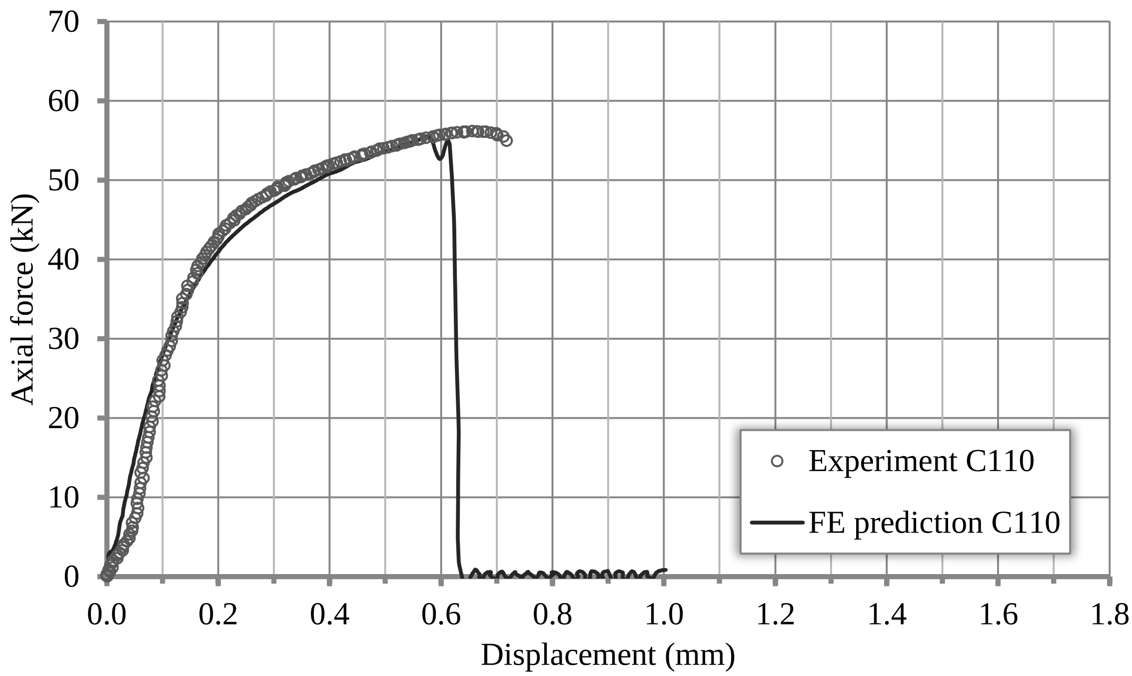

Figure 3.29: FE load–displacement response compared with the experiments of C110 specimen

Because the material post damage degradation phase was not included in this analysis, the point of the damage initiation can be easily distinguished. As observed from the experiments, the declination of the load curve indicates that some of the material in the gauge zone has already exceeded the material strain limit and entered the damage evolution phase; the FE model consistently predicted these experimental observations. The above load curves show that the onset of the material strength degradation occurred at different displacement/strain levels depending on the load case. The results demonstrate the applicability of the reduced JC damage model and the effectiveness of the model parameter calibration approach. The final damage and fracture model including post damage evolution will be addressed in the next section. Figure 3.30 shows the specimens used in this experiment after fracture. The fracture occurs in both sides of the specimen gauges simultaneously because of the gripping mechanism of the bottom side was designed to insure stability while the top flat upsetting surface being loaded.

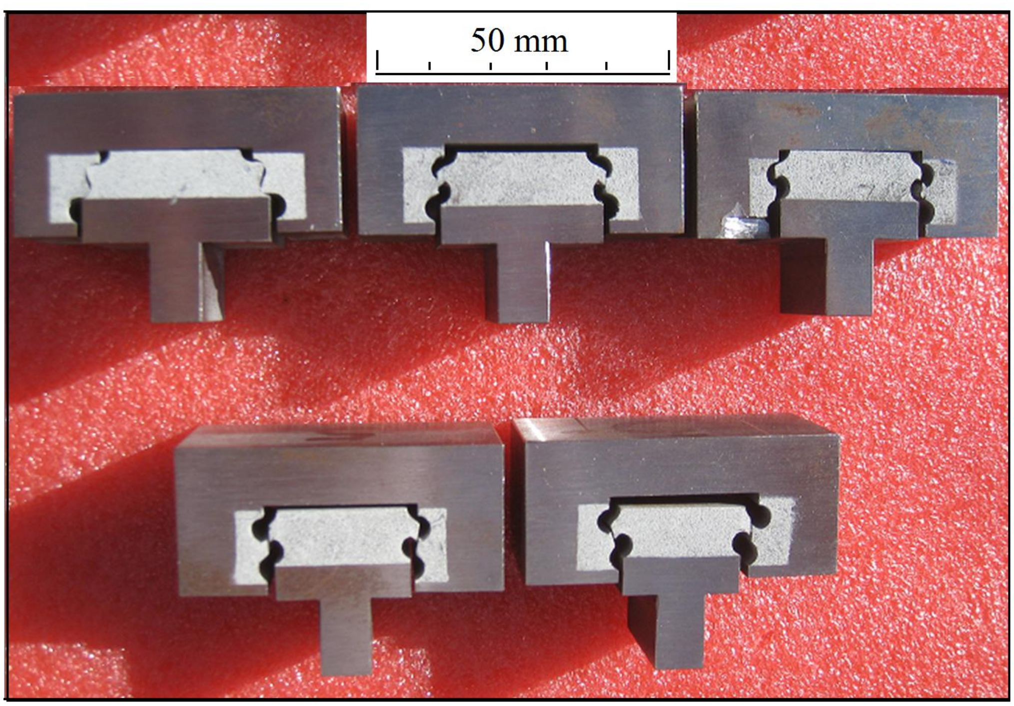

Figure 3.30: Double–notched specimens after fracture experiment

3.3.4.2 Material Damage Evolution

FE analysis at first was performed for the deformation and fracture without damage evolution coupling. This step is necessary to ensure the validity and predictability of the damage initiation site. The second step is to include the material degradation and material fracture energy dissipation in the analysis. Figure 3.31 and Figure 3.32 show the load–displacement response of the 90º pressure angle specimen (C90) for the two analyses respectively and compared with the experiments. The FEA and experimental load comparisons indicate three key points (1) The load–displacement response of the experiment was well predicted throughout the course of loading up to the damage initiation site (Figure 3.31), (2) The onset of the material damage and degradation process was consistent with the proposed fracture locus for the stress state condition of C90 experiment. This implies that the site of the maximum stress triaxiality state η and effective strain $\bar{\varepsilon}$ combination, weighted whichever more sensitive, are the natural outcome of the analysis when the material stress state sensitivity is considered. Therefore not only the state dependent damage initiation site can be estimated, but also the crack propagation path may become an additional outcome. (3) The material strength degradation shown in Figure 3.32 complies with the exponential damage evolution Equation (2.12). The degradation behavior is controlled by the amount of the material fracture energy density G_f and the exponent parameter α. G_f and α were numerically optimized and found $G_f = 320\ \mathrm{MJ/m^3}$ and $\alpha = 0.6$ for steel AISI 1045. This optimization was conducted to insure the best match of the numerical load degradation to the experiments in all specimens.

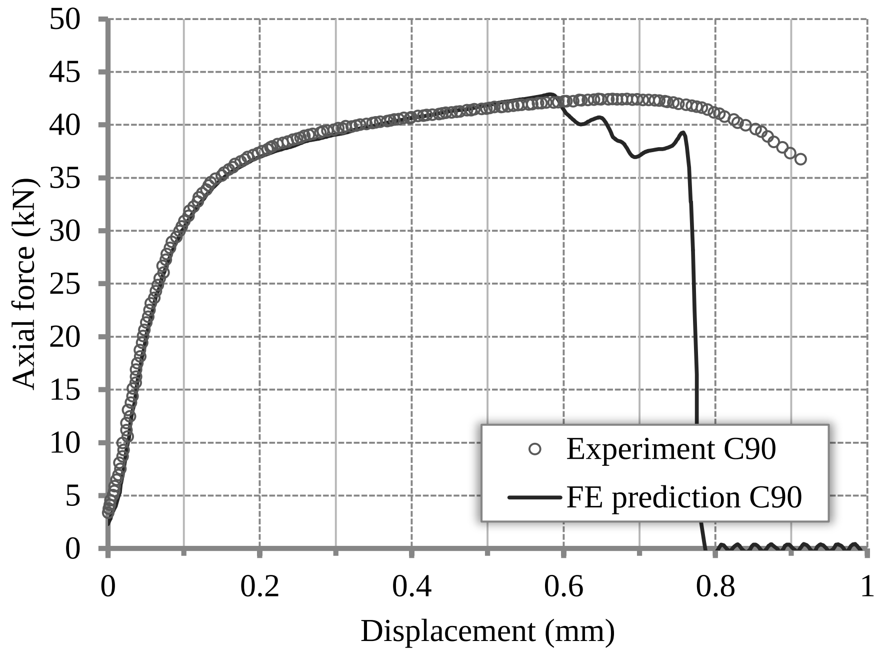

Figure 3.31: FE load–displacement response for steel AISI 1045 compared with the experiments – without damage evolution model

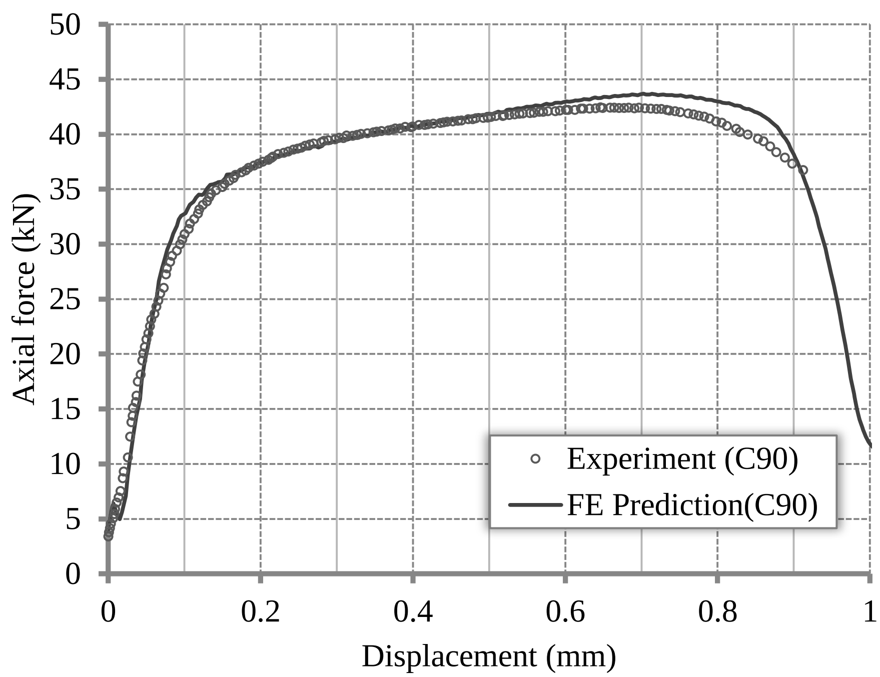

Figure 3.32: FE load–displacement response for steel AISI 1045 compared with the experiments–with damage evolution model

3.4 Conclusions

The conventional flat grooved specimens can be used to obtain material fracture parameters only for stress triaxiality parameters of 0.58 and above. It was found that such a specimen is not suitable for obtaining work material fracture parameters because machining in general and OMC in particular include a much greater range of the stress triaxiality parameter.

To address the issue, a double–notched specimen, which reveals those fracture parameters under large variation of the triaxiality state, has been developed. With this newly developed test specimen, the triaxiality state can be adjusted to the desired values by changing its geometrical configuration, i.e. the pressure angle. The stress triaxiality state parameter in this experiment was varied between -0.24 and +0.60 using five different configurations of the test specimen.

The test results obtained with the developed specimen were used to calibrate the fracture models by Rice and Tracey [78] and by Johnson and Cook damage model [98]. A comparison between the two models applied to steel AISI 1045 work material (Figure 3.33 and Figure 3.34) shows that to predict the material fracture using the flat–grooved specimen, a backward prediction due to lack of data is necessary to estimate material fracture strain at low triaxiality state. This prediction may underestimate the material strain limit at low and negative stress triaxiality state.

The validity of the developed experimental approach was investigated using the deformation field data obtained using digital image correlation (DIC) and load–displacement test data. The obtained material constitutive parameters including deformation and fracture were used to develop a user material subroutine for the material constitutive model proposed in Chapter 2 (see Appendix C).

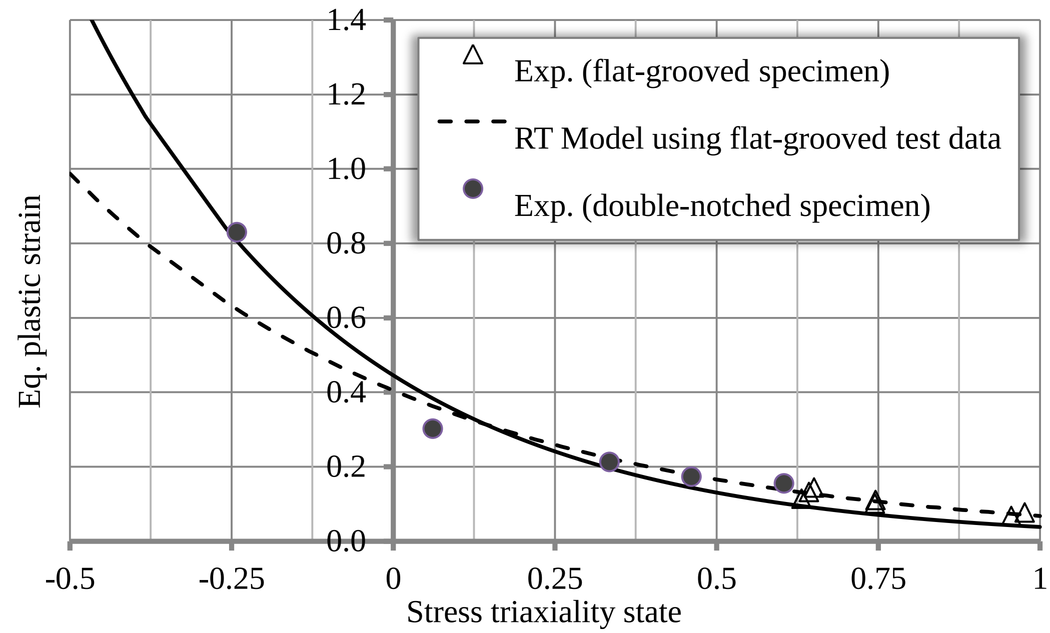

Figure 3.33: Fracture locus of steel AISI 1045 obtained from experiments using double–notched and flat–grooved specimens and fitted to Rice and Tracey (RT) model

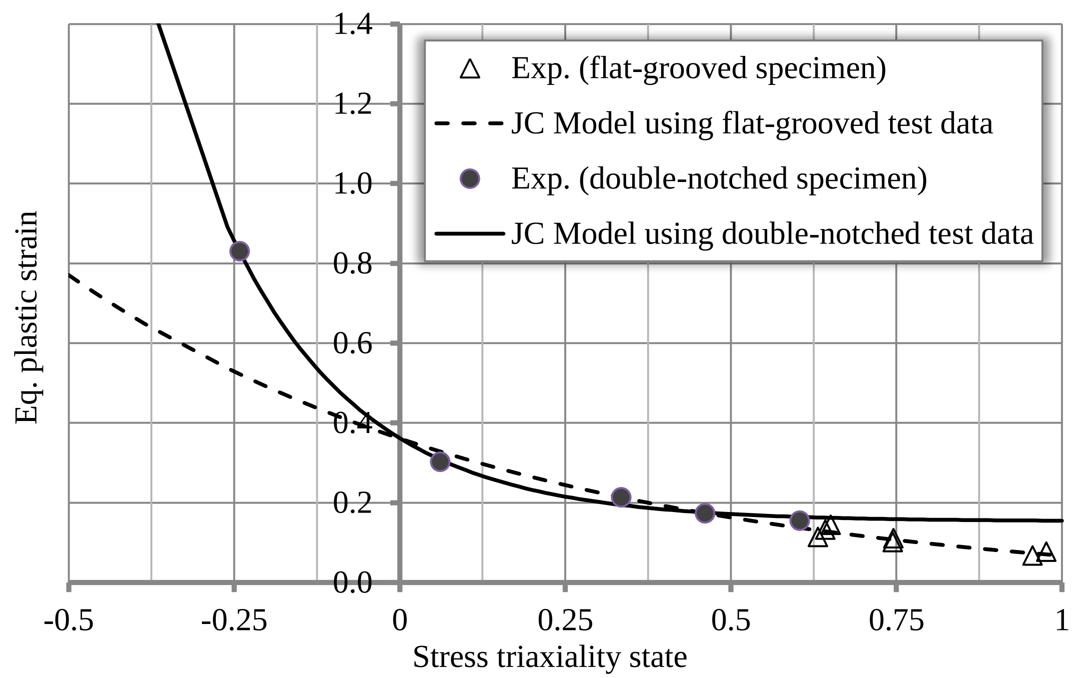

Figure 3.34: Fracture locus of steel AISI 1045 obtained from experiments using double–notched and flat–grooved specimens and fitted to Johnson and Cook (JC) model

To verify the validity of the developed model and accuracy of the obtained parameters of this model, FEA was carried out using this model. The strain distribution and intensity obtained by FEA were compared to the strain field calculated from DIC measurements. Similarity of the FEA and DIC results confirm the validity of the developed model. Additionally, the load–displacement responses of the five specimens were reasonably well predicted.

Chapter 4: FE Simulations and Validation of the Developed Model

To simulate the cutting of ductile metals, a material constitutive model and the procedure to obtain parameters in this model has been developed and presented in Chapter 2 and Chapter 3, respectively. The model considers the material damage initiation, damage evolution, and final fracture. The parameters related to the deformation and fracture parameters of steel AISI 1045 were obtained using a double–notched specimen designed with a tunable state of stress triaxiality. This chapter presents the validation of this model in metal cutting simulations. The model was implemented as a user material model in an explicit FEA code and used to simulate the orthogonal cutting process of steel AISI 1045. To accurately measure the cutting force, cutting experiments were carried out at a low feed rate using a servo–hydraulic load frame with a specially designed fixture. The chip structures generated in this setup are similar to those obtained in real cutting processes [92]. The simulation's results were compared with the experimental cutting forces and chip deformation parameters. The resistance of the work material to cutting and the chip compression ratio (CCR) were predicted within 8% error margin for the two load cases examined.

4.1 Metal Cutting Validation Experiment

The experiment is designed to identify material resistance to cutting and provide detailed insight of the chip formation patterns. Additionally, the experiment was used for validation of the developed metal cutting model.

To accurately measure the cutting force, cutting experiments were carried out at a low cutting speed, using a servo–hydraulic load frame with a specially designed fixture. Figure 4.1 shows a tool holder with a carbide cutting insert and Figure 4.2 shows the test setup with the load frame. The fixture was designed with a back roller to minimize the machine compliance effect and to ensure the system rigidity. The specimen used in the test is made of the same work material that is used in the material characterization experiment (steel AISI 1045). The steel AISI 1045 was chosen because it produces a typical chip and its microstructure characteristics can be distinctively seen under a proper magnification of the optical microscopy. Additionally, this material is broadly used in industry [92].

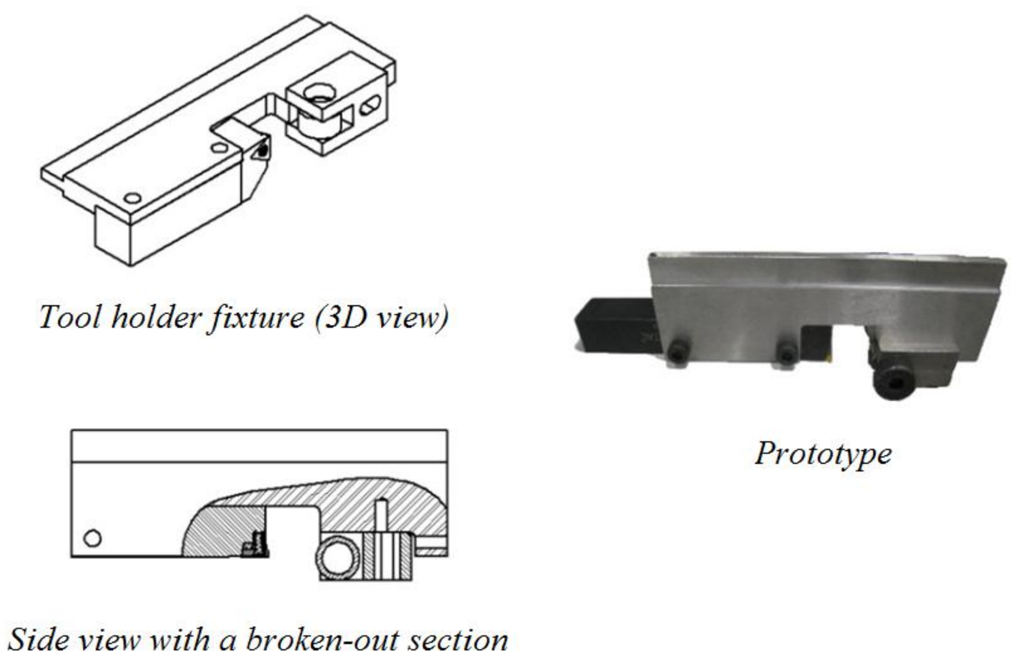

Figure 4.1: Design and prototype of the tool holder fixture developed for metal cutting model validation

Figure 4.2: Setup of metal cutting validation experiment

One main advantage of this approach over the traditional setup is the ability to extract a high resolution, precise force/tool–travel data which can be used to investigate the fingerprint of a particular cutting case. Depending on the cutting condition, the chip morphology may vary from a continuous chip formation to a segmented (also called serrated) chip [92]. An accurate load measurement may reveal the relationship between the cutting force and the chip morphology, such as the fragmentation phenomenon. For example, it is expected to observe load fluctuations corresponding to the chip segmentation occurrence and the creation of the shear bands.

The cutting test particularities were as follows:

Equipment

- Kennametal™ tool holder and tool holder fixture (see Figure 4.1)

- INSTRON™ biaxial testing machine (load frame model 1321)
- 8800 Series system controller
- INSTRON™ Console V8.1 and Wavematrix V1.4 application software
- Laser extensometer – LE (Electronic Instrument Research, EIR, Irwin, PA)
- x1000 magnification optical microscope.

Setup Parameters

- Cutting speed (1 mm/min)
- Sampling rate console (100 Hz)

Workpiece Properties

- Medium–carbon steel AISI 1045 work material
- 4 mm thickness of the test piece

Figure 4.3 shows four different chip microstructures obtained using the above tool holder fixture. The overall chip structure is very similar to what has been reported in the literature using a conventional lathe (ex. [94]). The figure shows three different magnifications for each experiment. All created chips deformed in the same manner except for the t_1=113 microns, In this particular case, because the uncut chip thickness t_1 is relatively large as compared to the other cases, the cutting force was high, and as a result the radial force became high due to tool–chip friction, causing the chip to stick on the tool rake face. After the cutting force became sufficiently high, a crack was created ahead of the tool tip which resulted in a drop in the cutting and friction forces. Therefore, the chip started to slide again and this cyclical nature caused a unique chip structure as shown in the 3rd row in Figure 4.3.

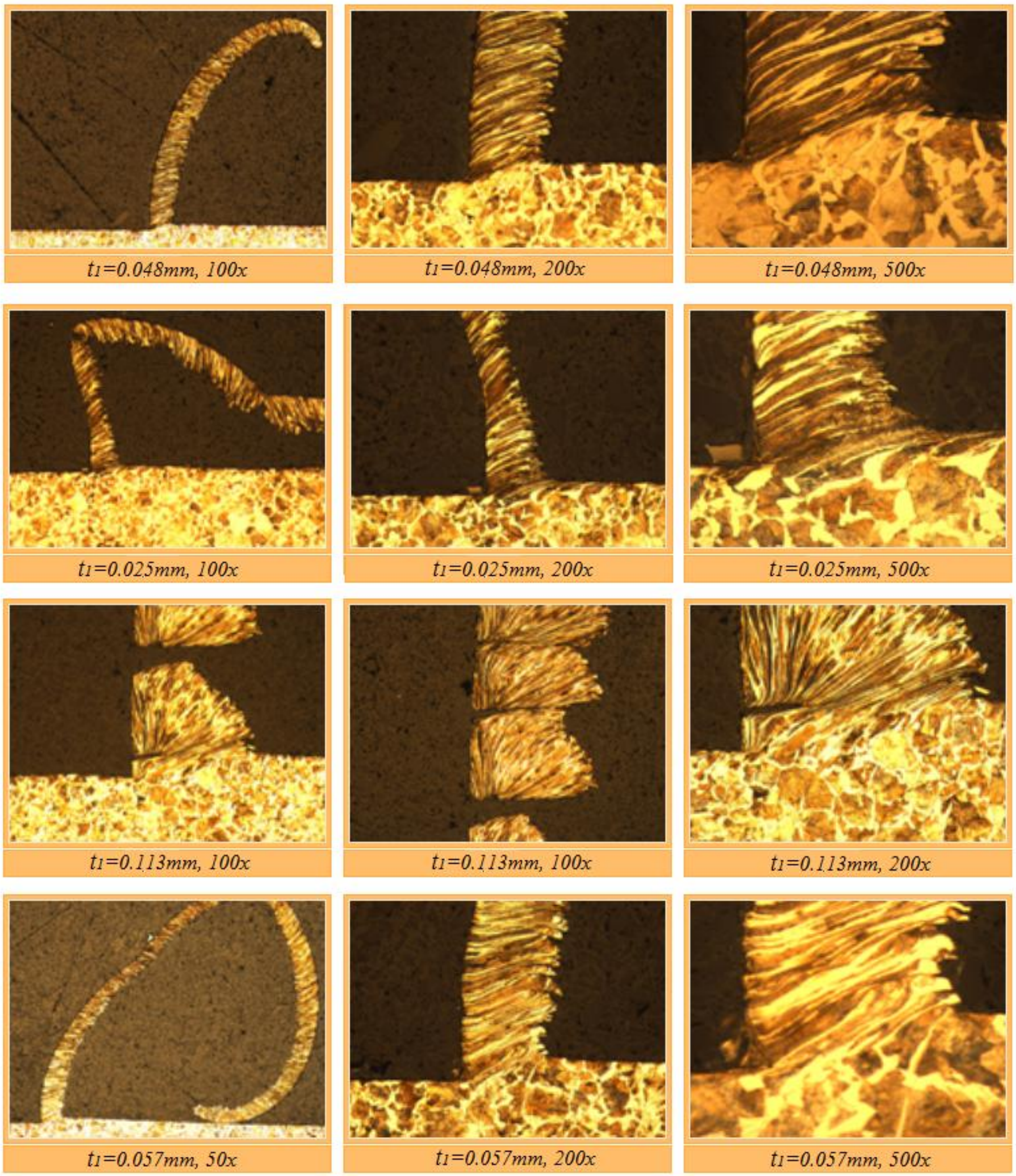

Figure 4.3: Optical microscope images of experimentally–obtained chips with different uncut chip thicknesses (t_1) at various magnifications

4.2 Computational Considerations for Metal Cutting Simulations

Commercial FEA software, ***ABAQUS™*** explicitly, was used to simulate OMC. The constitutive and damage approaches developed in this research were applied correspondingly to the elements of the workpiece. Figure 4.4 presents the FE model for cutting system. The model can be divided into four zones: (1) the lower portion of the workpiece where the material experiences very little local deformations; (2) the separation zone where the elements may be deleted (sacrificing element); (3) the zone of the layer being removed which undergoes a severe deformation therefore is modeled with a fine mesh; and (4) a deformable carbide flat cutting tool with a sharp edge modeled as linear elastic material. The workpiece and the cutting tool were meshed using 2D continuum bilinear plane strain quadrilateral elements CPE4RT with reduced integration. The size of the elements was two microns in the heavily deformed zones. The non–deformed mesh and the prescribed boundary condition are shown in Figure 4.4.

Due to the expected large deformations, high localized strains, and shear bands in the chip formation, element distortions are of great concern and should be handled with great care. To ensure structural mesh distribution and mesh quality throughout the analysis, the elements in the uncut layer and right below the cutting path were seeded with high element density. The element's size was minimized in these regions to improve the accuracy and ensure the forming of the actual chip morphology. The workpiece was fixed at the bottom side and all other edges were allowed to deform without restraints. The tool was moving in the cutting direction with a prescribed velocity at the nodes at the back side of the tool. This modeling method allows the deformation of the tool. If all nodes on the tool have the same velocity, the tool actually turns into a rigid body. Table 4.1 summarizes cutting process conditions under which the FE analyses were conducted.

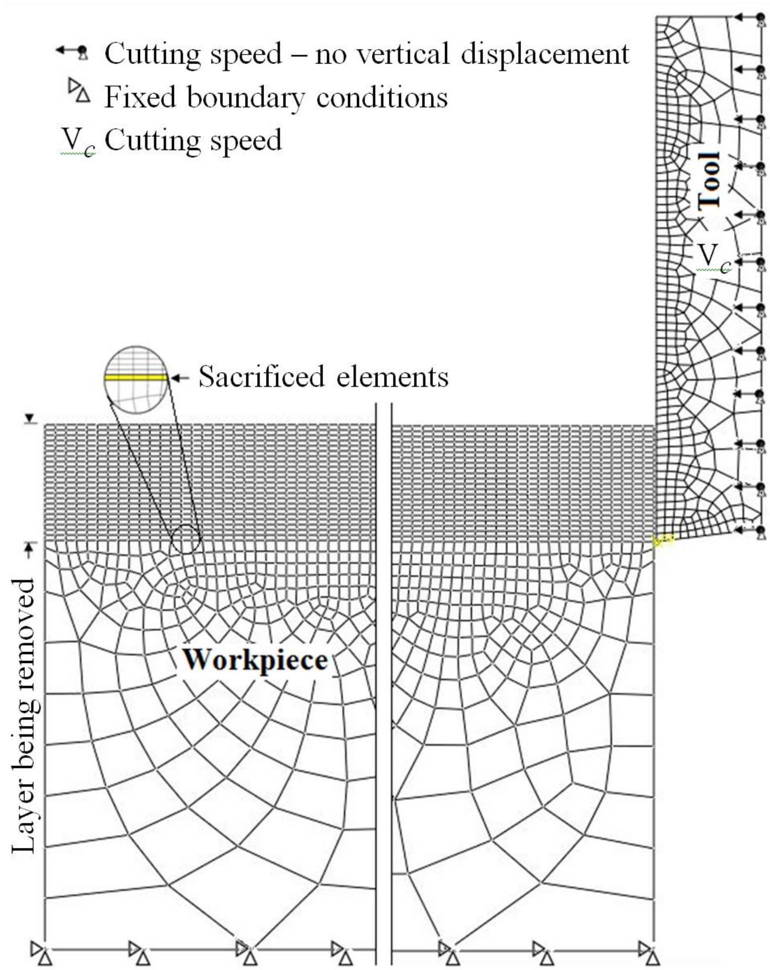

Figure 4.4: FE model: the undeformed mesh and the prescribed boundary conditions

Table 4.1: Cutting condition used in the FE validation model

Parameter	*Test# A*	*Test# B*
Cutting speed, V_o (mm/min)	1[a]	1[a]
Uncut chip thickness, t_o (mm)	0.042	0.025
Depth of cut, d_w (mm)	4	4
Rack angle, γ (deg.)	0	0
Tool clearance angle, α (deg.)	7	7
Tool edge roundness	Sharp	Sharp

[a] Strain rate effect was deactivated to reduce the computational time without introducing dynamic effect

4.2.1 Chip Separation Mechanism

According to the damage initiation model described Chapter 2 and the experimental results in Chapter 3 (see Figure 3.22), the elements under hydrostatic pressure start their post damage degradation behavior at considerably higher strains compared with the ones under a low or negative pressure state. Beyond damage initiation, the degradation evolution suggested by Equation (2.12) dictates that the material will lose all its load carrying capacity at some finite value of $\bar{\varepsilon}$. Therefore, all the severely damaged elements will partially or completely lose their strength. A 100% degradation of a material point represents an evolved crack and thus complete separation. On one hand, this local point in the material theoretically may not carry shear type of loading but still can carry hydrostatic pressure and represent a fluid–like contribution. On the other hand, depending on the pressure, the shear force due to internal friction between the two newly created surfaces may still be considerably high and represent soil–like contribution. This phenomenon suggests that the maximum degradation of a damaged material may not be 100% depending on the local pressure state. However, this hypothesis might be viewed as an implication of FE deficiency.

The separation mechanism used in this work is based on the elimination of the “fully” damaged elements. ”Full” degradation exist only when $\eta \geq 0$ if the above hypothesis is to be satisfied. To overcome this difficulty, the elements with a positive triaxiality are deleted when reaching a degradation of 99%. Those elements will be eliminated from the further analysis in the subsequent time increments, indicated as “sacrificed elements” in Figure 4.4. Although this separation mechanism is simple and computationally effective, this natural choice unavoidably creates voids and develops new system conditions which may lead to computational instability if not handled properly [106]. In this regard, other crack modeling techniques such as cohesive zone model (CZM) [107] and extended finite element method (XFEM) [108] may provide a better solution. These techniques, CZM and XFEM, should be investigated in future research because of their potential benefits for improving the separation phenomenon in metal cutting FE models.

4.2.2 Tool–Chip Interface Friction Model

Due to severe normal stress at the tool–chip interface, the conventional proportional friction theory, the so–called Coulomb friction model, may result in shear traction that exceeds the chip ultimate shear strength [2]. This usually occurs within the tool–chip contact length (l_c) near the cutting edge where the normal stress is high. To overcome this violation, a sticking–sliding contact model is usually implemented. The model limits the maximum shear stress to a prescribed value over the so–called plastic zone of the tool–chip interface [2]. In order to identify a friction model that is valid for metal cutting simulations, Rech et al. [109] performed the pin–on–ring system analysis and used the tribometer to extract experimental data such as sliding velocity and pressure. The study was made for annealed steel AISI 1045 with TiN coated carbide tools. It was assumed that the total friction coefficient is due to the effect of two phenomena: the ploughing and the adhesion. It is understood that for metal cutting simulations only the adhesion type of friction is to be considered.

To isolate the ploughing portion of the friction so that only the friction due to adhesion can be quantified for cutting applications, a thermo–mechanical numerical analysis was conducted by Rech et al. [109] to estimate the two quantities separately. The analysis was based on the comparison of the friction and heat flux with the experimental data obtained under similar conditions. The final static adhesion friction coefficient was found to be $\mu_{adh} = 0.498$ .The final dynamic adhesive friction coefficient (μ_{adh}) model which depends on the sliding velocity (V_{ls}) was governed by the following linear relationship

$$\mu_{adh} = 0.498 - 0.002 \cdot V_{ls} \tag{4.1}$$

The sliding velocity (V_{ls}) range used in the experiment was between 50 and 103 m/min. According to Equation (4.1), the higher the sliding velocity, the lower the adhesive friction coefficient. The above relation can be used in the FEM model to estimate the friction forces on the tool face. Depending on the cutting speed different friction values may be used. The sliding velocity (V_{ls}) on the Rech's experiment is the same as the sliding velocity of the chip on the tool rake face. Therefore the chip velocity can be used as the equivalent of the sliding velocity $(V_{ls} = v_2 = v_1 / \xi)$ in Equation (4.1). However, since CCR (ξ) is an output cutting parameter, instead of hard coding the tool–chip interface model in FEM, it is possible to automatically estimate the actual sliding velocity in a real time simulation and adjust the value of the adhesive friction coefficient (μ_{adh}) accordingly. This eliminates the need for the trial–and–error iterations to find the proper value μ_{adh}.

4.3 Model Validation

The validation of FEM is the final and mandatory stage of the FEM authentication in metal cutting. This is because the results obtained using FEM strongly depend on the particularities used and assumptions made in the FEM model. There are numerous FE metal cutting simulations, but the issue of model validation is rarely mentioned. Unless a certain level of confidence on the validity of the proposed model is confirmed by a proper authentication approach based on experimentation, FEM model cannot substitute the physical model.

4.3.1 Geometrical and Chip Structure Similarities

The simplest and most basic way to verify the FE–based model of metal cutting is to assure the geometrical and chip structure similarities of the simulation and test results [20]. For example, the chip shape and its parameters and structure obtained in the FEM modeling and that obtained in the validation test can be compared.

Depending on the complexity of the chip shape, the number of parameters to be used for such a comparison varies. For instance, the serrated chips may need more parameters than that needed for chips of an almost uniform thickness. Figure 4.5 shows an example where four basic parameters of the continuous fragmentary chip are to be compared [12, 2, 70]:

1 The maximum chip thickness of the modeled, w_{max-m} and experimentally–obtained chip thickness, w_{max-e}.

2 The minimum chip thickness, w_{min-m} and w_{min-e}.

3 The average pinch of the serrations, p_m and p_e.

4 The angle of chip maximum deformation, β_m and β_e.

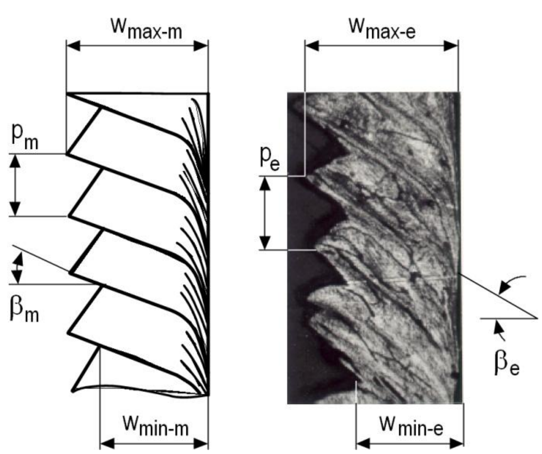

Figure 4.5: Comparison of the basic parameters of the modeled and experimentally–obtained chips

It is obvious that these parameters can hardly be the same for the simulated and experimentally–obtained chips due to the assumptions made in the modeling and imperfections of real machining. Therefore, a tolerable degree of similarity between the two was used as a measure in model validation.

4.3.2 Deformation Similarity

The similarity theory adopted for metal cutting [12, 2, 70] provides a great help in establishing the deformation similarity between FEM simulations and the experimental results. Two similarity criteria, namely the chip compression ratio (CCR) and the Poletica criterion (P_o) [70, 2], are of prime importance in this respect.

CCR reflects the amount of plastic deformation required for cutting a particular work material for a given cutting condition. Because the energy spent on plastic deformation of a wide variety of ductile work material is within the range of 70–80% of the total energy spent, this similarity criterion is probably the most important to verify the validity of a FEM. CCR ζ is determined as the ratio of the length of the cut (L_1) to the corresponding length of the chip (L_2) or the ratio of the chip thickness (t_2) to the uncut chip thickness (t_1), or the ratio of the cutting speed (v) to the chip velocity (v_2) i.e.

$$\zeta = \frac{L_1}{L_2} = \frac{t_2}{t_1} = \frac{v}{v_2} \tag{4.2}$$

CCR can easily be measured experimentally even in the shop floor [2]. Comparing the simulated and experimentally obtained CCRs, one can give a quantitative measure for the validity of FEM. Moreover, because for many common work materials, the CCR is already established as a functioning of major process parameters [28], the “express” analysis of the validity of the simulation can be used. For example, the CCR for turning 316L stainless steel is 2.5–3.5, therefore the average chip thickness in FEM simulations should be 2.5–3.5 times greater than the uncut chip thickness [1].

The Poletica criterion (*Po–criterion*) is used for the assessment of the length of the tool–chip interface. It is defined [2] as the ratio of the contact length (l_c) to the uncut chip thickness (t_1) i.e.

$$Po = \frac{l_c}{t_1} \tag{4.3}$$

In metal cutting, the tool–chip contact length, known as the length of the tool–chip interface, determines the major tribological conditions at this interface such as temperatures, stresses, tool wear, etc. Moreover, all the energy required by the cutting system for chip removal passes through this interface. Therefore, the similarity of the simulated and experimentally obtained Po–criteria assures the similarity of these phenomena in FEM and in reality.

4.4 Results and Discussions

The actual cutting of the workpiece made of steel AISI 1045 was carried out using a carbide ***Kennametal*™** flat insert (#TPUN160304, material K68–Ken). The workpiece material was prepared from the same block as that for material characterization specimens. Two different uncut chip thicknesses were evaluated to examine the chip morphology and the cutting forces. The thickness of the layer being removed from the first cutting experiment “Chip–A” is 42 microns while the other “Chip–B” has a smaller thickness of 25 microns. All other parameters are kept the same for the two experiments. The simulations were carried out based on the experimental setup and its measurements. Upon completion of the experiments, the samples were carefully handled and measurements were taken using the x1000 – magnification optical microscope. All the measurements were taken near chip root before and after the deformation zone.

4.4.1 Chip Morphology

To investigate the geometrical and metallographical similarities between simulations and experiments, the deformed shapes of the chips were compared. Figure 4.6 and Figure 4.7 show these comparisons for two cutting experiments. The chip geometry and its flow characteristics were predicted for each case and their thicknesses were measured as shown in Table 4.2.

The shear bands, which can be seen from the microstructure of the experimental samples, were predicted by the conducted analysis in both cases.

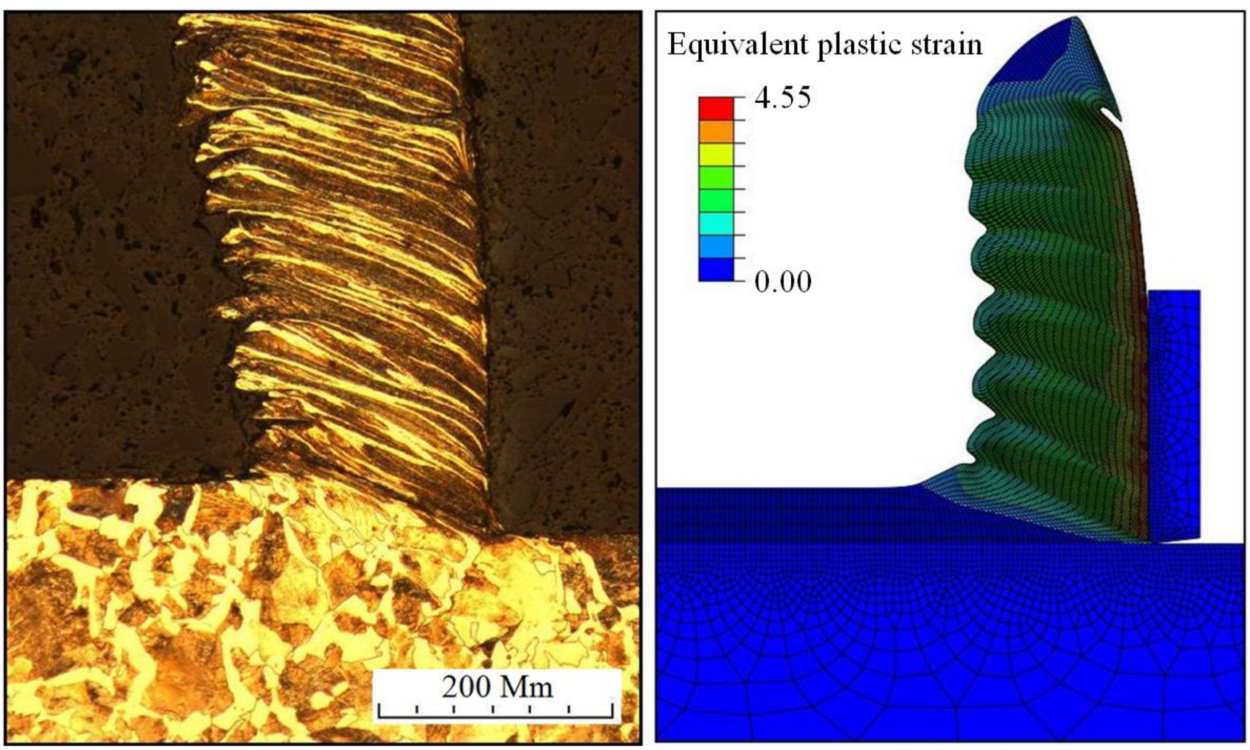

Figure 4.6: Chip–A FE prediction vs. experiment – chip morphology

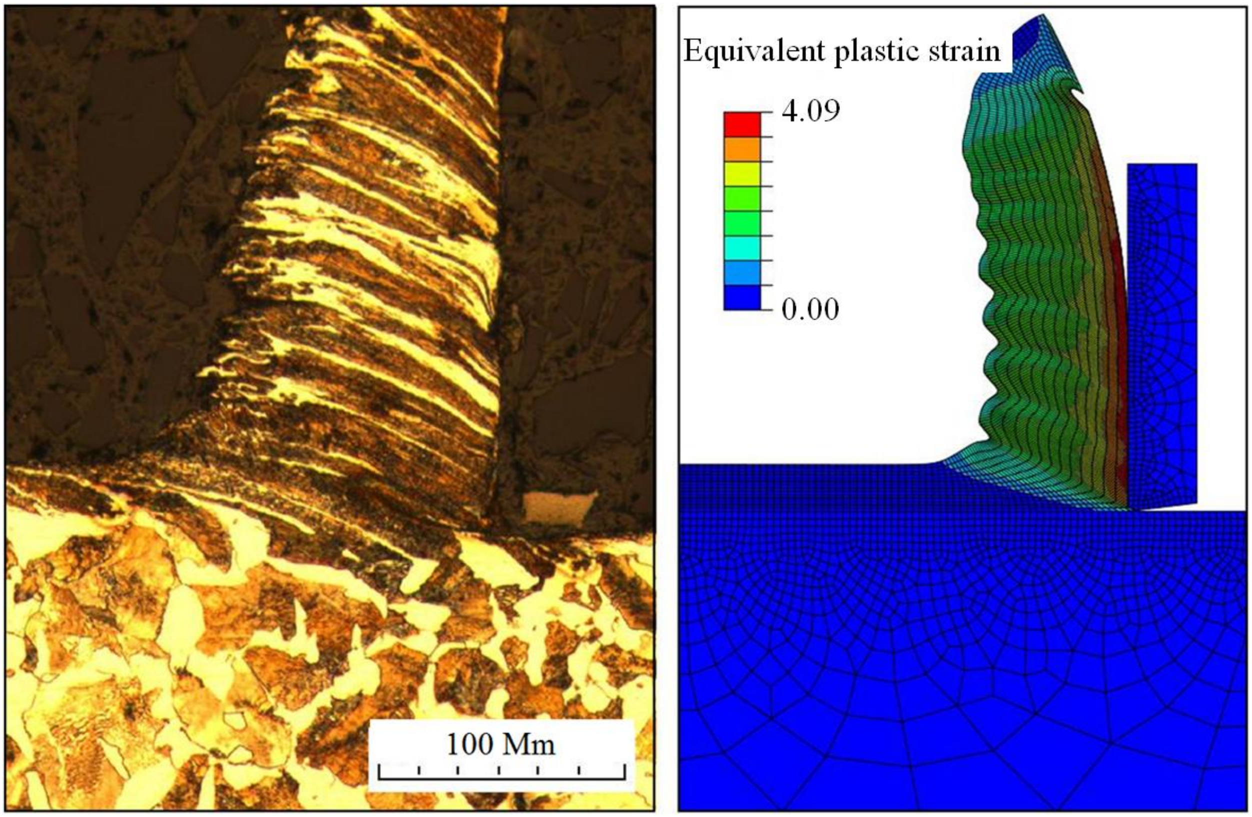

Figure 4.7: Chip–B FE prediction vs. experiment – chip morphology

To reveal the validity of the simulations, the uncut chip thickness and the chip thickness were measured from simulations and the CCRs were calculated based on these measurements. The CCRs of the chip samples from the two cutting experiments and simulations are shown in Table 4.2. The test/model values of the CCR are found to be close and the maximum error is 6.7%.

Table 4.2: Characteristics of chip morphology and cutting forces (F_c)

Chip#	t_1 *(mm)*	*Experiment*			*Prediction (FE)*		
		t_2 *(mm)*	*CCR*	F_c *(kN)*	t_2 *(mm)*	*CCR*	F_c *(kN)*
A	*0.042*	*0.151*	*3.556*	*0.475*	*0.161*	*3.796*	*0.438*
B	*0.025*	*0.104*	*4.074*	*0.279*	*0.098*	*3.851*	*0.272*

4.4.2 Cutting Forces

Figure 4.8 and Figure 4.9 present the cutting force vs. tool travel distance curves for Chip–A and Chip–B, respectively. The experimentally obtained cutting force was compared with the cutting force obtained from FE simulations. The cutting force depends on the cutting process parameters such as the tool geometry, depth of cut (which is the width of cut in OMC), cutting speed and chip–tool friction. Because all these parameters were not changed during this experiment, any change in the outcomes is, therefore, due to the thickness of the layer being removed (t_1). The cutting forces in the two different cases are well predicted by the FE simulations. Due to the compliance of the testing system, there was a considerable amount of change in the cutting force and chip thickness, particularly in the Chip–B case. Therefore, the most recent cut, i.e. the later segment of the experiment was selected as the window of interest for comparison with simulations, as shown in Figure 4.8 and Figure 4.9. The uncut chip thickness t_1 and chip thickness t_2 were measured over this period. The average values of the cutting force were calculated and summarized in Table 4.2.

To examine the range of stress triaxiality state η in OMC, a chip triaxiality map is presented in Figure 4.10. As can be seen, in the primary shear zone, where the deformation rate reaches the maximum, there are three ranges of η values: (1) less than -0.5, when the pressure may exceed the cutoff pressure for fracture; (2) -0.5 to 0, which is the state of the primary zone entrance; and (3) 0 to 0.5, which is the state of the primary zone outlet.

Figure 4.10 reveals the necessity of the experimental approach to uncover the material fracture behavior under extreme cutting conditions presented here. These conditions cannot be captured with the classical flat grooved specimens which cover only high triaxiality where $\eta > 0.6$.

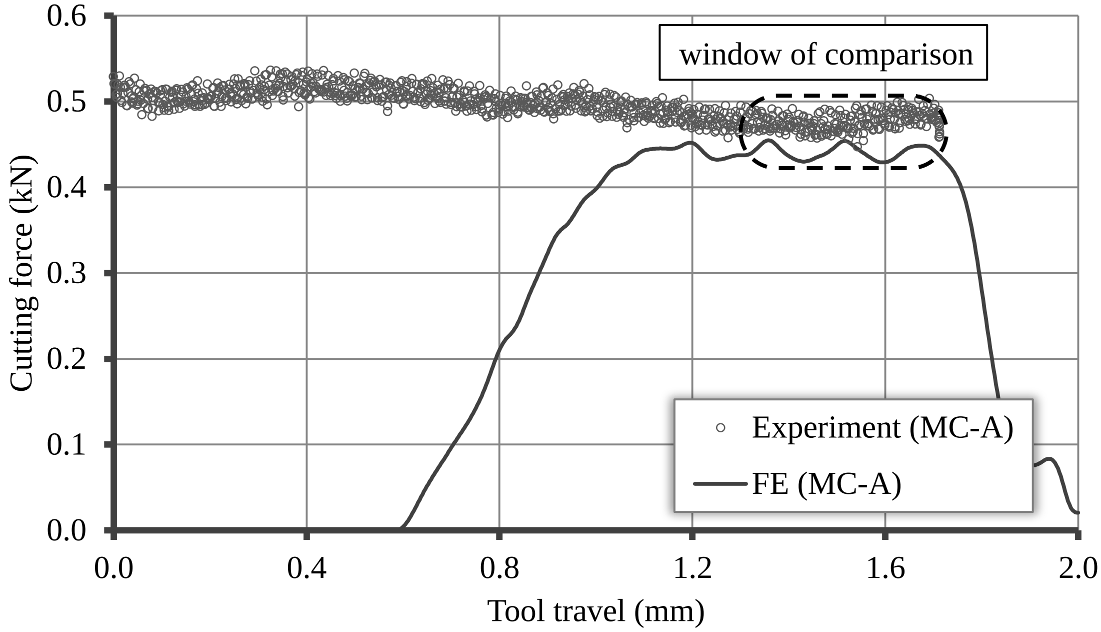

Figure 4.8: Chip–A FE prediction vs. experiment – cutting forces

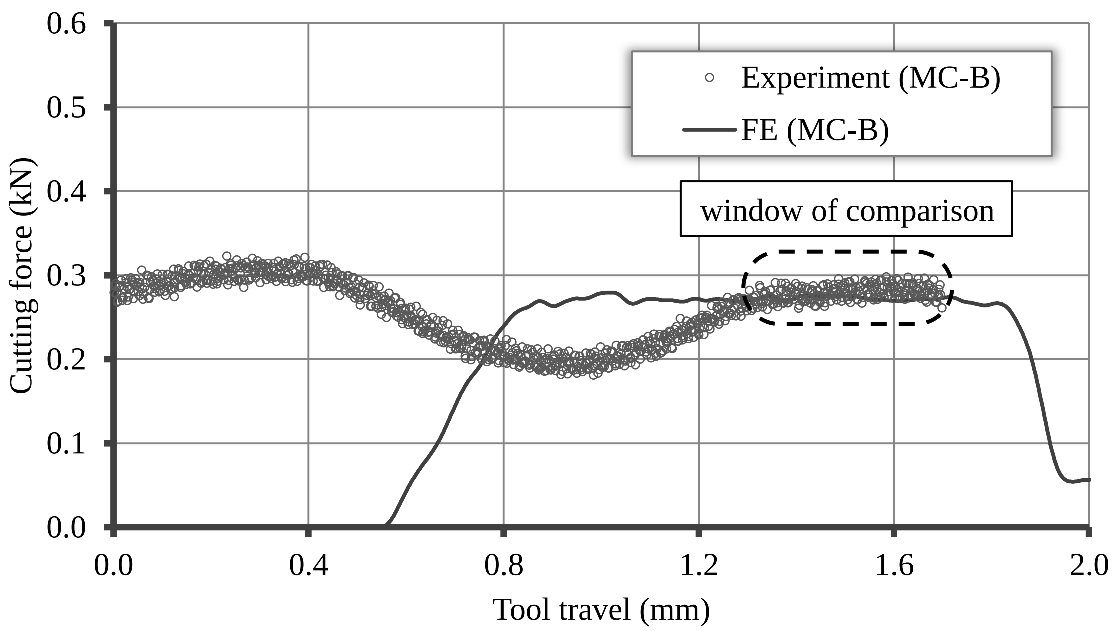

Figure 4.9: Chip–B FE prediction vs. experiment – cutting forces

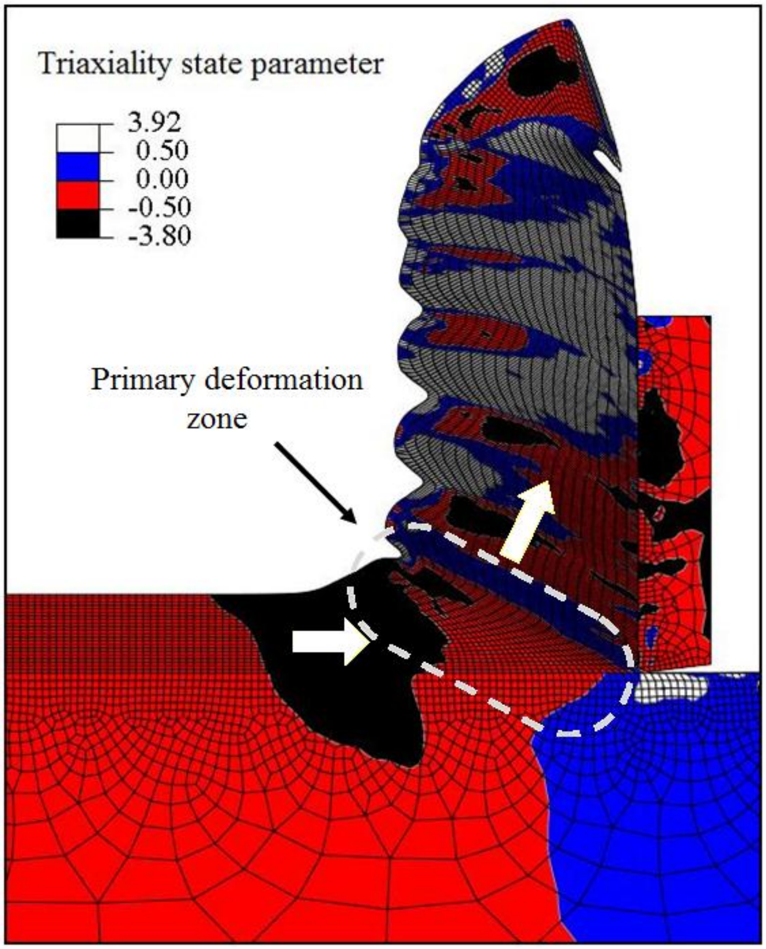

Figure 4.10: Chip–A triaxiality state parameter contours obtained from FEA

4.5 Conclusions

Authentication of FE simulations in metal cutting was carried out following the suggestions made by Astakhov [20]. To do that, a metal cutting experiment using universal material testing equipment instead of the traditional lathe machine was developed. In addition to the reliability and accuracy of the universal standard testing equipment, the proposed setup allows precise synchronization of the cutting force and tool–travel measurements.

The chip structures of AISI steel 1045 obtained at the cutting speeds used in the test fully resembles those obtained from the same work material at high cutting speeds. Figure 4.11 shows the microstructure of chip formation at high cutting speeds [110]. Comparing these structures with those obtained in our metal cutting experiment, one may conclude that the mode of chip plastic deformation (shearing) is the same regardless of the cutting speed. It also exemplifies why the cutting force does not change (practically) with the cutting speed [2]. This is also known from material testing practice where the change of strain rate by an order of magnitude results in the small change in the test force [111].

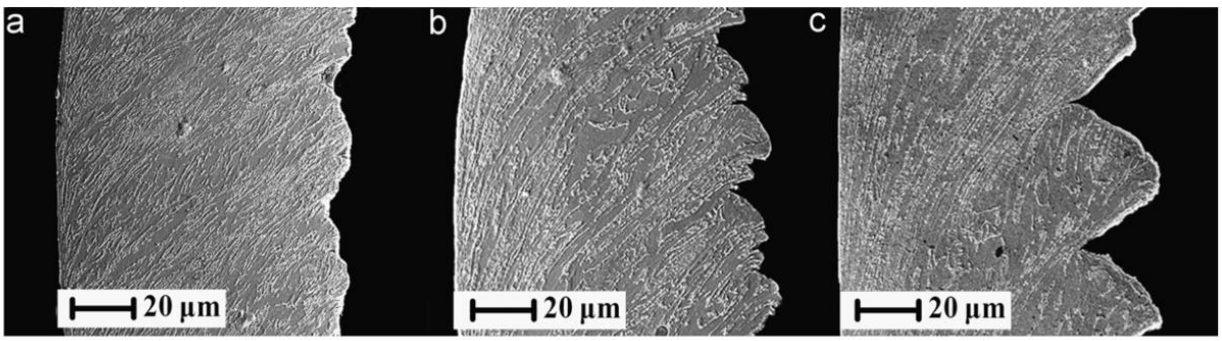

Figure 4.11: The SEM microstructure of chip formation at cutting speed of: (a) 30.8 m/s, (b) 38.6 m/s, (c) 67.3 m/s obtained by Ye et al. [110]

A 2D FE model for OMC was developed based on the physics and experiments discussed in the previous chapters. The developed material model was used in this analysis. The cutting forces obtained by FEA were compared with the experimental results under similar conditions. The predicted cutting forces were within 8%. In addition, the model was evaluated by investigating the chip shape and deformation similarities with experiments. The obtained chip morphology was realistically similar to that obtained in the actual cutting test. The predicted CCRs were within 7% which shows the good deformation similarity of the modeled and the test results.

As shown in Chapter 3, the double–notched specimen developed in the current study yields stress states at the low and negative triaxiality regions which are not covered by the classical flat grooved specimens. The suitability of this approach was revealed here by the triaxiality chart in the primary deformation zone obtained by simulations. Most of the chip deformation in this zone (for this particular study) occurs under a stress triaxiality state ranging from -0.5 to +0.5.

Chapter 5: Practical Applications of the "Energy–Triaxiality" State Relationship in Metal Cutting

Most of the energy spent on metal cutting is due to the unavoidable plastic deformation of the layer being removed in its transformation into the chip. As discussed in Chapter 4, the dominant parameter that controls fracture in OMC is the triaxiality state. Therefore, the chip triaxiality state in the deformation zone can be correlated to the energy of the unwanted plastic deformation for a particular cutting configuration. This chapter investigates this type of correlation by changing the cutting geometry and process configurations. A series of FE simulations were carried out for various tool rake angles, uncut chip thicknesses, and tool–chip frictions. Table 5.1 shows the test matrix under which the FE analyses were conducted.

5.1 Rake Angle

5.1.1 Known Facts and Unexplained Phenomena

The rake angle γ comes in three varieties, positive, zero (sometimes is referred to as neutral) and negative as shown in Figure 5.1 (a), (b), and (c), respectively. There is a great body of experimental and numerical modeling results dealing with the influence of the value and sign of the rake angle on the machining process. The role and importance of the rake angle in metal cutting is not well understood because these available data are contradictive and often misleading. Moreover, the available studies did not take a system approach in the consideration of the influence of the rake angle on various outcomes of the cutting process. Rather, one outcome parameter is normally considered, for example, the cutting force, while others, for example tool life, are ignored. Using these data, a practical tool/process designer cannot make an intelligent selection of the proper rake angle for a given application [1].

Table 5.1: Test matrix and the cutting conditions used to investigate triaxiality state effect on the cutting process energy

Parameter	*Test# RA*	*Test# UCT*	*Test# FR*
Cutting speed, V (m/min)	120.0	120.0	120.0
Uncut chip thickness, t_1(mm)	0.042	VAR[a] [50–250]	0.1
Depth of cut, d_w (mm)	4.0	4.0	4.0
Rack angle, γ (deg.)	VAR[a] [0–40]	20.0	20.0
Clearance angle, α (deg.)	7.0	7.0	7.0
Tool–chip friction	0.498	0.498	VAR[a] [0–0.6]
Tool edge roundness	Sharp	Sharp	Sharp
Tool material	TiN coated carbide	TiN coated carbide	TiN coated carbide
Workpiece material	Steel AISI 1045	Steel AISI 1045	Steel AISI 1045

[a] Test variable.

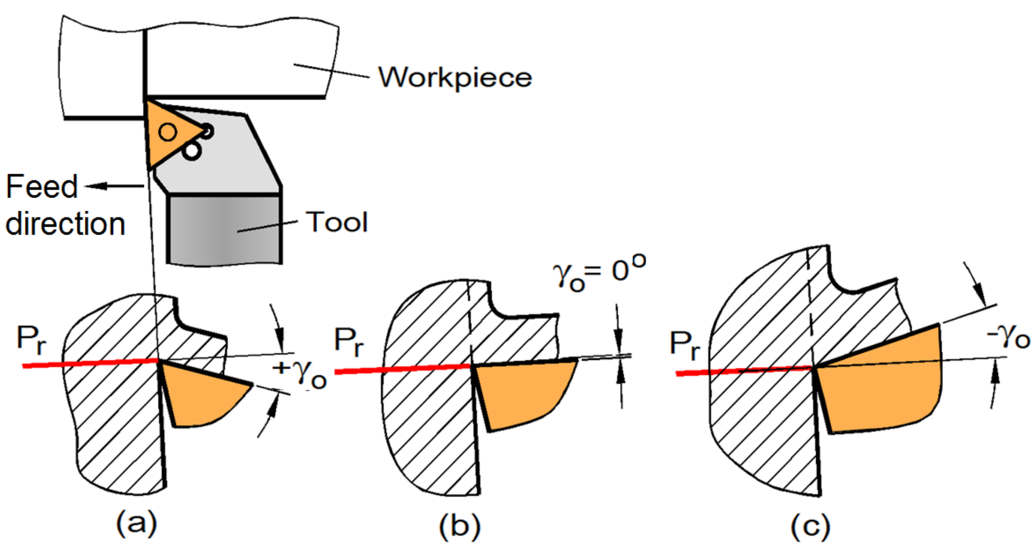

Figure 5.1: Sense of the positive (a), neutral (b), and negative (c) rake angles in turning

It was observed for a long time that the rake angle has a great influence on the cutting process. As a result, this angle has drawn great attention from the researchers and professionals. Shaw [112] argued that the specific cutting energy (and thus the cutting force) decreases about 1% per degree increase in the rake angle while Dahlman, Gunnberg and Jacobson [113] showed that by controlling the rake angle, it is possible to generate tailor–made machining residual stresses in the product. Günay et al. [114] in their experimental study found that a change in the rake angle from 0° to +2.5° resulted in a 2% reduction of the cutting force while a change from -2.5° to 0° resulted in a 3.4% reduction. Tetsuji, Hirokazu and Shigeo [115] in their tests on rock cutting found that the cutting force of the bit with a +20º rake angle decreased about 30–80 % (depending upon other machining parameters), compared to that of the bit with a -20º rake angle. Moreover, an increase in cutting force with the cutting depth becomes lower with increase in the rake angle. Gunay et al. [116] carried out a detailed experimental study of the influence of the rake angle in machining of AISI 1040 steel. They found a very small influence which diminishes at higher cutting speeds. Saglam et al.[117] carried out an extensive research program on machining of AISI 1040 steel bars hardened to HRC 40 in order to reveal the effect of tool geometry. It was also found that the influence of the rake angle depends on the tool cutting edge angle. More dramatic influences of the rake angle on the cutting force and temperature were found for high cutting speeds.

5.1.2 Physics of Material Causing the Influence of the Rake Angle

It is a common belief among the specialists in the field that a sharper cutting tool requires less cutting energy. However, no physical explanation is offered in how the material behaves when the rake angle changes and causes such enhanced performance. Furthermore, no explanation is provided for the fact that the tool life decreases with increasing rake angle because the reduced energy consumption (and thus lower cutting force) actually should lead to increased tool life.

The problem with explanation of the influence of the rake angle and other parameters of the tool geometry can easily be resolved, and thus selection of these parameters together with the parameters of the machining regime (e.g. the feed and depth of cut) can be optimized if the definition of the metal cutting process as the purposeful fracture of the work material is used. As the work of plastic deformation to fracture depends on the state of stress triaxiality in the deformation zone, it can be suggested that the variation of the stress triaxiality (and thus the energy required by the cutting system) causes the reported influence of the rake angle. This section aims to show that this is the case in metal cutting.

To investigate how the rake angle affects the triaxiality state and the energy required for cutting, a number of FE simulations of OMC of steel AISI 1045 were carried out. The cutting conditions were all similar except for the tool rake angle. The rake angle in this experiment was varied in the range from 0º to 40º. As shown in Figure 5.2, the triaxiality state values in the primary deformation zone increases significantly when the rake angle is reduced. This implies an increased material ductility for lower rake angles and consequently more deformation of the work material in its transformation into the chip. In addition, Figure 5.2 shows that the chip thickness, and thus CCR reduces when rake angle increases as observed in practice. Obviously, the simulation shows the state of triaxiality increases with the rake angle at the deformation zone, and more importantly near the point of chip separation from the rest of the workpiece which lowers the strain at fracture of the work material.

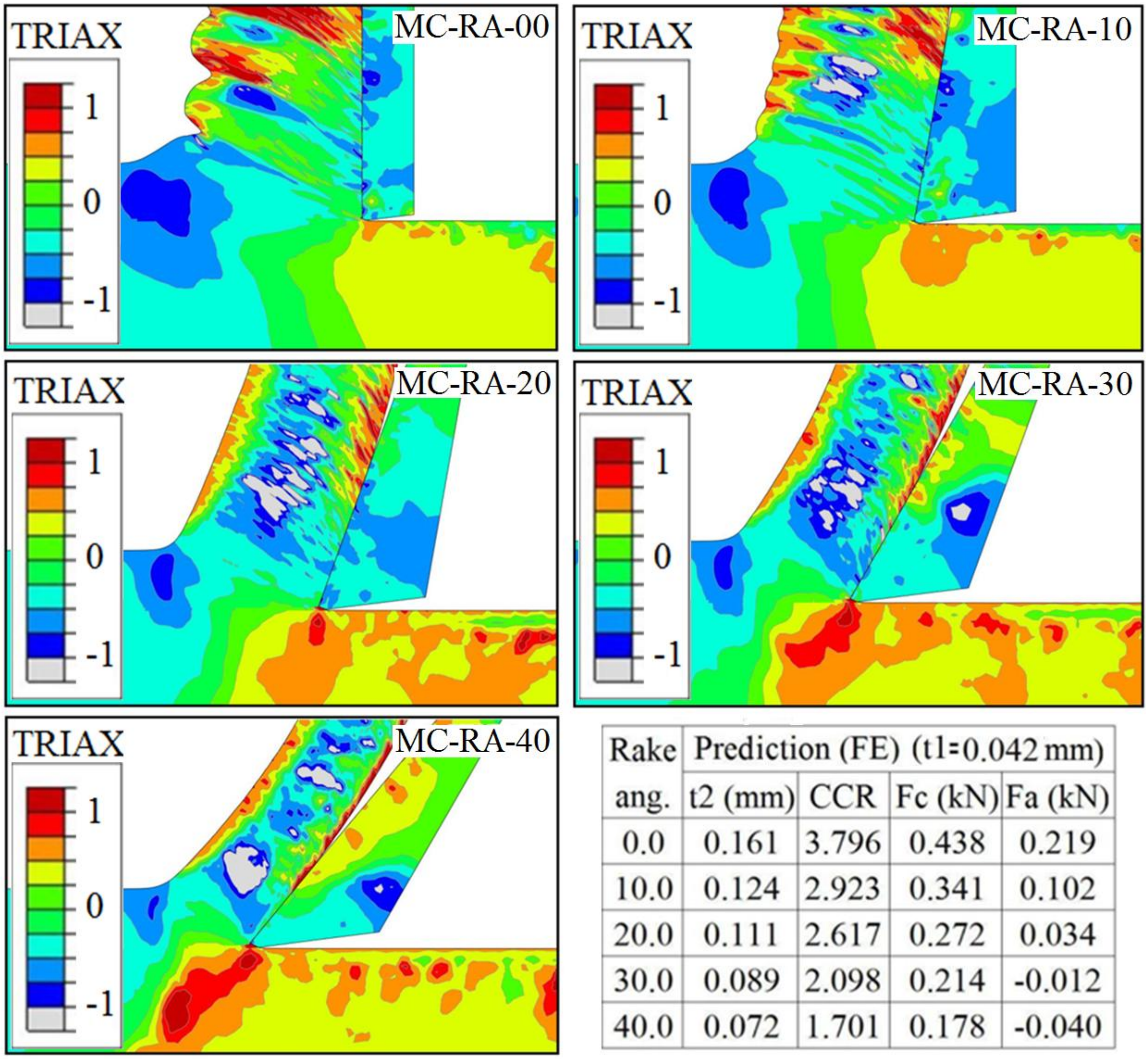

Rake ang.	Prediction (FE) (t1=0.042 mm) t2 (mm)	CCR	Fc (kN)	Fa (kN)
0.0	0.161	3.796	0.438	0.219
10.0	0.124	2.923	0.341	0.102
20.0	0.111	2.617	0.272	0.034
30.0	0.089	2.098	0.214	-0.012
40.0	0.072	1.701	0.178	-0.040

Figure 5.2: FE simulations of chip formation showing triaxiality state contours obtained from cutting tools with different rake angles

The chip structure also changes dramatically as rake angle increased. The chip structure shown in Figure 5.3 becomes smoother, much more uniform, and it undergoes much less plastic deformation as predicted.

As mentioned above, a possible decrease of tool life with increasing rake angle observed in some practical applications should be explained. Such an explanation directly follows from

Figure 5.3 which shows that the length of the tool chip interface reduces with increasing the rake angle. It is also follows from the Poletica criterion (Equation (4.3)) as discussed by Astakhov [2]. If the rate of the contact stress decreases in higher rake angles due to the reduction of the normal stress and is higher than the effect of a lower contact length leading to an increase in the contact stress, the tool life may be improved. Such a phenomenon was first noticed in the study of cutting tools with so–called restricted (or limited) length of the tool/chip interface as studied by Takeyama and Usui [118], Chao and Trigger [119], Usui and Shaw [120], Hoshi and Usui [121] and Usui, Kikuchi, and Hoshi[122].

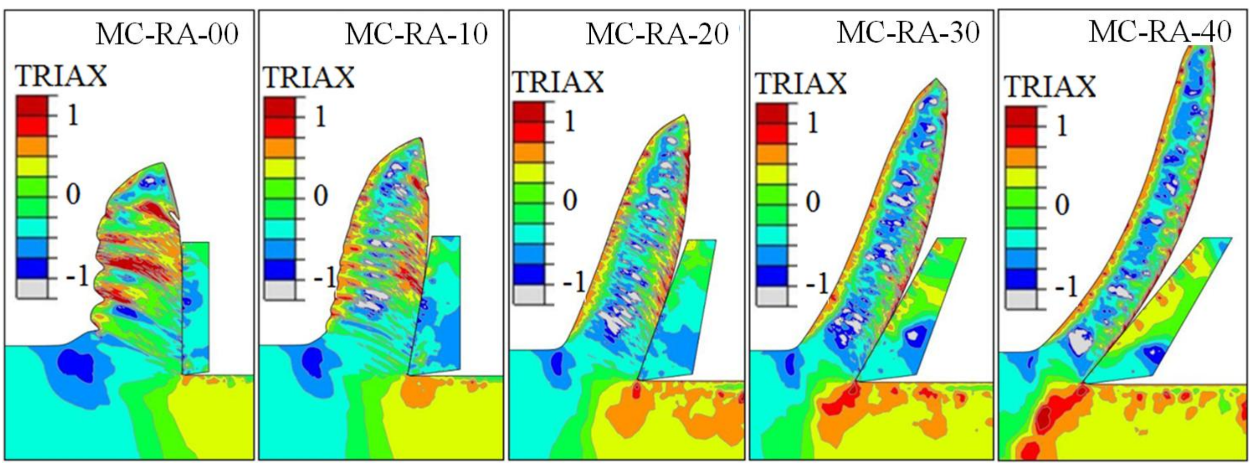

Figure 5.3: FE simulations of chip formation showing chip structure obtained from cutting tools with different rake angles

As discussed above, the amount of chip plastic deformation decreases because the loading conditions caused by the increased rake angle elevates the state of stress triaxiality and lowers the fracture strain at the separation zone near the tool tip. Therefore, the cutting energy/forces are expected to be lower accordingly. Figure 5.4 confirms the fact that the lower the rake angle, the higher the cutting forces required to overcome the material resistance. The simulation suggests that rake angle increase can reduce the energy spent on the cutting significantly (by up to 59%)

in the considered range. A summary table contains average cutting forces, average radial forces, as well as chip thickness and CCR are shown in Figure 5.2.

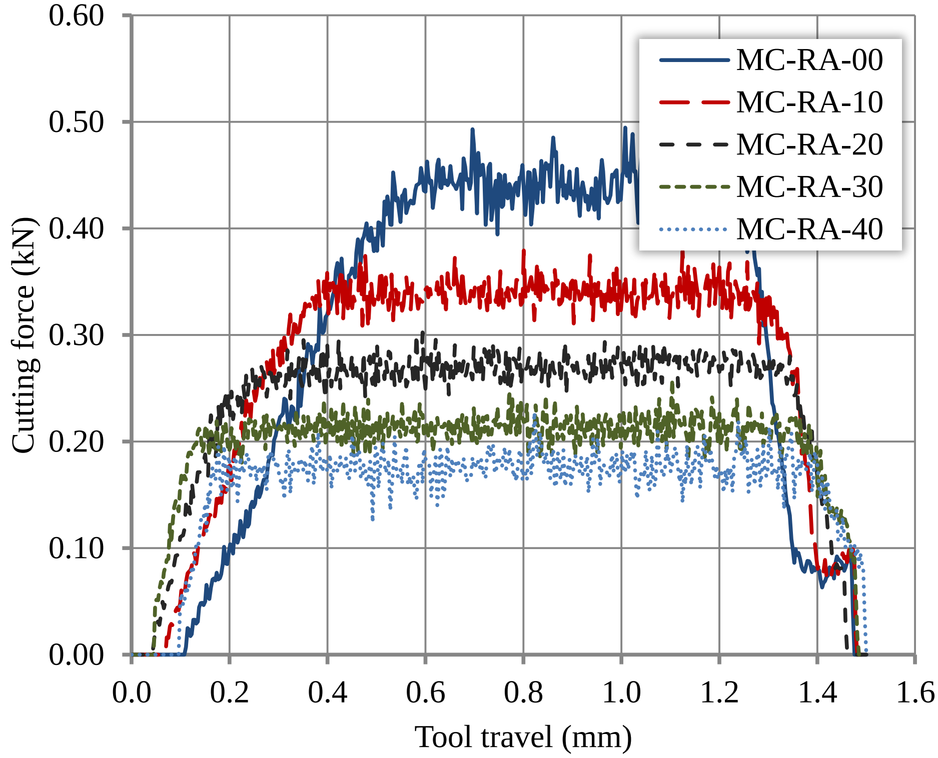

Figure 5.4: FE predictions of the cutting force for the cutting tools having different rake angles

Although the radial force (F_p) defined as the force acting perpendicular to the direction of the primary motion (the cutting speed) is considered as having no contribution to the cutting power (energy) as the tool does not move in this direction, it provides important information on:

1. FEM proper assessment of the radial force and thus adds to the validity of the whole model.
2. Extent of the 'negative' radial force that may cause tool chatter in real machining.

It was noticed in cutting soft work materials, such as brass, copper, Babbitt, using a tool with a high rake angle, the tool jumped ahead of the feed into the workpiece causing vibration, often referred to as chatter in machining.

To understand why it happens, consider a simplified force model for machining with a tool having a high rake angle as shown in Figure 5.5. When the tool works, the radial component F_p of the resultant force R normally pushes the tool out of the workpiece. However, it may not be the case in machining with a tool having a high rake angle. As follows from the model shown in Figure 5.5, the radial force is calculated as

$$F_p = F_f \cos\gamma - R\sin\gamma + F_q \tag{1.4}$$

where F_f is the friction force over the tool–chip interface and F_q is the force on the tool flank that depends on the flank angle, tool wear, MWF and other cutting parameters [2]. This force can be accounted fairly well when its specific value of 30–60 N per 1 mm of the cutting edge length is considered [1].

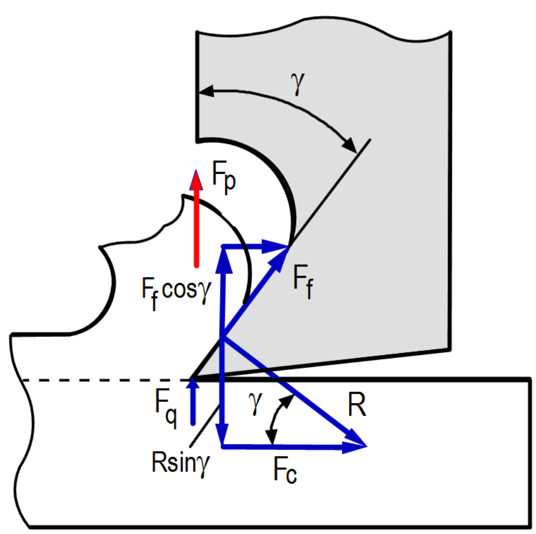

Figure 5.5: Simplified force model for machining with a tool having a high rake angle

The first component ($F_f\ cos(\gamma)$), which pushes the tool away from the workpiece, decreases with the rake angle while the second component ($R\ sin\gamma$), which pulls the tool into the workpiece, increases. Therefore, as the rake angle increases and a sharp cutting tool is used (small F_q), the radial force F_p can be directed into workpiece, which is the root cause of the described phenomenon (chatter). Its typical appearance is shown in Figure 5.6.

Figure 5.6: Chatter marks on the machined surface

Therefore, if FEM is constructed properly, the computational results should reveal the presence of the ‘negative’ radial force (validity of the model) and its extent (to be used in chatter prevention calculations) [123].

Figure 5.7 shows the predicted radial forces for the different tool rake angles. As expected, the F_P is proportional to the rake angle, the lower the angle, the higher the forces. What is more important, however, is the 'negative' radial force for high rake angles, which was predicted using a simple model of the normal stress over the tool [1]. The simulations support these notions and suggest that the point of radial force balance in this experiment occurs at about 28^{o} rake angle.

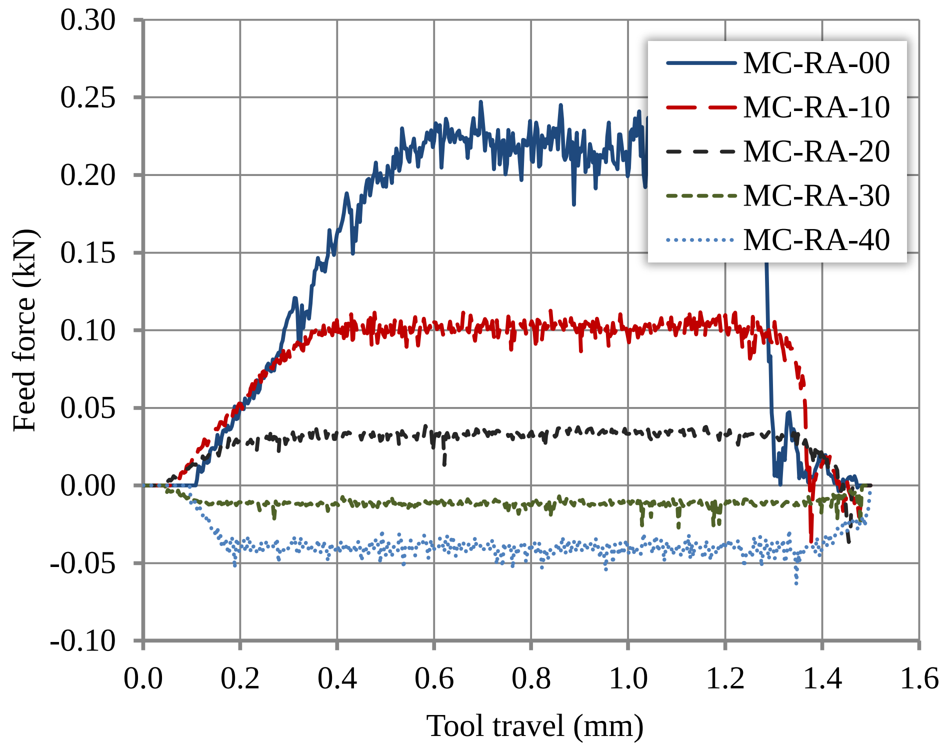

Figure 5.7: FE predictions of radial forces obtained from cutting tools with different rake angles

5.1.3 Practical Considerations

5.1.3.1 Strength of the Cutting Tool Wedge

Reading the previous section, one might argue, however, that a high positive rake angle is not very practical as the cutting tool wedge (the part of the tool material between the rake and the flank faces of the tool) becomes so weak that it can break easily if some fluctuations of the cutting force occur. Such fluctuations traditionally occur due to tool/workpiece runout, misalignments in the machining system, lack of structural rigidity in this system, etc. It is instructive to explain that although the listed factors can be significant, the whole described notion of tool fracture is a bit outdated.

As discussed In Chapter 1, in the not–too–distant past, the components of the machining system were far from perfect in terms of assuring normal tool performance. Under these conditions, the use of cutting tools with high rake angles was impossible particularly if such a tool was made of a “brittle” (for such conditions) tool material as, for example, a sintered carbide. Adjusting to these conditions, tool researches and manufactures developed “forgiving’ carbide tools made of high–cobalt carbide grades and with negative rake angles. The price to pay included a low tool life and limited cutting speed and feed (productivity). For many years, a stable though fragile balance between inferior–design/geometry cutting tools and poor machining system characteristics was maintained.

As discussed In Chapter 1, this has been rapidly changing since the beginning of the 21st century. Modern sub–micrograin carbides possess sufficient fracture toughness. For many years, polycrystalline diamond (PCD) brazed and indexable cutting inserts were used for this purpose with negative rake angles to cover up for imperfect machining systems. Due to recent development of ultra–micrograin PCDs, advanced cutting tools manufacturers began to offer PCD insert with high positive (up to 10^{o}) rake angles which have significantly improved high–speed machining of high–silicon aluminum alloys widely used in the automotive industry in terms of tool life, machined surface integrity, reduced cutting forces etc.. Unfortunately the available recommendations for the suitable tool geometries do not reflect great advances made in the last 5–10 years in the properties of tool materials and coatings.

Gradually, some tool manufacturers began to offer tool with extremely high rake angles primarily for machining of aluminum alloys and copper. For example, Robertson Precision, Inc (Redwood City, CA) developed Shear Geometry® cutting tools with extremely high rake angles. Figure 5.8 shows an example of such tools and the chip formed in machining of an aluminum alloy. The success of this tool became possible with the development of a special sub–micrograin sinter–HIPed carbide tool material.

Figure 5.8: Shear Geometry® cutting tool, formed chip and high–rake insert (Robertson Precision, Inc (Redwood City, CA))

Nowadays, milling tools with high rake angles have become common. For example, Big Kaiser Precision Tooling Inc. (Elk Grove Village, IL) offers full cut mill FCM type with 20º rake angle. Allied Machine & Engineering Corporation (Dover OH) offers high rake geometry on its drills which is specifically designed to improve chip formation in materials with very high elasticity, extremely poor chip forming characteristics, and low material hardness. Leading tool manufactures also offer high rake CCGT inserts (Figure 5.9) intended for non–ferrous materials instead of CCMT inserts. Practical machinists found soon that such inserts can cut practically anything. Although regular CCMT inserts often have some positive rake angle, CCGT inserts offer much higher rake angles. The major insert manufacturers have special lines of this style insert: ISCAR CCGT–AS, Kennametal CCGT–HP, Valenite CCGT–1L, Seco CCGT21.51F–ALKX etc. Each one has a slightly different sales pitch about why one should use the insert. ISCAR is pushing them as offering such a fine finish for aluminum that no grinding is needed, for example. The recommended materials even vary across the lines. What started out as aluminum super finishing insert, then extended in applications to high temperature alloys, stainless, and other possibilities.

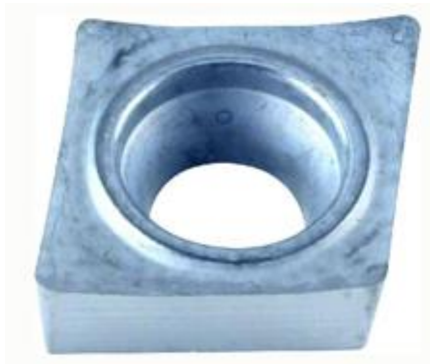

Figure 5.9: Typical high rakes CCGT insert

5.1.3.2 Chip Breakability

When using cutting tools with high rake angles, one needs to keep in mind the chip handling problem [1]. As the amount of plastic deformation of the layer being removed is significantly decreased with the use of such tools, CCR also decreases as a direct result. As such, much thinner and longer chip is produced. The handling of such a coiled chip presents a serious problem in industry. Therefore, increasing UCT or t_1 (Figure 1.2) must be necessary to increase the chip thickness, and thus its breakability.

5.2 Uncut Chip Thickness (UCT)

Figure 5.10 shows the FE simulations of OMC for various uncut chip thicknesses (t_1). The analysis supports the above theory by Astakhov, the chip structure tend to form shear bands as t_1 increases [2].

Although the stress triaxiality state decreases as t_1 increased near tool tip, the size of the low triaxiality state (region in blue) in the primary entrance zone, where most of the deformation occurs, decreases relative to t_1. In other words, a larger portion (percentage) of the overall deformed material with low stress triaxiality state occurs in the low t_1. Therefore, it is expected that the energy per unit volume may actually decrease as t_1 increases. In addition, the morphology of the chip is also affected by the state of triaxiality which causes the material to start to damage and fracture at an earlier stage compared to low t_1. This justifies the reason why we see in Figure 5.10 more shear bands formed as t_1 increased.

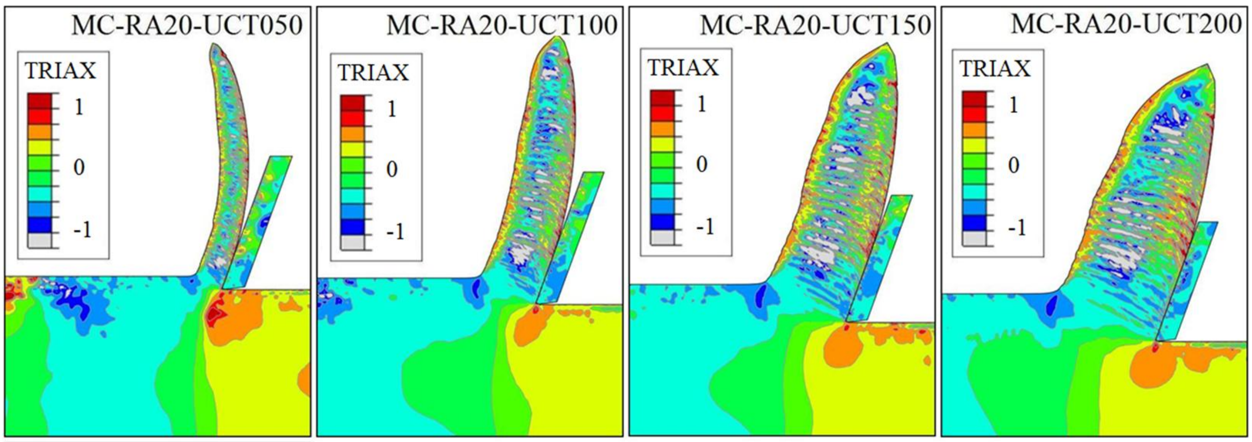

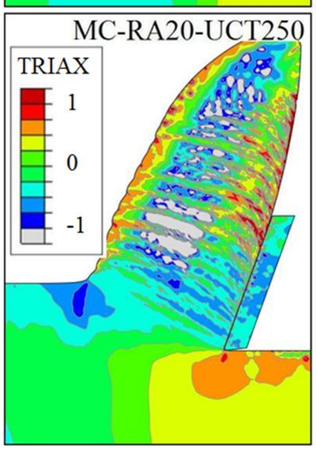

WP#	Rake ang.	t1 (mm)	Prediction (FE)			
			t2 (mm)	CCR	Fc (kN)	Fa (kN)
MC-RA20-UCT050	20.0	0.050	0.116	2.320	0.289	0.030
MC-RA20-UCT100	20.0	0.100	0.226	2.255	0.555	0.058
MC-RA20-UCT150	20.0	0.150	0.335	2.233	0.799	0.082
MC-RA20-UCT200	20.0	0.200	0.438	2.188	1.038	0.095
MC-RA20-UCT250	20.0	0.250	0.550	2.200	1.291	0.107

Figure 5.10: FE simulations of chip formation showing chip structure and stress triaxiality state contours obtained for various uncut chip thicknesses

A good indicator for amount of deformation in the material is CCR. According to Astakhov's theory [124], although F_c will increase as a greater volume of the work material is removed, CCR should decrease with t_1. This measures the amount of deformation in a continuum sense. The table in Figure 5.10 supports this hypothesis to a great extent. It can be seen as a general trend that the larger the t_1 the lower the CCR. However, when t_1 becomes large enough, the material behavior starts to depart from being continuum toward fracture. At this time more shear bands are created and hence the CCR becomes less indicative to cutting energy level. Furthermore, measuring CCR becomes a practical challenge as which t_2 value would better represent the CCR calculations.

The energy required to remove a larger material volume will be obviously larger since the required cutting forces to deform and shear–off the workpiece material is proportional to t_1 (Figure 5.11). However, the specific energy required to remove a unit volume may vary depending on the loading condition. Figure 5.12 shows the specific energy per unit volume of removed material for all various UCTs. The results imply that the process efficiency increases at higher material removal rates due to increased t_1. Although this energy saving may not be significant, the machine operation time and product manufacturing lifecycle may be lowered dramatically. Figure 5.13 shows the predicted radial forces.

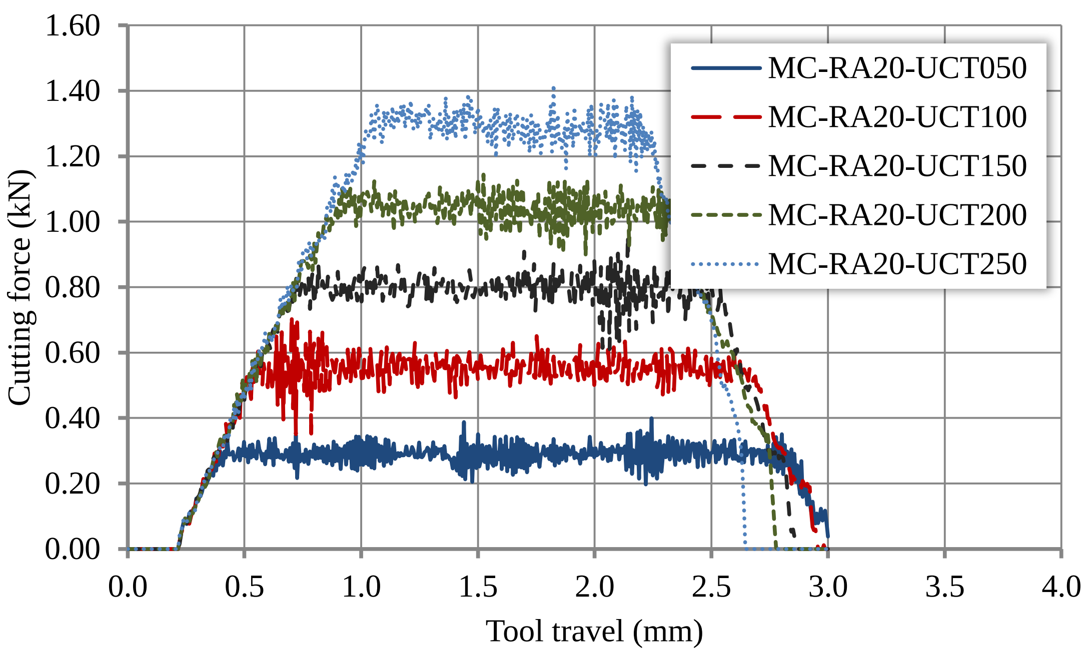

Figure 5.11: FE predictions of cutting forces obtained for various uncut chip thicknesses

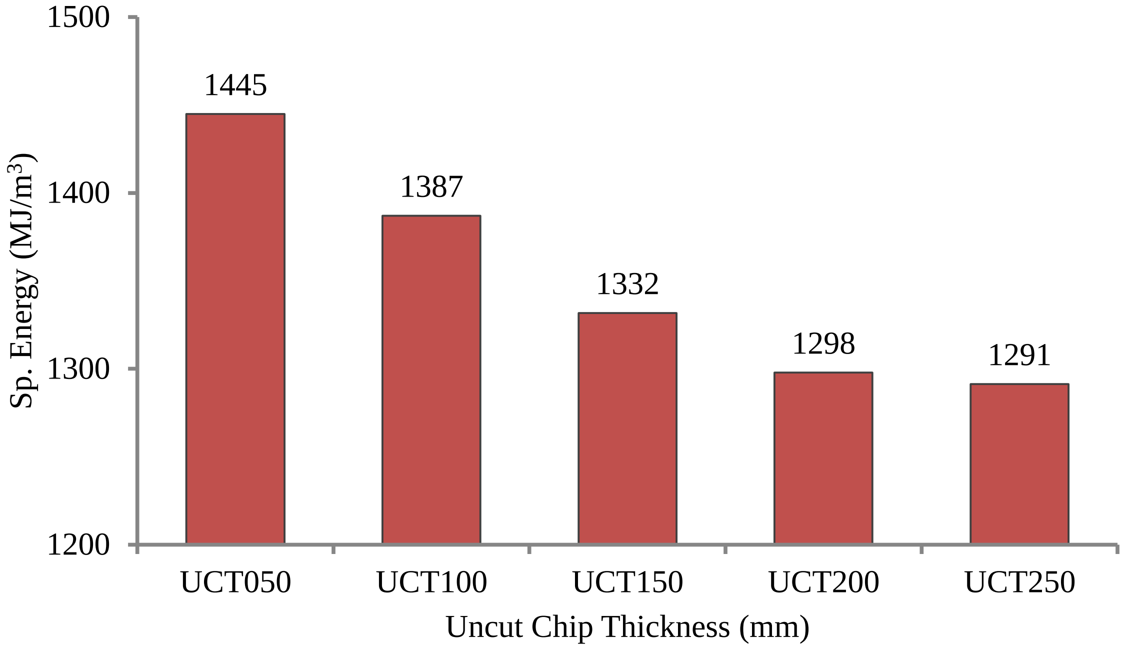

Figure 5.12: Energy required per unit volume of removed material for various uncut chip thicknesses

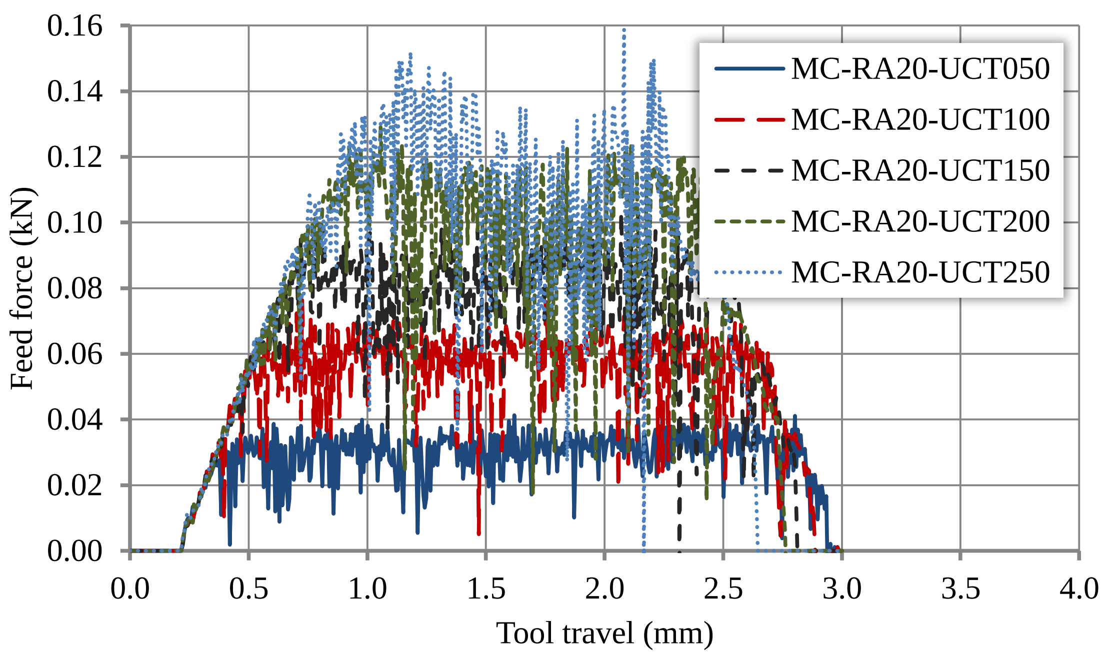

Figure 5.13: FE predictions of radial forces obtained for various uncut chip thicknesses

5.3 Chip Tool Interface

Improving the friction conditions over the tool–chip interface is the common trend in the enhancement of tool performance and tool life. A common method for such an improvement is the application of various coating on the cutting insert [125].

It is well observed that the energy required for a particular cutting condition is significantly reduced by altering the friction coefficient. To understand what causes such process enhancement, consider Figure 5.14. This figure shows the FE simulations of several load cases with different tool–chip friction coefficients. A similar distribution for all the cases but different levels of stress triaxiality state contours can be clearly seen in this figure.

As a general trend, the stress triaxiality state field decreases by elevating the friction coefficient. To some extent, the friction is responsible for resisting chip flow and therefore it increases the hydrostatic pressure (equivalently triaxiality state reduces) of the workpiece in the deformation zone and more noticeably at the tool tip. This causes an increase in the plastic deformation limit at the tool tip and the primary deformation zone. As a result, more energy is required to accomplish the cutting process. As discussed above, CCR can be a useful indicator for material deformation and hence the amount of plasticity energy. As expected, CCR proportionally increases with the friction coefficient (see Figure 5.14).

Perhaps the most noticeable outcome of these analyses is the chip curl. As clearly shown in Figure 5.14, the less friction applied, the smaller the chip curl radius. This is again a significant outcome which provides a simple way for model verification but more importantly it indicates less tangential tool resistance to the chip flow with a lower friction coefficient. In addition, a lower friction results in a smaller tool–chip contact length.

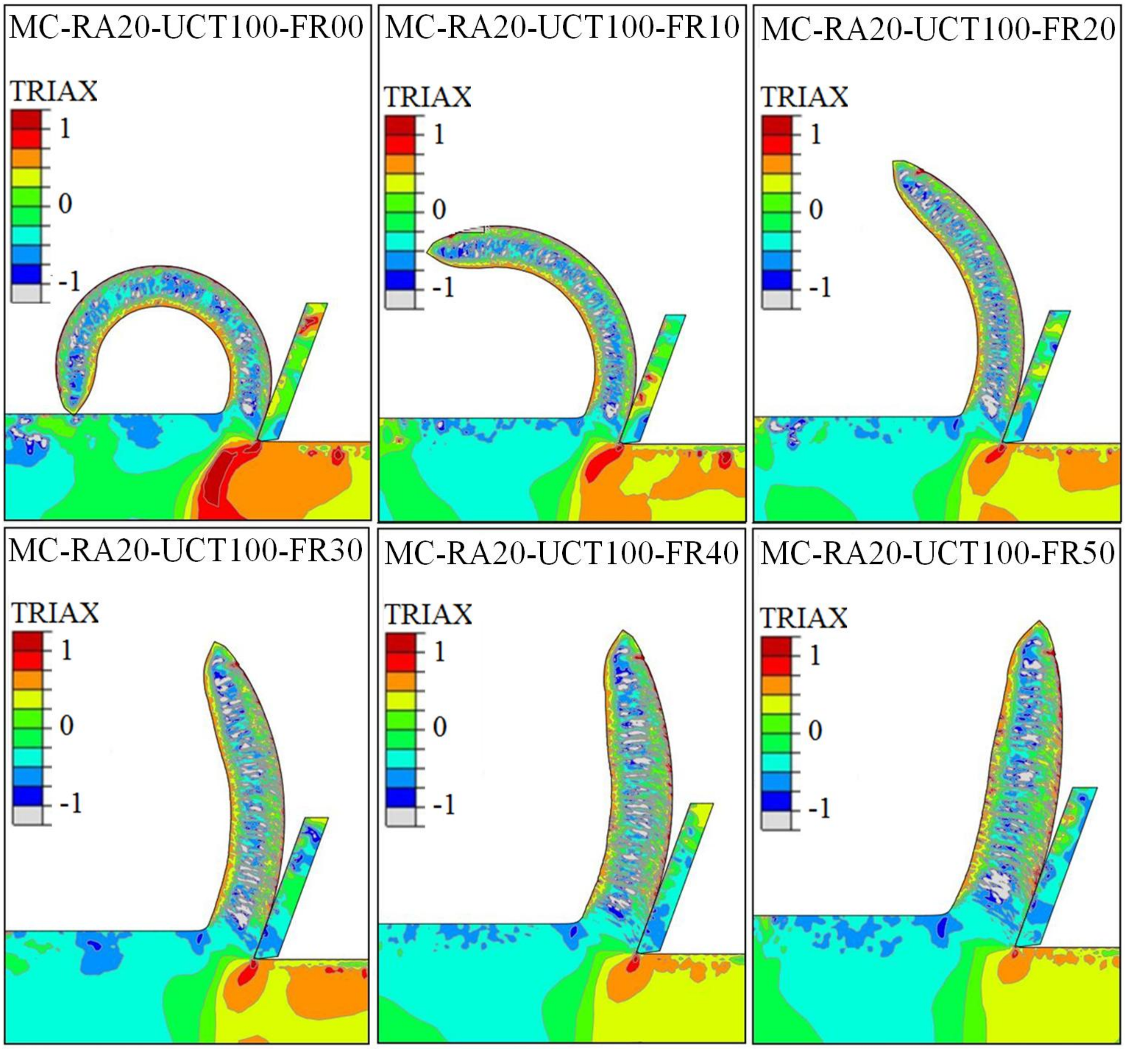

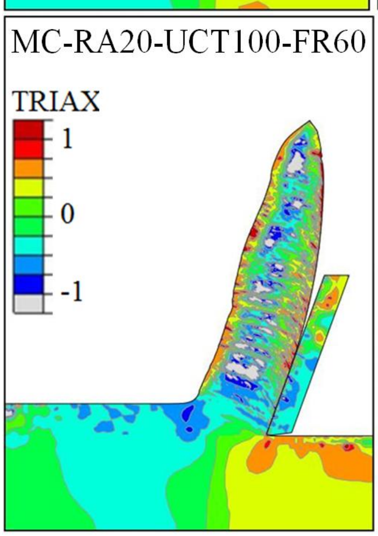

WP#	t1 (mm)	Friction coeff.	Prediction (FE) (Rake ang. 20^{0})			
			t2 (mm)	CCR	Fc (kN)	Fa (kN)
FR00	0.100	0.000	0.148	1.480	0.342	-0.123
FR10	0.100	0.100	0.160	1.600	0.373	-0.094
FR20	0.100	0.200	0.175	1.750	0.416	-0.062
FR30	0.100	0.300	0.189	1.890	0.457	-0.026
FR40	0.100	0.400	0.204	2.040	0.499	0.014
FR50	0.100	0.500	0.220	2.200	0.552	0.058
FR60	0.100	0.600	0.233	2.330	0.595	0.104

Figure 5.14: FE simulations of chip formation showing chip structure and stress triaxiality state contours obtained for different friction values of the tool–chip interface

The cutting forces obtained from these simulations shown in Figure 5.15, support the above argument. The elevated stress triaxiality state due to friction causes cutting forces, and hence energy, to increase accordingly. Although the increase of the cutting forces at higher frictions can be viewed as the additional contribution from the lateral component of the friction forces, this justification may not be applicable when zero rake angle is used. For this cutting configuration there is no lateral component but the same increase on the cutting forces is still observed. The more physically meaningful explanation is the change in stress triaxiality state as it can cause not only a higher material ductility but also a greater internal energy due to the elevated hydrostatic stress.

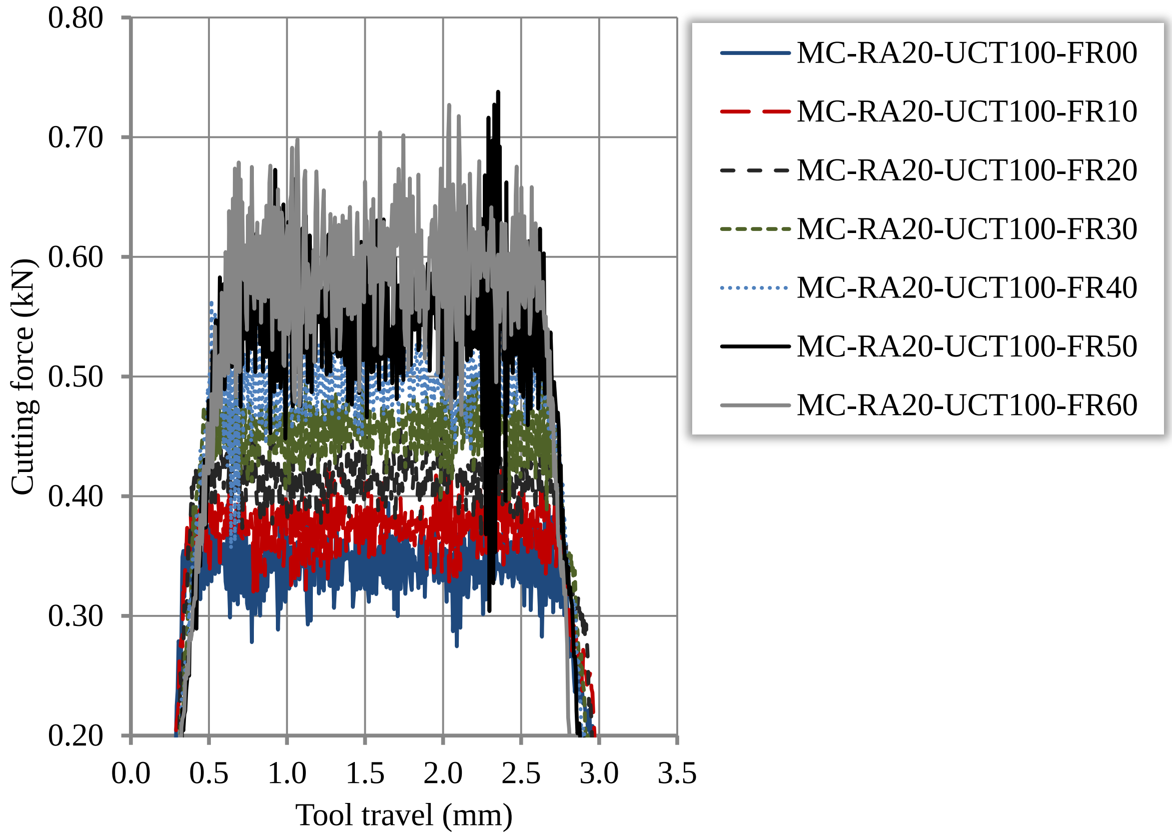

Figure 5.15: FE predictions of the cutting forces obtained for different friction values of the tool–chip interface

Because the radial force is manly driven by friction when the tool nose ploughing effect is neglected such as in this simulations where sharp tool tip is assumed, the radial force is expected to decrease by lowering the friction. In fact the negative radial forces can be seen in these simulations when friction coefficient is less than 0.37 (see Figure 5.16). It is expected to change if rake angle other than 20º is to be used.

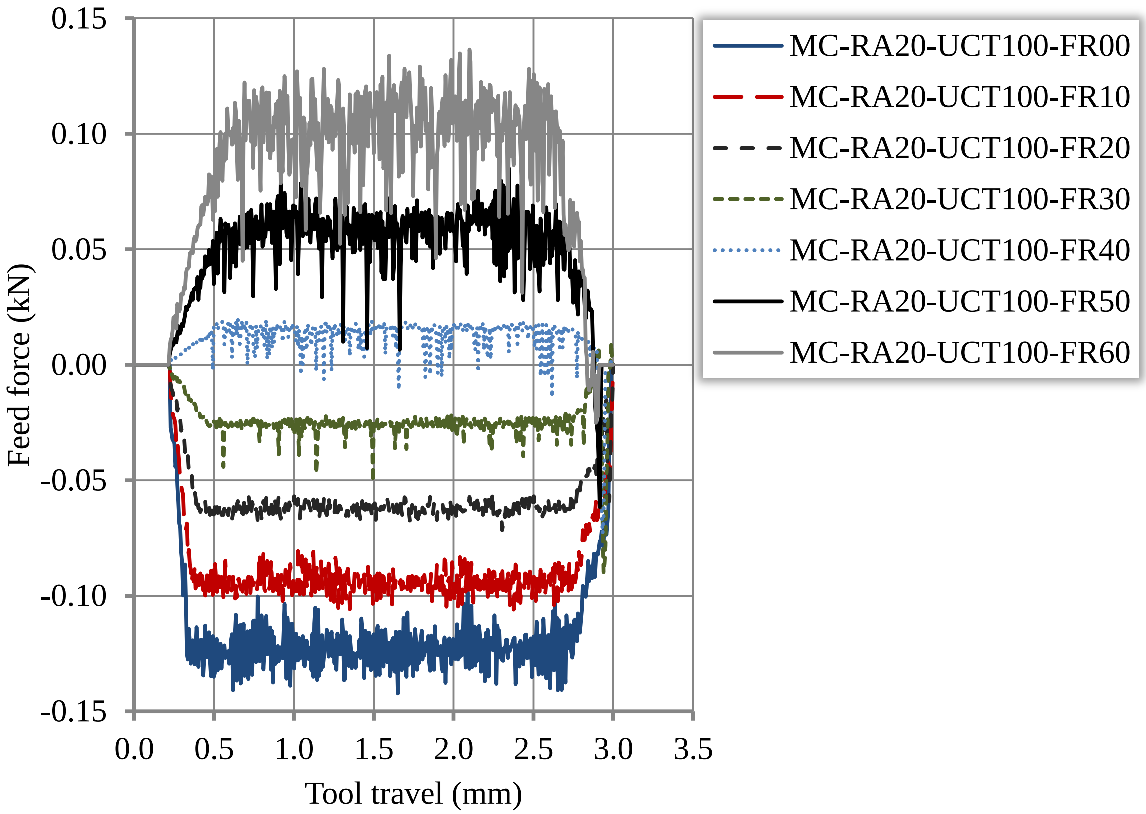

Figure 5.16: FE predictions of radial forces obtained for different friction values of the tool–chip interface

5.4 Rake Face Shape

For years, the chipbreaking is considered as a part of the process machinability, which has attracted much attension from the researchers [126]. Summarizing fifty–year efforts of improving chipbreaking, Jawahir and Van Luttervelt[126] showed that a reliable chipbreaking can be achieved with 2–D and 3D modifications of the tool rake face. Figure 5.17 shows the basic design of chipbreaking step on the rake face whereas Figure 5.18 shows the basic design of the chipbreaking groove made on the rake face. For many years, these basic chipbreaking means were studied to find their best parameters to achieve reliable chipbreaking for various groups of the work material. Although it was noticed that the tool life (and thus the process machinability) might decrease, increase or remain unchanged when a chipbreaker is applied, the studies were concentrated on the conditions to break the chip in its root while no attention was paid to the role of the state of stress in the deformation zone when a chipbreakes is used.

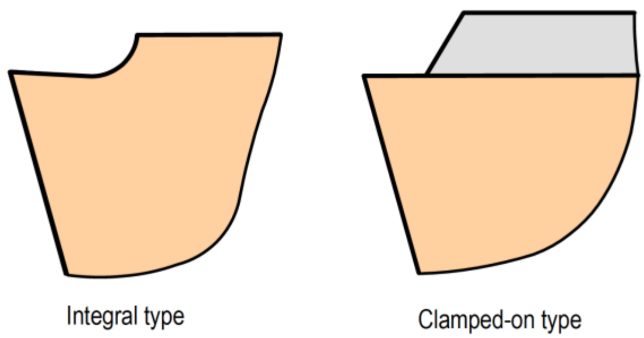

Figure 5.17: Chipbreaking steps on the tool rake face

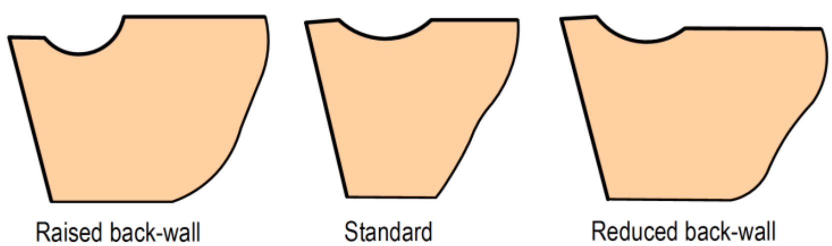

Figure 5.18: Conventional chip groove

Having noticed the change not only in chipbreaking conditions but also in tool life and the cutting force, the manufacturers of the cutting inserts designed thousands of different shapes of the tool rake face. Figure 5.19 shows some examples. Figure 5.20 shows the basic shapes of the rake face by Seco tools Co. As can be seen, these shapes are much more complicated than the basic chipbreakers shown in Figure 5.17 and Figure 5.18.

Figure 5.19: Some designs of the rake face of modern cutting inserts

Although the number of different shapes exceeds even the number of the work materials, it is still not clear what alters the performance of one shape from another. Good results with a certain shape for some cutting conditions may not be as good when one or more machining conditions are changed. It is possible that lack of understanding causes the development of such a great number of the indexable inserts covered by thousands of patents including the design patents.

In the author’s opinion, practically all major parameters of the cutting tool geometry combined with the contact properties of the tool material and parameters of the machining regime have significant yet not fully revealed influences on the state of stress in the deformation zone. As a result, the process outcomes such as the cutting force and tool life are also influenced. To confirm that this is the case and to verify this opinion, some numerical simulations on the influence of the chipbreakers and special shape of the tool rake face on the stress triaxiality were carried out.

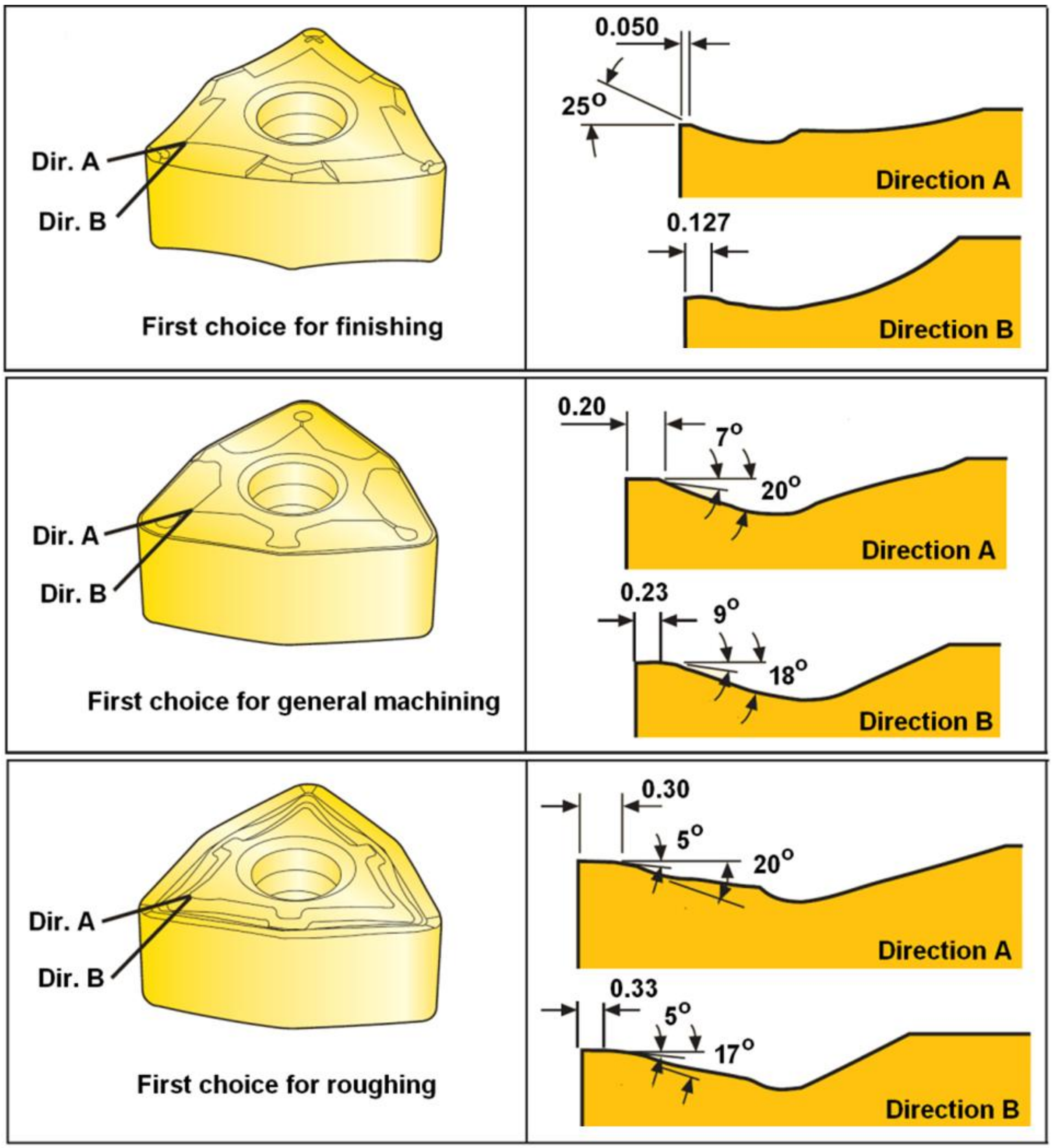

Figure 5.20: Basic rake face shapes used by Seco Tools Co.

Some simulation results are shown in Figure 5.21, Figure 5.22 and Figure 5.23 all of which used the same cutting parameters (t_1 = 0.150 mm, γ = 0º). The contours represent the stress triaxiality state with a unified scale throughout all figures. Figure 5.21 shows the conventional tool which can be thought of as the baseline for comparison. The chip structure in this particular configuration shows that shear bands (also called chip connectors) have already been developed at the deformation zone near chip root. The plastic strain in this particular region has exceeded the material strain limits and damaged elements have been formed in the deformation zone. As a result, the heavily–deformed chip has been created, which makes it easy to break. However, before final separation (fracture), the damaged material goes through a post damage evolution phase where the material strength progressively degrades (see the damage curve in Figure 2.8). However, if no sufficient farther deformation is applied, the chip may not break. In addition, the state of stress may play a vital role during this process. If the stress triaxiality state is low (high hydrostatic stress), particularly in the deformation zone and near tool tip, the material strain limit would be higher according to Figure 3.22 and the distinctive shear bands (chip connectors) may never have been created. On the other hand, a so–called healing phenomenon, the damaged and even fractured material can still regain its strength if a high pressure often combined with high chip temperature is applied. This means a higher value of stress triaxiality state is a desired outcome for shear bands creation, avoiding healing, and promoting material separation (hence chip breaks).

Figure 5.22 indicates clearly that by featuring the tool with a chip breaking step on the tool rake face, the stress triaxiality state can be significantly increased at the tool tip due to the additional bending force acting on the chip at the introduced step. Therefore, the material post damage degradation phase has been started earlier and the material has lost more strength as compared with the baseline. In addition, the effect of the material healing reduces as it directly depends on the stress triaxiality state. It can be concluded from the above discussion that this tool with the chip breaker feature would increase the chip breakability.

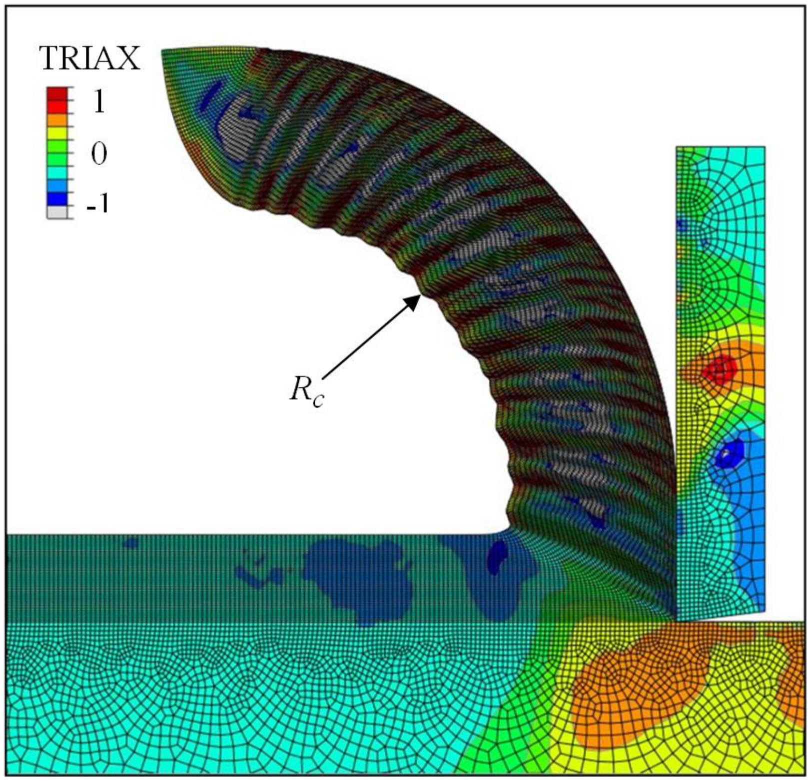

Figure 5.21: Chip shape and morphology in OMC of steel 1045 with zero rake angle

As discussed, the role of the state of stress (triaxiality state in OMC) is significant for successful chip breaking. However, for the chip to completely detach from the workpiece, a chip breaking mechanism takes place in a number of different scenarios. The obvious scenario of the chip breaking mechanism is that the heavily–deformed chip might break from the root driven by the above discussed factors (large deformation – higher stress triaxiality state – lower strain limit). The other scenario, which still depends on the same other factors, is that the chip might break at some finite distance from the chip root due to chip curl interaction with the surrounding cutting system components as observed in experiments (Figure 5.24 [126]).

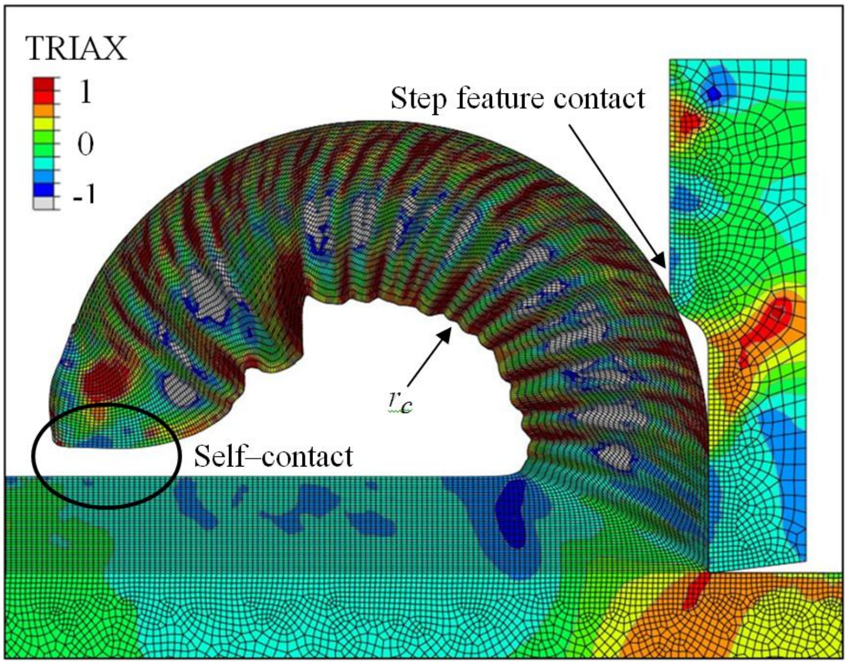

Figure 5.22: Chip shape and morphology in OMC of steel 1045 with zero rake angle when a chipbreaking step is applied on the tool rake face

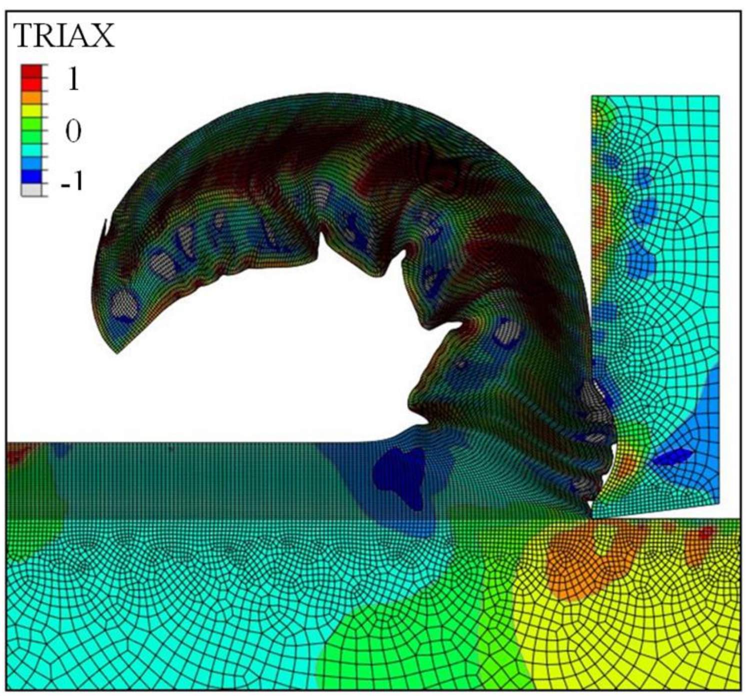

Figure 5.23: Chip shape and morphology in OMC of steel 1045 with zero rake angle when a standard chipbreaking groove is applied on the tool rake face

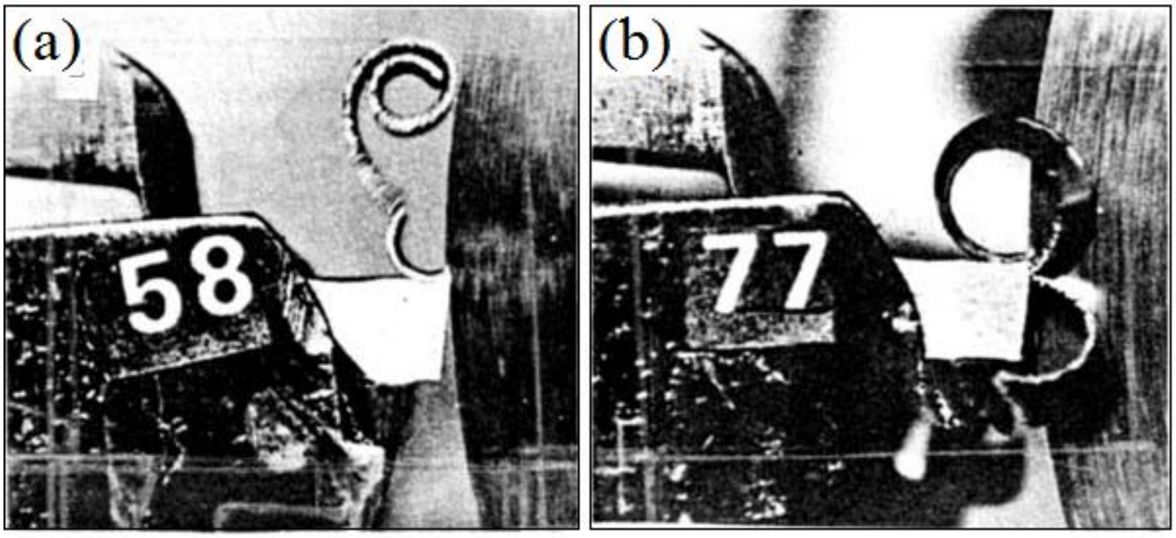

Figure 5.24: Chip breaking mechanism (a) by chip/work surface contact, (b) by chip/tool flank surface contact (three–dimensional chip breaking) [126]

As can be seen in Figure 5.24 (a), the chip interacts with the un–machined surface of the workpiece material that applies the additional bending moment so causing fracture. In some other cutting conditions where side curling exists such as in oblique cutting, non–rectilinear primary cutting motion, and varying chip thickness along its width, the chip may interact with other components such as the tool flank as shown in Figure 5.24 (b). All these cutting mechanisms can be thought of as the indirect chip breaking where the produced chip geometrical profile decides the occurrences of a particular mechanism.

The growing chip reel (Figure 5.24 (a)) consistently increases the deformation of the chip that eventually leads to its breakage. The chip fragmentation produced in this way will be much longer as compared with above direct chip breaking mechanism. How fast the chip breaks depends on two factors: the strength of the produced chip as discussed above, and the chip geometrical profile. The chip geometrical profile has two characteristics: the chip flow direction, and the curl radius. Both characteristics may significantly affect how soon a chip breaks. A smaller curl radius with a smaller angel of the chip initial flow accelerates chip breaking. In other words, the purposefully created smaller chip curl radius as well as altering the chip initial flow direction by the tool step feature ((r_c) in Figure 5.22 as compared with (R_c) in the baseline (Figure 5.21).) may cause the chip to intersect with the forehead work material sooner. As a result, the chip strain rate becomes higher as compared with a longer (larger curl radius) chip directed away from the work material and hence more tolerable to deformation (less strain rate). This self–contact mechanism clearly won't work if the cutting tool did not create a "weakened" chip with the desired high stress triaxiality at first place.

A smaller chip curl radius can be achieved by manipulating the shape of the tool rake face in many different ways. For example Figure 5.23 shows another common design to enhance chip breaking by making a groove on the rake face. As shown in the figure, the chip curl has a smaller radius as compared to the baseline similar to that produced by the above discussed tool with the step feature, therefore the chip breaking mechanism is very similar even though the underlying process is slightly different. The groove allows the material to flow in a circular path with a reduced deformation rate before it reaches the groove bottom. After that the tool rake starts pushing the chip in the cutting direction following the circular path of the groove, it causes a much higher deformation rate. As a result the chip forms the shear bands with a lower rate as compared with the above case. Although the stress triaxiality state did not increase as compared to the baseline, the chip deformation pattern had changed significantly. Such a mechanism results in much stronger and longer chip ligaments and much weaker shear bands (chip connectors) which enhances the chip breakability. Similar to the above cases, the final breaking mechanism will follow either the above discussed direct scenario with a high chip fragmentation frequency or the indirect scenario with a lower frequency and higher length of the chip fragment.

To ensure a practical chip fragments size, the above mentioned chip geometrical characteristics need to be optimized.

So far, the common chipbreaking means were analyzed. The next logical step is to understand why thousands of complicated rake face shapes (examples are shown in Figure 5.19 and Figure 5.20) are used. As an example, consider the rake shape design with a bulge or bump near the tool edge. To investigate what happens with the state of stress point of view, a simulation of the cutting system using this tool was conducted as shown in Figure 5.25. The early engagement of such a ‘bump’ with the workpiece exerts a very local deformation with much less tool–chip contact. This type of scenario improves the cutting process in a number of ways. Among them and perhaps the most important, is the triaxiality state near tool tip which is, as shown in the figure, much higher as compared with the baseline. This indicates a lower plastic deformation needed to create chip connectors, and furthermore, because the stress triaxiality state is very high near the tool tip the amount of the local deformation, which is also high, is not only enough to initiate the damage but also can create cracks a head of the tool tip. This makes the untraditional shape of the chip where the separation (crack) is developed at a finite distance from the tool tip. Such a very week chip connector is developed due to the excessive material damage combined with the cracked portion (near tool tip) that could not sustain such deformation because of the high stress triaxiality state.

The extremely deformed and partially cracked chip would be easy to break with a minimum additional deformation/load from the surrounding cutting system components. It is possible that the direct chipbreaking mechanism scenario discussed above with no additional deformation needed will take place if such ‘bump’ feature geometry was optimized.

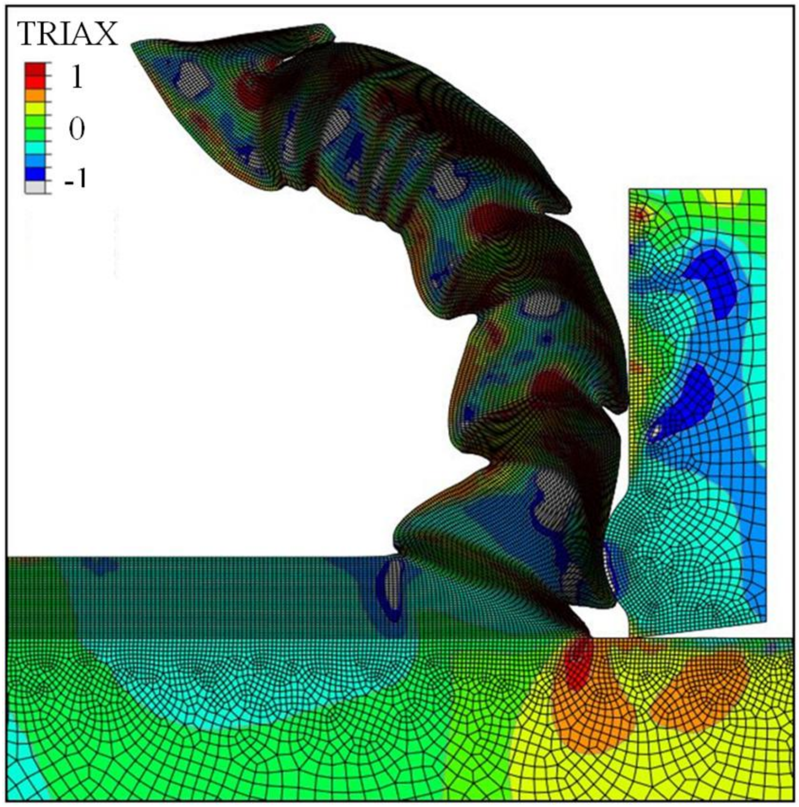

Figure 5.25: Chip shape and morphology in OMC of steel 1045 with zero rake angle and a bulge or ‘bump’ on the tool rake face

The results of this analysis shows that complicated shapes of the rake face of cutting insert can significantly alter the state of stress in the deformation zone that potentially can improve the process machinability in terms of both enhancing chip breakability and reduction of the energy of plastic deformation. Unfortunately, many of these shapes are developed with no clear understanding why it happens. It is not yet realized that practically all major parameters of the cutting tool geometry combined with the contact properties of the tool material and parameters of the machining regime have significant yet not fully revealed influence on the state of stress in the deformation zone, and thus on the process machinability. In the author’s opinion, the major problem for researchers and tool developers in the field of metal cutting and tool design is that the influence of the tool geometry parameters on the state of stress (and thus the process machinability) are intertwined, so it is impossible to study one parameter while paying a little attention to the others. Only when a realistic FEM model of metal cutting is applied and also the state of stress in the deformation zone is considered in the manner as discussed above, the finding of the evaluation of the optimality of the insert geometry for a given application can be carried out easily. As such, thousands of various shapes of the rake face of cutting inserts can be reduced to few dozen with enormous economic effect.

5.5 Conclusions

The rake angle in OMC is the most powerful mean to affect the deformation of the layer being removed in its transformation into the chip.

It is proven that the influence of the rake angle on this plastic deformation is due to the fact that this angle directly affects the state of stress in the deformation zone. The higher the rake angle, the smaller deformation of the layer being removed in OMC.

Although the use of high rake angles improves tool performance in terms of reducing the cutting force and energy spent in cutting, two new problems, namely the chip length and possible reduced tool life may arise.

The problem with chip length and its breakability may be solved by increasing the uncut chip thickness. When this solution is applied, not only the chip breakability improves, but also the machining efficiency increases. This is because the uncut chip thickness is directly correlated with the cutting feed, and thus with the tool penetration rate that determines the machining process efficiency. As such, the unit energy spent on the plastic deformation of the layer being removed decreases.

The reduction of direction over the tool–chip interface is an important method in the reduction of the energy spent in cutting and improving tool life. The results obtained reveal the influence of the friction on this interface on the machining process.

The major problem for researchers and tool developers in the field of metal cutting and tool design is that the influence of the tool geometry parameters on the state of stress (and thus the process machinability) is intertwined so it is impossible to study one parameter at a time. Only when a realistic FEM model of metal cutting is applied and the state of stress in the deformation zone is taken into consideration as in the manner discussed in Chapter 2, the finding of the evaluation of the optimality of the insert geometry for a given application can be carried out easily. The number of shapes of the rake face of the indexable inserts can be greatly reduced and the optimal shape for a given cutting conditions can be determined by FEM modeling.

The effect of a tool rake face design with a typical step and standard groove features study confirms the effectiveness of such features on increasing the chip breakability. Such tool shapes are designed purposely to reduce the length of the chip fragments to improve chip control and allow proper handling of the produced chip in an industrial facility. The chip breakability analysis of the tools with chip breaking features shows a strong dependency on the state of stress and the produced chip geometrical characteristics. While the state of stress controls the strength the produced chip, the curl radius and its flow direction characteristics affect chip strain rate thus the frequency of the produced chip fragments.

Chapter 6: Conclusions, Contributions, and Future Work

6.1 Concluding Remarks

A new model of orthogonal metal cutting (OMC) was developed to overcome the uncertainty associated with the long standing predictability issue. The framework of the current development is based on the recent developments in the field of damage and fracture mechanics of ductile metals and a new definition of the cutting process.

Metal cutting is a complex process where the workpiece material undergoes large deformation, exceeds the material plasticity limits and develops damage and fracture. A complete material constitutive law which describes all phases involved in the deformation and material separation, particularly damage initiation and evolution, is found to be of great importance in metal cutting simulations. With the focus on the role of fracture in modeling OMC, a new approach of material modeling was developed for loading conditions similar to that found in OMC. Authentication of FE simulations were carried out using the validation experiments.

Simulations of metal cutting in general are highly sensitive to the choice of the material fracture model. The proposed progressive damage approach was found to be suitable when all loading conditions of the cutting process are considered. The state of stress triaxiality in the primary deformation zone in OMC controls the material plastic strain limit. The range of the stress triaxiality state in this zone was found to be broad so that cannot be covered by the simple shear test results and/or the traditional flat–grooved specimen under a uniaxial tensile load. Therefore, a reconsideration of the test specimen design is needed to avoid the extrapolation on estimating the fracture strains at low and negative triaxiality.

To address the issue, a new, double–notched specimen was developed to obtain the work material stress–strain relationship under the entire range of stress triaxiality found in OMC. It allowed investigating the material ductility variation with the state of stress in plane strain condition. The numerical evaluation shows that the developed specimen can be tuned to yield the desired stress states at the low and negative triaxiality regions found in OMC that cannot be covered by the classical/standard flat grooved specimens. The suitability of this approach was confirmed by the stress triaxiality chart in the primary deformation zone obtained by simulations of OMC.

In order to find the material flow/fracture parameters, the equivalent plastic strains at the specimen gauge were calculated from the DIC measurements. As expected, the equivalent plastic strain $\bar{\varepsilon}_f$ values at damage initiation were found to be proportional to the gauge orientation termed as the "pressure angle", and hence to the triaxiality state. Because of non–uniform deformation, direct calibration approaches were not sufficient to obtain all material parameters. Instead, a numerical optimization based inverse method was used and a forward sequential strategy for the identification of material plasticity was developed. The Rice and the reduced form of the JC damage models were used as mathematical models for the fracture loci of the steel AISI 1045. The JC damage model with two damage parameters was found to be better suited to describe the plane strain experimental results. The performance of the new material model developed using this approach was verified by FEA. The specimens used in the experiment were numerically evaluated for predictability of test loads, damage initiation, and degradation.

Validation of FE simulations for metal cutting was carried out following the suggestion by Astakhov [127]. The simulations based on the new developed material model were subjected to a systematic authentication using the chip shape and deformation (the chip compassion ration – CCR) similarities. The predicted cutting forces were within 8%, the obtained chip morphology was realistically similar to the actual test, and the predicted CCRs were within 7%.

The verified model was used to investigate the influence of the stress triaxiality state on the cutting process energy. Stress triaxiality significantly affects the fracture strain as found by the material characterization experiment, and thus the energy required for plastic deformation of the layer being removed. This is because the energy associated with this deformation constitutes up to 70% of the total energy required by the cutting system for its existence [76]. This plastic deformation is a nuisance of metal cutting so that the associated energy is a total waste [1]. Because this energy accounts for up to 75% of the total energy required by the cutting system the reduction of this energy by adjusting stress triaxiality is the most effective means in increasing efficiency of the cutting process. The simplest yet a powerful mean to adjust stress triaxiality in the deformation zone are the parameters of the tool geometry and/or process. For example, the tool rake angle, tool coating and MWF, and uncut chip thickness are some of these parameters which have significant impact on the efficiency of a particular cutting regime. The conducted analysis of the tool rake angle variation in OMC shows that by changing the angle from 0º to 40º, a significant energy reduction of 59% can be achieved. The energy increase due to elevated friction is also considerably high and ranging between 7.2% and 8.3% for every 10% friction increment. Although the cutting forces increase proportionally and substantially with the uncut chip thickness (t_1), the specific energy saving (energy per unit volume of material removal) compared to the other investigated cases is small. However, the analysis indicates an improved cutting efficiency when cutting with a large material removal rate. In all of these mentioned cases, the field of stress triaxiality state parameter was proportional to the amount of energy saving, which explains what causes such performance variations.

6.2 Contributions to Science and Technology of Metal Cutting

The current thesis introduces a novel model of materials behavior in machining and considers the aspect of the metal cutting theory and practice. In other words, the finding of the thesis should be able to explain major known phenomena in metal cutting and, what is more important, to provide fundamental of the metal cutting process prediction. The thesis includes a number of novel notions, methodologies, and results with real values of which should be properly evaluated. The value of the proposed concepts, their verification results, and other results obtained in the course of the present work can be evaluated by their contributing to the science and technology of metal cutting.

6.2.1 Damage and Fracture in Metal Cutting

Any known metal cutting theory has in its very basis the model of the work material behavior in machining so that various theories differ only by such a model [1, 3, 4, 5]. Novelty of the proposed model compared to those used currently in metal cutting is accounting for material damage and fracture. The core of this work is based on the new definition of the cutting process according to which the external energy supplied to the cutting system causes the purposeful fracture of the layer being removed [12, 128]. Therefore material damage and fracture must be a part of the material constitutive law to account for the degradation of the material stiffness and separation of the layer being removed. However, fracture mechanics of ductile metals by itself is an evolving, active research and recent advancements made provide a better understanding of the large plastic deformation and fracture phenomena that opened new opportunities for realistic metal cutting modeling. The applicability of such advancements in metal cutting was limited because unique loading conditions involved. The experimental setups which were developed to calibrate the new fracture models were useful only for the branches where its conditions are similar to those experiments. For example the flat–grooved testpiece developed by Bai et al. [87] to obtain the fracture model parameters is only applicable for high triaxiality state and cannot be used for metal cutting where the triaxiality are in the low including negative regions.

Modeling chip formation in machining without a proper material model that includes damage and fracture results in unrealistic material behavior where the material flow unlimitedly with no material stiffness degradation and separation. The chip structure obtained by such incomplete models produces an unrealistic smooth chip with unlimited material stretching and hardening as shown in Figure 6.1 (a). On the contrary, the actual chip structure is expected to contain shear bands (chip connectors) in the manner shown in Figure 6.1 (b). These shear bands were formed due to the fact that the material has exceeded its maximum strain limit under its local loading conditions and the active damage and fracture model causes local degradation. The damage and fracture phase is in the core of the chip formation process and cannot be ignored, not only because it controls the chip structure pattern, but also because it affects all other cutting attributes such as cutting forces, process energies, tool life estimations, CCR, etc.

The testpiece discussed in Chapter 3 (Figure 6.2) was developed to determine the parameters of the damage and fracture material model applicable for the loading conditions of OMC. The main objective of the development of this specimen is to cover the low and negative triaxiality ranges that particular for the loading conditions found in the deformation zone in OMC. Such low triaxiality state condition exists in metal cutting due to the compressive nature of the stress that is caused by the tool face and workpiece interaction. Furthermore, the testpiece was designed to match the desired deviatoric state of stress where plane strain conditions apply. Although the intention of this development is to be implemented in machining modeling in general and OMC in particular, the proposed methodology applies the state of the art of ductile fracture mechanics theory and obviously its applicability can be extended to other applications were similar loading conditions exist.

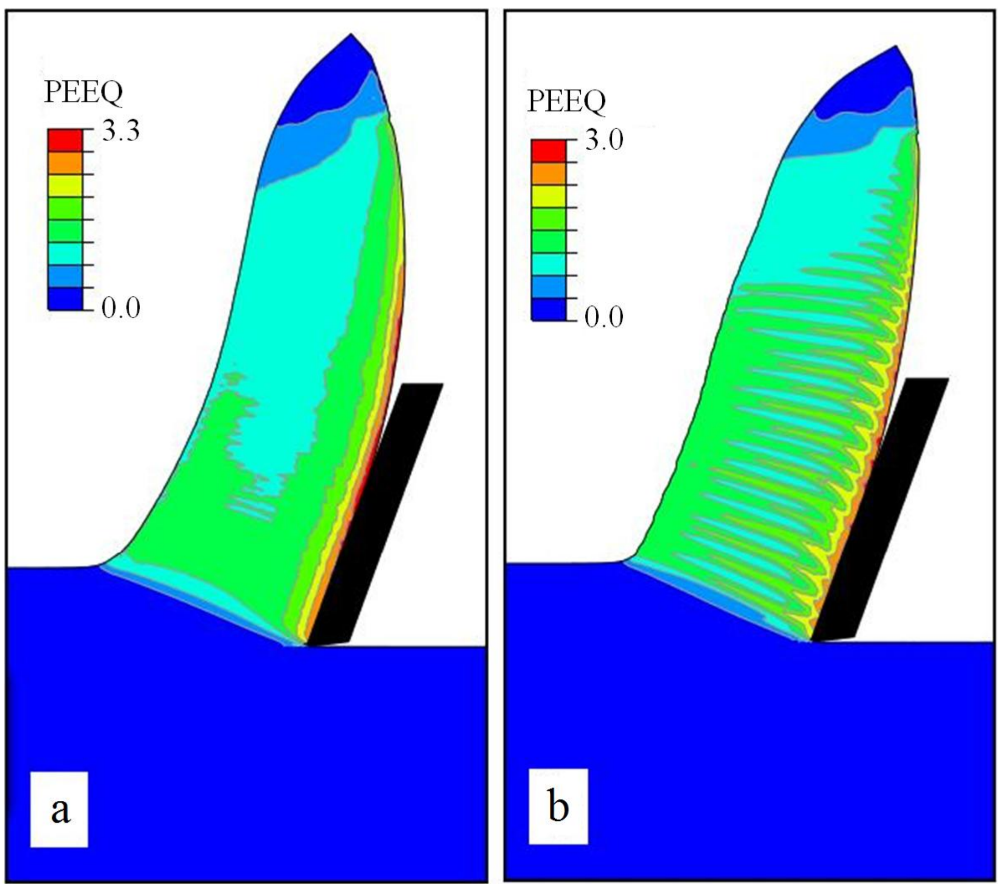

Figure 6.1: FE model of chip formation showing equivalent plastic strain fringes (MC–RA20–UCT150, MAT STEEL AISI1045) (a) deformation only material model (b) material modeled with active damage and fracture

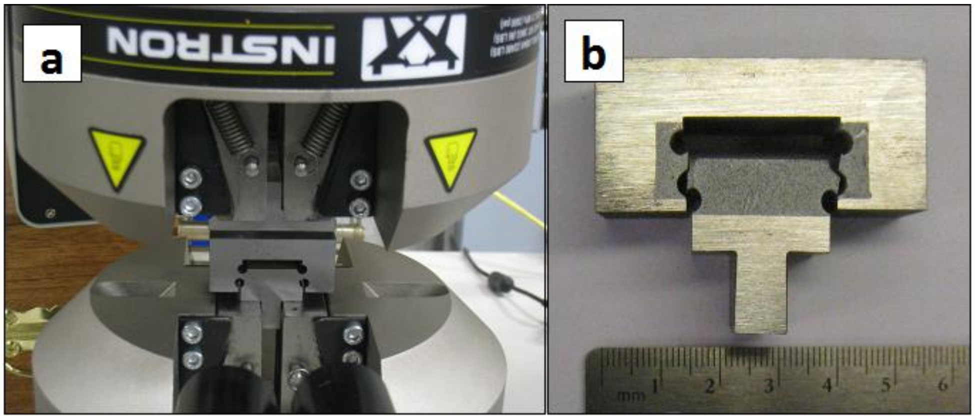

Figure 6.2: The double–notched testpiece (a) testpiece installation image (b) testpiece after fracture

It was shown (Figure 3.8) that by using this design, the triaxiality state can be controlled by changing the specimen geometrical configurations. In the design of the testpiece, the pressure angle – that is, the angle of the plane passing through the two centerlines of the circular holes (Figure 3.7) with the horizontal plane – controls the state of triaxiality in the specimen gauge. By running the test for multiple configurations with different pressure angles and using a proper strain measurement tools such as DIC (Figure 3.10) to record the strain limit for each case, the overall trend of the material fracture locus can be revealed. Furthermore, the double–notched testpiece can be used to extract the fracture energy density of the material which is a critical piece of information used to estimate the post damage and material degradation.

6.2.2 Deformation Law of Metal Cutting

The deformation law of metal cutting was formulated by Astakhov [1]. Studying energy partition in metal cutting, he found that the energy of the plastic deformation of the layer being removed in its transformation into the chip is the greatest in machining of ductile materials, e.g. steels [76]. The greater the energy of plastic deformation, the lower the tool life, quality of the machined surface, and process efficiency. Therefore, the prime objective of the cutting process design is to reduce this energy to its possible minimum by the proper selection of the tool geometry, tool material, machining regime, MWF and other design and process parameters. To accomplish this clear objective, i.e. to make the introduced law of practical significance, a reliable measure of this energy should be readily available to be used at various levels, from a research laboratory to the shop floor. A simple physics–based methodology to estimate the energy of plastic deformation in metal cutting is introduced in Appendix B. The current study uses this definition of the objective function in the context of the proposed fracture approach to explain some of the known phenomena in metal cutting.

6.2.3 Testing Methodology for Metal Cutting Model Validation

Although metal cutting testing has been conducted for more than 150 years to investigate various cutting parameters such as tool life, cutting forces, machined surface integrity, and energy consumption, there is still a lack on the methodology and data evaluation in metal cutting tests and very little common testing approaches can be found in the literature. As a result, metal cutting experiments are generally very costly and time consuming and require sophisticated equipment and trained personnel. Nevertheless, experiments are still the main drive of metal cutting technology and advances [2].

Even in its most uncomplicated form, testing a particular cutting setup usually involves many design and process parameters which may affect the outcomes of a desired variable. Test stage preparation and proper design of experiments (DOEs) can minimize the impact of such complexity and often lead to much more reliable results.

Figure 6.3 shows the experimental setup used to verify the FE metal cutting model which was developed using the new material characterization approach. To avoid the undesired effects of the other process variables, the experiment was intended to run in a universal material testing machine with hydraulic power drive. Such a choice minimizes customization of the test site to accommodate external sensing and mounting fixtures. Accessories such as dynamometers, cell loads, accelerometers, etc., may lead to inaccuracy due to special calibration handling, sensing issues, hardware/software compatibility issues, data acquisition and signal noise, etc.

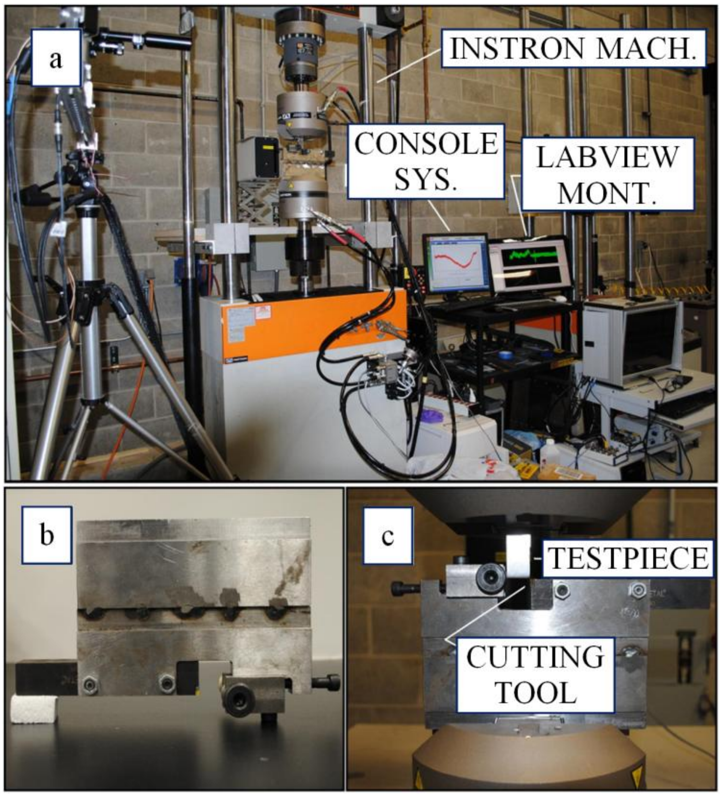

Figure 6.3: Metal cutting model validation experiment (a) experiment setup (b) tool holder fixture (c) tool holder fixture installation

It is well known in metal cutting that some of the test outcomes can vary even for the same test setup/iteration. For example, the cutting forces may vary significantly (up to 50%) due to system compliance which causes the feed to change and, as a consequence, the load cell reading changes. Chip deformation phase may also cause such fluctuation. Serrated chip formation is caused by the formation of the shear bands and as a result a sinusoidal cutting force can be observed. Regardless to the cause of such behaviour, the test setup must record the event and most importantly when this event happened. By utilizing universal testing equipment features the test ensures a standard hardware usage that has been calibrated and certified according to the manufacturer documentation. The built–in machine extensometer and load cell provide both precision and synchronization which are critically important in metal cutting in general and particularly for validation experiments.

The results obtained from this experiment shown in Figure 4.8 and Figure 4.9 signify this critical observation. For a proper validation, the FE simulations must be conducted under the same condition at the same point of time as the validation experiment. In other words, each test frame (in time space) represents a unique configuration and the FEA must be conducted according to this particular state.

6.3 Recommendations and Future Work

There are three principal pillars of realistic metal cutting modeling. They are a proper model of the work material behavior (resistance) in cutting (currently known as the chip formation model), a model that governs the contact process at the tool–chip interface, and a model of physical resource of the cutting wedge. In our opinion, future modeling of metal cutting should be directed in the development of these models which constitutes the model of metal cutting.

The current study dealt with the development of the work material behavior model based on a new definition of metal cutting as purposeful fracture of the work material. It accounts for large plastic deformation of this material, its degradation and fracture in the cutting process. However, the model and the test procedure including a special testpiece used in the test to obtain parameters of the developed model, is developed for the simplest condition, known as orthogonal metal cutting (see Figure 2.5 (a)). As such, the tool rake angle was studied as a mean to affect the state of stress in the deformation zone, and thus change the amount of plastic deformation of the work material to fracture. This was done to prove the applicability of the principle of minimum energy in metal cutting and to develop the methodological steps in the "construction" of the work material model behavior in metal cutting that accounts for its plastic deformation of this material, its degradation and its fracture. A number of 'hurdles' in the conversion/interpretation of the actual work material behavior in tests under triaxial state of stress into computational model to be used in FEM analysis were revealed and methods of their removal are proposed.

Using the experience gained in the development of the model of work material model behavior in OMC, the next logical step would be the development of such a model for oblique cutting (Figure 2.5 (b)). In oblique cutting, the cutting tool inclination angle, λ_s is another powerful mean to affect the triaxiality in the deformation zone. As can be seen in Figure 2.5 (b), the deformation of the layer being removed in its transformation into the chip is no more plain strain. Therefore, to determine the parameters of the material model in this case, a new design of the testpiece should be developed which may require 3–D digital image correlation (DIC) equipment to be used.

The proposed validation experiment, besides to other benefits, allows the cutting forces to be synchronized with the chip formation using standard testing equipment. The chip morphology obtained from this experiment was found to be similar to that obtained from conventional lathe under high cutting speed conditions (ex. Figure 6.4). Although observations drawn based on this experiment indicate that the effect of the strain rate may be overestimated in the literature, other cutting attributes such as the chip–tool interface may have been altered, which changed the process outcomes such as the cutting forces and/or chip pattern for a particular cutting setup.

In this regard, material as well as metal cutting testing at high strain rates is recommended to verify the material strain rate sensitivity parameter and metal cutting model at high cutting speeds.

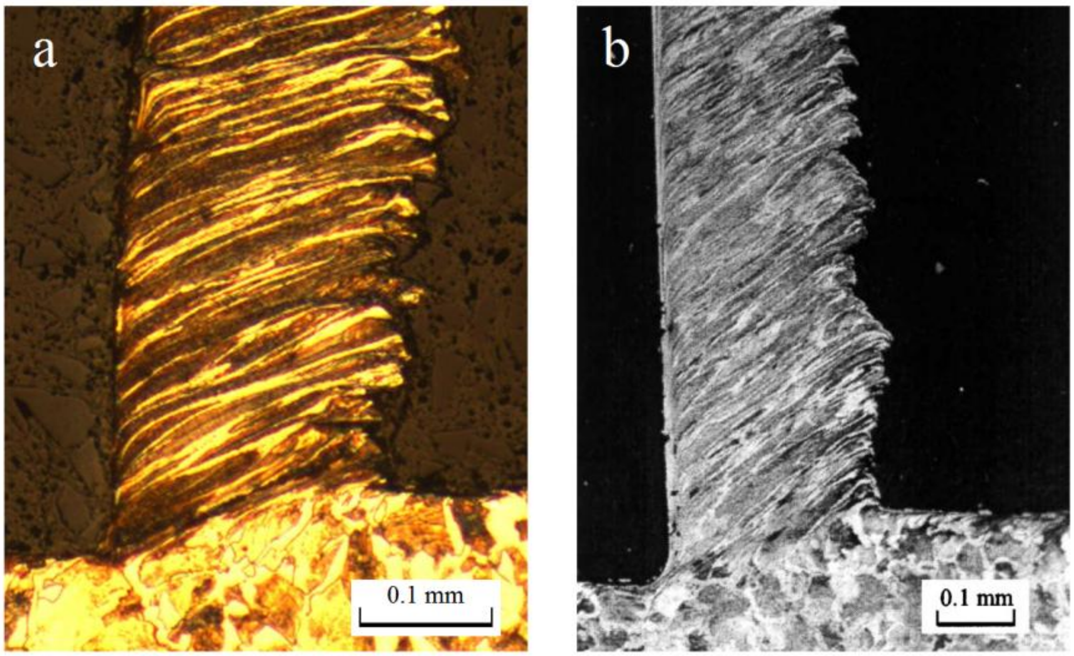

Figure 6.4: Optical microscope images of experimentally–obtained chips from steel AISI 1045. (a) t_1*=0.048 mm*, v_1*=0.001 m/min*, obtained by current experiment at low cutting speed. (b) t_1*=0.1 mm*, v_1*=120 m/min*, obtained by Jaspers and Dautzenberg using quick–stop device [92]

All of the simulations were performed assuming a sharp cutting edge of the tool. However in practice no such sharp edge exists, as even a brand new tool has a small tip radius which may increase the cutting and radial forces, alter plastic deformation, and change the chip deformation pattern particularly in small cutting feeds. To include this tool feature in the analysis, other FE modeling techniques may be used to avoid computational instability due to excessive element distortions caused by tool features such as tool tip radius. Mesh controls and adaptive meshing algorithms may overcome these difficulties. Additionally, other finite element techniques such as

Arbitrary Lagrangian–Eulerian (ALE) formulation combined with the proposed physical model may be worth investigations.

Among these computational difficulties is handling the chip separation, element deletion is the most common approach used to simulate crack propagation and material separation. However, in metal cutting other methods may improve the prediction of such cracks taking into consideration the compressive stress nature in the primary deformation zone, possibly causing the creation of unrealistic voids due to the deletion of elements, which can lead to collapse and cause analysis failure.

A number of case studies were conducted and analyzed with respect to the stress triaxiality state parameter. The purpose of these investigations was to show the relationship between the fracture parameter (η) and the plastic energy required for cutting a particular case in order to provide reasoning for the unexplained practical examples. Further investigations to quantify the metal cutting efficiency are recommended. In addition, the developed approach can be used for process optimization studies using the objective function as defined in the deformation law of metal cutting.

APPENDICES

Appendix A: Analysis of the Prevailing Model of the Materials Behavior in Metal Cutting

A.1 Introduction

Although it is pointed out in almost any book on metal cutting that the temperature, and particularly, its distribution has a great influence in machining [129], no one study actually quantifies this influence. Instead, it is stated in very general and qualitative terms that temperatures in metal cutting affect “the shear properties” of the work material and, therefore, they affect the chip–forming process itself, and through their effect on the tool, they determine the limits of the process and mode of tool wear. To address each of these points, a great number of works on temperatures in metal cutting have been published. Apart from many contradictive results that can be readily found in the published works and can be logically explained by the difference in the experimental methodologies and accuracy of calibration, numerical and analytical models and the assumptions adopted in both the models, a major concern with these works is their practical significance. In other words, there is no answer to a simple question: “What should one do with the obtained temperature and its distribution?” The same question arises in any FEM of metal cutting as a common result of such a modelling is colourful temperature field in the tool, workpiece and chip. A question: “Is the obtained result good or not?” cannot be answered because there is no gage to judge ‘goodness’ or ‘optimality’ of the obtained temperature results.

This study was carried out to assess the influence of the thermal energy (and the temperature of the work material on the work material behavior in metal cutting [130].

A.2 Short Literature Review

Trent and Wright concluded [33] that the major objective of heat consideration in metal cutting is to explain the role of heat in limiting the rate of metal removal when cutting the higher melting point metals. They concluded that there is no direct relationship between cutting forces or power consumptions and the temperature near the cutting edge.

Zorev [28] did not consider temperature as an important factor itself. Considering the energy balance in metal cutting, he calculated that the maximum temperature at the end of the chip formation zone does not exceed 270 ^{o}C for plain and alloyed steels while a considerable reduction in the mechanical properties of these materials starts only at temperatures over 300 ^{o}C. Therefore, he concluded that metal cutting is a cold–working process where temperature does not affect mechanical properties of the work material in the defamation zone although the chip leaving the cutting tool can be of cherry–red color

According to Childs et al.[32], the two goals of temperature measurements in machining are: (a) the quantitative measurements of the temperature distribution over the cutting region are more ambitious, but very difficult to achieve, and (b) is less ambitious to measure the average temperature at the tool–chip contact. The less ambitious goal makes sense if one know how to measure this average temperature and, that is more important, how to use the obtained result.

To understand the formation of the temperature fields in the tool, workpiece and the chip, the energy balance (in modern terminology – energy partition) in metal cutting has been considered in the published works. As the conservation law states, almost all the energy required by the cutting system for its existence (referred in the literature as the energy supplied to the cutting system) converts into the thermal energy or simply heat. The portions of the energy stored in the deformed chip and in the cold–worked machined surface hardly exceed 2–3% of the total energy. Therefore, the power that converts into heat in the cutting system can be calculated rather accurately as $F_c v$, where F_c is the power components of the cutting force and v is the cutting speed.

The next issue is the distribution (partition) of this power (converted in the form of heat) in the cutting system. The heat distribution in the cutting system is originated from study by Schmidt and Roubik [131], who, according to Komanduri [132], carried out calorimetric study in cutting and their measurements, thus obtained, permit computation of the work, the power, forces, the average temperature of the chip, etc. They also showed a good agreement between the calorimetric measurements and the power data obtained from torque and thrust measurements.

An example of Schmidt and Roubik results [133] is shown in Figure A.1. This example and its derivatives have been using in the literature since then (for example,[69, 134, 69]) up to modern books on the subject (for example,[135, 136]). In some modern books, however, this distribution simplified up to that shown in Figure A.2[137], i.e. became of more qualitative than quantitative nature. Our critical analysis of the published data on heat partition in the cutting system revealed an obvious drawback. The partition of heat is always shown as a function of the cutting speed. In other words, the cutting feed, thermal properties of the work and tool materials, influence of MWF and many other ‘thermal’ particularities of a given machining operation are not accounted for. For example, it is obvious that if a tool material of high thermo–conductivity, for example polycrystalline diamond (known as PCD in industry), is used than more heat flows into the tool compare to the case when a tool material of extremely low thermo–conductivity, for example ceramics, is used. Therefore, it may be stated that the heat partition in metal cutting is application specific and the ratio of the heat that go into each components is not fixed as shown in Figure A.2 but varies depending upon particularities of a given machining operation.

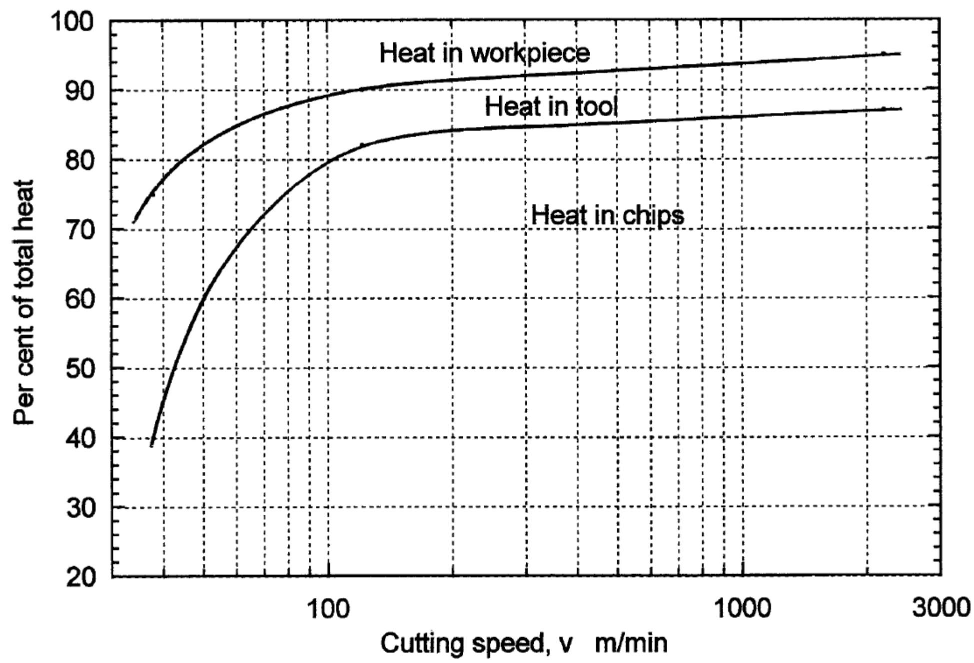

Figure A.1: Typical distribution of heat in the workpiece, the tool, and the chips with cutting speed; after Schmidt and Roubik [133]

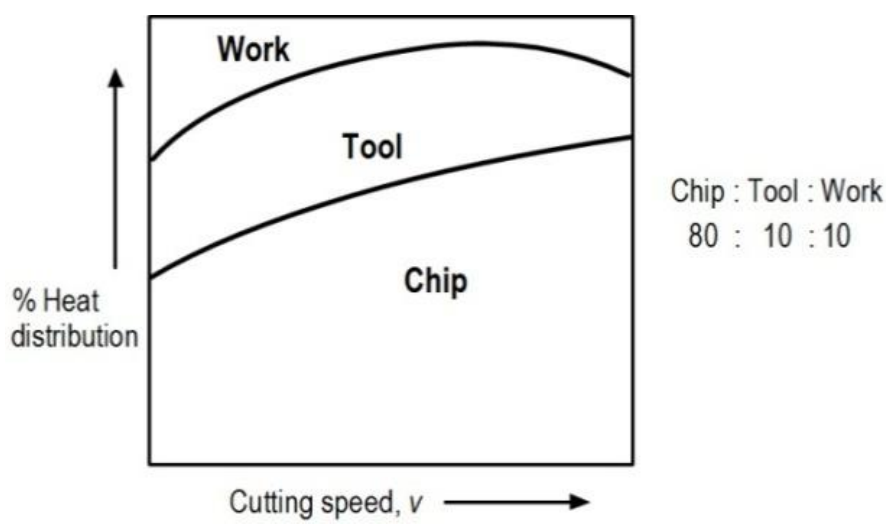

Figure A.2: Heat distribution between the chip, workpiece and tool [135]

A.3 Heat Balance and Temperature Distribution in the Deformation Zone – Apparent Contradiction with the Second Law of Thermodynamics

The common analysis of heat distribution and temperatures in the cutting system is based on the analysis of heat sources. Because practically all of the mechanical energy associated with chip formation ends up as thermal energy [12, 5, 28], the heat balance equation is of prime concern in metal cutting studies. This equation can be written as [12]

$$F_c v = Q_\Sigma = Q_c + Q_w + Q_t \tag{A.1}$$

where Q_Σ is the total thermal energy (heat) generated in the cutting process, Q_c is the thermal energy transported by the chip, Q_w is the thermal energy conducted into the workpiece, and Q_t is the thermal energy conducted into the tool. As shown in Figure A.1 and Figure A.2, under 'normal' cutting conditions, most of the thermal energy generated in the cutting process is conducted into the chip [12, 5, 28].

Example of energy balance shown in Table A.1[138] reveals two essential features:

- Most of the thermal energy generated in the cutting process is carried away by the moving chip (80–85%).
- The higher the cutting speed, the greater portion of the total heat is carried away by the chip.

These facts, however, are not followed by the traditional model of metal cutting. Figure A.3[138] is a heat generation model commonly used in metal cutting modeling. It illustrates the heat sources on each component of the cutting system, namely, on the tool, workpiece and chip. In this figure, t_1 is the uncut chip thickness, φ is the shear angle, AB is the length of the shear plane, AC is the tool–chip contact length, l_c, AM is the length of the plastic part, l_p of the tool–chip contact length, l_c, AD is the tool–workpiece contact length, Δ.

Table A.1: Energy balance in machining (steel 1045)

$v(m/s)$	Q_c (J/s)	Q_c/Q_Σ $(\%)$	Q_w (J/s)	Q_w/Q_Σ $(\%)$	Q_t $(\%)$	Q_t/Q_Σ $(\%)$	Q_Σ $(\%)$
0.10	47.9	50.2	38.4	40.2	9.2	9.6	95.5
0.20	93.7	55.7	63.7	37.8	11.0	66.6	168.4
0.5	272.3	70.3	100.3	25.9	14.7	3.8	287.3
1.00	501.6	76.2	136.9	20.8	19.7	3.0	658.3
2.00	1177.1	82.8	217.5	15.3	27.0	1.0	1421.6
4.00	2306.2	86.3	336.7	12.6	29.4	1.1	2572.3

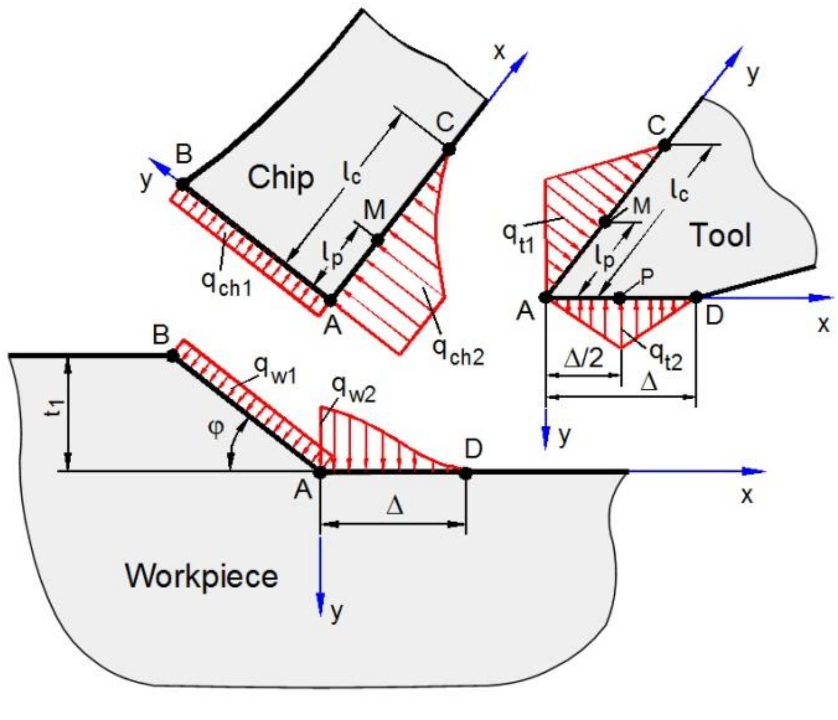

Figure A.3: Areas of heat generation on the tool, workpiece and chip [138]

The thermal energy in the cutting system is generated:

1. Due to plastic deformation of the work material on the shear plane, Q_{pd}. This energy partitions into portion that goes to the workpiece $Q_{pd-w} = \int_A^B q_{w1}(y)\cos\varphi dy$ and that goes to the chip $Q_{pd-ch} = \int_A^B q_{ch1}(y)dy$.

2. Due to friction on the tool–chip interface, Q_{Rr}. Its portion $Q_{fR-ch} = \int_A^C q_{ch2}(x)dx$ goes to the chip and $Q_{fR-t} = \int_A^C q_{t1}(y)dy$ goes to the tool.
3. Due to friction on the tool–workpiece interface, Q_{fF}. It portion $Q_{fF-t} = \int_A^D q_{t2}(x)dx$ goes to the tool and that $Q_{fF-w} = \int_A^D q_{w2}(x)dx$ goes to the workpiece.

The next question is about the intensity of the heat sources. As discussed in the literature (for example [5, 135, 2]), the greatest portion of the energy spent in the cutting system is due to plastic deformation of the work material. Figure A.4 shows an example [76]. In this figure P_{pd} is the energy spent on the plastic deformation of the layer being removed, P_{fR} is the energy spent due to friction at the tool–chip interface, P_{fF} is the energy spent due to friction at the tool–workpiece interface, P_{ch} is the cohesive energy spend on the formation of new surfaces (which can be thought of as spend on the shear plane). As follows, the energy spent on the shear plane is P_{fR} + P_{ch} = 73%. Therefore, 73% of the total thermal energy generated in cutting is due to plastic deformation of the work material.

As mentioned above, this total energy due to plastic deformation (P_{fR} + P_{ch}) is then partitions between the workpiece (portion Q_{pd-w}) and the chip (Q_{pd-ch}). Such a partition, however, does not apparently obey the second law of thermodynamics. The problem can be explained as follows.

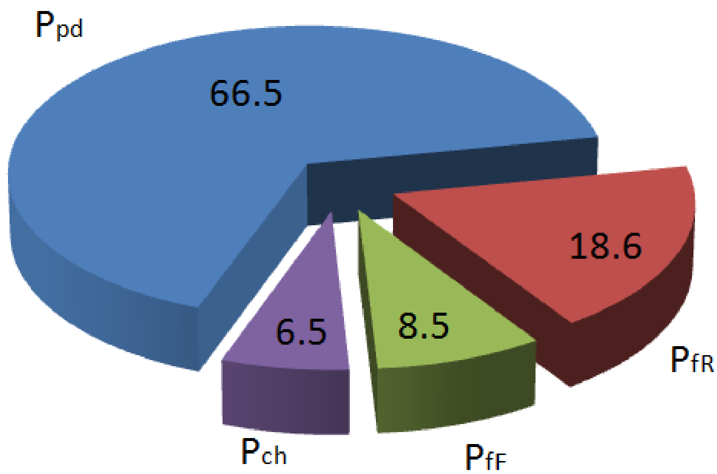

Figure A.4: Energies spent in the cutting system. Work material: AISI steel E52100, cutting speed v = 1 m/s, depth of cut d_w = 3 mm, cutting feed f = 0.4 mm/rev; Tool – standard inserts SNMG 432–MF2 TP2500 Materials Group 4 (SECO) installed into a tool holder 453–120141 R1–1 (Sandvik) [31]

Figure A.5 and Figure A.6 shows the results of actual temperature measurements in the cutting system obtained by Shaw [69] and Astakhov [2]. Similar results were obtained by many specialists, for example by Smart and Trent [139], who actually measured rather than to model the temperature distribution using FEM with unjustifiable input parameters. The comparison of these results with the data shown in Figure A.1, Figure A.2, and Table A.1 with the common heat generation model in Figure A.3 reveals a contradiction with the second law of thermodynamics. This law stated that the heat flows naturally from a region of higher temperature to one of lower temperature. Therefore, according to the second law of thermodynamics, portion Q_{pd-w} should be much higher than Q_{pd-ch}. Experimental results on heat partition, however, shows otherwise, i.e. a way greater part of the total heat flows into the small, hot chip than that to the large, cold workpiece. This contradiction cannot be resolved in principle using the existing notions in metal cutting due to the fact that the traditional model shown in Figure A.3 is incorrect [34].

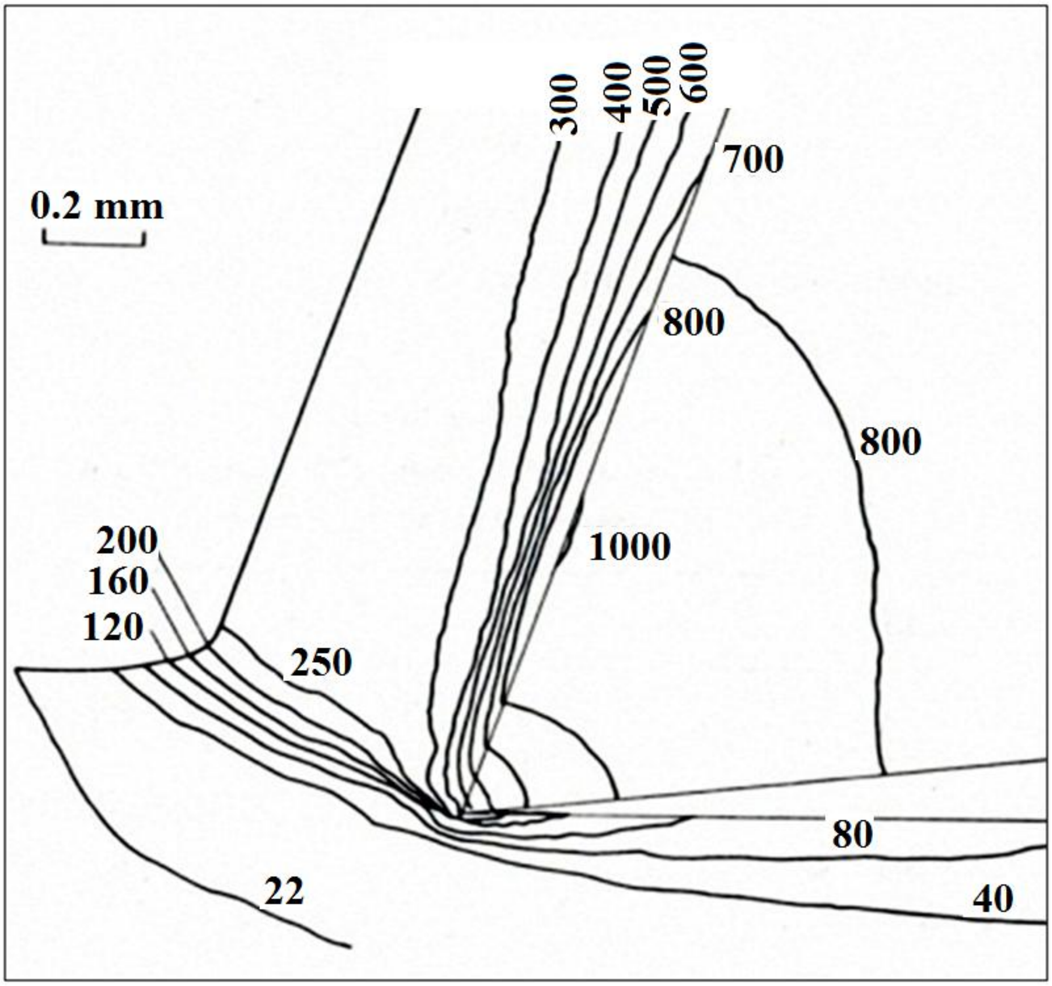

Figure A.5: Typical temperature field in metal cutting: Isotherms for dry orthogonal cutting of free machined steel with a carbide tool at cutting speed of 155 m/min and cutting feed of 0.274 mm/rev [69]

A.4 Experimental Study of Heat Partition

The objective of this study is to resolve the above–mentioned contradiction in heat partition in metal cutting. In other words, both sides of this contradiction, namely, the heat partition and the model shown in Figure A.3 are analyzed in order to understand which one of these two is the source of the contradiction.

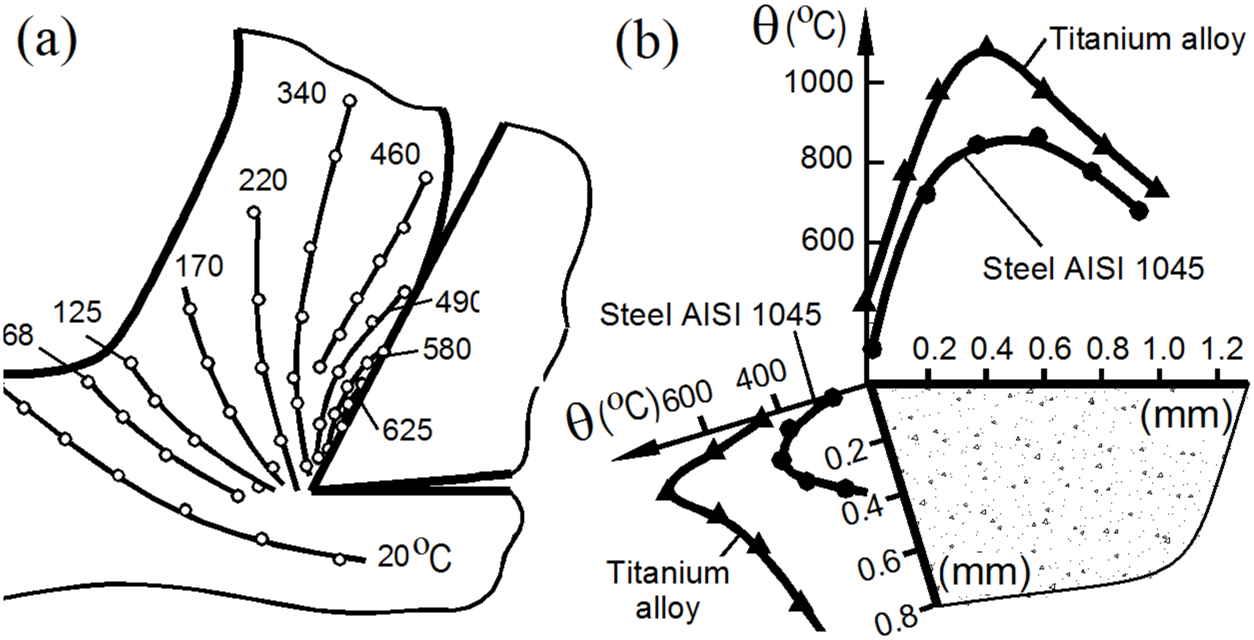

Figure A.6: Typical temperature field in metal cutting: (a) Isotherms for dry orthogonal cutting of ANSI 1045 steel with a carbide (P10) tool (rake angle 12°) at cutting speed of 60 m/min and uncut chip thickness 2 mm, (b) Temperature distributions over the tool rake and flank faces. Turning, a carbide cutting tool carbide M20 (92% WC, 8% Co), depth of cut a_p = 1.5 mm cutting speeds in machining of steel 1045 – 240 m/min, titanium alloy (Ti6Al4V) – 160 m/min, cutting feed – 0.25 mm/rev [2]

A.4.1 Complete Equation of Heat Balance in Metal Cutting

Using Equation (A.1) and energy balance shown in Figure A.4 as well as the idea of heat balance presented by Granovsky and Granovsky [140], the complete equation of heat balance in metal cutting system can be written in the following form

$$F_c v = Q_{\Sigma} = Q_{pd} + Q_{fR} + Q_{fF} + Q_{ch} + Q_m = Q_c + Q_w + Q_t + Q_{en} \qquad \text{(A.2)}$$

where Q_{pd} is the heat associated with plastic deformation of the layer being removed, Q_{fR} is the heat generated due to friction on the tool rake face, Q_{fF} is the heat generated due to friction on the tool flank face, and Q_{ch} is the heat due to formation of new surfaces, Q_m is the heat due to action of the minor cutting edge, Q_{en} is the heat that goes into environment. Note that Schmidt and Roubik [133] neglected this heat in their study assuming that it is negligibly small.

A.4.2 Experimental Apparatus and Methodologies

Dry machining tests were carried out to establish components of the heat balance Equation (A.2) experimentally at General Motors Toledo Transmission Plant. The measurement of the heat generation was carried according to methodology developed by Astakhov and Xiao [76], while heat partition, defined by calorimetry, was used according to the methodology presented in [2].

Machine – a special EMAG 250 DUO vertical turning center equipped with a SIMENS SINUMETRIC controller was used in the tests (Figure A.7). The machine is equipped with a motor–spindle prime drive of 35 kW so the power losses did not exceed 2–3%. The controller is capable to measure cutting power with no worse than 3% error (Figure A.8). As such, a wide range of power data sampling is available so that power variations can easily be visualized on the controller's monitor. Moreover, the frequency of chip formation can be distinguished by adjusting the data sampling.

Work materials – standard ANSI 1045 steel was used as the work material. Its properties are as follows: hardness, Brinell HB 170, tensile strength, ultimate 515 MPa, tensile strength, yield 485 MPa elongation at break 10.0 % in 50 mm, reduction of area 25.0 %, modulus of elasticity 200 GPa Poisson's ratio 0.2900, steel shear modulus 80.0 GPa. Test pieces were prepared as rings having dimensions $D \times d \times h = 180 \times 140 \times 50$.

Figure A.7: Machine used in the tests

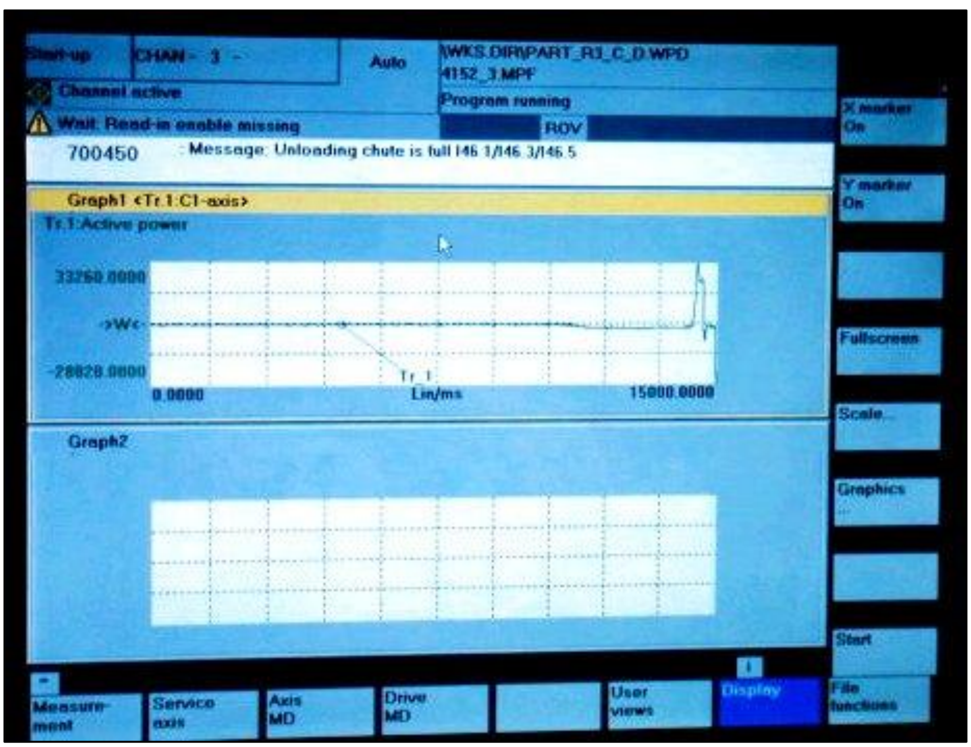

Figure A.8: Power reading on the controller's monitor

Tool – standard inserts SNMG 432–MF2 TP2500 Materials Group 4 (SECO Co.) installed into a tool holder 453–120141 R1–1 (Sandvik) (Figure A.9). The tool–in–machine tool geometry parameters are: the tool cutting edge angle $\kappa_r = 45^o$, tool minor cutting edge angle $\kappa_{r1} = 45^o$, nose radius $r_n = 1\ mm$, radius of the cutting edge $\rho_{ce} = 0.03 mm$, normal flank angle $\alpha_n = 7^o$, the normal rake angle $\gamma_n = -7^o$. Each insert used in the tests was examined using a digital vision system at a magnification of *x25* for visual defects such as chipping and microcracks.

Figure A.9: Cutting tool used in the test

AL–7014 dual–purpose calorimeter was a part of the experimental setup. It is designed to function as either a standard double wall calorimeter or as an electric calorimeter. It features a 300 ml inner vessel, 900 ml outer vessel with a molded cover, rubber stopper and fiber washer to support and insulate the inner vessel, and electric heating element. A digital thermometer MC–1000 with LCD display was used to measure the temperature in the calorimeter.

A.4.3 Experimental Results

The terms of the heat balance in Equation (A.2) were estimated for three cutting speed ranges. The first range is low (for the selected work material and cutting tool) cutting speeds (less than 100 m/min), second – for recommended cutting speeds (100–200 m/min), and third – for high (higher than recommended) cutting speeds (more than 200 m/min). Experimental results for terms of Equation (A.2) are shown in Figure A.10 and Figure A.11. As can be seen, the greatest source of heat generation in the machining system is plastic deformation of the layer being removed. As shown by experimental result, this source becomes relatively weaker with the cutting speed. The second largest source is the friction at the tool–chip interface. This source becomes stronger with the cutting speed as the chip velocity increases at this interface as the cutting speed increases. As can be seen in Figure A.10, other sources are much weaker.

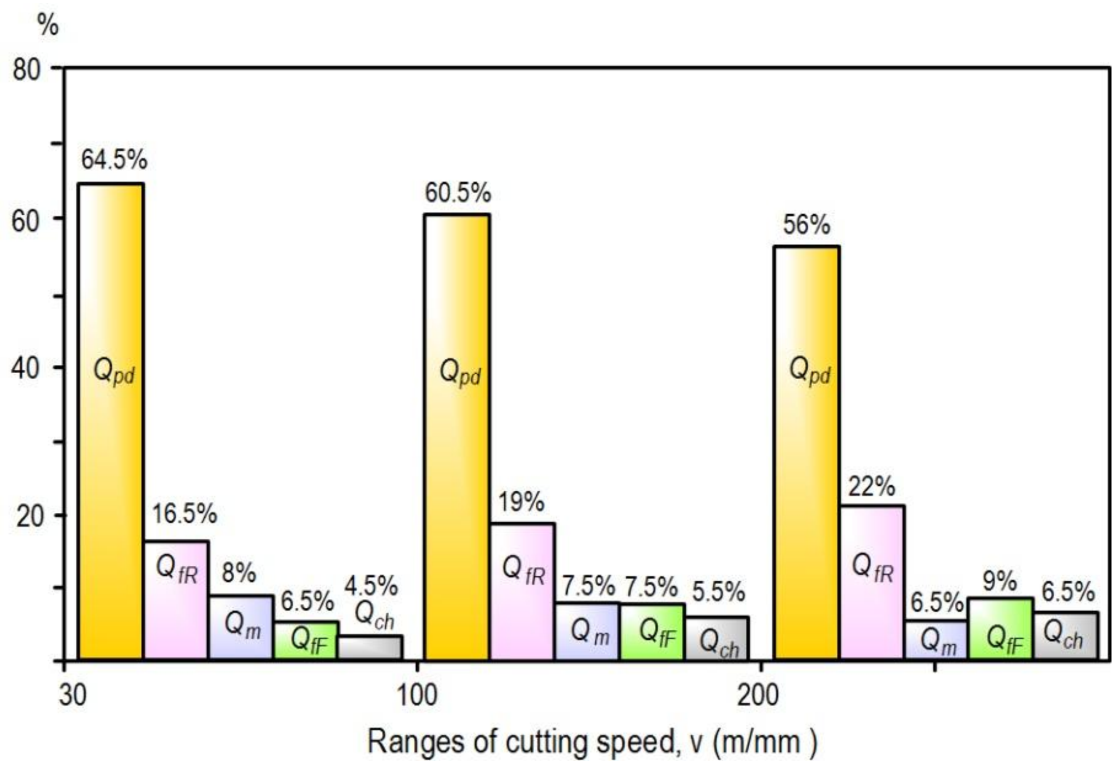

Figure A.10: Relative impact of the heat generating sources in the heat balance Equation (A.2)

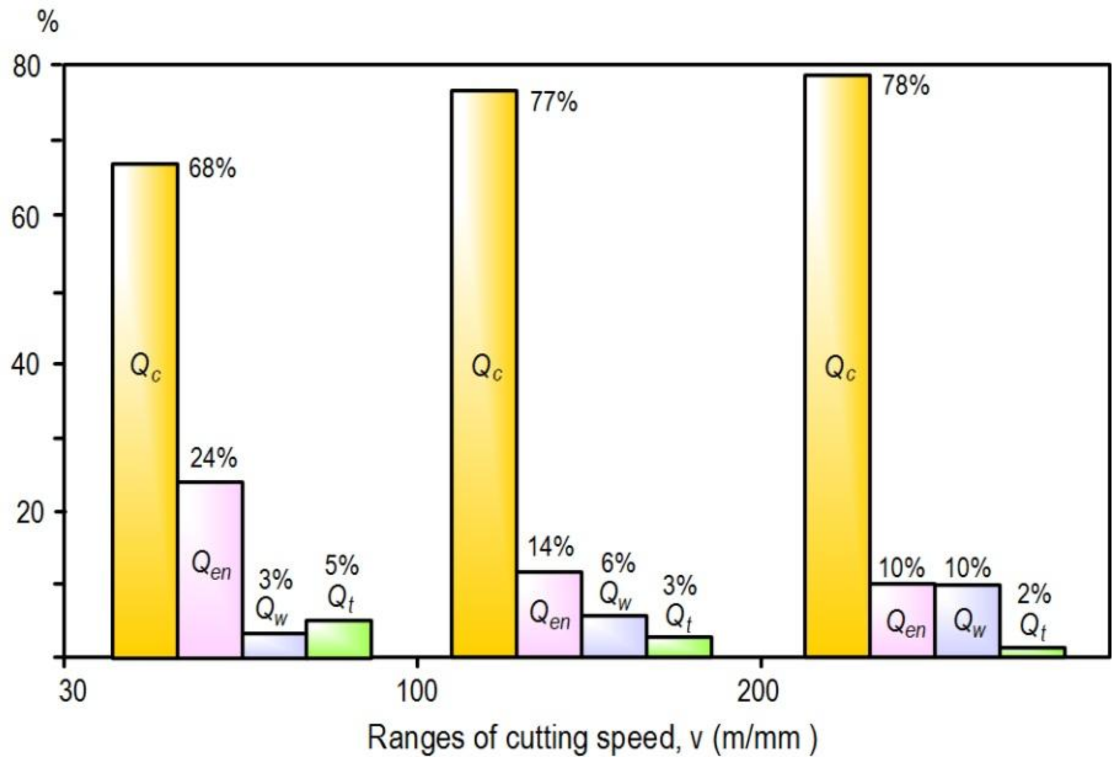

Figure A.11: Heat partition in the machining system in three cutting speed ranges

Analysis of the heat partition shown in Figure A.11 reveals the following:

1) The relative heat that goes into the chip is in agreement with the known experimental study although its values in any of three cutting speed ranges are lower than reported.
2) Surprisingly great amount of heat goes to environment although this term was not accounted for in the known studies. Moreover, in FEM analyses of the cutting process, this term is also ignored as the model is considered to be adiabatic.
3) The relative heat partition into the tool and the workpiece is the same as reported in the literature.

The obtained experimental results show that noting is incorrect in the results reported earlier in the literature on metal cutting so that this balance is not a problem in resolving the above–mentioned contradiction.

A.5 Proposed model and its governing heat partition equation

A.5.1 System Model

The system model is considered in Chapter 1 and depicted in Figure 1.22 where the stages in the formation of the continuous fragmentary chip, the most common chip type in metal cutting, are discussed in details within the system time frame.

A.5.2 Governing Equation

Many cases considered in the literature deal with the so–called stationary systems. There are examples of materials processes in which a solid body is moving out of a hot region and it sheds heat to the environment as it moves away from that heat source. Some examples of this configuration include a long slab of steel emerging from a furnace, a polymer strand leaving an extruder, metal wire being drawn, or a metal rod undergoing continuous induction hardening. The same can be said about moving chip. In many cases, the heat transfer can be approximated as occurring in one dimension (the direction of motion, or the axial direction) and treating heat losses in perpendicular directions as heat sinks. In order for this approximation to be valid, the heat flow in the body must be oriented so that it is mainly in the axial direction. If the heat flux in the direction of the moving body is much greater than the direction normal to motion, then the one–dimensional approximation is reasonable.

If the moving body can be modeled as one–dimensional, then one can define a control volume over which he/she can perform an energy balance in order to derive a conservation equation for thermal energy in terms of temperature [141]. In this control volume (of length Δx, cross–sectional area A_{ch}, and perimeter p_v), the thermal energy is transferred by conduction (q_x) and advection. Advection is the transport of energy due to the flow of the solid in the x direction through the control volume. The amount of energy which is brought into the control volume at location x by bulk solid motion is ($\dot{m}e_x$), where e_x is the specific enthalpy at x, The mass flow rate (which is constant along the length of the moving body) is $\dot{m} = \rho_{ch} A_{ch} v_{ch}$, where ρ_{ch} is the density of the work material, v_{ch} is the velocity of the chip relative the tool rake face. The rate at which the energy is advected out of the volume can be different and is written as ($\dot{m}e_x + \Delta x$). Also, heat can be generated in the volume ($\dot{q}$) and it is also lost to the ambient by convection. For the rest of this derivation, it is assumed that the volume velocity, material properties, and geometry which do not change along the direction of motion (x). It is a reasonable assumption for the chip because as it forms, its velocity relative to the tool and geometry do not change.

Using these conditions, Bejan [141] derived the energy conservation equation which describes the temperature along the length of the moving body, subject to heat generation and convective heat loss in the following form

$$\underbrace{k\,A_{ch}\frac{d^2T}{dx^2}}_{\text{Axial conduction}} - \underbrace{\left(\dot{m}c_p\right)\frac{dT}{dx}}_{\text{Advection}} - \underbrace{h_{cv}\;p\left(\theta_{ch} - \theta_{en}\right)}_{\text{Convection loss}} + \underbrace{\dot{q}\,A_{ch}}_{\text{Heat generation}} = 0 \tag{A.3}$$

where k is the thermo–conductivity of the work material (or material of the chip), c_p is the specific heat of this material, and h is the convection heat transfer coefficient of the process, θ_{ch} and θ_{ev} are the temperatures of the chip and environment, respectively.

It is useful to look carefully at this energy equation to remind ourselves of the physical phenomena which govern it. One must never view such an equation in a purely mathematical light, but keep in mind the physics represented by it. The first term represents the diffusion of thermal energy along the length of the body due to a temperature gradient within it. This diffusion of heat happens regardless of the magnitude of the motion and is independent of it. The second term is the change in the thermal energy of a mass as it moves through space. It is the difference between the energy advected into and out of a control volume of length *dx*. The third term is the heat lost through convection to the environment and the final term is heat generated in the body. In metal cutting, the chip move very fast so that the convection term can be neglected [2].

The heat transfer by conduction and convection are normally considered in the literature on metal cutting while that by advection does not attract so much attention. Thermal (or heat) advection is the transport of sensible or latent heat by a moving body, such as the chip in the considered case. Therefore, the role of heat advection, known also as mass transportation, as applicable to metal cutting should be examined in order to fulfill the objective of this study.

A.5.3 Péclet Number

To examine the role of advection in metal cutting, Equation (A.3) is considered together with a simplified model of chip formation shown in Figure A.12. In this model, the deformation of the layer being removed into the chip takes place 'instantly' on passing the shear plane so that the whole amount of heat due to the plastic deformation is generated along this plane. Being generated, the heat due to plastic deformation may go to the chip due to advection and to the layer being removed due to thermo–conductivity. Note that the structure of Equation (A.3) clearly shows that the generated heat cannot go into the chip by thermo–conductivity as per the second law of thermodynamics, i.e. because the temperature of the chip is higher than that of the shear plane and heat goes from a region of higher temperature to that of lower temperature. Therefore, there are two competing mechanisms of heat conduction: thermo–conductivity that attempts to bring a portion of the generated heat into the layer being removed and advection that attempts to bring a portion of this heat into the chip due to its motion.

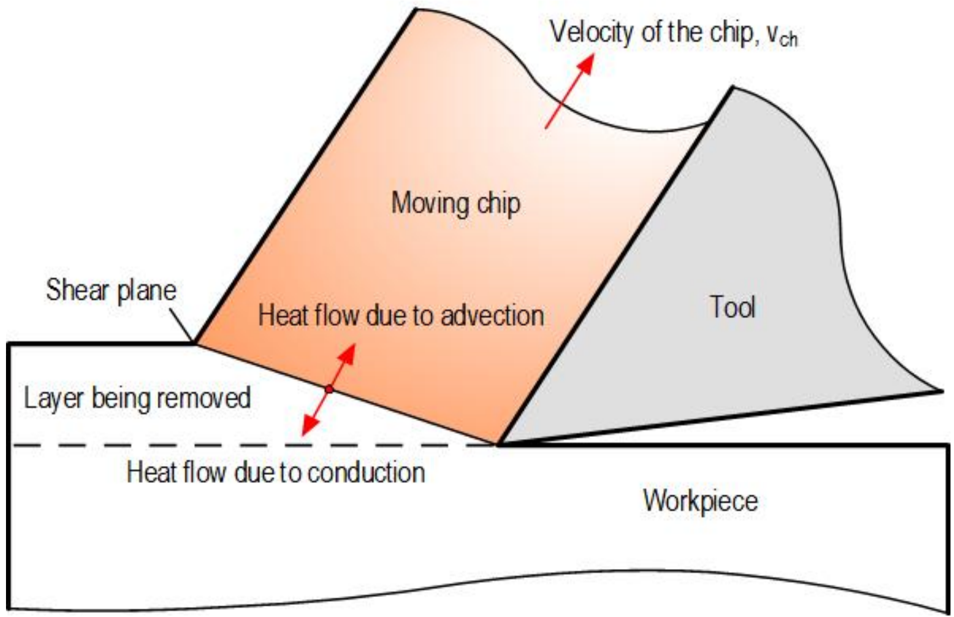

Figure A.12: Simplified model of chip formation in metal cutting

The next question to be answered is about the ratio of the portions of the heat generated on the shear plane due to thermo–conductivity and that due to advection. It is well–known in heat transfer studies that such a ratio is determined by the Péclet number [141]. This number is a dimensionless number relevant in the study of transport phenomena in fluid flows. It is named after the French physicist Jean Claude Eugène Péclet. It is defined to be the ratio of the rate of advection of a physical quantity by the flow to the rate of diffusion of the same quantity driven by an appropriate gradient, i.e.

$$Pe \equiv \frac{[\text{advection of heat}]}{[\text{conduction of heat}]} = \frac{VL}{\omega} \tag{A.4}$$

where V is the velocity scale, L is the length scale, and ω is the thermal diffusivity.

To comprehend the significance of this number, let's consider an example. Figure A.13 shows a flow of a fluid in a tube where a heater is installed. When the fluid is motionless, i.e. its velocity v_{fl} = 0, then the Péclet number is also zero according to its definition given by Equation

(A.4). As such, there is no advection. The heat from the heater flows in both sides at the same rate. When, however, the fluid velocity becomes $v_{fl} > 0$, then heat advection takes place so that, according to Equation (A.3), the temperature on the right side of the heater becomes greater than that on its left side. When the fluid velocity becomes great enough that the Péclet number is equal to 10, then only 1/10 of the heat supplied by the heater flows into the fluid in the left side of the heater while 9/10 of this heat flows to the fluid on its right side. No matter how powerful is the heater, this proportion is still the same.

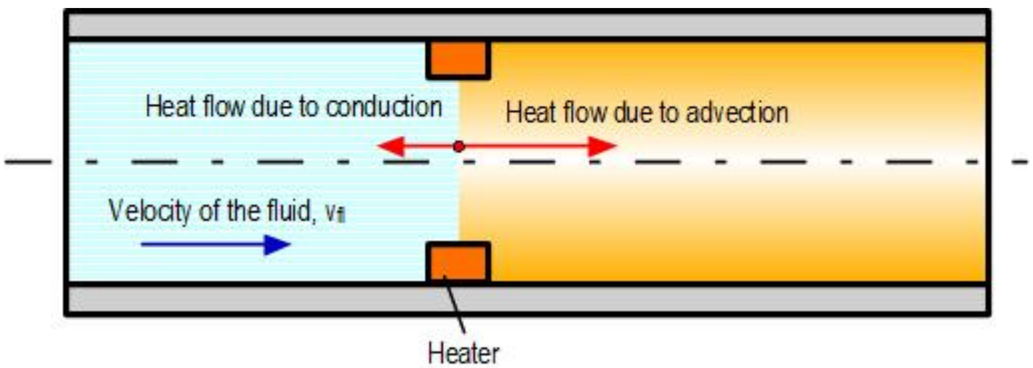

Figure A.13: Example of use of the Péclet number

In metal cutting, the Péclet criterion is represented in terms of machining process parameters as follows [2]

$$Pe = \frac{v_{ch} t_1}{w_w} \tag{A.5}$$

where v_{ch} is the velocity of a moving heat source, i.e. the velocity of chip relative the tool rake face (m/s), w_w is the thermal diffusivity of the work material (m^2/s),

$$w_w = \frac{k_w}{(c_p \rho)_w} \tag{A.6}$$

where k_w is the thermo–conductivity of the work material, (J/(m·s·C)), $(c_p \cdot \rho)_w$ is the volume specific heat of work material, (J/(m^3·C)).

As an example, consider machining of AISI 1040 steel under the typical machining conditions: operation – turning; Tool – MTJNR–1616H–09 (ISO 5608:1995) with a carbide insert; cutting speed v = 3 m/s (180 m/min); cutting feed f = 0.25 mm/rev, chip compression ratio ζ = 2, and thus the velocity of the chip with respect to the tool rake face is calculated as $v_{ch} = v/\zeta$ = 3/2 = 1.5 m/s . Thermal diffusivity of the work material is $6.67 \cdot 10^{-6}$ m^2/s. For the J–style tool holder, the tool cutting edge angle is $\kappa_r = 93^o$, thus the uncut chip thickness calculates as [1] $t_1 = f \cdot \cos(\kappa_r - 90^o) = 0.25 \cdot \cos(93^o - 90^o) = 0.24965 \approx 0.25$ mm. Thus, the Péclet criterion is calculated as $Pe = (1.5 \cdot 0.25 \cdot 10^{-3})/6.67 \cdot 10^{-6} = 66$. Therefore, 98.5% of the heat generated on the shear plane due to plastic deformation of the layer being removed flows into the chip while only 1.5% of this heat flows into the workpiece.

A.6 Conclusions

The obtained result has the following significance:

1) It explains the experimentally obtained low temperatures in the workpiece below the shear plane, for example those shown in Figure A.1 and Figure A.2. It explains why at low cutting speed the distribution of heat becomes more even. For example, referring to Table A.1, when v = 0.1 m/s then the amount of heat that goes into the chip is 47.9% while 38.4% goes into the workspace.
2) It explains the above–stated contradiction between the experimentally obtained heat balance in metal cutting (Figure A.1, Figure A.2 and Table A.1) and the model shown in Figure A.3. Moreover, it signifies the necessity of the system consideration of the chip

formation process in the manner shown in Figure 1.22 instead of its static analogue exclusively used in the literature.

3) It fully supports statement of Zorev [28] and definition of the cutting process by Astakhov[12] that the metal cutting process is a cold–working process because the temperature of the layer being removed just ahead of the tool hardly exceed 200 ^oC. In other words, the heat due to plastic deformation of the layer being removed does not affect the mechanical properties of the work material as this heat goes mostly into the chip due to mass transportation, i.e. advection.

One may argue, however, that the shear plane is not a plane in reality as suggested by some researches, e.g. Spaans and Oxley [142, 46], in a narrow zone. To discuss the influence of temperature in this case, Rosenberg [143] proposed to estimate the period of time necessary for a microvolume of work material to pass through the deformation zone. It follows from the above discussion that a microvolume of the layer being cut, passing through the shear zone, changes its velocity from the cutting speed v to the chip velocity $v_{ch} = v / \zeta$ where ζ is the chip compression ratio [2]. Thus, the average velocity of the microvolume is 0.5 v (1 - ζ). Therefore, the time T_p necessary to pass the shear zone having the width of h_{sz} would

$$T_p = \frac{h_{sz}}{0.5v\left(1+\frac{1}{\zeta}\right)} \tag{A.7}$$

Following a suggestion by Spaans, the width of the shear zone is h = 0.5t_1[142], one can estimate the time which is necessary for a microvolume to pass the deformation zone for a typical cutting regime using Equation (A.7). When the workpiece is made of plain carbon steel, a typical cutting regime is as follows: v = 120 m/min = 2 m/s; ζ = 2.5; uncut chip thickness t_1 = 0.2

mm. Thus, the estimated time is $T = 0.000071$ s. When the workpiece is made of a high–strength, low–alloy steel, the typical cutting regime may be as: $v = 120$ m/min = 2 m/s; $\zeta = 1.3$; $t_1 = 0.05$ mm. As such, $T = 0.000014$ s. As seen, the time necessary for a microvolume to pass the deformation zone is extremely short. As a result, heat generated in this zone due to plastic deformation of the layer being removed can be considered as occurring instantly, i.e. over the shear plane.

Appendix B: Energy Measures in Orthogonal Metal Cutting

B.1 Known Characterizations of Plastic Deformation in Metal Cutting

There are two characteristics of plastic deformation in metal cutting, namely, the chip compression ratio (CCR) and shear strain.

Historically, CCR was introduced in the earlier studies on metal cutting as a measure of plastic deformation of the work material in its transformation into the chip [28, 12]. A model of chip deformation in the simplest case of cutting (orthogonal cutting) is shown in Figure B.1. A flat section *abcd* having length L_1 and thickness t_1 is distinguished in the layer to be removed by the cutting tool. Once the distinguished section is deformed on its transformation into the chip, the section *abcd* transforms into section *a'b'c'd'*. In this transformation, called plastic deformation, the initial cross–sectional area does not change due to conservation of work material volume. Length L_1 of side *ab* becomes length L_2 of side *a'b'* while thickness t_1 (uncut chip thickness) becomes chip thickness t_2. The chip compression ratio (CCR or ζ) represents such a transformation due to plastic deformation according to Equation (4.2) as

$$\zeta = \frac{L_1}{L_2} = \frac{t_2}{t_1} \tag{B.1}$$

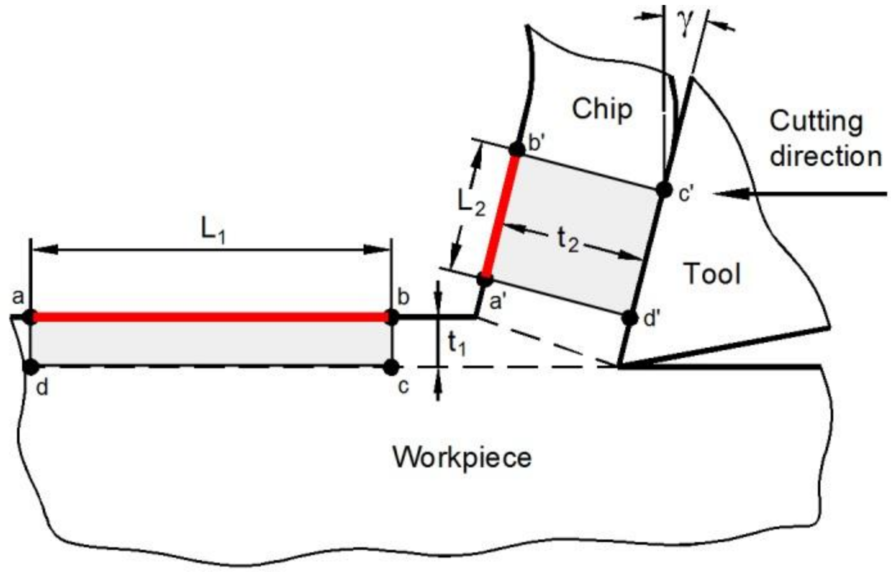

Figure B.1: Simple model of chip plastic deformation in orthogonal cutting

Although this parameter was widely used in metal cutting tests in the past [28], it was always considered as a secondary parameter to provide only qualitative support to certain conclusions. Since the real physical meaning of this parameter has never been revealed, it was gradually abandoned in metal cutting studies because nobody could explain the obtained results. For example, when one obtained in machining of a steel $\zeta = 2.5$ while in machining of a copper alloy $\zeta = 4.5$ at the same cutting speed, he/she should conclude that the plastic deformation and thus energy required for this deformation in the latter case is much greater than that in the former. However, the cutting force in machining of the steel is much greater than that in machining of the copper alloy. As the total energy required by the cutting system can be thought of as the product of the cutting force and the cutting speed, then unexplained contradiction between the values of the cutting force and CCR is obvious. That is why CCR is practically abounded in modern metal cutting studies. For example, although Shaw in his book [5] dedicated a full chapter to the analysis of plastic deformation in metal cutting, this parameter is not even mentioned. The same can be said about books by Trent and Wright [33, 33], Oxley [46] and

Gorczyca [3]; Altintas [144] just mentioned its definition in the consideration of the single shear plane model; Childs et al.[32] mentioned this parameter as related to the friction coefficient at the tool–chip interface. Not a single modern study on metal cutting correlates this parameter with the amount of plastic deformation in metal cutting.

The shear strain is another characteristic of plastic deformation in metal cutting. It is calculated as

$$\varepsilon = \frac{\cos\gamma}{\cos(\varphi-\gamma)\sin\varphi} = \frac{1-2\zeta\sin\gamma+\zeta^2}{\zeta\cos\gamma} \tag{B.2}$$

where φ is the shear angle.

Although Equation (B.2) is used practically in all books on metal cutting, there are some obvious problems with these equations in terms of its physical meaning and experimental confirmation [2]. If one calculates shear strain using Equation (B.2) (it can be easily accomplished by measuring the actual CCR) and then compares the result with the shear strain at fracture obtained in standard materials tests (tensile or compression), he/she easily finds that the calculated shear strain is much greater (2–5 folds) than that obtained in the standard materials tests. Moreover, when the chip compression ratio $\zeta = 1$, i.e. the uncut chip thickness is equal to the chip thickness so no plastic deformation occurs in metal cutting [145], the shear strain, calculated by Equation (B.2) remains very significant with no apparent reason for that. For example, when $\zeta = 1$, the rake angle $\gamma = -10^{\circ}$, Equation (B.2) yields $\varepsilon = 2.38$; when $\zeta = 1$, the rake angle $\gamma = 0^{\circ}$ then $\varepsilon = 2$; when $\zeta = 1$, $\gamma = +10^{\circ}$ then $\varepsilon = 1.68$. As shown by Astakhov [34], this severe physical contradiction is caused by the incorrect velocity diagram used to derive Equation (B.2).

The foregoing analysis suggests that apparently, there is no reliable measure of plastic deformation in metal cutting that can be used in tool and process designs as suggested earlier. Because the current work deals with the minimization of plastic deformation of the layer being removed in its transformation into the chip, a proper and reliable measure of plastic deformation in metal cutting should be found.

B.2 Proper Characterization of Plastic Deformation in Metal Cutting

CCR is the only post–process parameter of plastic deformation that objectively reflects the reality. This is because this parameter does not depend on a particular model of metal cutting and other restrictions. Therefore, to make this parameter useful, its physical meaning and correlation with work material mechanical properties should be revealed.

When a stress field applied to a body and, as a result, the relative position of its parts is changed then the body is said to be deformed or strained. A deformed state in a point can be represented by the strain components if the projections u_x, u_y, and u_z of the displacement of this point into corresponding coordinate planes are known

$$e_x = \frac{\partial u_x}{\partial x},\ e_y = \frac{\partial u_y}{\partial y},\ e_z = \frac{\partial u_z}{\partial z} \tag{B.3}$$

$$\gamma_{xy} = \frac{\partial u_x}{\partial y} + \frac{\partial u_y}{\partial x},\ \gamma_{yz} = \frac{\partial u_y}{\partial z} + \frac{\partial u_z}{\partial y},\ \gamma_{zx} = \frac{\partial u_z}{\partial x} + \frac{\partial u_x}{\partial z} \tag{B.4}$$

where e_x, e_y and e_z are the direct strains, γ_{xy}, γ_{yz}, and γ_{zx} are the engineering shear strains.

The imbalanced external forces applied to a body cause its deformation and thus lead to the displacement of its points until the equilibrium is established. As such, a certain amount of energy is absorbed. This energy depends on the work done in displacement of all points of the body. Such work can be calculated by integrating the work per unit volume. The work per unit volume done in the displacement of each point of the body is calculated as the product of the generalized force acting on a point and the change of the generalized displacement of this point caused by this force.

The von–Mises' stress [146]

$$\sigma_i = \frac{1}{\sqrt{2}}\left[\left(\sigma_x - \sigma_y\right)^2 + \left(\sigma_y - \sigma_z\right)^2 + \left(\sigma_z - \sigma_x\right)^2 + 6\left(\tau_{xy}^2 + \tau_{yz}^2 + \tau_{zx}^2\right)\right]^{1/2} \tag{B.5}$$

is considered as the generalized force and the equivalent strain

$$e_i = \frac{\sqrt{2}}{3}\left[\left(e_x - e_y\right)^2 + \left(e_y - e_z\right)^2 + \left(e_z - e_x\right)^2 + 6\left(e_{xy}^2 + e_{yz}^2 + e_{zx}^2\right)\right]^{1/2} \tag{B.6}$$

can be considered as the generalized displacement.

To correlate CCR with the amount of plastic deformation in metal cutting, the xyz coordinate system is set so that the y–axis is directed along the chip length, L1 (Figure B.1), the x axis is directed along the chip width, b, and the z axis is directed along its thickness, t_2. As such, the following expressions for the components of the true strain along the introduced coordinate axes can be written accounting for the definition of CCR [73]

$$\varepsilon_z = \ln \zeta_t\,,\ \varepsilon_x = \ln \zeta_b\,,\ \varepsilon_y = -\ln \zeta_L \tag{B.7}$$

As shown by Astakhov [73], in orthogonal cutting, the direction of the principal stress coincides with the introduced coordinate system. Then, Equation (B.6) could be re–written accounting for Equation (B.7) as

$$\varepsilon_i = \frac{\sqrt{2}}{3}\left[\left(-\ln \zeta_L - \ln \zeta_t\right)^2 + \left(\ln \zeta_t - \ln \zeta_b\right)^2 + \left(\ln \zeta_b + \ln \zeta_L\right)^2\right]^{1/2} \tag{B.8}$$

As shown in [73], if the chip parameters are properly measured in the orthogonal cutting test then $\zeta_b = 1$ as the chip width is equal to the width of cut, $\zeta_t = \zeta_L = \zeta$ thus the plane strain condition is the case in such a process. Therefore

$$\varepsilon_i = 1.15 \ln \zeta \tag{B.9}$$

It is important to mention that the above equation estimates the material strain due to perfect chip deformation based on continuum mechanics. Chip separation and segmentation due to shear bands limits the maximum attainable strain of the work material because of material damage and fracture. For example, according to the current research (Figure 5.2 – MC–RA–00) the maximum plastic strain of steel AISI 1045 in low triaxiality range (-0.25) which represents approximately most of the state of the primary deformation region is about 0.85 and CCR for this particular case is 3.796. However the calculated strain from Equation (B.9) is 1.534 which exceeds the material strain limit implies that the chip material exceeded the damage initiation point therefore shear bands and chip segmentation may occur in this particular case. The strain–CCR equation is best suitable for ductile metals where such discontinuity conditions do not exist. To account for such conditions, Equation (B.9) can be rewritten as

$$\varepsilon_i = \begin{cases} 1.15 \ln \zeta, & \text{if } \varepsilon_i \le \varepsilon_f \\ \varepsilon_f, & \text{if } \varepsilon_i > \varepsilon_f \end{cases} \tag{B.10}$$

B.3 Plastic Energy in Metal Cutting

Because the elementary work is $dA = \sigma_i e_i$, the total work done over a volume V then calculates as [73]

$$A = \int_V \sigma_i e_i \, dV \tag{B.11}$$

In the considered coordinate system, stress components σ_z and σ_y do not depend on the x coordinate (measured along chip width) and the σ_z component is determined as [147]

$$\sigma_x = 0.5\left(\sigma_z + \sigma_y\right) \tag{B.12}$$

substituting these results in Equation (B.5), one can obtain

$$\sigma_i = \frac{1}{\sqrt{2}}\left\{\left[\sigma_z - 0.5\left(\sigma_z + \sigma_y\right)\right]^2 + \left[0.5\left(\sigma_z + \sigma_y\right) - \sigma_y\right]^2 + \left(\sigma_y - \sigma_z\right)^2\right\}^{1/2} \tag{B.13}$$

or after simplification

$$\sigma_i = 0.87\left(\sigma_z - \sigma_y\right) \tag{B.14}$$

Two basic mechanical properties are used to characterise the strength of a material – the true fracture stress and the true fracture strain. The loading history to arrive to these characteristic is known as the flow curve. The flow curve for many metals in the region of plastic deformation can be expressed by the simple power curve relation [147, 63]

$$\sigma = K\varepsilon^n \tag{B.15}$$

where n is the strain–hardening exponent, and K is the strength coefficient. A log–log plot of true stress and true strain up to the strain at fracture will result in a straight line if Equation (B.15) that allows determining of n and K in the manner shown in Figure B.2. As seen, the linear slop is n, and K is the true stress at $\varepsilon = 1$. As shown in Figure B.3, the strain–hardening exponent may have values from $n = 0$ (perfectly plastic material) to $n = 1$ (perfectly elastic material). For common work materials, n has values between 0.10 and 0.50 as indicated in Table B.1.

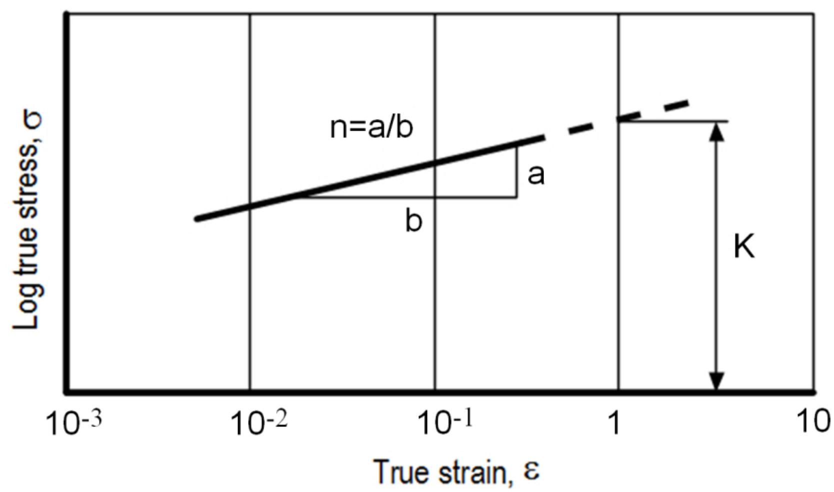

Figure B.2: Log–log plot of true stress–true strain curve to determine strain–hardening exponent *n* and the strength coefficient *K*

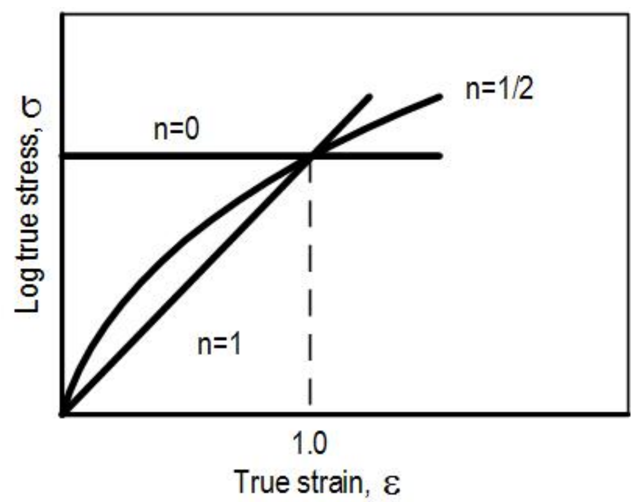

Figure B.3: Various forms of power curve $\sigma = \varepsilon n$

Some important deductions relevant to metal cutting directly follow from the above consideration:

1. The strength of a material is defined by the stress at fracture while the energy required to fracture a unit volume of a material is determined by both stress and strain at fracture and is represented by the area under the stress–strain curve.

2. The flow curve of a given materials reflects the manner in which material deforms, i.e. in which the strain hardening of material take place.

3. The flow curve characteristics n and K are very sensitive to even small change in the material composition, structure, inclusions, metallurgical characteristics and other parameters. For example, the data for 0.6% carbon steel show that changing the tempering temperature changes these characteristics significantly.

4. A simple standard tensile test can be used to obtain n and K for most of work materials.

Table B.1: Values for n and K for metals at room temperature [147]

Materials	*Conditions*	*n*	*K (MPa)*
0.05% carbon steel	Annealed	0.26	530
SAE 4340 steel	Annealed	0.15	641
0.6% carbon steel	Quenched and tempered at 540 ^{o}C	0.10	1572
0.6% carbon steel	Quenched and tempered at 705 ^{o}C	0.19	1227
Copper	Annealed	0.54	320
70/30 brass	Annealed	0.49	896

Substituting representation of the flow curve given by Equation (B.15) in Equation (B.14), one obtains

$$\begin{aligned}\sigma_i &= 0.87\left(K\varepsilon_z^n - K\varepsilon_y^n\right) = 0.87K\left(\varepsilon_z^n - \varepsilon_y^n\right) = 0.87K\left[\left(\ln\zeta_t\right)^n - \left(\ln\zeta_L\right)^n\right] \\ &= 0.87K\,2\left(\ln\zeta\right)^n = 1.74K\left(\ln\zeta\right)^n\end{aligned} \tag{B.16}$$

Because it was assumed that the chip has uniform deformation, the elementary work spent over plastic deformation of a unit volume of the work material is calculated as

$$A_u = \int_0^{\varepsilon_f} \sigma d\varepsilon = \frac{K\left(1.15\ln\zeta\right)^{n+1}}{n+1} \qquad \text{(B.17)}$$

The obtained result is of great significance to the experimental studies in metal cutting because it correlates in a simple and physically–grounded manner the work of plastic deformation done in cutting with a measurable, post–process characteristic of the cutting process such as CCR. Knowing the elementary work, the total work done by the external force applied to the tool is then calculated as

$$A = A_u v f d_w \tau_{ct} \qquad \text{(B.18)}$$

where f is the cutting feed and τ_{ct} is time of cutting.

The power spent on the plastic deformation of the layer being removed, P_{pd} can be calculated knowing the chip compression ratio and parameters of the flow curve of the work material as

$$P_{pd} = \frac{K\left(1.15\ln\zeta\right)^{n+1}}{n+1} v A_w \qquad \text{(B.19)}$$

A series of test were carried out to resolve above–mentioned contradiction between CCR and the cutting force in machining of steel and copper [76]. All the tests were conducted using the same cutting feed $f = 0.07\ mm/rev$ and the depth of cut $d_w = 1\ mm$. Three different types of the work material listed in Table B.2 were used in the tests. For each work material, the influence of the cutting speed on CCR was determined and the elementary work spent over plastic deformation of the work material was calculated using Equation (B.18).

Table B.2: Work materials and flow curve constants used in the tests [76]

Material	*K (GPa)*	*n*
AISI steel E52100, HB280 (0.981.10%C,1.45%Cr, 0.35%Mn)	1.34	0.25
Copper (99.7%)	0.40	0.24
Aluminium 1050–0, HB 21	0.14	0.27

The test results are shown in Figure B.4. As seen, although CCR is the greatest in the machining of copper and lowest in the machining of steel, the elementary work is the greatest for steel. In other words, the energy per unit volume spent on plastic deformation in the machining of steel is the greatest, which results in a much higher cutting force, amount of heat generated and in more significant tool wear. This conclusion is supported by multiple facts known from the everyday practice of machining.

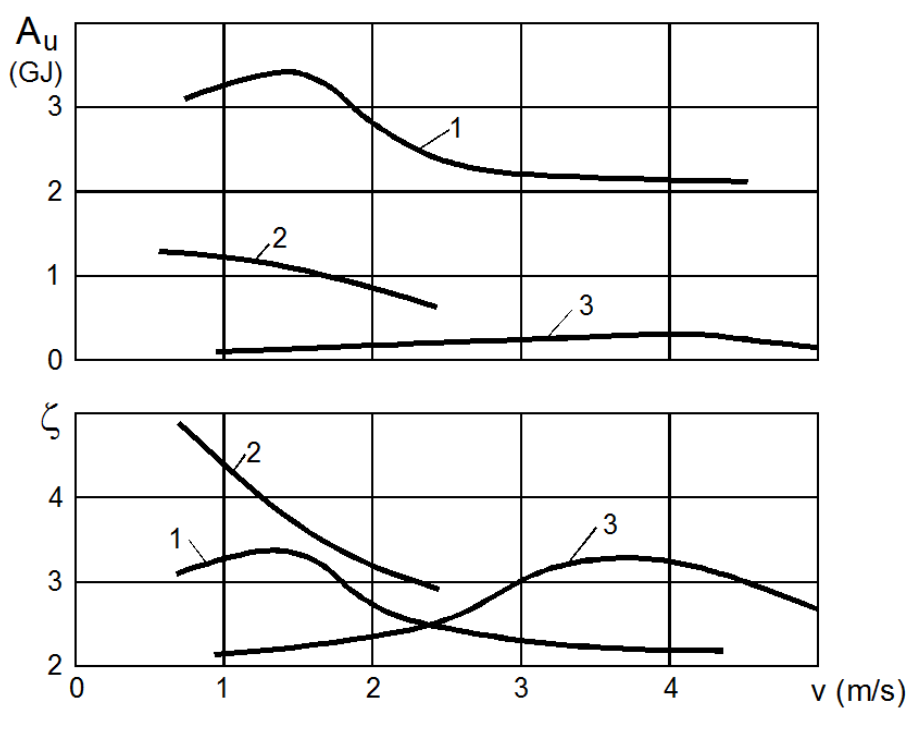

Figure B.4: Influence of the cutting speed on CCR and the work done in plastic deformation: (1) AISI steel E52100, (2) Copper, (3) Aluminum 1050 [145]

The accuracy of the estimation of the work done in plastic deformation can be improved if instead of just generic approximation for the flow curve given by Equation (B.15) is used, work material specific parameters of this curve accounting for a material or group of materials particularities are used. For example if the following reduced form of the JC plasticity model for static analysis is to be used

$$\bar{\sigma} = A + B\bar{\varepsilon}^{n} \tag{B.20}$$

then the elementary work corresponding to the above JC model is

$$A_u = \int_0^{\varepsilon_f} \sigma d\varepsilon = 1.15A \ln\zeta + \frac{B\left(1.15\ln\zeta\right)^{n+1}}{n+1} \tag{B.21}$$

and the power spent on the plastic deformation of the layer being removed, P_{pd} is

$$P_{pd} = \left(1.15A \ln\zeta + \frac{K\left(1.15\ln\zeta\right)^{n+1}}{n+1}\right) vA_w \tag{B.22}$$

B.4 Significance of CCR

The proposed method for determination of the work of plastic deformation in metal cutting gives new meaning to CCR. The chip compression ratio (or its reciprocal, the chip ratio) is the most reliable, physically grounded yet simple to determine measure of plastic deformation in metal cutting. In the author's opinion, anyone involved in the field should clearly understand its meaning, applications and methods of its determinations because the value of this characteristic in metal cutting and cutting tool studies, development, testing, and applications, cannot be overstated.

Knowing CCR, one can directly determine:

1) Power spent on plastic deformation of the layer being removed which is the largest portion of the power required by the cutting system and which is the major contributor to the cutting force. Using this power, the cutting force can be then calculated [76]

2) The so–called natural length of tool–chip interface.

3) The chip velocity relative to the cutting tool as the cutting speed divided by CCR.

4) Tribological conditions at the tool chip interface used in the design of chip breakers, selection of tool materials and coatings as well as the selection of the optimal cutting regime [2].

5) The maximum temperature and temperature distribution over the tool–chip interface [2, 12].

The Poletica criterion (*Po–criterion*) is introduced as the ratio of the contact length, l_c to the uncut chip thickness, t_1

$$Po = \frac{l_c}{t_1} \tag{B.23}$$

It was found [148] that for a wide variety of work materials this criterion can be calculated through CCR ζ as

$$Po = \zeta^{k_t} \tag{B.24}$$

where k_r =1.5 when ζ<4 and k_r =1.3 when $\zeta \geq 4$.

Therefore, the total length of the tool chip interface can be estimated by the following experimentally–obtained relationship

$$l_c = t_1 \zeta^{k_r} \tag{B.25}$$

Table B.3 shows the above *Po–criterion* calculated for different cutting conditions using FE. The Po values were calculated based on the measured length of contact l_c for various rake angle and friction coefficients.

Table B.3: *Po–criterion* and contact length obtained from FE and Equation (B.23)

WP#	*Rake (deg.)*	t_1 *(mm)*	*Prediction (FE)*				$l_c = t_1 \zeta^{k_r}$	
			t_2 *(mm)*	*CCR*	l_c *(mm)*	*Po–Cr*	k_r	l_c *(mm)*
MC–RA–00	0.0	0.042	0.161	3.796	0.153	3.607	1.5	0.314
MC–RA–10	10.0	0.042	0.124	2.923	0.124	2.923	1.5	0.212
MC–RA–20	20.0	0.042	0.111	2.617	0.103	2.428	1.5	0.180
MC–RA–30	30.0	0.042	0.089	2.098	0.093	2.192	1.5	0.129
MC–RA–40	40.0	0.042	0.072	1.701	0.078	1.839	1.5	0.094
MC–RA20–UCT100–FR00	20.0	0.100	0.148	1.480	0.101	1.010	1.5	0.180
MC–RA20–UCT100–FR10	20.0	0.100	0.160	1.600	0.105	1.050	1.5	0.202
MC–RA20–UCT100–FR20	20.0	0.100	0.175	1.750	0.125	1.250	1.5	0.232
MC–RA20–UCT100–FR30	20.0	0.100	0.189	1.890	0.153	1.530	1.5	0.260
MC–RA20–UCT100–FR40	20.0	0.100	0.204	2.040	0.177	1.770	1.5	0.291
MC–RA20–UCT100–FR50	20.0	0.100	0.220	2.200	0.201	2.010	1.5	0.326
MC–RA20–UCT100–FR60	20.0	0.100	0.233	2.330	0.224	2.240	1.5	0.356

The data presented in Table B.3 clearly indicate significant difference in contact length l_c between the FE predictions and the values obtained from Equation (B.25) using the k_r values suggested by Poletica. However, because in the experiment by Poletica, oblique cutting conditions were used thus the influence of the minor cutting edge on the contact length was significant which led to the above results, therefore such varition is expacted. The question is not what cause such variation rather does such relationship between *Po–criterion* and CCR exist. If such correlation exist, the non–dimentional nature of CCR and *Po–criterion* parameters would provide a general expression where its applicability can be implimented for varuis cutting conditions. To investigate whether an approximation of a *Po–criterion*, and thus l_c, can be acquired by knowing CCR, consider the data presented in Figure B.5 where the *Po–criteria* for different cutting conditions is plotted against CCR. It directly follows from Figure B.5 that near linear correlation exists between the two parameters eventhought the cutting conditions are entirely different.

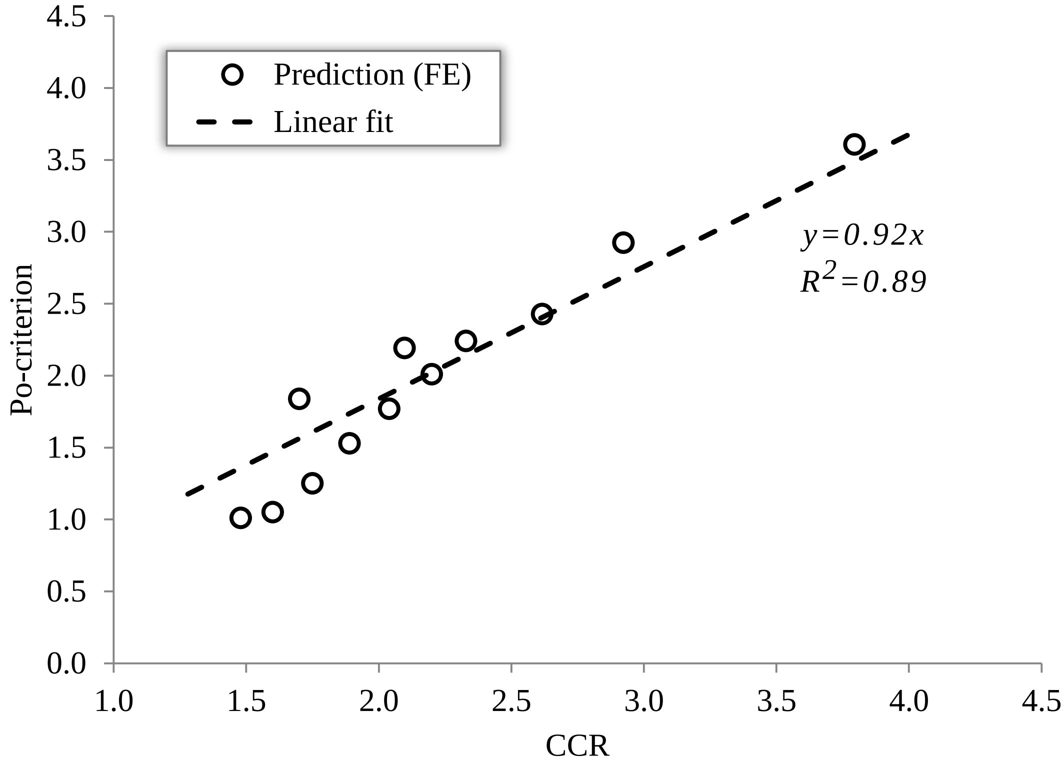

Figure B.5: *Po–criterion* obtained by FE for various cutting conditions and CCR

As was concluded previously that altering the cutting conditions such as rake angle, chip–tool friction, and other tool and process parameters changes the chip charecteristics and its flow pattren, it also alters the CCR which can be used as a general guideline to estimate other cutting charecteristecs that are meaningful such as the lenght of contact.

Moreover, Zorev [28] studied the length of the plastic part using a quick–stop device and conclusively proved that the whole contact length l_c is divided into two distinctive parts: the plastic part, l_{c-p} which extends from the cutting edge and the elastic part, l_{c-e} from the plastic part to the point of tool–chip separation. Similar experimental results were obtained by Poletica [148] and Loladze [149]. Summarizing the results of multiple experiments, Abuladze [74] proposed the following expression to calculate the length of the plastic part of the tool–chip interface

$$l_{c-p} = t_1\left[\zeta\left(1-\tan\gamma\right)+\sec\gamma\right] \tag{B.26}$$

According to Zhang [150], Klopstock in 1926 was the first to show that tool life and cutting forces could be favourably altered by restricting the tool–chip contact length. This was done using a composite rake face tool made of high speed steel.

Latter on, it was found by multiple researchers that the use of tools with the restricted contact length may result in up to a 30% reduction in the cutting force although the real reason for that is not clearly revealed. Limited–contact tools have been studied by Takeyama and Usui [118], Chao and Trigger[119], Usui and Shaw [120], Hoshi and Usui [121]. Detailed bibliography and analysis of the studies of this kind of tool were presented by Jawahir and Luttervelt [126], Zhang [150], Karpat and Ozel [151] and many others.

Two logical question to be answered when one tries to design/select a tool with restricted contact length are: (1) What is the rake angle for a tool with the restricted contact length?, (2) How does the restricted contact length affect tool life or to what extend this length can be restricted to maximise tool performance? Unfortunately, only a few known publications concern with answering these practical questions.

The most essential conclusions on the effects of the reduced contact length can be drawn from experimental results presented by Poletica [148] and Loladze [149], Zorev [28], Sadic and Lindstrom [152, 153]:

1) Tool life normally increases noticeably and the cutting force decreases when the tool–chip contact length is reduced from its natural length to the length of the plastic part of this contact.
2) Any further decrease of the tool–chip contact length beyond the length of the plastic contact leads to rapid reduction of tool life.

The foregoing analysis suggests that the maximum effect of the restricted tool–chip contact length is achieved when this length is equal to l_{c-p}, which, in turn, depends on the uncut chip thickness t_1 and CCR ζ in Equation (B.26). Even small deviation from the optimal l_{c-p} may lead to significant change in tool performance. For example, Rodrigues and Coelho found [154] that the reduction of 0.25 mm in chamfer length and increase of 1º in chamfer angle (from SNMG PR to SNMG PF tools) caused a reduction in the specific cutting energy nearly 28.6% and 13.7% for conventional cutting speed and high–speed cutting respectively.

The vast majority of practical cutting tools including those with indexable inserts, however, are meant for wide ranges of the machining regime and various machining systems. Because these inserts have a fixed restricted contact length, the performance of these inserts may vary significantly depending upon a given application. This explains great scatter in the performance of indexable carbide inserts observed in practice. Understanding the concept of CCR provided here and by measuring this important parameter in practical optimization of a cutting operation, any practitioner can select the proper insert for a given application.

Appendix C: Material User Subroutine

```
c User subroutine vuhard
c The subroutine calculates the material hardening surface
c according to the JC flow model and updates the state variables
c used for material damage initiation and degradation.
c User variables:
c      Y     : Material initial yield stress
c      Es    : Secant modulus of elasticity
c      Gf    : Fracture energy density
c      dmax  : Maximum degradation (this parameter can be
c              adjusted to account for material internal
friction
c              for low triaxiality)
c      damage: Damage scalar parameter
c      Lambda: Exponent parameter controls the material
c              degradation
c      Ep    : Plastic modulus
c      rn    : JC hardening coefficient
c      B     : JC hardening modulus
c      A     : JC initial yield strength
c      C     : JC strain rate sensitivity
c      TRIAX : Stress triaxiality state parameter
c      eqpsf : Equivalent plastic strain at damage initiation
c      Press : Hydrostatic pressure
c      P     : Total plastic energy density for the material
```

```
c              point
c      Pk     : Plastic energy density limit for the material
c              point
c
      subroutine vuhard (
c Read only -
     *     nblock,
     *     nElement, nIntPt, nLayer, nSecPt,
     *     lAnneal, stepTime, totalTime, dt, cmname,
     *     nstatev, nfieldv, nprops,
     *     props, tempOld, tempNew, fieldOld, fieldNew,
     *     stateOld,
     *     eqps, eqpsRate,
c Write only -
     *     yield, dyieldDtemp, dyieldDeqps,
     *     stateNew )
c
      include 'vaba_param.inc'
c
      dimension nElement(nblock),
     *     props(nprops),
     *     tempOld(nblock),
     *     fieldOld(nblock,nfieldv),
     *     stateOld(nblock,nstatev),
     *     tempNew(nblock),
     *     fieldNew(nblock,nfieldv),
     *     eqps(nblock),
     *     eqpsRate(nblock),
     *     yield(nblock),
     *     dyieldDtemp(nblock),
```

```
     *     dyieldDeqps(nblock,2),
     *     stateNew(nblock,nstatev),
     *     damage(nblock),
     *     ddamageDeqps(nblock)
c
      parameter (zero=0.0d0, half=0.50d0 , one=1.0d0, two=2.0d0)
      parameter (eqpsFail = 0.03)
c
      character*80 cmname
      parameter( nrData=6 )
      character*3 cData(maxblk*nrData)
      dimension rData(maxblk*nrData),
     *          jData(maxblk*nrData)
c    -----------------------------------------------------------
      Y = 333.0d0
      Es = 135811.0d0
      Gf = 320.0d0
      dmax = 0.9d0
      Lambda = 0.60d0
      ratio=(exp(Lambda)-Lambda*exp(Lambda)-one)/
     *      (Lambda*(one-exp(Lambda)))
c
      Ep = 70.2350d0
      rn = 0.12990d0
      B = 540.690d0
      A = Y
      C = 0.01340d0
c
      do k = 1, nblock
         TRIAX = stateNew(k,3)
```

```
          eqpsr = stateOld(k,5)
          Press = stateNew(k,8)
          de = eqps(k)-stateOld(k,1)
          eqpsd = eqps(k)
          sr = log(eqpsr/0.0010d0)
          if (sr .lt. zero) then
             sr = zero
          end if
c         For static analysis activate this line
c         sr = zero
          if (eqps(k) .le. zero) then
             yield(k) = Y
             dyieldDeqps(k,1) = Es
             damage(k) = zero
             ddamageDeqps(k) = zero
         else
             eqpsf = 0.154d0+0.209d0*exp(-4.862d0*TRIAX)
             P = stateOld(k,4)+de*stateOld(k,2)
             Pk = A*eqpsf + B/(rn+1) * eqpsf**(rn+1)
             if (P .gt. Pk) then
                G = Gf
                Gt = G/ratio
                y1 = (A+B*eqpsf**rn)*(one+C*sr)
                Ep = (B*rn*eqpsf**(rn-one))*(one+C*sr)
                eqpsf2 = (-y1+(y1**two+two*Ep*Gt)**half)/Ep+eqpsf
                estar = (eqpsd-eqpsf)/(eqpsf2-eqpsf)
                damage(k) = (one-exp(Lambda*estar))/(one-
     *                      exp(Lambda))
                ddamageDeqps(k) = (-Lambda/(eqpsf2-eqpsf1)*
     *                            exp(Lambda*estar))/(one-
```

```
     *                           exp(Lambda))
            else
               damage(k) = zero
               ddamageDeqps(k) = zero
               eqpsr =  eqpsRate(k)
               TRIAX = stateNew(k,3)
            end if
            stateNew(k,6) = one
            if (cmname .eq. "AISI1045-JC-S") then
               if (damage(k) .gt. one) then
c                 Deactivate damaged elements for chip
separation
                  stateNew(k,6) = zero
               end if
            end if
            if (damage(k) .lt. zero) then
               damage(k) = zero
            end if
            if (damage(k) .gt. one) then
               damage(k) = one
            end if
            if (damage(k) .ge. dmax) then
               d = dmax
            else
               d = damage(k)
            end if
            yield(k) = (A+B*eqpsd**rn)*(one+C*sr)
            yield(k) = (one-d)*yield(k)
            dyieldDeqps(k,1) = (B*rn*eqpsd**(rn-one))*(one+C*sr)
         end if
```

```
c        Update state variables
         stateNew(k,1) = eqps(k)
         stateNew(k,2) = yield(k)
         stateNew(k,3) = TRIAX
         stateNew(k,4) = P
         stateNew(k,5) = eqpsr
         stateNew(k,7) = damage(k)
         stateNew(k,8) = Press
         if (damage(k) .le. zero) then
            stateNew(k,9) = eqps(k)
         else
            stateNew(k,9) = stateOld(k,9)
         end if
         stateNew(k,10) = eqpsd
      end do
c
      return
      end
c    -----------------------------------------------------------
c    ===========================================================
c
c     This subroutine updates state variables used by vuhard
      subroutine vusdfld(
c Read only -
     *   nblock, nstatev, nfieldv, nprops, ndir, nshr,
     *   jElem, kIntPt, kLayer, kSecPt,
     *   stepTime, totalTime, dt, cmname,
     *   coordMp, direct, T, charLength, props,
     *   stateOld,
c Write only -
```

```
     *   stateNew, field )
c
      include 'vaba_param.inc'
c
      dimension jElem(nblock), coordMp(nblock,*),
     *          direct(nblock,3,3), T(nblock,3,3),
     *          charLength(nblock), props(nprops),
     *          stateOld(nblock,nstatev),
     *          stateNew(nblock,nstatev),
     *          field(nblock,nfieldv)
      character*80 cmname
c
c     Local arrays from vgetvrm are dimensioned to
c     maximum block size (maxblk)
c
      parameter( nrData=6 )
      character*3 cData(maxblk*nrData)
      dimension rData(maxblk*nrData), jData(maxblk*nrData)
c    -----------------------------------------------------------
      jStatus = 1
      call vgetvrm( 'S', rData, jData, cData, jStatus )
c
      if( jStatus .ne. 0 ) then
         call xplb_abqerr(-2,'Utility routine VGETVRM '//
     *      'failed to get variable.',0,zero,' ')
         call xplb_exit
      end if
c
      call setField( nblock, nstatev, nfieldv, nrData,
     *   rData, stateOld, stateNew, field)
```

```
c
      return
      end
c     ------------------------------------------------------------
c     ============================================================
c
c      This subroutine calculates the following:
c      stateNew(k,3): Stress triaxiality state parametr
c      stateNew(k,8): Hydrostatic pressure
      subroutine setField( nblock, nstatev, nfieldv, nrData,
     *   stress, stateOld, stateNew, field )
      parameter (zero = 0.0d0, half = 0.50d0, one = 1.0d0,
     *            two = 2.0d0, three = 3.0d0)
      include 'vaba_param.inc'
      dimension stateOld(nblock,nstatev),
     *   stateNew(nblock,nstatev),
     *   field(nblock,nfieldv), stress(nblock,nrData)
c     ------------------------------------------------------------
      do k = 1, nblock
         c=half*(stress(k,1)+stress(k,2))
         r=(half*(stress(k,1)-
     *      stress(k,2))**two+stress(k,4)**two)**half
         s1 = c+r
         s2 = c-r
         y = (s1-s2)*half*three**half
         TRIAX = half*(s1+s2)/y
         s1 = stress(k,1)
         s2 = stress(k,2)
         s3 = stress(k,3)
         s12 = stress(k,4)
```

```
      y = (((s1-s2)**two+(s2-s3)**two+(s3-s2)**two
     *        +6.0d0*s12**two)*half)**half
      sm = (s1+s2+s3)/three
      TRIAX = sm/y
      stateNew(k,3) = TRIAX
      stateNew(k,8) = zero-sm
   end do
   return
   end
c     -----------------------------------------------------------
c     ===========================================================
```

BIBLIOGRAPHY

BIBLIOGRAPHY

[1] Astakhov, V.P., Geometry of single-point turning tools and drills: Fundamentals and practical applications, London: Sptinger, 2010.

[2] Astakhov, V.P., "Tribology of Metal Cutting," in *Mechanical Tribology. Material Characterization and Application*, vol. 52, London, Elsevier, 2006.

[3] Gorczyca, F.Y., Application of Metal Cutting Theory, New York: Industrial Press, 1987.

[4] DeGarmo, E.P., Black, J.T., and Kohser, R.A., Materials and Processes in Manufacturing, 10th Ed. ed., New York: John Wiley and Sons, 2007.

[5] Shaw M.C., Metal cutting principles, 2nd ed., Oxford: Oxford University Press, 2005.

[6] "System, T.W.," AdvantEdge 4.6, 2004. [Online]. Available: http://www.thirdwavesys.com.

[7] Kalpakjian, S. and S.R. Schmid, Manufacturing Engineering and Technology, 4th edition ed., New Jersey: Prentice-Hall, 2001.

[8] Boothroyd, G. and Knight, W.A., Fundamentals of Machining and Machine Tools, T. ed., Ed., Boca Raton: CRCPress, 2006.

[9] Merchant, M.E., "Mechanics of the metal cutting process. I. Orthogonal cutting and a type 2 chip," *Journal of applied physics*, vol. 16, no. 5, pp. 267-275., 1945.

[10] Ernst, H., and Merchant, M. E., "Chip formation, friction and high quality machined surfaces. Surface Treatment of Metals," *ASM*, vol. 29, pp. 299-378, 1941.

[11] Astakhov, V.P., "A treatise on material characterization in the metal cutting process. Part 1: A novel approach and experimental verification," *Journal of Materials Processing Technology*, Vols. 96(1-3), pp. 22-33, 1999.

[12] Astakhov, V.P., Metal cutting mechanics, Boca Raton: CRP Press, 1999.

[13] Mackerle, J., "Finite-element analysis and simulation of machining: a bibliography (1976-1996)," *Journal of Materials Processing Technology*, Vols. 86(1-3), pp. 17-44, 1999.

[14] Mackerle, J., "2D and 3D finite element meshing and remeshing: A bibliography (1990-2001)," *Engineering Computations: Int J for Computer-Aided Engineering*, vol. 18(8), pp. 1108-1197, 2001.

[15] Mackerle, J., "Finite-element analysis and simulation of machining: an addendum A bibliography (1996-2002)," *International Journal of Machine Tools and Manufacture,* vol. 43, pp. 103-114, 2003.

[16] Ceretti, E., et al., "Application of 2D FEM to Chip Formation in Orthogonal Cutting,"

Journal of Materials Processing Technology, Vols. 59(1-2), pp. 160-180, 1996.

[17] Marusich, T.D. and M. Ortiz, "Modeling and Simulation of High-Speed Machining," *Int.ernational Journal for Numerical Methods in Engineering,* vol. 38, pp. 3675-3694, 1995.

[18] Mamalis, A.G., Horvath, M., Branis, A.S. and Manolakos, D.E., "Finite element simulation of chip formation in orthogonal metal cutting," *Journal of Materials Processing Technology,* vol. 110, pp. 19-27, 2001.

[19] Grzesik, W., "Determination of temperature distribution in the cutting zone using hybrid analytical-FEM technique," *International Journal of Machine Tools and Manufacture,* vol. 46, pp. 651-658, 2006.

[20] Astakhov, V.P., "Authentication of FEM in Metal Cutting," in *Finite Element Method in Manufacturing Processes*, J. Davim, Ed., Willey, 2011, pp. 1-43.

[21] Merchant, M.E., "Mechanics of the Metal Cutting Process. II. Plasticity Conditions in Orthogonal Cutting," *Journal of Applied Physics,* vol. 16, pp. 318-324, 1945.

[22] Hill, R., The Mathematical Theory of Plasticity, London: Oxford University Press, 1950.

[23] Hill, R., "The mechanics of machining: a new approach," *Journal of the Mechanics and Physics of Solids,* vol. 3, pp. 47-53, 1954.

[24] Pugh, H.L.D., "Mechanics of metal cutting process," in *Proc. IME Conf. Tech. Eng. Manufacture*, London, 1958.

[25] Chisholm AWJ., "A review of some basic research on the machining of metals," in *Proc. IME Conf. Tech. Eng. Manufacture,* London, 1958.

[26] Bailey, J.A., and Boothrouyd, G., "Critical review of xome previous work on the mechanics of the metal-cutting process," *ASME Journal of Engineering for Industry,* vol. 90, pp. 54-62, 1969.

[27] Creveling, J.H., Jordon, T.F., and Thomsen, E.G., "Some studies on angle relationship in metal cutting," *ASME Journal of Applied Mechanics,* vol. 79, pp. 127-138, 1958.

[28] Zorev, N.N., Metal cutting mechanics, Oxford: Pergamon Press, 1966.

[29] Zorev, N.N., "Results of work in the field of the mechanics of the metal cutting process," in *Proc. IME Conf. Tech. Eng. Manufacture,* London, 1958.

[30] Atkins, A.G. and Mai, Y.W., "Metals, Polymers. Ceramics, Composites, Biological Materials," in *Elastic and plastic fracture,* New York, John Wiley & Sons, 1985, p. 773.

[31] Atkins, A.G., "Modelling metal cutting using modern ductile fracture mechanics: quantitative explanations for some longstanding problems," *International Journal of Mechanical Science,* vol. 43, p. 373–396, 2003.

[32] Childs, T.H.C., Maekawa, K., Obikawa, T., and Yamane, Y., Metal Machining. Theory

and Application, London: Arnold, 2000.

[33] Trent, E.M.and Wright, P.K., Metal Cutting, 4th ed., Boston: Dutterworth-Heinemann, 2000.

[34] Astakhov, V.P., "On the inadequacy of the single-shear plane model of chip formation," *International Journal of Mechanical Sciences,* vol. 47, pp. 1649-1672, 2005.

[35] Outeiro, J.C., "Application of Recent Metal Cutting Approaches to the Study of the Machining Residual Stresses," in *Department of Mechanical Engineering, University of Coimbra*, Coimbra, 2003.

[36] Reuleaux, F., "'Über den taylor whiteschen werkzeugstahl verein sur berforderung des gewerbefleissen in preussen'," *Sitzungsberichete,* vol. 79, p. 179–220, 1900.

[37] Kingsbury, "Report of the present status and future problems in the art of cutting and forming metals," ASME Committee Report, 1924.

[38] Mallock, A., "The Action of Cutting Tools," in *Proceedings of the Royal Society of London*, 1881-1882.

[39] Kick, F., "Zur folge der wirkungsweise des taylor-white and der bohler-rapid-stahles," vol. 6, p. 277, 1901.

[40] Byers, J.P., Metalworking Fluids, Boca Raton: CRC Press, 2006.

[41] Taylor, F.W., "On the art of cutting metals," in *Transactions of ASME*, 1907.

[42] Reznikov, A.N., Theory of Metal Cutting (in Russian), Kyiv: ONTI State Publisher of Ukraine, 1934.

[43] Leeuw, A.I.D., Metal Cutting Toold: Their Principles, Action and Construction, London: McGraw-Hill, 1922.

[44] Klopstock, H., "Recent investigations in turning and planing and a new form of cutting tool," in *Transactions of the ASME*, 1925.

[45] Lee, E.H. and Shaffer, B.W., "The theory of plasticity applied to a problem of machining," *Journal of Applied Mechanics,* vol. 18, pp. 405-413, 1951.

[46] Oxley, P.L.B., Mechanics of machining: an analytical approach to assessing machinability, New York, USA: John Wiley & Sons, 1989, p. 242.

[47] Finnie, I., "Review of the metal-cutting analysis of the past hundred years," *Mechanical Engineering*, vol. 78, p. 715–721, 1956.

[48] Sampath, W.S. and Shaw, M.S., "Fracture on the shear plane in continuous cutting," in *11th NAMRI Conference*, Dearborn, 1983.

[49] Didjanin, L. and Kovac, P., "Fracture mechanisms in chip formation processes," *Materials Science and Technology,* vol. 13, p. 439–444, 1997.

[50] Merchant, M.E., "Basic Mechanics of Metal Cutting Process," *Journal of Applied Mechanics,* vol. 11, pp. A168-A175, 1944.

[51] "American National Standard Tool Life Testing With Single-Point Turning Tools ANSI/ASME B94.55M," in *ASME*, New York, 1985.

[52] Tool-life testing with single-point turning tools, ISO Standard 3685, 1993.

[53] Piispanen, V, "Lastunmuodostumisen teoriaa," *Teknillinen aikakauslehti 27* , pp. 315-322, 1937.

[54] Time, I., "Resistance of metals and wood to cutting," in *Dermacow Press House*, St. Petersbourg, Russia, 1870.

[55] Time, I., "Memore sur le rabotage de métaux," St. Petersbourg, Russia, 1877.

[56] Carroll, J.T. and J.S. Strenkowski, "Finite Element Models of Orthogonal Cutting with Application to Single Point Diamond Turning," *International Journal of Mechanical Sciences,* vol. 30, pp. 899-920, 1988.

[57] Zhang, B. and A. Bagchi, "Finite Element Simulation of Chip Formation and Comparison with Machining Experiment," *Journal of Engineering for Industry,* vol. 116(3), pp. 289-297, 1994.

[58] Komvopoulos, K., and Erpenbeck, S. A., "Finite element modeling of orthogonal metal cutting," *ASME Journal of Engineering for Industry,* vol. 113(3), pp. 253-267, 1991.

[59] Shih, A.J., "Finite Element Simulation of Orthogonal Metal Cutting," *Journal of Engineering for Industry,* vol. 117(1), pp. 84-93, 1995.

[60] Hashemi, J., A.A. Tseng, and P.C. Chou, "Finite Element Modeling of Segmental Chip Formation in High-Speed Orthogonal Cutting," *Journal of Materials Engineering and Performance,* vol. 3(5), pp. 712-721., 1994.

[61] Lin, Z.C., and Lin, S.Y., "A coupled finite element model of thermo-elastic-plastic large deformation for orthogonal cutting," *Journal of Engineering Materials and Technology,* vol. 114, pp. 218-226, 1992.

[62] Ernst, H., Physics of Metal Cutting, Cincinnati, OH, USA: The Cincinnati Milling Machine Co, 1938.

[63] Dieter, G., Mechanical Metallurgy, 2nd ed. ed., New York: McGraw-Hill, 1976.

[64] Blake, A., Handbook of Mechanics, Materials, and Structures, New York: John Wiley & Sons, 1985.

[65] Hamrock, B.J., Schmid, S.R., and Jacobson, B.O., Fundamentals of machine elements, Boston: McGraw-Hill Higher Education, 2005.

[66] Itava, K. and Ueda, K., "The significance of the dynamic crack behavior in chip formation," *Annals of the CIRP,* vol. 25, p. 65–70, 1976.

[67] Subbiah, S., and Melkote, S.N., "Evidence of ductile tearing ahead of the cutting tool and modeling the energy consumed in material separation in micro-cutting," *Journal of engineering materials and technology*, vol. 129(2), pp. 321-331, 2007.

[68] Roll, K., "Simulation of sheet metal forming–necessary developments in the future," in *LS-DYNA Anwenderforum*, Bamberg, Germany, 2008.

[69] Shaw, M.C. and J.O. Cookson, "Metal cutting principles," in *Tribology International*, 1985.

[70] Astakhov, V.P., "System outlook of research and application aspects," in *Metal cutting: research advances*, New York, NOVA SCIENCE PUBLISHERS, 2010, pp. 1-37.

[71] Tresca, H., "Sur l'ecoulement des corps solides soumis a de fortes pression," *C.R.Acad.Sci.*, vol. 59, pp. 754-791, 1864.

[72] Tresca, H., "'Mémores sur le rabotage des metaux', bulletin de la société d'encouragement pour l'industrie nationale," vol. 15, p. 585–685, 1873.

[73] Astakhov, V.P. and Shvets, S.V., "A system concept in metal cutting," *Journal of Materials Processing Technology*, Vols. 79(1-3), pp. 189-199, 1998.

[74] Abuladze, N.G., "The Tool-Chip Interface: Determination of the Contact Legth and Properties (in Russian), in Machniability of Heat Resistant and Titanium Alloys," *Kyibashev Regionsl Publ. House: Kyibashev (Russia)*, pp. 87-96, 1962.

[75] Astakhov, V.P., Svets, S.V. and Osman, M.O.M., "Chip structure classification based on mechanics of its formation," *Journal of Materials Processing Technology*, vol. 71(2), pp. 247-257, 1997.

[76] Astakhov, V.P. and Xiao, X., "A methodology for practical cutting force evaluation based on the energy spent in the cutting system," *Machining Science and Technology*, vol. 12, pp. 325-347, 2008.

[77] Liu A.F., Mechanics and Mechanisms of Fracture: An Introduction, Materials Park, OH: ASM International, 2006.

[78] Rice, J.R. and Tracey, D.M., "On the ductile enlargement of voids in triaxial stress fields," vol. 17, no. 0022-5096, pp. 201-217, 1969.

[79] Wierzbicki, T., Bao, Y., Lee, Y.W. and Bai, Y., "Calibration and evaluation of seven fracture models," *International Journal of Mechanical Sciences*, vol. 47, no. 0020-7403, pp. 719-743, 2005.

[80] McClintock, F.A., "A criterion for ductile fracture by growth of holes," *ASME Journal of Applied*, vol. 35, p. 363–71, 1968.

[81] Atkins, A.G., "Fracture in forming," *Journal of Materials Processing Technology*, vol. 56, pp. 609-618, 1996.

[82] Oyane, M., Sato, T., Okimoto, K., and Shima, S., "Criteria for ductile fracture and their

applications," *Journal of Mechanical Working Technology,* vol. 4, pp. 65--81, 1980.

[83] Leppin, C. and Hooputra, H. and Werner, H. and Weyer, S. and Buchi, RV, "Crashworthiness simulation of aluminium pressure die castings including fracture prediction," in *VIII International Conference on Computational Plasticity* , Barcelona, 2005.

[84] Wilkins, M.L. and Streit, R.D. and Reaugh, J.E., "Cumulative strain damage model of ductile fracture: Simulation and prediction of engineering fracture tests," 1980.

[85] Bai, Y. and Wierzbicki, T., "A new model of metal plasticity and fracture with pressure and Lode dependence," *International Journal of Plasticity,* vol. 24, no. 0749-6419, pp. 1071-1096, 2008.

[86] Wierzbicki, T. and Xue, L., "On the effect of the third invariant of the stress deviator on ductile fracture," Impact and Crashworthiness Laboratory, Cambridge, MA, 2005.

[87] Bai, Y., Teng, X. and Wierzbicki, T., "On the application of stress triaxiality formula for plane strain fracture testing," *Journal of Engineering Materials and Technology,* vol. 131, p. 021002, 2009.

[88] Teng, X. and Wierzbicki, T., "Evaluation of six fracture models in high velocity perforation," *Engineering Fracture Mechanics*, vol. 73, pp. 1653-1678, 2006.

[89] Xue, L., "Damage accumulation and fracture initiation in uncracked ductile solids subject to triaxial loading," *International Journal of Solids and Structures,* vol. 44, no. 0020-7683, pp. 5163-5181, 2007.

[90] Davim, J.P. and Maranhao, C., "A study of plastic strain and plastic strain rate in machining of steel AISI 1045 using FEM analysis," *Materials & Design,* vol. 30, no. 0261-3069, pp. 160-165, 2009.

[91] Jaspers, S. and Dautzenberg, J.H., "Material behaviour in conditions similar to metal cutting: flow stress in the primary shear zone," *Journal of Materials Processing Technology,* vol. 122, pp. 322-330, 2002.

[92] Jaspers, S. and Dautzenberg, J.H., "Material behaviour in metal cutting: strains, strain rates and temperatures in chip formation," *Journal of Materials Processing Technology,* vol. 121, no. 0924-0136, pp. 123-135, 2002.

[93] Zhang, Y.C., Mabrouki, T., Nelias, D. and Gong, Y.D., "Chip formation in orthogonal cutting considering interface limiting shear stress and damage evolution based on fracture energy approach," *Finite Elements in Analysis and Design,* vol. 47, pp. 860-863, 2011.

[94] Duan, C.Z., Dou, T., Cai, Y.J. and Li, Y.Y., "Finite element simulation and experiment of chip formation process during high speed machining of AISI 1045 hardened steel," *International Journal of Recent Trends in Engineering,* vol. 1, pp. 46-50, 2009.

[95] Velasquez, J., Bolle, B., Chevrier, P., Geandier, G. and Tidu, A., "Metallurgical study on chips obtained by high speed machining of a Ti–6 wt.%Al–4 wt.%V alloy," in *Mate Sci*

Eng A, 2007.

[96] Umbrello, D., "Finite element simulation of conventional and high speed machining of Ti6Al4V alloy," *Journal of Materials Processing Technology,* vol. 196, no. 0924-0136, pp. 79-87, 2008.

[97] Johnson, G.R. and Cook, W.H., "A constitutive model and data for metals subjected to large strains, high strain rates and high temperatures," in *Proceedings of the 7th International Symposium on Ballistics*, Netherlands, 1983.

[98] Johnson, G.R. and Cook, W.H., "Fracture characteristics of three metals subjected to various strains, strain rates, temperatures and pressures," *Engineering Fracture Mechanics,* vol. 21, no. 0013-7944, pp. 31-48, 1985.

[99] Hillerborg, A., Modeer, M., and Petersson, P.E., "Analysis of crack formation and crack growth in concrete by means of fracture mechanics and finite elements," *Cement and concrete research,* vol. 6, pp. 773-781, 1976.

[100] Clift, S.E., Hartley, P., Sturgess, C.E.N., and Rowe, G.W., "Fracture prediction in plastic deformation processes," *International Journal of Mechanical Sciences,* vol. 32, pp. 1-17, 1990.

[101] Bridgman, P.W., Studies in large plastic flow and fracture with special emphasis on the effects of hydrostatic pressure, McGraw-Hill, 1952.

[102] Bao, Y. and Wierzbicki, T., "On fracture locus in the equivalent strain and stress triaxiality space," *International Journal of Mechanical Sciences,* vol. 46, no. 0020-7403, pp. 81-98, 2004.

[103] Peters, W.H. and Ranson, W.F., "Digital imaging techniques in experimental stress analysis," *Optical Engineering,* vol. 21, 1982.

[104] Su, C. and Anand, L., "A new digital image correlation algorithm for whole-field displacement measurement," 2003.

[105] Stander,N., Roux,W., Goel, T., Eggleston, T. and Craig, K., A design optimization and probabilistic analysis tool for the engineering analyst, V4.2 ed., Livermore: Livermore Software Technology Corporation, 2012.

[106] Abushawashi, Y., Xiao, X. and Astakhov, V.P., "FEM Simulation of metal cutting using a new approach to model chip formation," *Int. J. Advances in Machining and Forming Operations,* vol. 3, pp. 71-92, 2011.

[107] M. Elices, G.V.Guinea, J.Gomez, J Planas, "The cohesive zone model: advantages, limitations and challenges," *Engineering Fracture mechanics,* vol. 69, pp. 137-163, 2002.

[108] N. Sukumar, N. Moës, B. Moran, T. Belytschko, "Extended finite element method for three-dimensional crack modelling," *International Journal for Numerical Methods in Engineering*, vol. 48, no. 11, p. 1549–1570, August 2000.

[109] Rech, J., Claudin, C. and D'Eramo, E., "Identification of a friction model-application to the

context of dry cutting of an AISI 1045 annealed steel with a TiN-coated carbide tool," *Tribology International*, vol. 42, no. 0301-679X, pp. 738-744, 2009.

[110] Ye, G. G., Xue, S. F., Ma, W., Jiang, M. Q., Ling, Z., Tong, X. H., and Dai, L. H. , "Cutting AISI 1045 steel at very high speeds," *International Journal of Machine Tools and Manufacture*, vol. 56, pp. 1-9, 2012.

[111] Meyers, M.A., Dynamic behavior of materials, New York: Wiley, 1994.

[112] Shaw, M.C., and Booser, E.R., "Metal removal," in *CRC Handbook of Lubrication: Theory and Practice of Tribology, Volume II: Theory and Design*, Boca Raton, CRC Press, 1988, pp. 335-356.

[113] Dahlman, P., Gunnberg, F., and Jacobson, M., "The influence of rake angle, cutting feed and cutting depth on residual stresses in hard turning," *Journal of Materials Processing Technology*, vol. 47(2), pp. 181-184, 2004.

[114] Gunay, M., Korkut, I., Aslan, E. and Seker, U., "Experimental investigation of the effect of cutting tool rake angle on main cutting force," *Journal of Materials Processing Technology*, vol. 166, pp. 44-49, 2005.

[115] Tetsuji, O., Hirokazu, K., and Shigeo, M., "Influence of clearance and rake angles on the cutting force of rock," *Journal of NIRE (National Institute for Resources and Environment)*, vol. 2(3), pp. 73-80, 1999.

[116] Gunay, M, Seker, U., and Sur, G., "Design and construction of a dynamometer to evaluate the influence of cutting tool rake angle on cutting forces," *Materials and Design*, vol. 27, pp. 1097-1101, 2006.

[117] Saglam, H., Yaldiz, S., and Unsacar, F., "The effect of tool geometry and cutting speed on main cutting force and tool tip temperature," *Materials and Design*, vol. 29, pp. 101-111, 2007.

[118] Takeyama, H., and Usui, H., "The effect of tool-chip contact area in metal cutting," *ASME Journal of Engineering for Industry*, vol. 79, pp. 1089-1096, 1958.

[119] Chao, B.T., and Trigger, K.J., "Controlled contact cutting tools," *Transactions of the ASME*, vol. 81, pp. 139-151, 1959.

[120] Usui, E., and Shaw, M.C., "Free machining steel - IV: Tools with reduced contact length," *Transactions of the ASME*, vol. B84, pp. 89-101, 1962.

[121] Hoshi, K., and Usui, E., "Wear characteristics of carbide tools with artificially controlled tool-chip contact length," in *Proceedings of the Third International MTDR Conference*, New York, 1962.

[122] Usui, E., Kikuchi, K., and Hoshi, K., "The theory of plasticity applied to machining with cut-away tools," *Transactions of the ASME*, vol. B86, pp. 95-104, 1964.

[123] Davim, J.P., and Astakhov, V.P., "Modern machining technology," in *Turning*, Cambrige, Woodhead , 2011, pp. 1-78.

[124] Astakhov, V.P., "The assessment of cutting tool wear," *International Journal of Machine Tools and Manufacture,* vol. 44, pp. 637-647, 2004.

[125] Wick, C., and Veilleux, R.F., Tool and Manufacturing Engineers Handbook: Materials, Finishing, and Coating (Vol. 3), Dearborn: SME, 2006.

[126] Jawahir, I. S., and Van Luttervelt, C. A., "Recent Developments in Chip Control Research and Applications," *Annals of the CIRP,* vol. 42(2), pp. 659-693, 1993.

[127] Astakhov, V.P. and Joksch, S., "Metal working fluids for cutting and grinding: fundamentals and recent advances," Woodhead, London, 2011.

[128] Astakhov, V.P., Tribology of Metal Cutting, New York: Marcel Dekker, 2004, pp. 307-346.

[129] Schey, J.A., "Tribology in metalworking," in *American Society for Metals,* Metals Park, Ohio, 1983.

[130] Abushawashi, Y., Xiao, X. and Astakhov, V.P., "Heat Conduction vs. Heat Advection in Metal Cutting," *Int. J. Advances in Machining and Forming Operations,* vol. 4, no. 2, pp. 133-151, 2012.

[131] Schmidt, A.O., Gilbert, W.W., and Boston, O.W., "A thermal balance method and mechanical investigation of evalutating machinability," *Transactions of ASME,* vol. 67, pp. 225-232, 1945.

[132] Komanduri, R., and Hou, Z.B., "A review of the experimental techniques for the measurement of heat and temperatures generated in some manufacturing processes and tribology," *Tribology International,* vol. 34, p. 653–682, 2001.

[133] Schmidt, A.O., and Roubik, J.R., "Distribution of heat generated in drilling," *Transactions of ASME,* vol. 7, pp. 242-245, 1949.

[134] Kronenberg, M., Machining Science and Application. Theory and Practice for Operation and Development of Machining Processes, Pergamon Press, 1966.

[135] Klocke, F., Manufacturing Processes 1: Cutting, Berlin: Springer-Verlag, 2011.

[136] Grzesik, G., Advanced Machining Processes Of Metallic Materials: Theory, Modelling and Application, Oxford: Elsevier, 2008.

[137] Parashar, B.S.N., and Mittal, R.K., Elements of Manufacturing Process, New Delhi: Prenstice, 2006.

[138] Silin, S.S., Similarity Methods in Metal Cutting (in Russian), Moscow: Mashinostroenie, 1979.

[139] Smart, E.F. and Trent E.M., "Temperature distribution in tools used for cutting iron, titanium and nickel," *International Journal of Production Research,* vol. 13.3, pp. 265-290, 1975.

[140] Granovsky, G.E., and Granovsky, V.G., Metal Cutting (in Russian), Moscow: Vishaya Shkola, 1985.

[141] Bejan, A., Heat Transfer, New York: John Wiley & Sons, 1993.

[142] Spaans, C., "Treatise on the streamlines and the stress, strain, and strain rate distribution, and on stability in the primary shear zone in metal cutting," *ASME Journal of Engineering for Industry,* vol. 94, pp. 690-696, 1972.

[143] Rosenberg, A.M., and Rosenberg, O.A., "The state of stress and deformation in metal cutting, (in Russian)," *Superhard Materials (Sverhtverdye Materaily),* vol. 41(5), 1988.

[144] Altintas, Y., Manufacturing Automation. Metal Cutting Mechanics, Machine Tool Vibrations, and CNC Design, Cambridge University Press, 2000.

[145] Astakhov V.P. and Shvets, S.V., "The assessment of plastic deformation in metal cutting," *Journal of Materials Processing Technology,* vol. 146(2), pp. 193-202, 2004.

[146] Slater, R.A.C., Engineering Plasticity: Theory and Application to Metal Forming Processes, London: The Macmillan Press Ltd., 1977.

[147] Davis, J.R., Tensile Testing, Materials Park, OH: ASTM, 2004.

[148] Poletica, M.F., "Contact Loads on Cutting Tool Interface Surfaces (in Russian)," *Mashinostroenie,* 1969.

[149] Loladze, T.N., Strength and Wear of Cutting Tools (in Russian), Moscow: Mashgiz, 1958.

[150] Zhang, J.H., Theory and Technique of Precision Cutting, Oxford, NY: Pergamon Press, 1991.

[151] Karpat, Y., and Ozel, T., "Analytical and thermal modeling of high-speed machining with chamfered tools," *Journal of Manufacturing Science and Engineering,* vol. 130, pp. 1-15, 2008.

[152] Sadic, M.I., and Lindstrom, B., "The role of tool-chip contact length in metal cutting," *Journal of Materials Processing Technology,* vol. 37, pp. 613-627, 1993.

[153] Sadic, M.I., and Lindstrom, B., "The effect of restricted contact length on tool performance," *Journal of Materials Processing Technology,* vol. 48, pp. 275-282, 1995.

[154] Rodrigues, A.R., and Coelho, R.T., "Influence of the tool edge geometry on specific cutting energy at high-speed cutting," *Journal of the Braz. Soc. of Mech. Sci. and Eng.,* vol. XXIX, pp. 279-283, 2007.

[155] Abushawashi, Y., Xiao, X. and Astakhov, V.P., "A novel approach for determining material constitutive parameters in orthogonal machining," *International Journal of Mechanical Sciences,* 2012.

[156] Duan, C.Z., Dou, T. and Wang, M., "Research on Influence of Material Hardness and Cutting Conditions on Serrated Chip Formation Process during High Speed Machining of AISI 1045 Hardened Steel," in *Computer Engineering and Technology (ICCET), 2nd*

International Conference, Chengdu, 2010.

[157] Atkins, T., The Science and Engineering of Cutting, Amsterdam: Butterworth-Heinemann, 2009.

[158] Astakhov, V.P. and Davim, P.J., "Tools (geometry and material) and tool wear, in machining: fundamentals and recent advances," P.J.Davim, Ed., London, Springer, 2008, pp. 29-58.

[159] Bareggi, A., O'Donnell, G.E. and Torrance, A., "Modeling thermal effects in machining by finite element methods," in *International Manufacturing Conference.* , Waterford, 2007.

[160] Abukhshim, N.A., Mativenga, P.T., and Sheikh, M.A., "Heat generation and temperature prediction in metal cutting: A review and implications for high speed machining," *International Journal of Machine Tools and Manufacture,* vol. 46, no. 0890-6955, pp. 782-800, 2006.

[161] Fang, G. and Zeng, P., "Three-dimensional thermo–elastic–plastic coupled FEM simulations for metal oblique cutting processes," *Journal of Materials Processing Technology,* vol. 168, pp. 42-48, 2005.

[162] Grzesik, W., Bartoszuk, M. and Nieslony, P., "Finite element modeling of temperature distribution in the cutting zone in turning processes with differently coated tools," *Journal of Materials Processing Technology,* Vols. 164-165, p. 1204–1211, 2005.

[163] Majumdar, P., Jayaramachandran, R. and Ganesan, S., "Finite element analysis of temperature rise in metal cutting processes," *Applied Thermal Engineering,* vol. 25, no. 1359-4311, pp. 2152-2168, 2005.

[164] Guo, Y.B. and Yen, D.W., "Study of discontinuous chip formation in had machining," *Journal of Materials Processing Technology,* Vols. 155-156, pp. 1350-1356, 2004.

[165] Komarovsky, A.A. and Astakhov, V.P., "Physics of strength and fracture control: fundamentals of the adaptation of engineering materials and structures," Boca Raton, CRC Press, 2002.

[166] Huq, M.Z. and Celis, J.P., "Expressing wear rate in sliding contacts based on dissipated energy," *Wear,* vol. 252, pp. 375-383, 2002.

[167] Ivester, R.W., Kennedy, M., Davies, M., Stevenson, R.J., Thiele, J., Furness, R. and Athavale, S., "Assessment of machining models: progress report," Sydney, Australia, 2000.

[168] Jawahir, I.S. and Zhang, J.P., "An analysis of chip curl development, chip deformation and chip breaking in orthogonal machining," *Transactions-North American Manufacturing Research Institution of SME,* pp. 109-114, 1995.

[169] Boothroyd, G. and Knight, W.A., Fundamentals of machining and machine tools, 2nd edition ed., New York: Marcel Dekker, 1989.

[170] Usui, E. and T. Shirakashi., "Mechanics of metal cutting–From "Description" to

“Predictive” Theory," in *On the Art of Cutting Metals–75 Years Later*, 1982.

[171] Boothroyd, G., Fundamentals of metal machining and machine tools, Kogakusha: McGraw-Hill, 1975.

[172] Black, P.H., Theory of metal cutting, New York: McGraw-Hill, 1961.

[173] A. Nadai, Theory of flow and fracture of solids, 2nd ed., vol. 1, New York: McGraw-Hill New York, 1950, pp. 347-349.

[174] Briks, A.A., "Metal cutting (in Russian)," 1896.

[175] Zvorykin, K.A., "‘On the force and energy needed to separate the chip from the workpiece (in Russian)’," *Tekhicheskii Sbornik i Vestnic Promyslinosty*, vol. 123, p. 57–96, 1896.

[176] DeGarmo, E.P., Black, J.T., and Kohser, R.A., Materials and Processes in Manufacturing, Upper Saddle River, NJ: Prentice Hall, 1997.

[177] Stenphenson, D.A., and Agapiou, J.S., Metal Cutting Theory and Practice, New York: Marcel Dekker, 1996.

[178] Abushawashi, Y., Xiao, X. and Astakhov, V.P., "Ductile Fracture in Orthogonal Metal Cutting: Numerical Simulations and Verification Experiment," *International Journal of Machine Tools and Manufacture*, 2013.

[179] Abushawashi, Y., Xiao, X. and Astakhov, V.P., "Modeling of serrated chip formation with a fracture locus approach," in *American Society of Mechanical Engineers (ASME)*, Denver, CO, USA, 2011.

[180] Astakhov, V.P., "A treatise on material characterization in the metal cutting process. Part 2: cutting as the fracture of workpiece material," *Journal of Materials Processing Technology*, Vols. 96(1-3), pp. 34-41, 1999.